Control and stability of magnetised plasma columns : plasma-cathode interactions and helicon plasma operation

Francis Pagaud

To cite this version:

Francis Pagaud. Control and stability of magnetised plasma columns : plasma-cathode interactions and helicon plasma operation. Plasma Physics [physics.plasm-ph]. Ecole normale supérieure de lyon - ENS LYON, 2024. English. NNT : 2024ENSL0016 . tel-04679798

HAL Id: tel-04679798
https://theses.hal.science/tel-04679798
Submitted on 28 Aug 2024

THÈSE

en vue de l'obtention du grade de Docteur, délivrée par

l'École Normale Supérieure de Lyon

École Doctorale N°52
École Doctorale de Physique et Astrophysique de Lyon (PHAST)

Discipline : Physique

Soutenue publiquement le 01/07/2024, par :

Francis PAGAUD

Control and stability of magnetised plasma columns:
plasma-cathode interactions and helicon plasma operation

Contrôle et stabilité des colonnes de plasma magnétisées :
interactions plasma-cathode et opération d'un plasma hélicon

Devant le jury composé de :

ARNAS, Cécile	Directrice de recherche	PIIM, CNRS	Rapportrice
HEURAUX, Stéphane	Professeur des universités	IJL, Université de Lorraine	Rapporteur
FURNO, Ivo	Professeur adjoint	Swiss Plasma Center, EPFL	Examinateur
GUEROULT, Renaud	Chargé de recherche, HDR	LAPLACE, CNRS	Examinateur
TSIKATA, Sedina	Professeur des universités	Georgia Institute of Technology, CNRS	Examinatrice
PLIHON, Nicolas	Directeur de recherche	LPENSL, CNRS	Directeur de thèse

REMERCIEMENTS

Le voilà enfin entre vos mains ce manuscrit de thèse ! Après des centaines d'heures d'expériences, plusieurs mois de rédaction et beaucoup de moments passés à essayer de comprendre ce foutu plasma, ces pages mettent du sens derrière ces trois années de doctorat - à mes yeux en tout cas. Peut-être que vous y trouverez une figure inspirante, une interprétation élégante ou une explication convaincante, alors j'en serai ravi. Bien qu'il représente beaucoup pour moi, que j'y ai investi du temps et un peu de ma personnalité, ce manuscrit sera vite oublié et obsolète, j'en suis bien conscient. Cette minuscule brique élémentaire de la physique des plasmas froids magnétisés restera une contribution modeste à la recherche scientifique. Mais cette thèse me laisse une trace bien plus importante, et j'en aurai tiré une compréhension grisante de la physique des plasmas, une maturité grandie dans le monde de la recherche et de l'enseignement. Surtout j'en retiendrai des rencontres spéciales, des interactions marquantes, des pauses cafés (plus ou moins longues) mémorables... En somme, un millier de moments inoubliables. Alors dans cette courte partie à laquelle je tiens profondément, je souhaite mentionner les personnes qui m'ont entouré, soutenu, accompagné au cours de ces trois années si spéciales.

Tout d'abord je souhaiterais adresser mes premiers remerciements à mon jury de doctorat. Merci à **Cécile Arnas** et **Stéphane Heuraux** d'avoir accepté d'évaluer mes travaux avec autant d'indulgence et d'intérêt. Merci également à **Ivo Furno**, **Renaud Gueroult** et **Sedina Tsikata** pour leur participation à ma soutenance de thèse. Ce jury m'honore vraiment, puisqu'il est constitué de scientifiques renommés et de personnes bienveillantes que je respecte sincèrement.

En premier lieu, je voudrais adresser des remerciements tout particuliers à **Nicolas**. Durant cette thèse je me suis épanoui sous ta supervision. Tu m'as toujours accompagné tout en me laissant une grande autonomie. J'ai pu poser toutes mes questions, développer mes idées, prendre confiance et grandir. Avec tout ce que tu as pu m'apporter, je rentre dans le monde de la recherche de la meilleure des manières, avec envie et une formation unique. Mais le plus important à mes yeux, c'est tout ce qu'il y a autour. Merci d'avoir été autant à l'écoute, aussi empathique et humain. Durant cette thèse, j'aurai appris bien plus que la physique des plasmas, et c'est en grande partie grâce à toi.

Un grand merci également à **Vincent**, pour ton regard critique et ta bonne humeur. Ces travaux ne pourraient pas non plus exister sans les expertises de **Marc** et **Pascal**. A vous trois, merci pour votre implication, votre patience et votre gentillesse. Je remercie égalements les stagiaires **Till**, **Eitan** et **Vassili** que j'ai pu encadrés avec beaucoup de plaisir. Enfin, merci à **Jean-Christophe**, **Erika** et **Fatiha**, qui sont tant moteurs au quoitidien au sein du laboratoire.

Durant ces trois années, j'ai eu la chance de rencontrer de nombreux et nombreuses spécialistes de la physique des plasmas avec qui j'ai eu grand plaisir d'échanger. Je souhaiterais remercier **Renaud** et **Baptiste** du laboratoire LAPLACE, **Ivo** et son groupe au Swiss Plasma Center, et plus particulièrement **Rémy** et **Philippe**. Le groupe SoPlasma a aussi beaucoup contribué à mes travaux grâce à des discussions de qualité, que ce soit dans le Vieux port de Marseille ou dans les ruelles du vieux Lyon. Enfin, je dois une fière chandelle à mes deux grands frères de thèse, **Victor** et **Simon**, pour avoir chouchouté l'expérience VKP et développé des outils puissants et indispensables à mes travaux. Mais aussi pour m'avoir accordé leur temps avec énormément de bienveillance, et ce même pendant la rédaction de thèse. Maintenant que j'ai traversé cette épreuve, je t'en suis d'autant plus reconnaissant Simon !

Ensuite, au-delà du domaine scientifique, je souhaiterais remercier mes amis et mes proches qui m'ont entouré pendant ces trois années. Merci à **mes parents**, **mon frère**, et plus largement toute **ma famille**, pour leur soutien, leur patience et leur compréhension face à tout ce que j'ai pu traverser pendant mes études (à défaut de partager mon enthousiasme pour mes problèmes bizarres, et pourquoi ça t'intéresse ce truc, mais ça sert à quoi en fait ?).

Ces années exceptionnelles ont été marquées par des beaux moments passés avec les cool kids du labo. Un immense merci du fond du cœur pour tous les moments chaleureux passés en compagnie de **Julie**, **Brivaël**, **Nicolas**, **François Liénard**, **Coco**, **Thomas**, **Saskia**, **François Gu**, **Steph**, **Louis** et j'en passe ! Merci à tous les membres de **Topic-BG**, que je ne vais pas tous nommer puisque j'en oublierai forcément, pour tous les moments de science et de vie, avec en point d'orgue la légendaire sortie pizza chez Zappo.

Ce travail de thèse m'est tout personnel, il contient un peu de moi et beaucoup des gens qui m'entourent. Alors je veux adresser des remerciements à mes fidèles amis si importants à mes yeux. Je pense à mes amis jurassiens bien sûr, à savoir **Mathis**, **Camille**, **Victor**, **Charline**, **Sarah**, **Théo**, **Duf** et **Pierre**. Avec ma famille, ils forment un endroit que je considère comme chez moi malgré les années expatriées loin de mes montagnes jurassiennes ! Ensuite, j'ai passé d'incroyables moments (et enduré des blessures plus ou moins handicapantes) dans le fantasque club de rugby du COL. Merci à mes courageux coachs **Jacquo**, **Zyk** et **Montalban** et à tous mes coéquipiers, avec en tête **Pike**, **Adri** et **Thibault**. Un grand merci à mes amis lyonnais qui m'ont accompagnés, natifs ou d'adoption. Merci à **Arturito**, **Fenrilito**, **QRF**, **Marwane**, **Raph**, **Louis Combe**, **Fred**, **Rémi**, **Solène**, **Jules** & **Jules**, et j'en passe et des meilleurs. Pour finir cette longue liste, je veux garder un mot spécial pour certaines personnes dont la présence a particulièrement comptée durant ces trois années. À **Emma**, merci pour les aventures flinguées qui m'ont donné tant de force et d'optimisme, qu'elles soient apaisantes ou pleines de paillettes. Merci pour ton authenticité et ton écoute sans faille. À **Loulou** (même si c'est pas mon surnom préféré), merci pour les jeux de mots pourris, les parties rageantes de jeu de société et les soirées folles. Merci surtout d'avoir été là à tout moment, avec ton empathie sincère et réconfortante. À **Nono**, merci pour ta profonde gentillesse, ton sourire à toute épreuve et ton ouverture aux amis qui t'entourent, dont je suis heureux de faire partie. Et à **Mariane**, dont la rencontre aura changé tellement de choses, merci de m'avoir emmené au-delà des horizons, avec ce parfum de liberté si grisant.

Enfin, je voudrais remercier les trois acolytes avec qui j'aurai véritablement vécu cette période, à commencer par **Elian**. Merci pour toutes les discussions passionnantes de science, de cinéma et de couleur de cheveux, les épopées en Chartreuse et en sortie de bar... Tous ces moments qui ont apportés leur sel à ces trois années. Mais surtout merci de t'être autant soucié des autres (dont moi) pendant ces années. En te souhaitant plein de courage pour ta thèse à ton tour !

Un grand merci à **Dop**, qui aura rendu le labo un peu moins studieux mais terriblement plus vivant ! Pour ta générosité, toutes tes performances hors du commun, les discussions infernales (ne reparle plus jamais du Jura comme ça par contre), les fous rires et les questions existentielles, merci mille fois.

Enfin, un immense merci à **Gauthier**, sans qui cette thèse n'aurait jamais été ce qu'elle est devenue. Pour tous les moments studieux et les craquages dans le bureau idéal, pour nos foultitudes d'aventures même en dehors du labo, pour ton soutien indéfectible, ta sincérité et ton ouverture d'esprit à (presque) chaque instant qui m'ont fait grandir pendant ces trois années : merci infiniment. T'es vraiment le GOAT !

RÉSUMÉ

Le transport, les ondes et les instabilités sont des problématiques courantes des plasmas magnétisés, à l'origine de problèmes fondamentaux et de limites opératoires pour les plasmas de fusion, les accélérateurs de particules à plasma ou la propulsion plasma. Le contrôle des propriétés du plasma est souhaitable mais complexe. Ce doctorat vise à utiliser une cathode émissive comme nouveau paramètre de contrôle et à comprendre la stabilité du plasma hélicon.

Le dispositif expérimental est une enceinte à vide cylindrique de 80 cm de long et 20 cm de diamètre, connecté à un tube source en verre de 11 cm de diamètre. L'argon est injecté en continu à 0,13 Pa et ionisé par une antenne radiofréquence inductive de 1 kW enroulée autour du tube source. Un champ magnétique de 170 G à 340 G garantit une faible magnétisation. Une cathode chaude injecte un fort courant thermionique à l'autre extrémité de la colonne de plasma. Les mesures optiques de température de la cathode ont révélé un profil fortement inhomogène dû aux interactions plasma-cathode, et fut reproduit numériquement avec succès par un modèle thermique détaillé. Le régime opératoire prédit est en excellent accord avec les expériences.

L'influence expérimentale de l'injection d'électrons sur les propriétés plasmas, et plus particulièrement le potentiel plasma, a été couplée à une approche analytique basée sur un modèle de plasma magnétisé. Un accord qualitatif entre les prédictions théoriques et le contrôle effectif du potentiel plasma a été trouvé. La perspective de l'utilisation d'une cathode émissive comme nouveau paramètre de contrôle ouvre la possibilité d'un réglage fin de la dynamique globale du plasma, ainsi que la mitigation du transport et des instabilités au sein du plasma. Des améliorations sont discutées en vue d'une prédiction quantitative accrue.

Enfin, une source de plasma hélicon haute densité a été implémentée afin d'atteindre des taux d'ionisation importants et un couplage antenne-plasma optimal. Ce nouveau système a été caractérisé à l'aide de sondes et d'imagerie rapide. Des signatures typiques des plasmas hélicons ont été retrouvées telles que des transitions de mode E-H-W, une rupture de symétrie liée au champ magnétique et la propagation d'ondes whistler m = +1. En outre, des oscillations basse-fréquence telles que des oscillations H-W et W-W, et des instabilités coexistantes de Rayleigh-Taylor et Kelvin-Helmholtz ont été identifiées. Une forte instabilité multi-échelles à 1080 G a été également brièvement explorée. L'identification des mécanismes d'instabilité via le calcul des taux de croissance, la décomposition 2D-FT et POD ont permis de comprendre les mécanismes physiques à l'œuvre.

ABSTRACT

Radial transport, azimuthal waves and instabilities are common features in magnetised plasmas, causing major challenges for plasma propulsion, plasma wakefield particle acceleration or fusion devices. Plasma properties control is desirable yet complex. This PhD thesis follows two goals, one being the use of an emissive cathode as a new parameter control and the other being the fundamental understanding of the helicon plasma operational stability.

Firstly, the role of the injection of electrons inside a magnetised plasma column has been studied experimentally and numerically. The experimental set-up is a 80 cm long and 20 cm diameter vacuum vessel connected to a 11 cm wide glass tube. The argon gas at a base pressure of 0.13 Pa is ionised by a 3-turns inductive radio-frequency antenna supplied at 1 kW. Magnetic field ranging from 170 G to 340 G, ensures a weak magnetisation of the plasma. A large tungsten hot cathode was placed at the end of the plasma column to inject an important thermionic current. Electrical and optical measurements of the cathode temperature revealed a highly inhomogeneous cathode temperature profile due to plasma–cathode interactions. A detailed thermal modelling solved numerically accurately reproduces the heterogeneous rise in temperature witnessed experimentally. The operating regime was predicted in excellent agreement with experimental results.

The fine understanding of the emissive cathode behaviour in presence of a surrounding magnetised plasma permitted to explore its influence on the plasma properties, and especially the plasma potential. An analytical approach based on a two-fluids plasma model and anisotropic electrical conductivities, predicting plasma potential control and plasma rotation regulation as a function of thermionic emission, has been applied and compared to a wide experimental dataset of plasma properties. The works presented confront the role of cross-field ion transport to experimental radial plasma potential scans with a semi-quantitative agreement, highlighting a new major application of emissive cathodes.

Finally, a state-of-the-art helicon plasma source has been implemented to produce higher ionisation rates. This new system required a complete characterisation of plasma properties through electrostatic probes and high-speed camera imaging. It reproduced well-known helicon plasma features such as E-H-W mode transitions, bistability and hysteresis, chirality emerging from the external magnetic field direction and the propagation of $m = +1$ whistler waves. Besides, it displayed complex behaviours such as H-W and W-W oscillations, or coexisting low-frequency Kelvin-Helmholtz and Rayleigh-Taylor instabilities. A strong multiscale core instability at 1080 G was also briefly investigated. Wave-mode identification based on theoretical growth rates, 2D-FT modal decomposition and POD has been conducted, unravelling the physical mechanisms at stake.

TABLE DES MATIÈRES

INTRODUCTION

Le plasma est souvent appelé quatrième état de la matière. Pourtant, si les états solide, liquide et gazeux sont familiers auprès du grand public, l'état plasma est largement méconnu. La raison est sa présence limitée sur Terre en l'absence d'action humaine. Il existe tout de même quelques exemples notables, tels que la foudre ou les flammes très chaudes. En regardant au-delà de la troposphère, les exemples deviennent plus nombreux : les queues des comètes, la ionosphère ou même la magnétosphère sont composées de plasma. Dans l'espace, cet état de la matière est omniprésent. Le vent solaire, les milieux interplanétaire et interstellaire, les nébuleuses, les disques d'accrétion et bien sûr les étoiles sont tous composés de plasma, si bien que 99% de la matière observable est sous l'état de plasma. La compréhension de ce milieu apparait comme fondamentale et essentielle.

Un plasma est un milieu gazeux ionisé globalement neutre, et démontrant des effets collectifs. Ainsi, cet état est composé d'ions et d'électrons en grande quantité. Cela n'est possible qu'à des températures de l'ordre de plusieurs dizaines de milliers de Kelvin, nécessaires afin d'atteindre l'ionisation. Ces processus énergétiques intenses se produisent difficilement dans notre environnement proche. En effet, la forte pression atmosphérique induit une diffusion thermique trop importante pour qu'un gaz atteigne durablement ces températures avec les énergies typiquement observées sur Terre. En comparaison, les milieux spatiaux dilués rendent possible l'existence de particules suffisament énergétiques pour ioniser la matière neutre et rendre possible la transition à l'état plasma. De l'autre côté du spectre, les milieux très denses observables aux échelles stellaires permettent d'atteindre des hautes pressions et hautes températures, et l'existence d'un plasma fortement énergétique. De par leur composition d'espèces chargées, ces milieux gazeux, décrits par la mécanique des fluides, sont également sensibles aux interactions électromagnétiques. Il en résulte une dynamique et une complexité uniques. Par exemple, l'application d'un champ électrique ou magnétique extérieur modifie la dynamique de ce milieu. De plus, des comportements collectifs à longue portée émergent, comme l'apparition de nouvelles ondes et instabilités mécaniques ou électromagnétiques.

L'étude de ces milieux est récente à l'échelle de la physique moderne. D'abord motivé par l'analyse de la propagation des ondes radio, Irving Langmuir se concentre pour la première fois sur cet état de la matière dans les années 1920, et lui attribuera alors sa dénomination d'état « plasma ». Ces travaux ont été poursuivis et étendus à d'autres domaines d'application, motivés par la croissance rapide de l'électronique et l'étude fondamentale des milieux astrophysiques. Hannes Alfvén s'intéresse ensuite aux plasmas magnétisés dans les années 1940, observables au sein de la magnétosphère de certaines planètes et étoiles, et ouvre un large pan de la physique des plasmas. Les expériences consacrées aux plasmas de fusion, destinées à la compréhension des réactions au cœur des étoiles, connait une expansion majeure à la fin des années 1960. En pleine guerre froide, une collaboration scientifique internationale émergea entre britanniques et soviétiques. De cette dynamique fructueuse s'est dégagée une effervescence autour des tokamaks, dans lesquels des plasmas de plus de 10 millions de Kelvin ont été observés pour la première fois. Ces efforts se poursuivent encore aujourd'hui avec l'expérience internationale ITER. L'application des plasmas à l'échelle industrielle survient à partir des années 1980, avec l'avènement de la micro-électronique. Les processus énergétiques se déroulant dans un plasma sont mis à profit pour la gravure de circuits à l'échelle sub-millimétrique. De nos jours, alors que la compréhension de l'état plasma progresse et que la production des hautes énergies s'avèrent de plus en plus accessible, le plasma ouvre de nombreuses perspectives technologiques. Ainsi, les plasmas à faible densité permettent une propulsion spatiale efficace et à moindre coût. Les plasmas à pression atmosphérique démontrent de prometteuses avancées dans le domaine du vivant, telles que le traitement de cellules cancéreuses, l'accélération des processus de cicatrisation ou l'amélioration de la croissance de graines stérilisées par plasma. Le développement massif des lasers hautes intensités rend possible la génération de plasmas très haute densité. Ceux-ci se sont révélés de premier plan pour l'étude des milieux chauds et des réactions de fusion nucléaire au National Ignition Facility (Livermore, Etats-Unis). Ainsi, un rendement de réaction de fusion supérieur à 1 a été observé pour la première fois en 2021, et ne cesse de progresser depuis. Enfin, la complexité de ce milieu et les perspectives ambitieuses qu'il permet sont incarnées par la fusion thermonucléaire par confinement magnétique.

Étude des plasmas magnétisés

La fusion par confinement magnétique consiste à atteindre des températures suffisamment élevées afin de déclencher des réactions de fusion sur des échelles de temps de l'ordre de la minute. Les expériences les plus développées prennent la forme d'un tokamak, c'est-à-dire un tore confiné par un champ magnétique intense. Les espèces du plasma sont magnétisées, et le contact avec les murs extérieurs est limité. Ainsi, le cœur du plasma, qualifié de plasma chaud, atteint des températures jusqu'à 100 millions de Kelvin, avec des densités de l'ordre de 10^{20} m^{-3}. D'autre part, le bord est un plasma froid de quelques dizaines de milliers de Kelvin et de densité de l'ordre de 10^{18} m^{-3}. Au-delà de l'investigation fondamentale de la fusion nucléaire et de la compréhension apportée à l'étude des étoiles, ces réacteurs portent l'espoir d'une énergie nucléaire décarbonée, accessible et non dangereuse. Ce domaine très dynamique connait une croissance rapide via de multiples collaborations internationales sur les tokamaks les plus avancés du monde [Wur+22]. Par exemple, en Décembre 2023, le tokamak Joint European Torus (JET) à Culham (Royaume-Uni) a battu des records de production d'énergie dans sa dernière campagne de mesure, démontrant une puissance de plus de 13 MW pendant 5 secondes. D'autre part, les différents tokamaks dans le monde fournissent des données complémentaires en testant divers équipements. On peut citer les tokamaks TCV à Lausanne (Suisse), très modulable et permettant d'explorer différentes géométries, WEST à Cadarache (France), consacré à l'étude du diverteur, l'élément faisant face aux plus importantes contraintes thermiques dans l'enceinte, ou encore les installations de premier plan D-III D à San Diego (Etats-Unis), ASDEX Upgrade à Garching (Allemagne), KSTAR à Daejon (Corée du Sud) ou EAST à Hefei (Chine). L'effervescence partagée autour de ces thématiques est motivée par l'assemblement prochain de ITER, le premier projet de fusion nucléaire par confinement magnétique destiné à produire plus d'énergie que n'en est consommée pour le chauffage du plasma. La réussite de ce projet est un jalon essentiel, puisqu'il représente un premier pas vers le développement d'une centrale nucléaire à fusion. Les ambitions de commercialisation de l'énergie nucléaire de fusion sont destinées à 2050.

Cependant, l'aspect multi-échelles de la fusion nucléaire rend sa physique très complexe. Le temps de confinement devant être maximisé afin d'augmenter les réactions de fusion et la production d'énergie associée, la stabilité du plasma est un enjeu majeur. Or, il est perturbé par de nombreuses instabilités aux bords du plasma, dénommées Edge Localized Modes (ELM), causant un important transport d'énergie du cœ]ur vers l'extérieur. De plus, la turbulence qui se développe au sein de ces plasmas induit un transport accru d'énergie en direction des parois. La mitigation des instabilités et de la turbulence au sein des plasmas chauds est essentielle. De plus, le flux thermique résultant peut endommager la structure du tokamak, et l'enceinte doit pouvoir endurer des contraintes thermiques élevées. C'est pourquoi l'étude des interactions plasma-surfaces est un enjeu crucial pour le développement de la fusion par confinement magnétique. Une dernière problématique que l'on peut mentionner est celle du chauffage. Afin d'atteindre des températures aussi élevées, le développement des dispositifs de chauffage tels que les injecteurs de neutres (NBI) ou le chauffage par onde hélicon est nécessaire. Cette courte liste n'est pas exhaustive, et de nombreuses questions scientifiques et technologiques persistent. Cependant, les tokamaks étant des structures lourdes et difficiles à contrôler, de plus petites structures expérimentales sont utilisées afin de poursuivre des études fondamentales ciblées.

Les dispositifs linéaires, c'est-à-dire des infrastructures en géométrie cylindrique et magnétisées, présentent des alternatives modulables de taille moyenne pour l'étude fondamentale des plasmas froids. La forme cylindrique et les champs magnétiques atteignant jusqu'à $\sim$ 200 mT limitent le temps de confinement de ces plasmas. Ainsi, l'équilibre thermodynamique n'est pas atteint, et une modélisation bi-fluide du plasma, modélisant indépendamment les ions et les électrons, est souvent nécessaire. Les densités plasmas résultantes s'étalent de 10^{15} à 10^{19} m^{-3}, et les températures électroniques de 10^3 à 10^5 K. Les sources utilisées pour générer le plasma appartiennent à trois catégories : les décharges thermioniques, les sources radio-fréquences et les plasmas chauffés par ondes. La première catégorie consiste en l'émission d'électrons primaires à partir d'un métal ou d'un cristal émissif. Si les électrons produits sont suffisamment énergétiques, ils peuvent ioniser les atomes neutres via des collisions. On peut citer l'expérience LAPD à Los Angeles (Etats-Unis), ou MISTRAL à Marseille (France). Les larges gammes de densité, champ magnétique et température résultants en font des outils pertinents pour l'étude des instabilités dans un plasma. Ensuite, les sources radio-fréquences permettent une ionisation facilement réalisable et efficace du plasma. Enfin, les plasmas chauffés par ondes tels que les plasmas hélicons présentent un taux d'ionisation optimal et sont en fort développement. C'est le cas des infrastructures CSDX à San Diego (Etats-Unis), MPEX à Oak Ridge (Etats-Unis) ou RAID à Lausanne (Suisse). Leurs hautes densités jusqu'à 10^{19} m^{-3} permettent par exemple l'étude des interactions plasma-surface pour la fusion nucléaire. Cette liste est non-exhaustive, un lecteur curieux pourra se référer à l'article de Geuroult, Rax et Fisch [Gue+19] ou au livre de Shinohara consacré aux plasmas hélicons [Shi22] pour une présentation plus complète et quantitative des dispositifs linéaires.

Présentation de l'expérience Von-Kármán Plasma

L'infrastructure Von-Kármán Plasma (VKP) exploité au cours de cette thèse est un dispositif linéaire de 80 cm de long et 20 cm de diamètre [Pli+15]. Cette expérience a initialement été mise en œuvre avec une antenne radio-fréquence inductive en 2014. De plus, l'expérience est pensée pour être utilisée avec deux antennes radio-fréquences se faisant face. Cette conformation, déjà explorée ailleurs [Mil+98a ; Jac+23], est envisagée pour obtenir de très grandes densités. Une application directe est le développement du projet AWAKE [Gsc+22], qui vise à devenir la nouvelle génération d'accélérateurs à particules, et de remplacer à terme les coûteuses infrastructures de la physique des particules telles que le Large Hadron Collider (LHC). Ainsi, une grande densité et une remarquable homogénéité des propriétés plasmas pourraient être maintenues. Au-delà d'un effet additif des antennes radio-fréquences, ce dispositif expérimental ouvre la possibilité d'étudier des écoulements de Von-Kármán [Pli+15]. Cette conformation, consistant à la génération de tourbillons au sein d'un fluide dans une enceinte cylindrique par le mouvement contra-rotatif de deux disques, est largement étudiée en mécanique des fluides dans l'étude fondamentale de la turbulence. L'expérience Von-Kármán Sodium (VKS) a étendu cette étude aux fluides conducteurs [Mon+09]. L'effet dynamo, consistant en la génération d'un champ magnétique macroscopique stable à partir d'un écoulement turbulent, a été mis en évidence et compris à la fin des années 2000. Cependant, les fluides conducteurs ayant une forte densité et viscosité, les effets inductifs ne se produisent qu'à haut nombre de Reynolds. Une puissance conséquente est nécessaire pour atteindre ces régimes, et une dynamique chaotique émerge.

L'expérience VKP a pour but d'étudier l'écoulement de Von-Kármán en présence d'un plasma. Ce milieu, bien que moins conducteur, est à faible densité. Les effets inertiels sont moins significatifs que dans le cas d'un liquide, tout en garantissant une bonne conductivité. VKP permettrait d'étendre les études de turbulence et de dynamo à de nouveaux régimes, rendant possible une exploration plus complète de l'espace des paramètres. Cependant, l'utilisation d'un plasma s'accompagne de multiples difficultés. Tout d'abord, le contrôle de la rotation d'une colonne de plasma magnétisée est difficile. Cet aspect a été étudié sur VKP par le passé, en démontrant le contrôle de la rotation du plasma par injection de courant via une cathode émissive [Dés+21]. Une expertise de ces problématiques a été développée au sein de l'équipe plasma du Laboratoire de Physique à l'ENS de Lyon. Mais si cette observation empirique est robuste, la compréhension des phénomènes physiques sous-jacents était lacunaire au commencement de ce doctorat. L'un des objectifs majeurs de cette thèse a été de comprendre l'origine physique du contrôle de la rotation par une cathode émissive. Ensuite, la mesure des propriétés plasmas est difficile. Divers diagnostiques avancés ont été développés pour VKP, tels que les sondes émissives, 5-tips et l'imagerie rapide [Bou+15 ; Vin+22]. Ces atouts ont été mis au service d'études fondamentales de la physique du plasma, telles que l'importance des fluctuations de température électronique sur l'émission lumineuse [Vin+22] et les interactions non-linéaires entre les ondes au sein du plasma [Vin+23]. Un renforcement de ce pôle diagnostique était envisagé pour l'étude de l'écoulement de Von-Kármán via le développement de sondes électrostatiques avancées. Enfin, l'implémentation d'une source hélicon, permettant d'atteindre une gamme plus large de densité et un taux d'ionisation élevé, était planifiée au cours de ce doctorat.

Structure du manuscrit

Les travaux présentés dans ce manuscrit se concentrent en deux parties principales. D'abord, les interactions entre une colonne de plasma magnétisée et une cathode chaude sont détaillées. Ensuite, la mise en service d'une source hélicon, la caractérisation des propriétés plasmas et l'étude des oscillations basse-fréquence sont présentées.

Le chapitre 1 est dédié à la présentation du dispositif expérimental VKP, mis en œvre via une source inductive radio-fréquence. Une description détaillée des conditions expérimentales est présentée. Les propriétés générales des plasmas froids sont ensuite décrites. Cette approche a pour but d'introduire les phénomènes fondamentaux nécessaires à la compréhension des travaux réalisés. Ainsi, le concept de gaine, les ordres de grandeur importants, les collisions entre particules, l'effet de la magnétisation, la conduction électrique, la description mathématique du plasma et les bilans d'énergie et de particules sont présentés avec une approche généraliste. Ces concepts essentiels seront ensuite appliqués au cas spécifique de l'expérience VKP. Cette connaissance fine des paramètres plasmas et des phénomènes physiques en jeu est cruciale pour le dimensionnement de nouveaux diagnostiques par exemple. Une connaissance approfondie des ordres de grandeur permet également une interprétation éclairée des données expérimentales. Les différents diagnostiques sont détaillés dans une dernière section. Le principe et la réalisation pratique des sondes de Langmuir sont introduits. L'accent est mis sur l'importance des fluctuations radio-fréquences et l'assemblage d'une sonde de Langmuir compensée, nouvellement réalisée au cours de ce doctorat. Elles sont utilisées pour des mesures de densité plasma, de température électronique et de potentiel flottant. Le principe de la sonde 5-tips est ensuite expliqué. Cette sonde avancée permet des mesures simultanées et résolues dans le temps et dans l'espace de densité, de température électronique et de potentiel flottant. La sonde émissive, sonde de référence pour les mesures de potentiel plasma et de ses fluctuations, est décrite. Le principe et la calibration de la sonde B-dot sont mis en avant. Cette sonde dédiée à la mesures des ondes magnétiques radio-fréquences au sein du plasma a été réalisée au cours de ce doctorat. Enfin, les techniques d'imagerie rapide sont décrites.

Le second chapitre se concentre sur l'opération d'une cathode émissive de tungstène en interaction avec le plasma environnant. Après un bref état de l'art de l'utilité des cathodes émissives, les méthodes expérimentales sont présentées en détail. La cathode, consistant en un fil de tungstène enroulé en forme de spirale, est chauffée par effet Joule et polarisée négativement en son centre. Ainsi, en présence d'un plasma, un courant électronique est injecté par émission thermionique. Ce système très simple démontre cependant une variété de comportements selon les conditions expérimentales. Une étude complète des propriétés thermiques de la cathode en présence de plasma révèle un échauffement significatif et hétérogène du filament de tungstène. Un modèle thermodynamique original est dressé, reposant sur le bilan d'enthalpie du filament en interaction avec le plasma. Une résolution numérique se basant sur un unique paramètre libre donne des résulats en accord qualitatif et quantitatif avec les expériences. Ainsi, un régime d'opération stable à faible émission thermionique, et un autre à très forte émission sont mis en avant. Ce modèle thermodynamique élégant permet une compréhension fine des interactions cathode-plasma, ainsi qu'une connaissance essentielle des phénomènes ayant lieu à la cathode. Ce chapitre a fait l'objet d'une publication au journal *Plasma Sources Science and Technology*, et est ici enrichi de multiples ajouts.

Fort de cette compréhension approfondie de l'utilisation de la cathode émissive en tungstène, l'impact de l'injection de courant sur le potentiel plasma est étudié. Le principe du contrôle de potentiel plasma par une cathode émissive repose sur le changement des flux de particules chargées au sein de la colonne de plasma, et la modification résultante du potentiel plasma via la loi d'Ohm locale. Un modèle analytique simple, reliant la chute de potentiel radiale dans la colonne de plasma au courant injecté, est détaillé en premier lieu. Les prédictions théoriques sont confrontées aux mesures expérimentales complexes, où l'ensemble des propriétés plasmas sont modifiées par l'injection d'électrons. Un accord qualitatif est obtenu entre le modèle et les expériences. Cependant, les prédictions théoriques ne permettent pas un accord quantitatif fin. Jusqu'à un ordre de grandeur sur la chute de potentiel radial existe entre les résultats théoriques et expérimentaux. De plus, une gaine anodique prédominante est observée aux parois, impactant fortement le profil radial de potentiel plasma. Des pistes d'amélioration du modèle sont également discutées. Ces travaux ont été réalisés en collaboration avec Renaud Gueroult et Baptiste Trotabas (Laboratoire LAPLACE, Toulouse), qui ont contribués significativement à la compréhension du modèle et l'interprétation des données.

La seconde partie du manuscrit s'intéresse à l'implémentation d'une source hélicon. Le chapitre 4 se concentre sur la caractérisation des principales propriétés plasmas. Un état de l'art des plasmas hélicons est d'abord dressé. Il retrace l'origine des ondes whistlers au sein d'un plasma et le fort couplage entre les propriétés plasma et la propagation de ces ondes, détaille le cas des ondes hélicons, c'est-à-dire les ondes whistlers au sein d'une cavité délimitée, l'excitation spécifique de certaines ondes hélicons à l'aide de sources hélicons particulières, et introduit la phénoménologie riche et unique des plasmas hélicons. L'amélioration pratique de l'expérience est d'abord détaillée. La phénoménologie des plasmas hélicons est explorée et comparée avec succès à la littérature. Une caractérisation approfondie des modes hélicons et de ses propriétés spatiales est également réalisée. Enfin, l'effet de l'injection de courant sur les propriétés du plasma hélicon est étudié. Un lien important est fait avec les expériences présentées dans le troisième chapitre.

Le dernier chapitre s'intéresse aux oscillations basse-fréquences observées au sein du plasma. Après une brève présentation de l'importance des oscillations basse-fréquences et la caractérisation de quelques instabilités majeures dans les dispositifs linéaires, une étude expérimentale des fluctuations basse-fréquences dans VKP est menée. L'espace des paramètres est exploré, et diverses instabilités sont étudiées. Des mesures par imagerie rapide, couplées à des analyses approfondies par sondes électrostatiques, permet de documenter les fluctuations existantes. Les propriétés majeures de ces oscillations sont quantifiées afin d'identifier les mécanismes sous-jacents à leur génération. Cette étude brève est conclue par la présentation d'un régime fortement instable et présentant de multiples tourbillons. Ce sujet est encore à l'étude actuellement.

PART I:
CURRENT INJECTION IN A PLASMA COLUMN

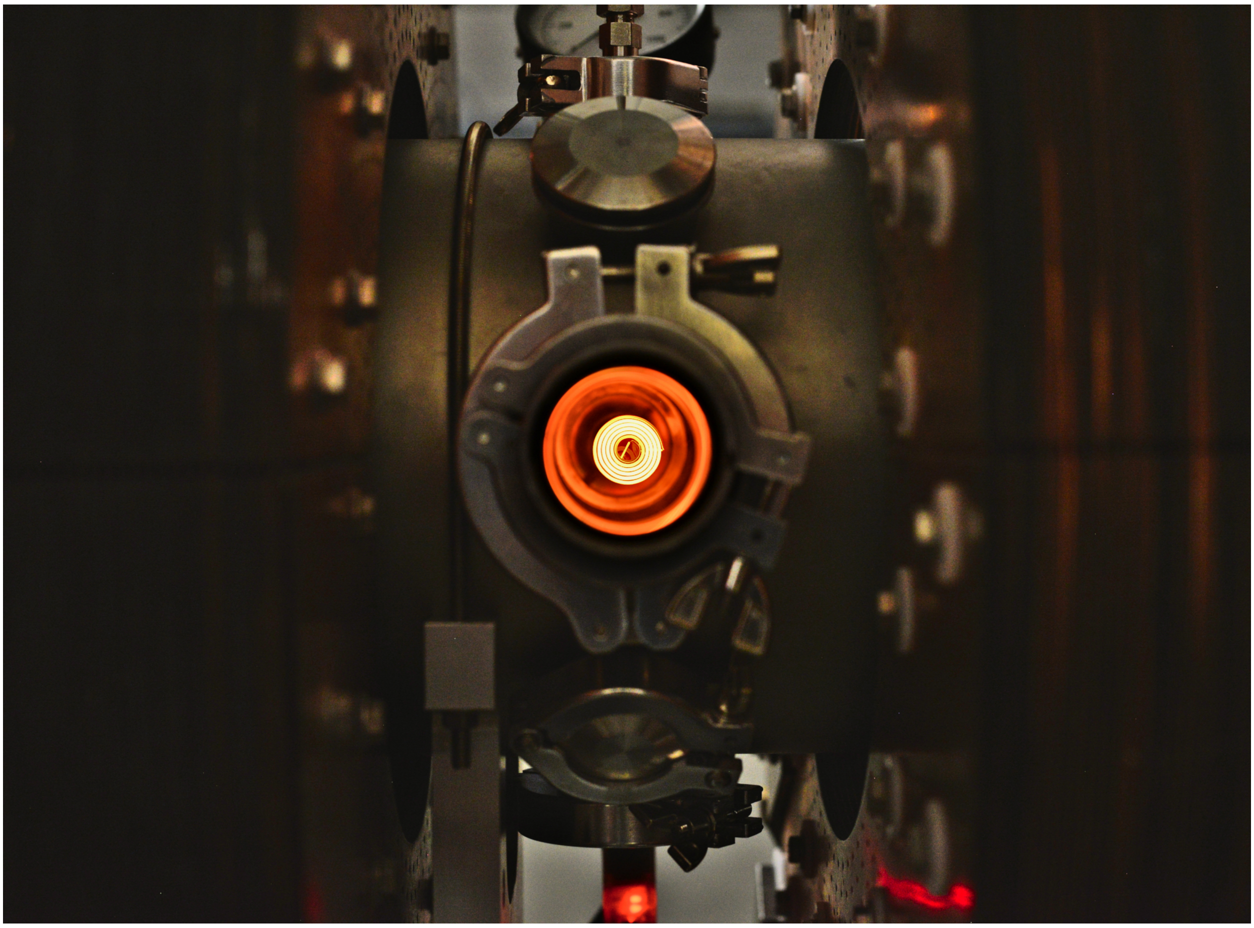

CHAPITRE

I

INDUCTIVELY-COUPLED PLASMA DEVICE AND DIAGNOSTICS

Ce chapitre est dédié à la présentation du montage expérimental Von-Kármán Plasma, fonctionnant avec une antenne radiofréquence inductive. Le plasma résulte donc d'un couplage plasma-antenne inductif. Les propriétés pertinentes du plasma telles que les longueurs et fréquences typiques observées dans les régimes étudiés sont d'abord présentées. Enfin, les divers diagnostiques et leur routine opératoire sont détaillés, avec une description approfondie des sondes de Langmuir compensées et B-dot, qui ont été produites au cours de ce doctorat.

I.1 Generation of an inductively-coupled plasma column

I.1.1 The experimental set-up

The first stage of the Von-Kármán Plasma experimental set-up was operated from 2015 to 2022. Prior focus was set on plasma flow control [Dés+21], plasma light emission [Vin+22] and observation and mitigation of fluid instabilities in a weakly magnetised plasma column. Throughout the first half of this PhD, the primary goal has been the investigation of the interactions between a plasma and a cathode, and the understanding of plasma transports properties. This stage of the experimental set-up sustains a plasma using an inductive radio-frequency antenna. In the three following sections, the Von-Kármán Plasma - Inductively-Coupled Plasma set-up will thus be referred to as VKP-ICP.

The plasma diffusion chamber consists in a cylindrical stainless steel vessel of $L = 80$ cm in length and $R = 10$ cm in radius. It is connected at one end to a borosilicate tube with an inner diameter of 11 cm and a length of 20 cm. The ends of the vacuum vessel are electrically insulated, using either nitride boron disks or borosilicate windows. On the other hand the stainless steel vacuum chamber is grounded. Access ports are located at $z = 16$ and 49 cm (blue dashed lines in figure I.1a)), where probes can be inserted. The set-up is represented and pictured in figure I.1.

Vacuum is obtained using a primary and a turbo-molecular pump attached at $z = 49$ cm, which enable to reach a base pressure of 10^{-4} Pa. Argon is then injected at $z = 16$ cm near the source tube, at a controlled pressure of the order of 0.13 Pa. Argon is a noble gas, ensuring a low ionisation energy and the absence of complex chemistry. A full range pressure gauge (Penningvac PTR 90), corrected for argon and reliable down to 10^{-6} Pa, is used as the reference pressure gauge. It is supplemented by a capacitive pressure gauge (Ceravac CTR 91). Both are located at the pump inlet. The low-pressure reduces the collisionality and ensures a mean free path λ of a few centimetres to a few tens of centimetres as will be shown in subsection I.2.3.

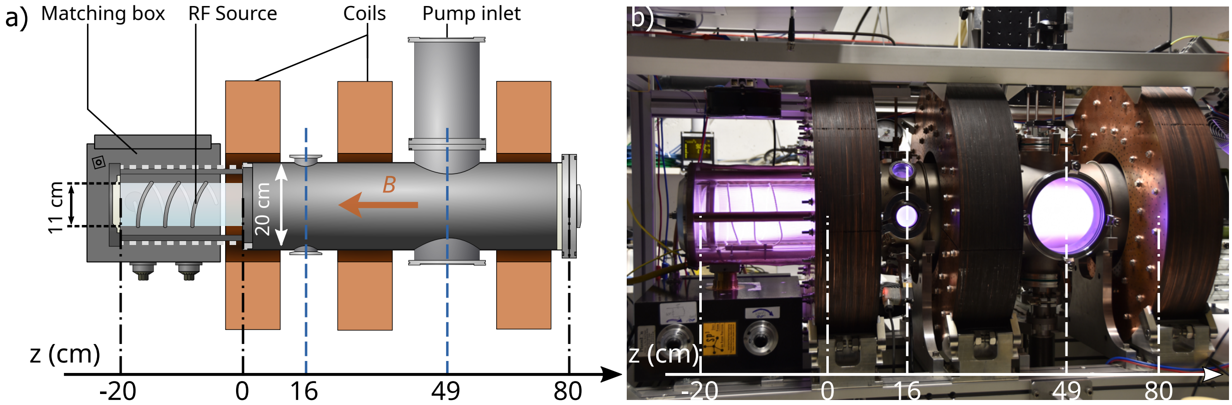

FIGURE I.1 – *a)* Drawing of the Von-Kármán Plasma experiment with an inductive radio-frequency source (VKP-ICP). Both ends of the plasma chamber are electrically insulated, the stainless steel vessel is grounded. *b)* Picture of the VKP-ICP set-up operating with argon and magnetic confinement. Credit: Simon Vincent [Vin21].

The plasma is sustained using a 3-loops radio-frequency antenna. The antenna is fed by a radio-frequency power supply up to 3.5 kW at $f_0 = 13.56$ MHz (MKS SurePower QL 3513) and surrounded by a Faraday cage. The radio-frequency current through the antenna generates an oscillating azimuthal electromagnetic field via induction at the vicinity of the antenna inside the borosilicate tube. Charged particles are trapped and accelerated by this electromagnetic field, causing electrons to gain energy up to a few electronvolts. Then, their energy are transferred to ions and electrons via successive elastic, ionising or exciting collisions. The plasma expands in the dif-

p_0 (Pa)	P_w (kW)	B (G)
0.06 - 1.3	0.5 - 3.5	170 - 1400

TABLE I.1 – Typical ranges for the experimental parameters.

fusion chamber with a typical radius of 5 cm, densities of the order of $n \sim 10^{18}$ m^{-3}, electron temperature about $T_e \sim 4$ eV and ion temperature $T_i \sim 0.2$ eV [Dés18].

The global impedance of the antenna and the plasma has to be matched to the 50 Ω output impedance of the power generator. The plasma being inductively coupled to the antenna, the impedance of the system varies with the plasma characteristics. Simple models represent this coupling by a resistor in series with an inductor [Cha+11]. Therefore a manually adjustable L-type matching box consisting of two variable capacitors is set between the power supply and the antenna. The capacitors C_{load} and C_{tune} can be adjusted up to 500 pF and 1000 pF respectively in order to achieve impedance matching and convey as much power as possible from the antenna to the plasma.

Three external coils are placed around the vacuum chamber to apply a longitudinal external magnetic field. They are placed at $z = 3$, 29 and 69 cm, and made of 100 annular copper slabs stacked with annular half-disc dielectric slabs, resulting in 50-turns coils. The coils are fed in series with a DC voltage supply TDK Lambda delivering up to 10 V and 1000 A. The impedance of each coil is about ~ 30 mΩ, and it generates up to 1400 G at their center. A deeper insight into the shape of the magnetic field will be provided in subsection I.1.2.

The three experimental control parameters are the argon pressure p_0, the power fed to the antenna P_w and the external magnetic field B. They are listed in table I.1 along with the ranges of the values used in this thesis.

I.1.2 The external magnetic field

The external magnetic field **B** constraints the motion of charged particles perpendicular to **B**, while they displace freely along **B**. Consequently, they follow a helical trajectory along **B** in absence of collisions.

The effect of the magnetic field on a plasma is to tailor its shape. A longitudinal magnetic field in a linear plasma device imposes an axisymmetric shape to the plasma and enables to conduct a 2D cylindrical analysis. A cylindrical magnetised plasma develops specific properties, such as a rotation along its axis of symmetry or specific waves or instabilities. These features need to be understood for fundamental plasma physics as well as many magnetised plasma applications like plasma mass separation techniques [Zwe+18]. The exact knowledge of the external magnetic field applied is crucial to predict the plasma behaviour.

A numerical computation of the magnetic field resulting from the three external coils is conducted and displayed in figure I.2. The coils are 11.5 cm thick (with a neglected experimental variability of about 5%), $r_{in} = 13$ cm in inner radius and $r_{out} = 28$ cm in outer radius. A fixed current I_B flows through each turn. Yet, because of the radial extension of each annular slab, the radial current distribution is uneven. Each copper slab can be seen as a concentric stack of loops of variable radii r. The resistance of a loop being proportional to r and the potential drop of all the loops being the same, the current flowing through a loop of radius r and width dr is

$$\mathrm{d}I(r) = \frac{I_B}{\ln\left(r_{out}/r_{in}\right)} \frac{dr}{r} \tag{I.1}$$

with $I_B = \int_{r_{in}}^{r_{out}} \mathrm{d}I(r)$ the experimental control parameter.

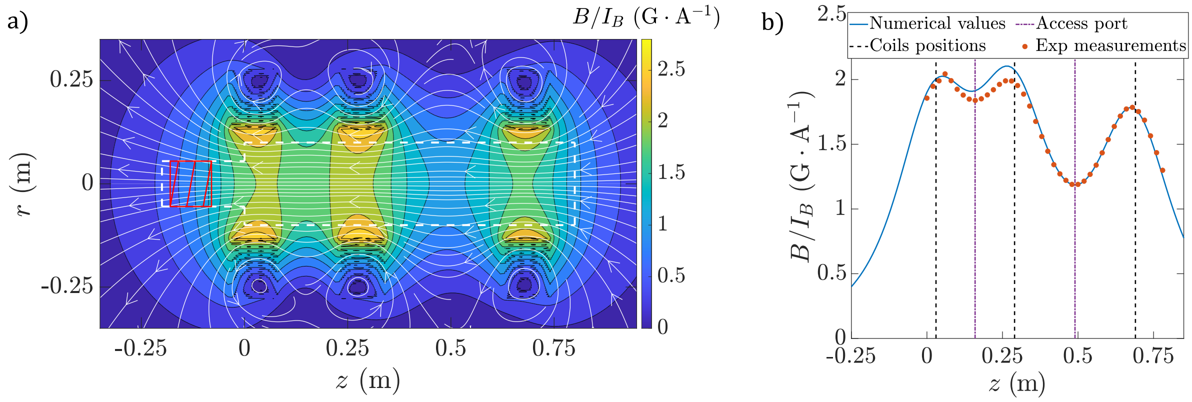

Figure I.2 – *a)* Numerically computed magnetic field for the VKP-ICP set-up. Magnetic field values are normalized by the current intensity I_B going through the coils. The white dashed lines represent the vacuum chamber and the red solid lines the 3-loops inductive antenna. *b)* Magnetic field normalized by I_B along the symmetry axis of the device.

The numerical computation models the 50-turns coils, each turn being divided into 30 concentric loops, with the radial current distribution given by equation I.1. The Biot-Savart formula is solved in all the spatial domain for each of these loops and added to one another, resulting in the magnetic field normalized by I_B showed in figure I.2a). The colormap represents the magnetic field intensity while the stream lines are the magnetic field lines. The inductive antenna is highlighted by the red solid lines, and the vacuum vessel by the white dashed lines.

The resulting magnetic field on the longitudinal axis is plotted in I.2b) and compared to experimental teslameter measurements. One can see a remarkable agreement between the model and the experiments, supporting the reliability of the numerical simulation. The model shows a strong longitudinal variation of the magnetic field, with a 44% decrease from the maximum at $z = 26$ cm to the minimum at $z = 49$ cm. It indicates that there is a widening of the magnetic field lines at the access port used for probe measurements, which has to be considered for a careful interpretation of the plasma properties using high-speed camera imaging [Vin+22]. On the other hand, the magnetic field presents a heterogeneity in the radial plane up to 4% between $r = 0$ cm and $r = 5$ cm, which is the plasma core location, and up to 20% between $r = 0$ cm and $r = 10$ cm.

Ultimately it allows us to confidently convert the experimental control parameter I_B into the value of the magnetic field. The conversion factor for VKP-ICP between I_B and B, *i.e.* the mean value along the symmetry axis between $z = 0$ and 80 cm, is $\langle B/I_B \rangle = 1.70$ G · A^{-1} (the notation $\langle \cdot \rangle$ denotes the mean value).

I.2 Plasma properties and description

The goal of the present section is to draw a general picture of the plasma investigated in this thesis. The gas used is argon and typical orders of magnitude are $n \sim 2 \times 10^{18}$ m^{-3}, $T_e \sim 4$ eV, $T_i \sim 0.2$ eV, $B \sim 170$ G and $p_0 \sim 0.13$ Pa [Dés18; Vin21]. Note that temperatures of the plasma particles are expressed in electronvolts unless mentioned. As a reminder, 1 eV = 11600 K. Thermal energies are written as eT_e instead of $k_B T_e$ for instance, with k_B the Boltzmann constant. It allows an immediate comparison of the particles kinetic energy with the electrostatic potential energy.

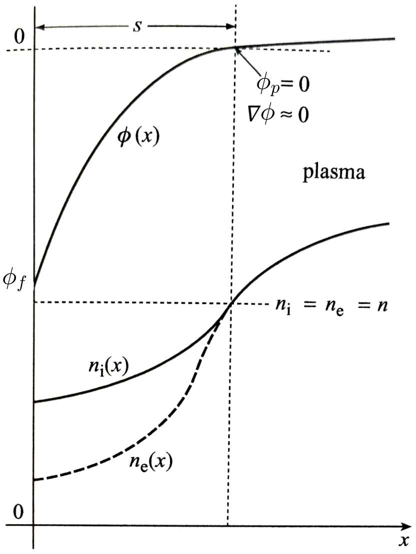

FIGURE I.3 – Electric potential $\phi(x)$, ion density $n_i(x)$ and electron density $n_e(x)$ at the vicinity of a floating surface. Sketch taken from [Cha+11].

I.2.1 Introduction to the plasma sheath

This section is a brief introduction to the plasma sheath physics. It is a vast and complex topic, and it will not be detailed thoroughly. A curious reader could refer to reference books from Lieberman and Lichtenberg [Lie+05] or Chabert and Braithwaite [Cha+11].

In the bulk of an unmagnetised cold plasma, the ion and electron fluxes J_i and J_e are isotropic. This thermal diffusion ensures the quasi-neutrality of the plasma, namely ion density n_i and electron density n_e are equal, which enables to define the plasma density $n = n_i = n_e$. Since $T_e \gg T_i$ and m_e the mass of the electron is small before m_i the mass of the ion, one can observe that

$$J_e \propto \sqrt{\frac{T_e}{m_e}} \gg J_i \propto \sqrt{\frac{T_i}{m_i}} \tag{I.2}$$

The local electric field in the plasma can be computed by combining the electrostatic plasma potential definition and the Poisson equation

$$\mathbf{E} = -\nabla\phi \quad \text{and} \quad \Delta\phi = -\frac{e(n_i - n_e)}{\epsilon_0} \tag{I.3}$$

with ϕ the local electric potential in the plasma, and ϵ_0 the vacuum permittivity. In the bulk quasi-neutral plasma, this set of equations shows that no electric field arises. The bulk electric potential is uniform and is called the plasma potential ϕ_p.

However, this is no longer true when a surface perturbs the plasma. A floating surface implies a zero net current at the boundary, meaning that $J_i = J_e$. But as mentioned before for an isotropic homogeneous plasma, $J_e \gg J_i$, so the predominant electron flux would charge the surface negatively. The resultant surface charge repels the incoming electrons and attracts ions, until a stationary state is reached where J_e and J_i are balanced. The region at the vicinity of the surface is no longer quasi-neutral and is called a sheath. A sketch taken from Chabert and Braithwaite [Cha+11] is displayed in figure I.3. The electric potential at the surface is called the floating potential $\phi_f < \phi_p$.

Sheath extension: Let us consider a sheath extending between a floating surface at $x = 0$ and the sheath thickness $x = s$ in a semi-infinite plasma. The sheath is a perturbed plasma region, and knowing its width is essential. It can be estimated using various refined sheath models relying on a common physical interpretation. The electron population is thermalized at a constant electron temperature T_e, experiences no global electron drift and is assumed to be in a stationary state. A non-uniform external electric field $\mathbf{E} = -\nabla\phi(x)$ is applied. Electrons being at the local thermodynamic equilibrium, the electrostatic potential energy is opposed to the electron kinetic energy. Using a momentum balance between the electron pressure gradient and the external electric field, one can derive the Boltzmann equilibrium for electrons

$$en_e \nabla\phi(x) = \nabla\left(eT_e n_e(x)\right) \quad \Leftrightarrow \quad n_e(x) = n_e(x=s)\exp\left(\frac{\phi(x)-\phi_p}{T_e}\right) \tag{I.4}$$

with $\phi_p = \phi(x=s)$ the plasma potential. The local electric potential in the sheath can be computed combining equations I.3, I.4 and assuming a homogeneous ion density in the sheath. For the sake of simplicity, the plasma potential ϕ_p is set at 0 V and the equation is linearised, thus yielding

$$\frac{\mathrm{d}^2\phi(x)}{\mathrm{d}x^2} = \frac{en}{\epsilon_0 T_e}\phi(x) \quad \Leftrightarrow \quad \phi(x) = \phi_f \exp\left(-\frac{x}{\lambda_D}\right) \quad \text{where} \quad \lambda_D = \sqrt{\frac{\epsilon_0 T_e}{ne}} \tag{I.5}$$

λ_D is the Debye length and is the typical length scale of the sheath. Beyond λ_D, the potential drop at the wall is screened and the plasma potential is recovered. In the present experiment, the Debye sheath is of the order of 10 to 50 μm.

Bohm sheath criterion: The ion flux is increased at the wall in order to recover the net-zero current condition $J_e = J_i$. One can demonstrate [Lie+05] that quasi-neutrality can be verified only if the ion speed is below the ion sound speed, often called the Bohm speed

$$u_B = \sqrt{\frac{eT_e}{m_i}} \tag{I.6}$$

Hence, ions are accelerated in the quasi-neutral pre-sheath region up to u_B at the sheath entrance, where quasi-neutrality is no longer possible. This is called the Bohm sheath criterion. A small potential drop of the order of $T_e/2$ is responsible for this acceleration. Then, the plasma density at the sheath entrance is reduced by a factor $\alpha = \exp(-1/2) \simeq 0.6$ compared to the bulk plasma density n. Note that the α value is strongly dependent on the wall geometry and the plasma collisionality. More details will be provided when discussing Langmuir probe analysis in subsection I.3.1.1. Because of the continuity equation, the ion flux at the wall is the same than the ion flux at the sheath entrance

$$J_{is} = e\alpha n u_B \tag{I.7}$$

By equating this incoming ion flux to the incoming thermal electron flux at the floating wall at a potential ϕ_f, one can quantitatively predict the potential drop at the sheath

$$\phi_p = \phi_f + \Lambda T_e \quad \text{with} \quad \Lambda = \ln\left(\sqrt{2m_i/(\pi m_e)}\right) \tag{I.8}$$

Λ is a sheath parameter commonly evaluated at 5.35 for an argon plasma. A finer formula for Λ can be found in the work of Baalrud [Baa+20] and gives $\Lambda = 5.2$.

I.2.2 Classical orders of magnitude

The Debye length λ_D, *i.e.* the screening length of an electrostatic charge in the plasma, has already been presented and is of the order of 10 μm. Some important orders of magnitude, including λ_D, are detailed herein and listed in table I.2. The criterion $\lambda_D \ll R$ ensures quasi-neutrality in the plasma chamber.

Charged species are denoted s, i meaning ion and e electron. Plasma frequencies $\omega_{p,s}$ is the characteristic frequency of density oscillations propagating through the plasma. Hence $\omega_{p,s}^{-1}$ is the inertial time response of charged particles under the application of an external electric field. Its expression is:

$$\omega_{p,s} = \sqrt{\frac{ne^2}{m_s \epsilon_0}} \tag{I.9}$$

As shown in table I.2, the radio-frequency excitation angular frequency ω_0 is ordered this way: $\omega_0 < \omega_{p,i} \ll \omega_{p,e}$. It means that the plasma follows closely the density fluctuations imposed by the antenna.

Thermal speeds $v_{th,s}$ are the mean absolute values of the charged particles. If one assumes their energetic distribution to be maxwellian with a temperature T_s, the equipartition theorem reads

$$v_{th,s} = \sqrt{\frac{3eT_s}{m_s}} \tag{I.10}$$

Neutral pressure can be estimated using the perfect gas law at an intermediate temperature of 500 K lying between 300 K and $T_i \simeq 2000$ K. The typical neutral pressure is then $n_n \simeq 2 \times 10^{19}$ m^{-3}, meaning that the degree of ionisation γ ranges between 1 % and 40 %. It highlights the importance of ion-neutrals and electron-neutrals interactions since neutrals are predominant.

λ_D	$\omega_{p,e}$	$\omega_{p,i}$	$v_{th,e}$	$v_{th,i}$	γ
11 μm	13 GHz	47 MHz	1500 km $\cdot$ s^{-1}	1.2 km $\cdot$ s^{-1}	1 - 40 %

TABLE I.2 – Orders of magnitude of some characteristic plasma quantities. Frequencies are expressed in Hz for the sake of simplicity.

I.2.3 Collision rates

Collisions are complex and a comprehensive review would be tedious. A more comprehensive overview can be found in the textbook by Lieberman and Lichtenberg [Lie+05]. Orders of magnitude of the collision rates will be discussed to understand the plasma overall behaviour. The plasma is composed of three different species, *i.e.* neutrals, ions and electrons. The collision between two particles depends strongly on the species involved as well as the type of collision (elastic or inelastic). Consequently, the collisions depend on the particles kinetic energy. The complexity of these collisions are contained in the cross-sections formulas, which express the probability of particles interactions as an effective particle cross section.

Let us consider an incoming particle α moving at speed v_α onto an immobile particle β. An essential quantity characterizing the collision between these two particles is the cross-section $\sigma_{\alpha\beta}$. It represents the effective surface area of particle β for interaction with particle α. Hence, a collision would occur if the particle α approaches the particle β within the range $b < \sqrt{\sigma_{\alpha\beta}(v_\alpha)}$. Then, the collision frequency of a single particle α in a medium of particles β at a density n_β would read

$\nu_{\alpha\beta} = n_\beta \sigma_{\alpha\beta} v_\alpha$. Now, since the population of α particles have a wide speed distribution, a single particle has a certain probability to move at a given v_α speed. The realistic collision frequency should account for discrepancies in the speed distribution. That is why it is calculated according to the ensemble average on the distribution function f of the particles α [Lie+05]

$$\nu_{\alpha\beta} = n_\beta \langle \sigma_{\alpha\beta} v_\alpha \rangle \simeq n_\beta \sigma_{\alpha\beta}(T_\alpha) \langle v_\alpha \rangle \tag{I.11}$$

The exact calculation of collision frequencies should include an accurate computation of the constant rate $K_{\alpha\beta} = \langle \sigma_{\alpha\beta} v_\alpha \rangle$ over the exact distribution function. In most cases, the distribution is considered maxwellian [Lie+05]. Using the approximation that $\sigma_{\alpha\beta}$ is constant over the distribution, a simple order of magnitude is be given in equation I.11, where $\langle v_\alpha \rangle$ is equal to $\sqrt{\frac{8eT_\alpha}{\pi m_\alpha}} \simeq 0.9\, v_{th}$ for a maxwellian distribution.

Constant rates and collision frequencies highly depend on the exact cross-section values. Cross-sections between neutrals and charged particles are extensively studied experimentally and theoretically. Experimental measurements in argon for σ_{in} [Phe94] and σ_{en} [Alv14] are shown in figure I.4.

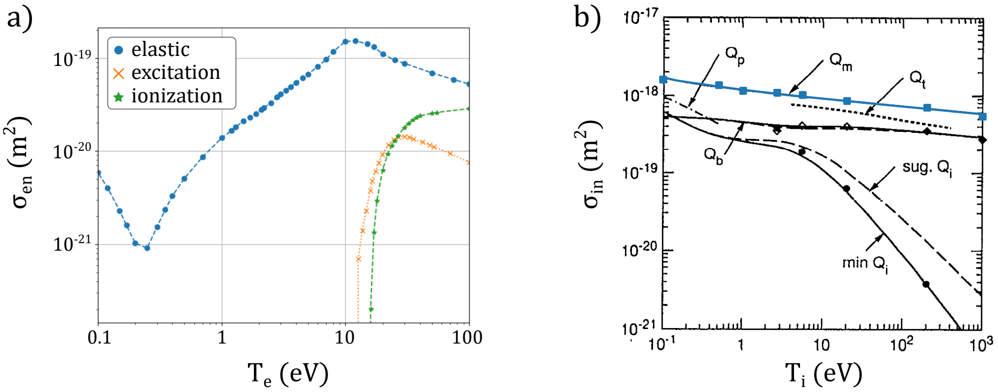

FIGURE I.4 – Experimental cross sections for *a)* σ_{en} (taken from LXCAT database [Alv14]) and *b)* σ_{in} (taken from [Phe94]) where the blue solid line is the total cross-section for ion-neutrals collisions.

Electron-ion cross-sections are much broader because of long-range Coulomb collisions and are derived theoretically. The cross section associated to small angle collisions is given by the following formula [Bel06]:

$$\sigma_{ei} = \frac{1}{2\pi} \left(\frac{e^2}{\epsilon_0 \mu_0 v_e^2} \right)^2 \ln \left(\frac{4\pi\epsilon_0 \mu_r v_e \lambda_D}{e^2} \right) \tag{I.12}$$

where μ_r is the reduced mass $\mu_r = \frac{m_\alpha m_\beta}{m_\alpha + m_\beta}$ and $\ln\left(\frac{4\pi\epsilon_0\mu_r v_e \lambda_D}{e^2}\right) \simeq 10$ is the Coulomb logarithm. The temperature dependence is mostly encapsulated in v_e, meaning that σ_{ei} evolves as $T_e^{-1/3}$.

The orders of magnitude of are summarized in table I.3. Note that ν_{en} and ν_{in} are relative to elastic collisions, while ν_{iz} stands for ionising collisions. The most frequent collisions are electron-ions. Because of the high m_i/m_e ratio, electron-ions collisions are responsible of electron scattering and isotropisation of the electron energy distribution function. A slight transfer of energy from electrons to ions occurs as well, but a longer plasma confinement time is required to reach thermodynamic equilibrium between electrons and ions because of the high m_i/m_e ratio. In the works presented herein, the plasma confinement time is not enough for thermodynamic equilibrium between electrons and ions to be established. For similar reasons, electron-neutrals elastic collisions

σ_{ei}	σ_{en}	σ_{in}	ν_{ei}	ν_{en}	ν_{in}	ν_{iz}
6×10^{-18} m^2	5×10^{-20} m^2	1.3×10^{-18} m^2	15 MHz	1.3 MHz	33 kHz	14 kHz

TABLE I.3 – Cross-sections and collision rates estimations in VKP-ICP.

cause electron scattering and a slight heating of neutrals. Both types of collisions contribute to the quick electron isotropisation, and the convergence to a Maxwell distribution.

On the other hand, ion-neutrals collisions cause ion scattering and an important momentum transfer from the plasma to the neutrals. Finally, ionising collisions represent a loss of high-energy electrons and a new friction term for the ion dynamics. Indeed, the newly created ions are colder than the surrounding existing ions. Hence, thermalisation of these two ion populations will result in an energy loss for the existing ions. Since the orders of magnitude of ν_{in} and ν_{iz} are similar, a quantitative investigation of the plasma dynamics and the friction applied on ions require a careful examination of both effects.

The mean free path of each particle $\lambda_\alpha = v_{th,\alpha}/\nu_{\alpha\beta}$ can be estimated at a few centimetres.

I.2.4 Magnetisation

The external magnetic field constraints the perpendicular motion of charged particles as they follow helical trajectories. These orbital motions occurs at the cyclotron frequency $\omega_{c,s}$ and with an spatial amplitude given by the Larmor radius ρ_s:

$$\omega_{c,s} = \frac{eB}{m_s} \quad \text{and} \quad \rho_s = \frac{m_s v_{th,s}}{eB} \tag{I.13}$$

An increase in B reduces the orbit size of the charged particles, which become more efficiently confined. The magnetic confinement is antagonist to the particles diffusion caused by collisions, as mentioned in the previous subsection. Ions are not displaced by collisions with light electrons, but only with neutrals. On the other hand, electrons change their orbit at any collision. So, the order of magnitude to consider electrons and ions to be magnetised are respectively

$$\begin{cases} \omega_{c,e} \gg \nu_{ei} + \nu_{en} \\ \rho_e \ll R \end{cases} \quad \text{and} \quad \begin{cases} \omega_{c,i} \gg \nu_{in} \\ \rho_i \ll R \end{cases} \tag{I.14}$$

The condition on $\omega_{c,s}$ grants a high number of orbits before colliding with another particle. When a collision occurs, the displacement is estimated at ρ_s, hence the second condition: the gyroradius must be small before the size of the device in order for a charged particle to be considered magnetised. Orders of magnitude are summarized in table I.4. Both conditions are verified for electrons, ensuring them to be efficiently magnetised. However ions do not verify any of the conditions, meaning that they diffuse much more easily in the vacuum chamber.

The introduction of the magnetic Lorentz force in the plasma fluid equations introduces a volume force analogous to a pressure term. This new term is called the magnetic pressure $p_B = B^2/2\mu_0$. The plasma is repelled by high magnetic field regions, *i.e.* high magnetic pressure p_B zones. A dimensionless key parameter of the magnetohydrodynamics (abbreviated MHD, see subsection I.2.6) model for magnetised plasmas is the ratio β of the kinetic pressure to the magnetic pressure

$$\beta = \frac{p_0}{p_B} = \frac{neT_e}{B^2/2\mu_0} \tag{I.15}$$

If $\beta < 1$, the flow is governed by the magnetic confinement and the energy is mostly contained in the magnetic field. Otherwise, the magnetic field is dominated by the plasma flow and the

ρ_e	ρ_i	$\omega_{c,e}$	$\omega_{c,i}$	β
0.49 mm	29 mm	480 MHz	6.5 kHz	0.01

TABLE I.4 – Orders of magnitude of plasma quantities relative to magnetisation. Frequencies are expressed in Hz for the sake of simplicity.

energy is mostly kinetic. Given the experimental conditions, the VKP-ICP plasma is operated at $\beta \sim 10^{-2}$, which classifies it as a low β plasma.

The axisymmetric configuration of the homogeneous cylindrical plasma leads to a radial electric field to appear. Combined to an axial magnetic field, the ions and electrons experience a rotational motion [Rax05]. Most importantly, electrons and ions flow in the same direction, which causes a macroscopic azimuthal rotation of the plasma. It is called the $\mathbf{E} \times \mathbf{B}$ drift and illustrated in figure I.5. The associated drift velocity is

$$\mathbf{v}_{\mathbf{E}\times\mathbf{B}} = \frac{\mathbf{E} \times \mathbf{B}}{B^2} \tag{I.16}$$

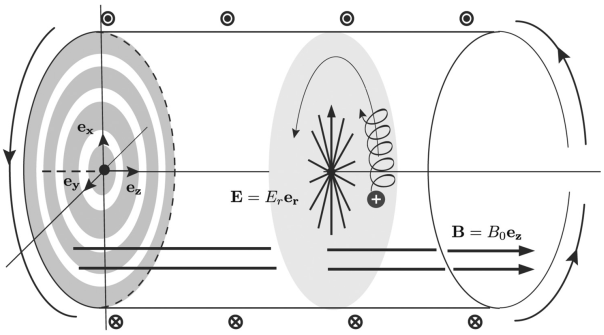

FIGURE I.5 – Illustration of the cylindrical $\mathbf{E} \times \mathbf{B}$ drift configuration. Sketch taken from [Zwe+18].

The $\mathbf{E} \times \mathbf{B}$ drift velocity is the main source of azimuthal flow in the VKP-ICP device, yet it is not the only one. A ion diamagnetic azimuthal drift is to be considered for a finer analysis of the plasma flow. Eventually, the plasma experiences a strong drag from collisions with neutrals, reducing the expected rotational speed by a factor 2 to 10 in the VKP-ICP device [Dés+21]. Overall, the magnetised plasma flow is strongly correlated to the radial electric field, and its control is essential (see chapter III).

I.2.5 Electrical transport properties

The plasma conductivity is the ability to transport charged particles under the application of an external electric field. It is a ohmic process, meaning that the conductivity is bounded because of friction between the plasma particles. The simplest model for describing the conductivity is the Drude model [Ash+22].

Drude model: This model relies on a classical mechanics approach at a microscopic scale. Let us consider a single charged particle s in a fully ionised plasma moving under the application of an external electric field $\mathbf{E}$. There is a probability ν_s per unit time for an elastic collision with another particle to occur, which would redistribute the particle momentum isotropically. The particle speed after impact $\mathbf{u}$ presents a null average over all the particles s $\langle \mathbf{u} \rangle = 0$. The temporal evolution of the particle momentum $\mathbf{p_s}$ reads

$$\mathbf{pv}(t+dt) = (1 - dt/\tau)\,\mathbf{pv}(t) + \nu_s dt m_s \mathbf{u} + (\pm e)\mathbf{E}dt \tag{I.17}$$

the first right-hand side term (respectively the second term) models the probability that no collision occurred during dt (resp. a collision occurred). The third one is the work transferred from the electric field to the charged particle during dt and its sign depends on the particle type. By averaging equation I.17 over all the s-type plasma particles, it leads to the following global momentum equation

$$\frac{\mathrm{d}\langle \mathbf{p_s} \rangle}{\mathrm{d}t} = \langle \mathbf{p_s} \rangle \nu_s + (\pm e)\mathbf{E} \tag{I.18}$$

The mean momentum of the s particles can be written as $\langle \mathbf{p_s} \rangle = m_s \mathbf{v_s}$, with $\mathbf{v_s}$ the mean velocity of the charged particles s. The stationary assumption simplifies equation I.18 down to the stationary speed expression

$$\mathbf{v_s} = \frac{(\pm e)}{m_s \nu_s}\mathbf{E} \tag{I.19}$$

By using the definition of the current density in the plasma $\mathbf{J}$ and the local Ohm's law, one can write

$$\mathbf{J} = ne\,(\mathbf{v_i} - \mathbf{v_e}) = \frac{1}{\eta}\mathbf{E} \tag{I.20}$$

with η the plasma resistivity. Since $\mathbf{v}_e \gg \mathbf{v}_i$, one can derive the Spitzer resistivity η_{Sp} by combining equations I.19 and I.20 and considering mainly electron-ions collisions $\nu_e = \nu_{ei}$:

$$\eta_{Sp} = \frac{m_e \nu_{ei}}{ne^2} \tag{I.21}$$

Refinements: This model can be refined to the partially ionised magnetised case. The magnetic field creates a transport anisotropy. As the electrons are strongly magnetised, contrarily to ions, the current transport along $\mathbf{B}$ is imputable to electrons while the transport perpendicular to $\mathbf{B}$ is attributable to ions. Furthermore, ions diffuse via collisions with neutrals, as they are 10^4 times heavier than electrons.

Secondly the presence of neutrals increase the collision rates of electrons and ions. Given both these refinements, the parallel and perpendicular resistivities read [Gue+19]:

$$\eta_{\parallel} = \frac{m_e\,(\nu_{ei} + \nu_{en})}{ne^2} \quad \text{and} \quad \eta_{\perp} = \frac{m_i \nu_{in}}{ne^2}\left(1 + \frac{\omega_{c,i}^2}{\nu_{in}^2}\right) \tag{I.22}$$

With the VKP-ICP experimental conditions at 170 G, one obtains $\eta_{\perp}/\eta_{\parallel} \sim 370$, and up to ~ 1000 for 680 G. It underlines the highly anisotropic character of electrical transport, even in a weakly magnetised plasma. The implication of this anisotropy on plasma potential will be thoroughly explored in section III.

I.2.6 Plasma description

The plasma description is a wide topic. The current subsection aims at giving the fundamental concepts, and follows the approach taken from Lieberman and Lichtenberg [Lie+05]. Plasma can be modelled at various scales, from the microscopic to the macroscopic point of view. The relevancy of each model will now be briefly reviewed.

Kinetic theory of gases: The most comprehensive modelling scales down to the atom size. Each particle of type s at position $\mathbf{r}$ and velocity $\mathbf{v}$ at time t can be described through the distribution function $f(\mathbf{r}, \mathbf{v}, t)$ in the phase space.

This function recovers the conservation of particle through a continuity equation that accounts for external forces and particle interactions. The resulting governing equation for $f(\mathbf{r}, \mathbf{v}, t)$ is the Boltzmann transport equation

$$\frac{\partial f}{\partial t} + \mathbf{v} \cdot \nabla_{\mathbf{r}} f + \frac{\mathbf{F}}{m_s} \cdot \nabla_{\mathbf{v}} f = \left.\frac{\partial f}{\partial t}\right|_c \tag{I.23}$$

where the right-hand side term is subscripted c as it represents collisions.

This modelling requires to compute every particle interaction in a 7-dimension phase space and non-trivial collision processes. Despite being very heavy, the kinetic theory is the most accurate plasma description. One can then compute finely the particles density, velocity or kinetic energy by computing the three first velocity moments of the distribution function:

$$n_s(\mathbf{r}, t) = \iiint_{-\infty}^{+\infty} f(\mathbf{r}, \mathbf{v}, t)\, \mathrm{d}^3\mathbf{v} \tag{I.24}$$

$$\langle \mathbf{v}_s(\mathbf{r}, t) \rangle = \frac{1}{n_s(\mathbf{r}, t)} \iiint_{-\infty}^{+\infty} \mathbf{v} f(\mathbf{r}, \mathbf{v}, t)\, \mathrm{d}^3\mathbf{v} \tag{I.25}$$

$$w_s(\mathbf{r}, t) = \frac{m_s}{2} \iiint_{-\infty}^{+\infty} \mathbf{v}^2 f(\mathbf{r}, \mathbf{v}, t)\, \mathrm{d}^3\mathbf{v} \tag{I.26}$$

An important result from this description is the distribution function of a particle species in thermal equilibrium with itself. For a stationary system in absence of external spatial gradients and forces, equation I.23 reduces to

$$\left.\frac{\partial f}{\partial t}\right|_c = 0 \tag{I.27}$$

which can be solved to find back the Maxwell distribution function

$$f(v) = n_s \left(\frac{m_s}{2\pi e T_s} \right)^{3/2} \exp\left(-\frac{m_s v^2}{2 e T_s} \right) \tag{I.28}$$

The Maxwell distribution assumption is strong and should be discussed with care in many experimental works. ionisation or multiple heating mechanisms could be sink or source terms localized in energy, deforming the energy distribution functions and leading to non-maxwellian distributions. Bi-maxwellian or Druyvenstein distributions [Che03; God+11] are possible but no occurrence have been confirmed in the VKP set-up.

Kinetic models are often used in numerical simulations where the collisionless Boltzmann equation, called the Vlasov equation, is solved continuously in space and time. Particles are distributed over a meshgrid and the moments I.26 are averaged at this intermediate spatial scale. Therefore calculations are lighter and can be achieved up to the millisecond temporal scale [Luc+20]. This method is called the Particle-In-Cell (PIC) method.

Multi-fluid model: The previous microscopic description can be extended to the macroscopic scale. By considering equation I.23 for each particle species and integrate it over velocity space, one can derive the macroscopic continuity equation

$$\frac{\partial n_s}{\partial t} + \nabla \cdot (n_s \mathbf{v_s}) = S - L \tag{I.29}$$

where S and L are respectively the source and loss terms associated to ionisation and recombination. A similar integration over velocity space of equation I.23 multiplied by $\mathbf{v_s}$ gives the momentum conservation equation

$$m_s n_s \left[\frac{\partial \mathbf{v_s}}{\partial t} + (\mathbf{v_s} \cdot \nabla)\, \mathbf{v_s}\right] = \pm e n_s (\mathbf{E} + \mathbf{v_s} \times \mathbf{B}) - \nabla P_s + \mathbf{f_s}|_c \tag{I.30}$$

with P_s the pressure tensor, assumed to be isotropic, and $\mathbf{f_s}|_c$ the collisional term that accounts for drag, ionisation and recombination. This approach is analogous to the classical fluid mechanics formalism applied to each plasma species independently. Microscopic fluctuations are smoothed to focus on the macroscopic plasma dynamics, therefore it is relevant for near-equilibrium systems or for non quasi-neutral systems such as sheaths.

Magnetohydrodynamic model: A stronger coupling between the ions and electrons would lead to a global thermodynamic equilibrium and a ion-electron coupled dynamics. The magnetohydrodynamic model, often called MHD, attempts to capture the main resulting features by relying on the following assumptions:

1. Electron inertia is negligible compared to ions: $m_e \ll m_i$;
2. Quasi-neutrality is always verified: $n_e - n_i \ll n_e + n_i$;
3. Electromagnetic waves are neglected, meaning that the displacement current in Maxwell equation is small before the current density: $\left|\epsilon_0 \frac{\partial \mathbf{E}}{\partial t}\right| \ll |\mathbf{J}|$;
4. Larmor radius is small before the system size $\rho_s \ll R$, meaning that magnetisation is strong compared to kinetic effects: $\mathbf{V} \times \mathbf{B} \gg \frac{1}{ne} \nabla P$, with V the plasma velocity.

Hence the MHD model describes accurately slow plasma dynamics and macroscopic scales. The MHD speed is then mostly governed by the ions flow $\mathbf{V} \simeq e n_i \mathbf{v}_i$ and the density is approximated to the ion density $\rho \simeq n_i m_i$. These assumptions enables to combine equations I.29 and I.30 so that it yields the following set of equations:

$$\frac{\partial \rho}{\partial t} + \nabla \cdot \rho \mathbf{V} = 0 \tag{I.31}$$

$$\rho \frac{D\mathbf{V}}{Dt} = -\nabla P + \mathbf{J} \times \mathbf{B} \tag{I.32}$$

where $\frac{D\mathbf{V}}{Dt}$ is the material derivative of $\mathbf{V}$ and $P = P_e + P_i$ is the total pressure. Once combined to Maxwell equations and the state equation of the plasma, this set of equations is closed and provides a rich description of the plasma properties. This model was proven to be reliably describing plasma instabilities, waves and transport properties in tokamaks. However in the VKP set-up, the magnetised assumption is invalidated, so the relevant model for the plasma is the multifluid model.

I.2.7 Particle and energy balance in an inductive discharge

A global model relying on a particle and energy balance in the plasma enables to compute a preliminary analysis on plasma density and electron temperature. The model presented here follows the approach found in [Lie+05] and [Cha+11].

I.2.7.1 Particle balance

The most simple model consists in a cylindrical low-pressure unmagnetised quasi-neutral plasma discharge. Ions and neutrals are considered cold. The cylinder dimensions are a length L and a radius R. The model is qualified as 0D, meaning that the plasma the plasma properties such as density n, electron temperature T_e and plasma potential ϕ_p are considered homogeneous except at the floating walls. A particle balance for the species s over a volume $\mathcal{V}$ in the bulk plasma reads:

$$\frac{\mathrm{d}}{\mathrm{d}t}\left(\iiint_{\mathcal{V}} n_s\,\mathrm{d}V\right) = S_s - L_s \tag{I.33}$$

where S_s and L_s are respectively the sources and the losses terms.

By considering the plasma in a stationary state, the time-varying term can be equated to 0. Then, the source term results from ionising collisions between energetic electrons and neutral atoms in the plasma bulk. The rate of ionisation for each electron-neutral collision, of respective densities n and n_n, is called the reaction rate. It is noted K_{iz} and it corresponds to the constant rate for electron-neutral ionisation cross-section (see subsection I.2.3). It strongly depends on the electron temperature. Overall, the source term is $K_{iz}(T_e)nn_n\mathcal{V}$. On the other hand, the losses occur in the plasma bulk or at the wall. By considering a low-pressure plasma, the ion-electron recombinations in the bulk are negligible. The loss term consists mainly in an important particle flux at the walls, which cover a surface $\mathcal{S}_{wall}$. The electron flux at the floating wall is given by the Bohm sheath criterion [Rie91] and reads $nu_B(T_e)\alpha\mathcal{S}_{wall}$, with α the sheath-to-bulk density ratio introduced in subsection I.2.1. α is roughly estimated at 0.5 in the case of our low-density cylindrical plasma. The total particle balance equation I.33 thus yields

$$nu_B(T_e)\alpha\mathcal{S}_{wall} = K_{iz}(T_e)nn_n\mathcal{V} \quad \Leftrightarrow \quad \frac{n_nK_{iz}(T_e)}{u_B(T_e)} = \alpha\frac{\mathcal{S}_{wall}}{\mathcal{V}} \tag{I.34}$$

Counter-intuitively, the particle balance allows to compute the electron temperature and not the plasma density. Solving equation I.34 requires the knowledge of the complex reaction rate. Is has been done here using the fit proposed by Lieberman and Lichtenberg [Lie+05] in the range 1 eV − 7 eV. It leads to the calculation of the electron temperature in the fully magnetised VKP-ICP case as a function of the neutral pressure, the gas species and the device geometry, as shown in figure I.6a).

The ratio $\frac{\mathcal{S}_{wall}}{\mathcal{V}}$ is key for the electron temperature, because it represents the ratio of the plasma particles surface losses to the volume source. The magnetic confinement reduces $\mathcal{S}_{wall}$ from the total cylindrical surface $2\pi R\,(R+L)$ to the disk bases of the fully magnetised plasma column $2\pi R^2$. An estimation for the VKP-ICP case gives $T_e = 5.23$ eV in the unmagnetised case, and $T_e = 2.78$ eV in the fully magnetised case (see figure I.6a)). Since the plasma column is weakly magnetised, the empirical electron temperature is most likely to lie between these two extremal values. The experimental values ranging between 3 and 4 eV, the 0D particle balance yields only a rough estimate of the electron temperature, but it captures most of the underlying physics.

A decrease in $\frac{\mathcal{S}_{wall}}{\mathcal{V}}$ means an increased confinement time for the plasma. It is associated to more particle collisions, consequently a enhanced heat transfer from electrons to ions and neutrals and a decreased electron temperature. This effect has to be considered when inserting a probe in the plasma: besides being intrusive and creating a new sheath, adding a surface to the plasma modifies the plasma particle balance. Note also that the neutral gas evolution has not been discussed here. Neutrals are depleted through ionisation and refilled via diffusion. Their dynamics should not be neglected as it impacts the plasma behaviour significantly (see chapters III and V and references [Fru17 ; Deg+99a ; Vin21]).

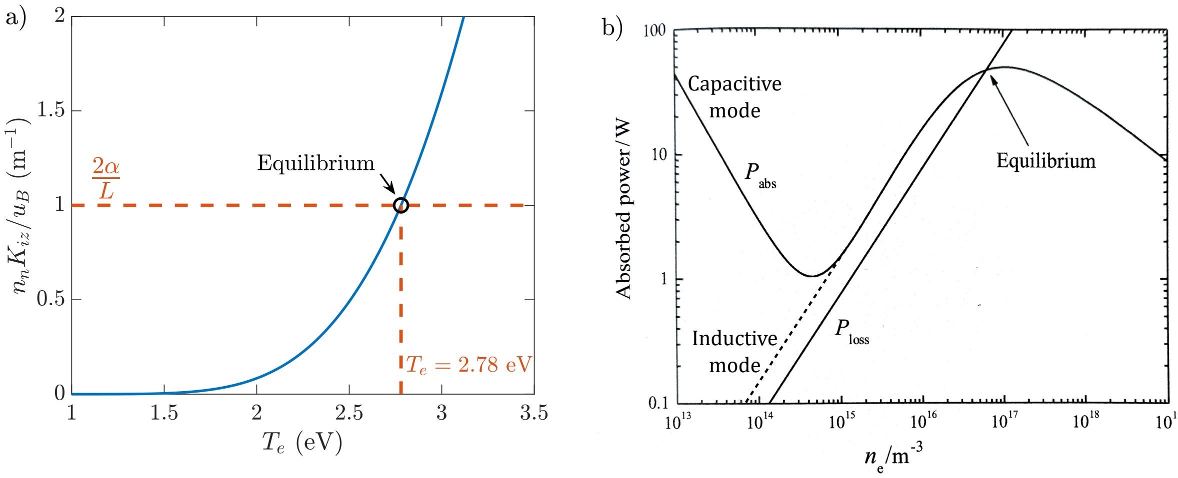

FIGURE I.6 – *a)* Particle balance and resulting electron temperature at equilibrium for $p_0 = 0.13$ Pa. Equilibrium for the magnetised VKP-ICP case is reached at $T_e = 2.78$ eV. *b)* Capacitive-inductive mode transition in an inductively-coupled plasma resulting from the $P_{abs} = P_{loss}$ equilibrium. Taken from [Cha+11].

I.2.7.2 Energy balance

Similarly, an energy balance for the whole plasma can be derived. The plasma energy is mainly concentrated in the electron kinetic energy since ions are cold. Electrons are considered as a perfect gas, so the energy balance over the volume $\mathcal{V}$ reads

$$\frac{\mathrm{d}}{\mathrm{d}t}\left(\iiint_{\mathcal{V}} \frac{3}{2} n e T_e \,\mathrm{d}V\right) = P_{abs} - P_{loss} \tag{I.35}$$

with P_{abs} and P_{loss} respectively the absorbed and lost powers.

The stationary assumption enables to cancel the left-hand side term. The absorbed power is complex and will be discussed further in subsection I.2.7.3. It is identified as the antenna power P_w for now. The energy is absorbed by the electrons and transferred to ions through ionising collisions. On the other hand, the loss term is due to the fluxes at the wall. For each electron-ion recombined pair, the lost energy E_T is the sum of the collisional energy loss E_c, which includes the first ionisation energy of an argon atom $\mathcal{E}_i$, the ion kinetic energy E_i and the electron kinetic energy E_e [Lie+05]. An estimation yields $E_T \simeq 75$ eV.

Overall, the energy balance in a stationary plasma reads

$$P_w = n u_B(T_e)\alpha \mathcal{S}_{wall} e E_T \quad \Leftrightarrow \quad n = \frac{P_w}{u_B(T_e)\alpha \mathcal{S}_{wall} e E_T} \tag{I.36}$$

The input power drives primarily the plasma density. Once again, the wall surface can be reduced by magnetisation. Pressure influences n via the plasma collisionality and the factor α, and the electron temperature is given by the particle balance. The estimated density for $P_w = 1$ kW in the magnetised VKP-ICP case yields $n = 3.6 \times 10^{18}$ m^{-3}. This order of magnitude is consistent with experimental measurements. Besides, the quasi-linear dependency of the plasma density on the RF power has been evidenced on the VKP-ICP device [Dés18].

I.2.7.3 Absorbed power

The power absorbed by the plasma is non-trivial. The power fed to the antenna P_w is partly radiated by the antenna, reflected or lost through Joule heating or eddy currents in the matching network, the Faraday cage and the metallic structure [Pie+92; Hop94]. The reflected power is negligible because the matching box allows a fine tuning of the output impedance. Overall, the RF power transfer efficiency to the plasma is expected to be about 60 to 90 % of P_w depending on the antenna, borosilicate tube dimensions and the experimental parameters [Cha+11; Zie+21].

Then, the radio-frequency antenna is inductively coupled to the plasma. Strong inductive electromagnetic fields penetrate through the plasma on a typical length scale called the skin depth δ. In the case of a collisionless plasma, the skin depth is

$$\delta = \frac{c}{\omega_{p,e}} = c\sqrt{\frac{m_e \epsilon_0}{ne^2}} \tag{I.37}$$

At low plasma density, the skin depth is larger than the radius of the glass tube. The induced RF electromagnetic fields are not dampened, and an increase in the density is proportional to the power absorbed by the plasma. However, when δ is smaller than the glass tube radius, an increased plasma density would result in a smaller skin depth, which reduces the power deposited into the plasma. The absorbed power follows a $n^{-1/2}$ trend at high plasma density, which limits the plasma density at high RF power.

The high voltage generated at the antenna vicinity is strong enough to generate a collisionless capacitive heating. Large oscillating sheaths develop at the antenna proximity, trapping and heating electrons at the plasma edge. The power absorbed by the capacitively-coupled plasma is inversely proportional to the plasma density, meaning that this coupling mode is prominent at low density and thus low power. The coexistence of these two coupling modes causes a non-trivial plasma density dependency for P_{abs}. P_{loss} being linear in n, the equilibrium is reached by equating the two as in figure I.6b), taken from Chabert and Braithwaite [Cha+11].

An increase in power P_w results in a non-linear increase in n of a few orders of magnitude as the plasma experiences a transition between a capacitive coupling and an inductive coupling. This mode transition often exhibits a hysteresis associated to the existence of a bistable configuration.

The VKP-ICP antenna being optimised for an inductively-coupled plasma at $f_0 = 13.56$ MHz, the inductive mode is observed even at low power. However, the upgrade to a half-helical helicon antenna induces a more complex operation diagram with multiple mode transitions. The supplementary helicon plasma modes are added to the pre-existing capacitive and inductive phenomenology. This feature will be detailed in chapter IV.

I.2.8 Summary

The orders of magnitude classify the plasma as a cold low-pressure weakly magnetised plasma column. The collision rates lie between 10 kHz and 10 MHz. The correct plasma modelling is the multi-fluid model as the plasma is not magnetised enough to meet MHD conditions. Then this model will be considered for further interpretation.

I.3 Diagnostics

The various electrostatic and optical diagnostics used over the course of this PhD are listed herein. Their use was not restricted to the VKP-ICP case, and has been adapted to the helicon plasma case presented in chapter IV. Moreover, high-speed imaging, the compensated Langmuir probe and the B-dot probe were only used for helicon plasma characterization as they were particularly relevant for high plasma density conditions and helicon wave investigation. Then, the typical protocol of operation and the mean plasma properties profiles in the VKP-ICP case are presented and discussed.

I.3.1 Langmuir probe

I.3.1.1 Basic Langmuir probe theory

The Langmuir probe is a simple electrostatic probe, which consists in an electrode immersed into the plasma. It is constituted of a thin alumina probe shaft of ~ 2 mm in diameter and a robust metal tip, such as molybdenum, tungsten or tantalum (see figure I.7a)). It can be biased and collect charged species in the bulk plasma depending on its potential V_{Lang}. The resulting $I-V$ characteristics measurement is fundamental. Indeed, it probes the electron and ion energy distribution functions, mentioned in sub-section I.2.6, by spanning a wide range of potential energies [God+11].

The data analysis principles and the practical application will now be detailed.

Experimental application: The electrical circuit of the Langmuir probe is presented in figure I.7b). The bias applied to the probe V_{Lang} is swept and the corresponding collected current I_{Lang} is measured. The impedance of the plasma is not represented and is large before the shunt resistor R_{sh}. The ideal $I-V$ curve for a cold plasma is pictured in figure I.7c).

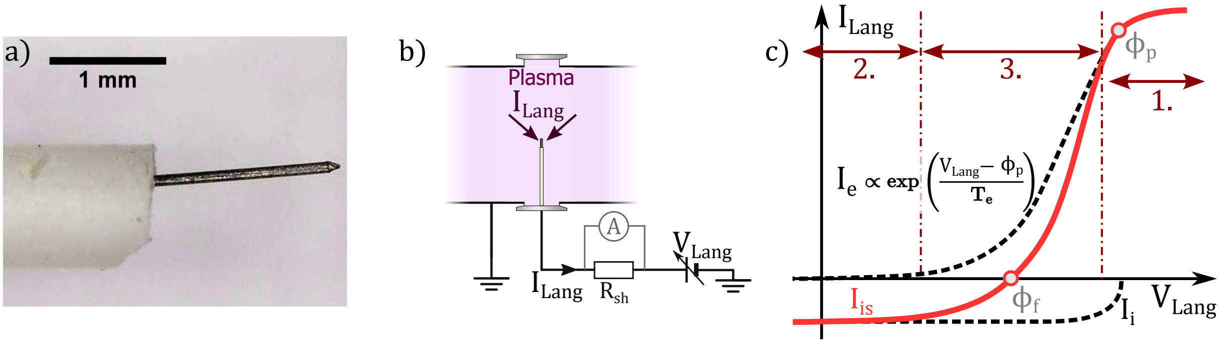

FIGURE I.7 – *a)* Microscope picture of a Langmuir probe tip. *b)* Electrical circuit for a Langmuir probe measurement. The non-trivial impedance of the plasma is not represented. *c)* Ideal Langmuir $I-V$ characteristics.

The $I-V$ characteristics can be divided in three different zones noted 1., 2. and 3. in figure I.7c). The interpretation of this curve requires to understand its shape:

1. Electron saturation: A potential $V > \phi_p$ attracts the electrons within the sheath to the probe tip while cold ions are repelled. The most common convention is to consider this current positive. It results in a current threshold I_{es} appearing beyond ϕ_p, allowing to measure either the plasma potential or the plasma density.

2. Ion saturation: Reciprocally, a low potential attracts ions within the sheath to the probe tip. Ions are considered cold, *i.e.* $T_e \gg T_i \simeq 0$. Their attraction to the probe tip is modelled with a free fall model. The accelerated ions reach the Bohm speed u_B at the sheath entrance, meaning that the total current collected at the probe in the ion saturation regime is

$$I_{is} = en_i \mathcal{S} \alpha u_B \tag{I.38}$$

with $\mathcal{S}$ the probe surface and α a correction factor for the density depletion at the sheath vicinity (see subsection I.2.1). When assuming quasi-neutrality ($n_i = n_e = n$), this zone offers a reliable measurement of the plasma density given that T_e is measured beforehand. I_{is}/I_{es} being proportional to $\sqrt{m_i/m_e}$, the ion saturation current is much weaker, which can be an experimental challenge to measure accurately, but mostly a benefit as ion saturation regime perturbs less the plasma and is less wearing for the probe.

3. Transition regime: In the intermediate zone, cold ions and hot electrons are attracted. This regime contains the floating potential ϕ_f above-mentioned (see subsection I.2.1), which corresponds to the balance between the ion and the electron fluxes at the probe. Then, the electrons being thermalized at a temperature T_e as mentioned in equation I.4, the electron flux to the probe results from a balance between thermal agitation and the electric field applied between the plasma and the probe. On the other hand, the ion current is small before the electron current and steeper around ϕ_p, since ions are cold. Overall, the total current at the probe is

$$I_{Lang} = I_e - I_i \quad \text{with} \quad I_e = I_{es} \exp\left(\frac{V_{Lang} - \phi_p}{T_e}\right) \quad \text{and} \quad I_i = I_{is} \exp\left(-\frac{V_{Lang} - \phi_p}{T_i}\right) \tag{I.39}$$

In summary, this transition regime allows us to measure T_e and the floating potential ϕ_f. These two quantities combined provide another estimation of ϕ_p using equation I.5.

Data analysis: In practice, the exploitation of Langmuir probe data is complex, and comprehensive reviews of the various methods can be found elsewhere [Hop95; God+11]. The routine analysis used throughout this PhD is represented in figure I.8, for a helicon plasma generated at 180 G, 1.4 kW and 0.13 Pa.

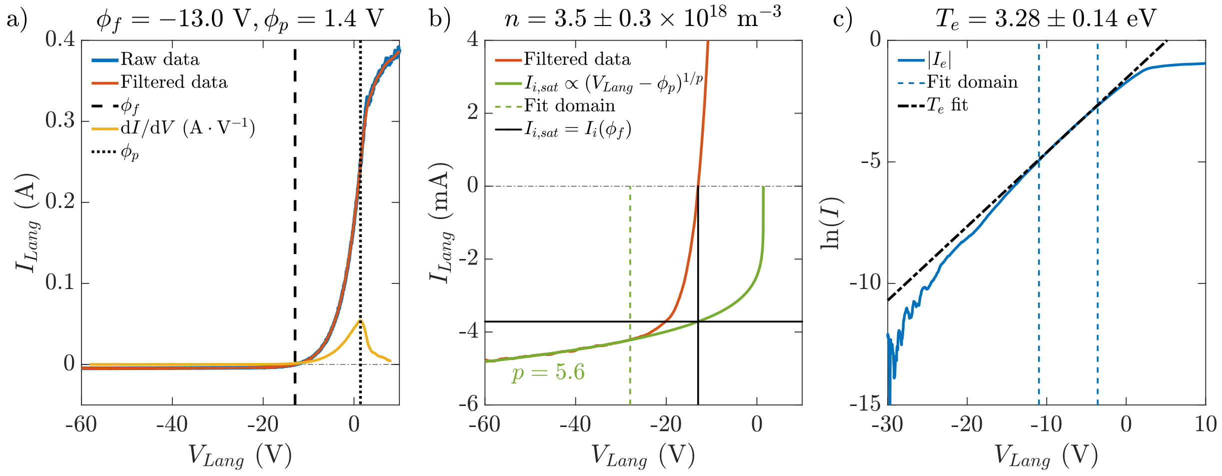

FIGURE I.8 – Langmuir scan for a helicon plasma at 180 G, 1.4 kW and 0.13 Pa. *a)* Floating and plasma potential measurements; *b)* Plasma density measurement; *c)* Electron temperature measurement.

1. Firstly, raw data are filtered using a second-order Savitzky-Golay filter. Then, the floating potential value is directly found as the zero-current point, which yields $\phi_f = -13.0$ V in the present case. The plasma potential value can be estimated by identifying the maximum in the derivative of the $I - V$ characteristics dI_{Lang}/dV_{Lang} (yellow line in figure I.8a)) and is found at $\phi_p = 1.4$ V. This estimation is questionable as the maximum in the $I - V$ derivative is accurate up to a factor T_e. The high electron saturation current extracted from the plasma modifies the plasma equilibrium as well.
2. Secondly, the I_{is} domain is fitted in the low potential region ($V_{Lang} < \phi_f - 20$ V, see figure I.8b)). The strong biasing at low potential leads to an expansion of the sheath. In the case of

a planar probe, the sheath expansion does not lead to an increased ion saturation current, because the sheath surface remains constant. However, the cylindrical probe geometry and dimensions should be carefully considered to understand the sheath expansion and the ion saturation current increase. The cylindrical ABR theory aims at computing the plasma sheath extension to improve the ion saturation regime analysis and the plasma density calculation [Che01]. The Debye length and the sheath size can be computed in the frame of the cylindrical ABR theory. It enables to calculate reliably the α correction factor depending on the plasma density and the probe dimensions [Che+02]. This refinement was implemented during previous PhD works [Dés18] and exploited in the work herein. Hence, a power law fit of the form $I_{is} \propto \left(V_{Lang} - \phi_p\right)^{1/p}$ is used to compute the ion current at $V_{Lang} < \phi_p$ ($p = 5.6$ in the current case). Plasma density is then calculated recursively from the ion current at ϕ_f using equation I.38 coupled to cylindrical ABR theory, and is estimated at $3.5 \pm 0.3 \times 10^{18}$ m^{-3} here. The error estimation arises mostly from the error in the probe surface measurement (about 10%), and secondarily from the error in electron temperature measurement (about 5%).

3. Finally, the electron current can be inferred from the ion current fit obtained previously and the I_e equation I.39. The logarithm of the electron current is fitted linearly over a wide range of potential. The slope of the fit gives the inverse of the electron temperature, measured here at $T_e = 3.28 \pm 0.14$ eV. The error estimation is attributed to the fit domain, and is evaluated by displacing the fit boundaries of ± 3 V.

The practical implementation of Langmuir probes comprises a few caveats to be addressed rigorously. The surface state of the probe might hinder the measurement reproducibility, and it is advised to clean it before measurement by ion bombardment for instance. Another issue might be a poor electrical contact to the ground. Since the electron current collected at the probe has to be balanced by an ion current at the ground in order to conserve electrical charge, a bad grounding leads to an artificial electron saturation because of a poor collection of ions at the vessel ground. Besides, the effect of the magnetisation should be treated carefully, as it impacts significantly the electron current. It may distort the electron saturation regime, leading to a skewed estimation of the plasma potential and electron temperature [Che03]. Finally one recurrent source of error is the existence of fast plasma potential fluctuations, which can be corrected using compensated probes. This point will be discussed in the next subsection.

I.3.1.2 Compensated Langmuir probe upgrade

An $I - V$ characteristics consists in a sweep in bias divided over a finite sample of points. Each point corresponds to a current measurement averaged over a time period $\tau \sim 10^{-4}$ s. But if a plasma potential fluctuation of amplitude $\phi_{p,0}$ at a frequency $f \gg 1/\tau$ is present, the measured electron current is

$$\langle I_e \rangle = I_{es} \left\langle \exp\left(\frac{V - \left(\phi_p + \phi_{p,0} \cos\left(2\pi f t\right)\right)}{T_e} \right) \right\rangle_\tau \tag{I.40}$$

The averaged measurement is deformed due to the non-linearity of the exponential as drawn in figure I.9a), leading to an overestimated T_e measurement and an underestimated ϕ_f measurement. It is especially present in radio-frequency plasmas, where strong ϕ_p fluctuations up to $\phi_{p,0} = 5T_e$ may arise at f_0 and its n-th harmonics f_n.

A solution is to add a compensatory system to keep a constant potential drop between the probe bias and the plasma. It can be done by actively subtracting the plasma potential fluctuations

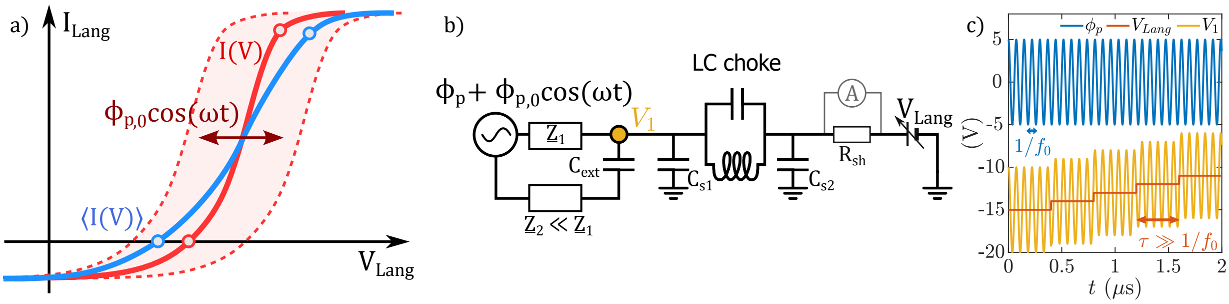

FIGURE I.9 – *a)* Ideal $I(V)$ (red line) and distorted $\langle I(V)\rangle$ (blue line) Langmuir $I - V$ characteristics because of fast plasma potential fluctuations (red pale area). *b)* Electrical circuit for the passive compensated probe design. *c)* Time resolved voltages in the electrical circuit. V_1 is the electrical potential at the electrode.

to the probe bias [Dys+00], or by designing a passive system that allows the probe tip bias to fluctuate along with the plasma potential [Cha+91 ; Sud+94].

Compensated Langmuir probes prototypes were designed for VKP-ICP a few years ago, but no significant effect on the $I - V$ characteristics was detected. However, helicon plasmas may exhibit stronger plasma potential fluctuations. A new RF-compensated Langmuir probe for the helicon plasma upgrade (see chapter IV) has been constructed over the course of this PhD during the Master internship of Eitan Soussan that I co-supervised (see figures I.10a) and b)). The probe design follows the electrical schematics shown in figure I.9b). A first short electrode is immersed in the plasma. The electrode surface being small, the non-trivial plasma sheath impedance $\underline{Z}_1$ is high. The compensated Langmuir probe incorporates a large secondary floating electrode wrapped around the end of the probe shaft. In practice, a 1 cm high plate of tantalum soldered to a tantalum wire is wounded at the end of the ceramic shaft. The goal is to reach a low plasma sheath impedance $\underline{Z}_2$, enabling an accurate acquisition of the plasma potential fluctuations [Can+15]. This electrode is connected through the external capacitor $C_{ext} = 1$ nF to the measuring tip so that the latter follows the high-frequency plasma potential fluctuations. By doing so, a constant potential drop is maintained between the measuring electrode and the plasma, contrarily to the uncompensated probe case.

Then, two high-impedance high quality factor LC bandstop chokes centred around the fundamental f_0 and the first harmonic f_1 are added between the measuring electrode and the DC voltage supply. The LC chokes are made of ceramic capacitors and diamagnetic-core (PVC) inductors. The role of the chokes is to absorb the RF fluctuations and to dissociate efficiently the two electrodes from the DC voltage supply. The goal of the compensation circuit is to impose a bias V_1 at the electrode so that the voltage difference $\phi_p - V_1$ remains constant over the measuring time τ (see figure I.9c)). Its efficiency depends on the choke impedance, and is notably hindered by a high plasma sheath impedance $\underline{Z}_2$ and the cable stray capacitance C_{s1}. Finally, the current collected I_{probe} is measured using the shunt resistor R_{sh}.

The plasma sheath impedance can be modelled as a non-linear parallel RC circuit with the following components [Sud+94]

$$R_2 = \frac{\lambda_D^2}{\epsilon_0 \alpha \mathcal{S} u_B} \quad \text{and} \quad C_2 = \frac{\epsilon_0 \mathcal{S}}{2^{7/4}\lambda_D}\left(\frac{\phi_p - V}{T_e}\right)^{-3/4} \tag{I.41}$$

which results in a total impedance at f_0 of the order of magnitude $|Z_2| \simeq 40 - 400\ \Omega$ for densities ranging between 10^{19} m^{-3} and 10^{18} m^{-3}. This impedance is minimised by increasing the auxiliary probe size.

On the other hand, the stray capacitance C_{s1} is mostly due to the alumina tube surrounding the electrodes. The dielectric acts as a capacitance and is connected to the ground through the plasma. Hence, this stray capacitance is hardly measurable in practice, but it can be roughly estimated at $100\ \mathrm{pF} \cdot \mathrm{m}^{-1}$. It is the typical value of a stray capacitance for a millimetre dielectric coaxial cable. A pluggable box containing the chokes has been designed and can be added at the electrical vacuum feedthrough, 50 cm away from the electrodes. C_{s1} is thus estimated at 50 pF, and its associated impedance is about 250 Ω at f_0. The second stray capacitance C_{s2} being placed after the chokes, the high-frequency fluctuations are weak and its role is negligible.

The chokes of impedance Z_{ck} coupled to the stray capacitor have an equivalent impedance

$$Z_{eq} = \frac{Z_{C_{s1}} Z_{ck}}{Z_{C_{s1}} + Z_{ck}} \tag{I.42}$$

so a good design of the chokes involves $Z_{ck} \gg Z_{C_{s1}}$ so that Z_{eq} is as high as possible. In this case, $Z_{eq} \simeq Z_{C_{s1}}$ and an upgraded LC choke would not improve the RF compensation. In other words, the stray capacitance impedance $Z_{C_{s1}}$ is the limiting factor in the compensation efficiency. The efficiency condition of the compensation system has been established by Sudit and Chen [Sud+94]

$$\left|\underline{Z}_{eq}\right| \gg \left|\underline{Z}_2\right| \left(\frac{\phi_{p,0}}{T_e} - 1\right) \tag{I.43}$$

The impedance of the complete compensated probe is measured using a vector network analyser (VNA) Anritsu MS2034A. It is composed of a $Z_0 = 50\ \Omega$ output port and a $Z_0 = 50\ \Omega$ input port. It probes the electrical response of the component under test by sending a signal that excites a wide range of high frequencies from the output port, and analysing the power reflected to the output port and the power transmitted to the input port. The VNA signal passes through the compensated probe from the electrode tips to the end of the chokes. The resulting global impedance of the compensated probe is displayed in figure I.10c). The stray capacitance being absent without plasma, the total impedance is assimilated to Z_{ck}. The total impedance at f_0 (respectively f_1, the first harmonics) reaching 17 kΩ (resp. 6.4 kΩ), the criterion $Z_{ck} \gg Z_{C_{s1}}$ is verified. Ultimately, the compensation is efficient up to $\phi_{p,0} = 1 - 3T_e$ fluctuation amplitude.

The compensated probe has been used on helicon plasmas only, at densities larger than $5 \times 10^{18}\ \mathrm{m}^{-3}$. Larger densities reduces $|\underline{Z}_2|$, improving the efficiency of the RF compensation. Its effect is illustrated in figure I.10d), with the uncompensated (blue line) and the compensated (red line) Langmuir scans at the helicon plasma core, for 180 G, 0.13 Pa and 1.2 kW. The comparison between the two scans suggests a plasma potential fluctuation of about $1 - 2T_e$, so the compensated probe appears to be efficient in this range as expected. The electron temperature fits are shown in insert. T_e decreases from 5.9 eV to 4.3 eV using the compensated probe, thus illustrating the efficiency of the compensation.

The stray capacitor is detrimental to the accomplishment of an efficient compensation system. It can be reduced by placing the chokes as close as possible to the probe tips. Such an upgrade could improve significantly the efficiency of the compensation up to a factor 5. Moreover, the assembled compensated probe seems inefficient at low plasma density $n < 10^{18}\ \mathrm{m}^{-3}$, *i.e.* at the plasma edge or at low RF power. Such an upgrade could extend the use of the compensated probe to low plasma density regimes.

I.3.2 5-tips probe

The 5-tips probe is an advanced Langmuir probe constituted of five close-packed electrodes separated by 0.8 mm each (see figure I.11a)). It allows to conduct temporally-resolved measurements of plasma properties n, T_e, ϕ_f and to assess ϕ_p. The probe is oriented such that the tips 2 and 4 are aligned horizontally along z, while the tips 1 and 5 are aligned vertically along the azimuthal coordinate of the cylindrical vacuum chamber θ. The sampling rate was set up to 200 kS/s.

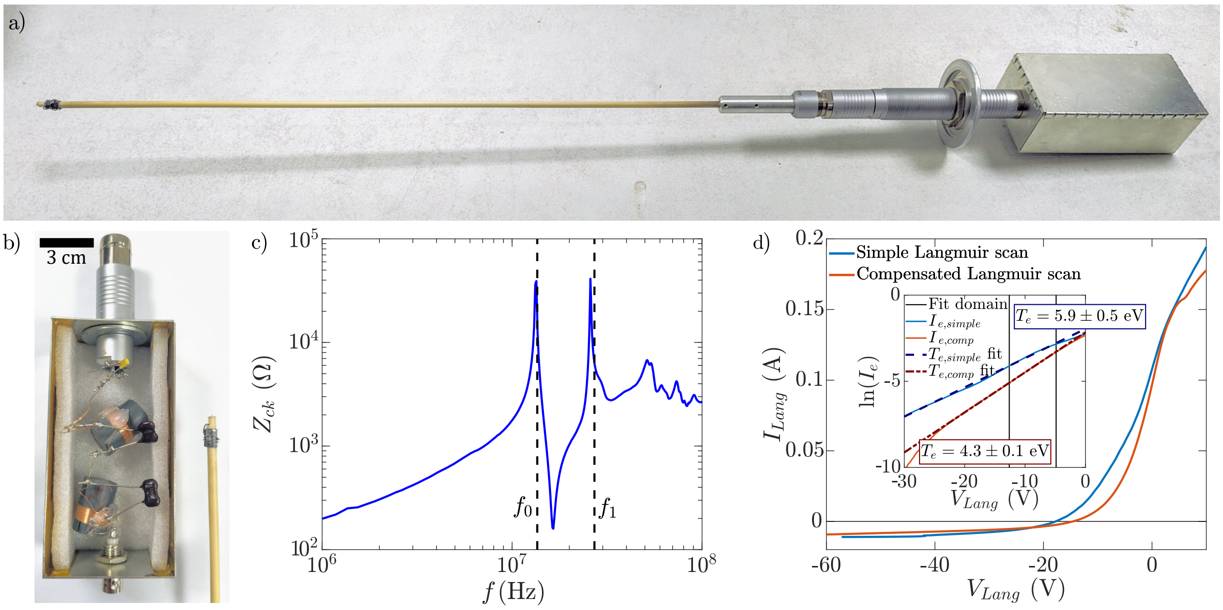

FIGURE I.10 – *a)* Picture of the fully assembled compensated Langmuir probe. *b)* Compensated probe tip and chokes. In the box from top to bottom: external capacitor C_{ext}, f_1 and f_0 LC chokes. *b)* Impedance of the complete probe in absence of plasma. *c)* Uncompensated (blue) and compensated (red) $I - V$ scan. Insert: corresponding electron temperatures.

Its working principle is detailed in previous articles [The+11; Vin+22] and will not be reviewed thoroughly here, but the working principle will be explained.

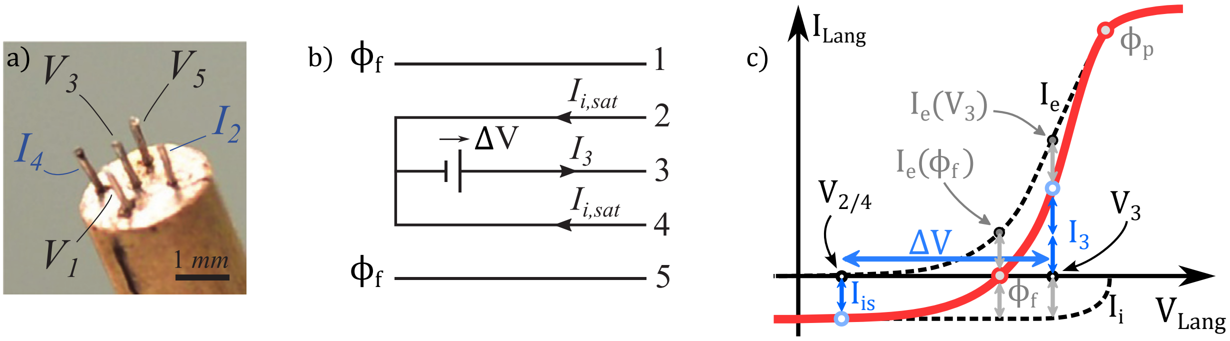

FIGURE I.11 – *a)* Picture and *b)* electrical circuit of the 5-tips probe. Credit: Simon Vincent [Vin+22]. *c)* Operation principle of the 5-tips probe based on the $I - V$ characteristics of a Langmuir probe.

The five tips electrical circuit is detailed in figure I.11b). The probe is operated this way:

- Tips 1 and 5 are left floating and the temporal evolutions of V_1 and V_5 are recorded. The measured floating potential is averaged: $\phi_f = (V_1 + V_5)/2$.
- Tips 2 and 4 are negatively biased in the ion saturation regime and each one measures a temporally resolved ion saturation current I_2 and I_4. The mean ion saturation current is obtained by averaging the collected currents $I_{is} = (I_2 + I_4)/2$.
- The central tip 3 is positively biased in the transition regime. The temporal evolution of the potential V_3 is recorded. The tips 2, 3 and 4 are floating altogether, meaning that the current collected at the tip 3 is counterbalanced by the ion saturation current: $I_3 = I_2 + I_4 = 2I_{is}$.

The principle of operation is illustrated in figure I.11c). The biased applied between the tips is imposed by the user with a default value of $\Delta V = 42$ V unless mentioned. The transition regime above ϕ_f being steep, and the tips 2, 3 and 4 being floating, V_3 is expected to be close to ϕ_f while V_2 and V_4 are strongly biased, ensuring to collect ion saturation current.

Temporally-resolved electron temperature measurement: By assuming a constant ion current between $V_{2/4}$ and V_3, one can compute the electron current I_e at ϕ_f and V_3, *i.e.* $I_e(\phi_f) = I_{is}$ and $I_e(V_3) = 2I_{is} + I_{is} = 3I_e(\phi_f)$. By recalling the expression of the electron current I.39, it results in the following equation for T_e:

$$\frac{V_3 - \phi_p}{T_e} = 3\frac{\phi_f - \phi_p}{T_e} \quad \Leftrightarrow \quad T_e = \frac{V_3 - \phi_f}{\ln(3)} \tag{I.44}$$

This calculation is refined by taking into account more complex profiles of ion saturation current such as described by the cylindrical ABR theory. It provides a temporally-resolved measurement of T_e at the location of the probe tip.

Plasma density measurement: Once the electron temperature is known, one can compute density at each tip using ion saturation current according to equation I.38. This value is proper to each tip, meaning that the local plasma density gradient between the tips 2 and 4 can be investigated.

Plasma potential estimation: As mentioned in section I.2.1, the plasma potential at the tips 1 and 5 can be estimated using the floating potential and the electron temperature (see equation I.8). The measured plasma potential gradient enables to compute the azimuthal electric field $\mathbf{E}_\theta$, and thus the radial $\mathbf{E}_\theta \times \mathbf{B}$ drift and its fluctuations. Coupled to the temporally-resolved density fluctuation measurements $\tilde{n}$, the computed radial plasma flow fluctuations $\tilde{v}_r$ allows to compute the turbulent transport $\Gamma = \langle \tilde{n} \cdot \tilde{v}_r \rangle$ [Vin21]. This advanced technique permits the measurement of the radial transport in presence of intermittency or low-frequency coherent modes, and the investigation of the overall plasma stability during a glow discharge. However, the investigation of the turbulent transport has not been conducted over the course of my PhD.

I.3.3 Emissive probe

An emissive probe is a reliable method for plasma potential measurements. It consists in a hot filament placed in contact with the plasma. A hot electrode emitting thermionic electrons at high temperature, the goal is to emit an outward electron flux important enough to counterbalance the incoming electron flux. The filament is no longer charged by an important incoming electron flux, and the surrounding sheath is cancelled. Then the probe potential follows closely the plasma potential.

The electrons within a crystal exhibit energetic stabilization, consequently the extraction of an electron from the solid requires an external energy work. The energy amount for a single electron is called the work function W. Their order of magnitude is about a few eV, but their value depends on the material itself. The tungsten work function is 4.5 eV [Kaw22]. A mean to overcome this energetic cost of extraction of the electrons within the metal is to heat the material at a temperature T_W. The energetic distribution of the electrons widens, and the most energetic particles can overcome the potential barrier. The complete statistical thermodynamic calculation predicts the following thermionic emission current

$$I_{em} = A_g \mathcal{S} T_W^2 \exp\left(-\frac{eW}{k_B T_W}\right) \tag{I.45}$$

where A_g is the Richardson constant, which depends mildly on the metal material, k_B is the Boltzmann constant and T_W is the metal temperature in Kelvin [Her+49]. This is called the Richardson current, and it represents an upper limit for thermionic emission when the metal is biased negatively, *i.e.* $V < \phi_p$. Indeed, electrons cannot be extracted from the metal if the plasma potential is lower than the metal potential, because the emitted electrons would be electrostatically repelled. Consequently, $I_{em} = 0$ A for $V > \phi_p$. A sharp transition region of typical width $T_W \ll T_e$ exists between these two extremal regimes. Besides, there are numerous refinements about thermionic emission, but they are not essential for understanding the operation principles of emissive probes. They will be discussed in chapter II. The total current at the emissive probe reads

$$I = I_e - I_i - I_{em} \tag{I.46}$$

The resulting typical $I - V$ curve is drawn in figure I.12a). The floating potential of the probe V_{probe} is increased as T_W rises up, until saturation occurs when $V_{probe} = \phi_p$ [She+11]. At this point, the probe is hot enough and the electron emission is strong enough to cancel the surrounding sheath. The floating point method consists in acquiring V_{probe} once the probe has been calibrated at the right temperature.

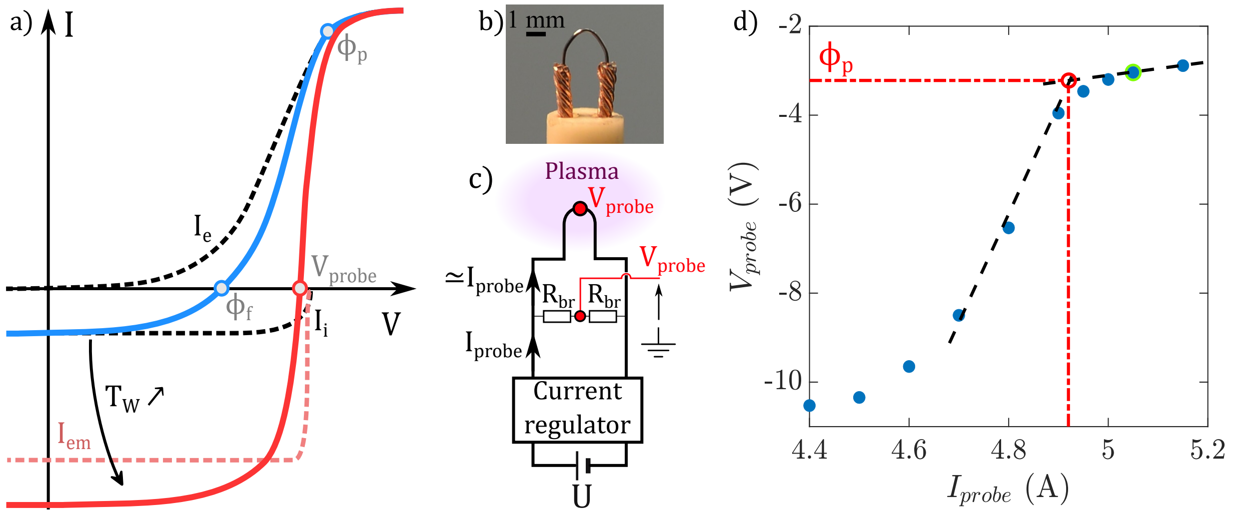

FIGURE I.12 – *a)* I-V characteristics for an emissive probe. I_{em} represents the thermionic current from the metal to the plasma. *b)* Photo of the tip of an emissive probe. Credit : Simon Vincent [Vin21]. *c)* Heating and measurement circuit of the emissive probe. *d)* Typical calibration curve for a plasma generated at 0.13 Pa, 340 G and 1 kW. The green circle is the chosen operation point.

Emissive probes are made of a short 0.15-mm large thoriated tungsten filament held at both ends by five 1-mm large copper wires twisted altogether (see figure I.12b)). The tungsten filament represents the main electrical resistor in the circuit. Thoriated tungsten is used for its low work function, ranging between 2.6 and 4.0 eV depending on its surface state [Sil+10], allowing to reach strong thermionic emission at lower temperature and to improve the lifetime of the filament.

The heating and measuring electrical circuit is displayed in figure I.12c). A DC regulated current supply is alimented by a 12 V-50 Ah battery. It enables the electrical circuit to be floating. The current supply generates a heating current I_{probe} adjustable up to 8 A, which heats the tungsten filament via Joule effect up to 3000 K. The only reference potential in the electrical circuit is the filament potential V_{probe} imposed by the plasma. A symmetric resistor bridge (resistance noted R_{br}) is used to measure it reliably. This system requires R_{br} to be larger than the filament resistance so that I_{probe} is not shunted. Hence, R_{br} was set at 1 kΩ and placed in a grounded stainless steel box. Moreover, this resistor bridge assumes the two copper strands holding the tungsten filament to be perfectly symmetric, *i.e.* having the same length and the same electrical contact with the tungsten filament. Otherwise, the resistor bridge would provide a measurement skewed by about 0.1 to 1 V. Finally, V_{probe} is digitised using the National Instruments PXIe-6368 acquisition card at a sampling rate of 200 kS/s.

The experimental routine is the following:

1. The filament is quickly pre-heated up to 5 A. The bulk thorium in the thoriated tungsten filaments migrates to the metal surface at high temperature, modifying the mechanical and thermodynamic properties of the filament. The goal of the pre-heating phase is to trigger early the thorium migration and to avoid it during calibration or measurement [Wen+21].
2. The calibration is meticulously conducted with 0.1 A increments in the heating current I_{probe} up to saturation of the probe potential V_{probe}, which occurs commonly at $\sim$ 4.5 A. One can see an experimental calibration in figure I.12d) for a plasma generated at 0.13 Pa, 340 G and 1 kW. V_{probe} rises very rapidly with I_{probe} as the filament temperature increases. When the thermionic current I_{em} (see equation I.45) counterbalances the thermal incoming electron flux, the sheath potential drop is cancelled and V_{probe} saturates at the plasma potential ϕ_p. In practice, this saturation occurs smoothly because of the cylindrical filament geometry [She+11]. The plasma potential is identified at the transition between a weakly and a strongly emissive regime. In these extremal regimes, the two trends in V_{probe} with respect to I_{probe} are extrapolated linearly, and the plasma potential is found at their intersection (see black dashed lines in figure I.12d)). An emissive probe would be operated ideally at the transition point. However, the working current after calibration is generally set about 0.2 A above. The goal is to minimize the measurement error on ϕ_p if the filament properties change slightly, as the V_{probe} variations are minor in the hotter regime. The plasma potential value is highlighted with a red dashed line while the working point set for measurements is circled in green.
3. Once the calibration point is determined, the radial or longitudinal scan is conducted. Then the calibration is to be reiterated for other experimental parameters.

The floating point method technique provides a high degree of reliability for plasma potential measurements in any plasma conditions, even at high magnetic field. Moreover, measurements display a remarkable reproducibility. Therefore, it is an advanced diagnostic for plasma potential measurements. The time-resolved measurements gives also access to plasma potential fluctuations, which are essential for low-frequency oscillations investigation or a careful design of new electrostatic probes.

Nonetheless, a mindful experimentalist should be aware of the drawbacks inherent to this experimental method. The intrinsic error between V_{probe} and ϕ_p is of about $T_e/2$ due to the shape of the $I - V$ characteristics [She+11 ; Bou+15]. Besides, the calibration point is reached for higher thermionic emission when the density increases [Bou13 ; Vin21]. That is why calibration is always done at the plasma column center, where n is expected to be approximately the maximum. So, the measured plasma potential at the plasma column edge could be slightly overestimated up to 1 V. Ultimately, emissive probe measurements are technically challenging, and filaments can bear about 100 plasma shots in average before breaking. It strongly depends on plasma properties and especially on plasma density, as a higher filament temperature will cause more mechanical constraints, filament thinning over time and an increased risk of breaking the tungsten filament.

I.3.4 B-dot probe

A B-dot probe is an electrostatic probe relying on induction to measure time-varying magnetic field in the plasma. The most simple design would be a copper loop place inside the plasma: a potential drop e_{ind} arises from the fluctuations of magnetic flux Φ crossing the loop of surface $\mathcal{A}\mathbf{n}$ according to Maxwell-Faraday's law for a motionless circuit:

$$e_{ind} = -\frac{\mathrm{d}\Phi}{\mathrm{d}t} \quad \text{with} \quad \Phi = \int_{\mathcal{A}} \mathbf{B} \cdot \mathbf{n} \, \mathrm{d}S \tag{I.47}$$

This technique is more sensitive as the magnetic flux varies rapidly, making this experimental technique suitable for radio-frequency magnetic waves. In this thesis, the B-dot probe was mainly used to investigate and identify $f_0 = 13.56$ MHz electromagnetic waves properties and its n-th harmonics f_n.

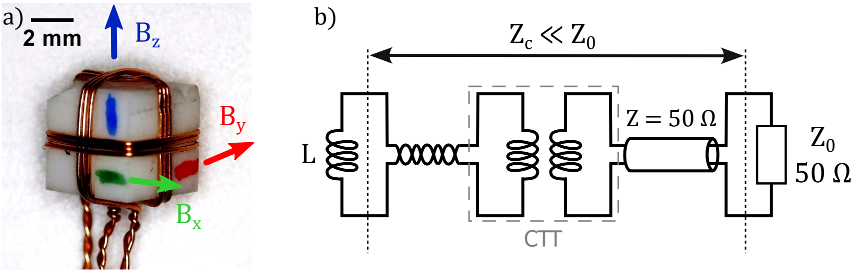

FIGURE I.13 – *a)* Picture of the 3D B-dot head. *b)* Electrical circuit of one B-dot loop of inductance L. The output signal is delivered to a centre-tapped transformer (CTT) through a twisted pair of wire. Then the signal is transmitted via a $Z = 50\ \Omega$ coaxial cable, and acquired using an oscilloscope with a $Z_0 = 50\ \Omega$ output impedance.

Probe design: A 3D B-dot has been engineered over the course of this PhD, of which the head is shown in figure I.13a). The head is composed of three copper coils wrapped around a 5-mm Macor cube in order to measure magnetic fields along three orthogonal directions, so the surface of each loop is approximately $\mathcal{A} = 25$ mm^2. The enamelled copper wire is 0.2 mm in diameter and coils are made of $N = 3$ turns. Great care was dedicated to the orientation of the coils in order to recover the correct sign in equation I.47. The wires are twisted in pairs and then twisted altogether, inserted in a grounded brass tube and covered with a 5-mm wide ceramic tube. These precautions are necessary to limit electrostatic pick-up which would yield a poor signal-to-noise ratio. Then the cables are connected to an electrical vacuum feedthrough Fischer, and connected to three 1:1 ratio center-tapped transformers ADTT1-1+ (abbreviated CTTs) which presents a strong common mode rejection and thus an efficient electrostatic pickup rejection [Fra+02; Jac+19] . The resulting signals are transmitted through shielded coaxial cables to an oscilloscope set at a 50 Ω input impedance. The corresponding electrical circuit is displayed in figure I.13b).

The assembled B-dot probe is displayed in figure I.14a). The probe head is on the right, the hermetic electrical feedthrough is at the middle and the CTTs are contained in the stainless steel box on the left.

Sensitivity: The use of a B-dot probe requires a careful calibration. Its design involves many elements and the sensitivity requires an accurate measurement [Mes+06; Rei+09; Pol+17]. For a harmonic magnetic field B of angular frequency ω and an output signal V_B, the sensitivity β_j in $\mathrm{V} \cdot \mathrm{s} \cdot \mathrm{G}^{-1}$ for the coil along the spatial coordinate j can be defined in this manner:

$$\beta_j(\omega) = \frac{V_B}{i\omega B} \tag{I.48}$$

with i the notation for the pure imaginary number. The magnetic flux crossing a single loop is $\mathcal{A}B$, inducing a total electromotive force in the coil $N\mathcal{A}B$. Let us assume that the signal is measured with an impedance $Z_0 = 50\ \Omega$, and the coil is modelled as an inductor L. The cables and CTTs

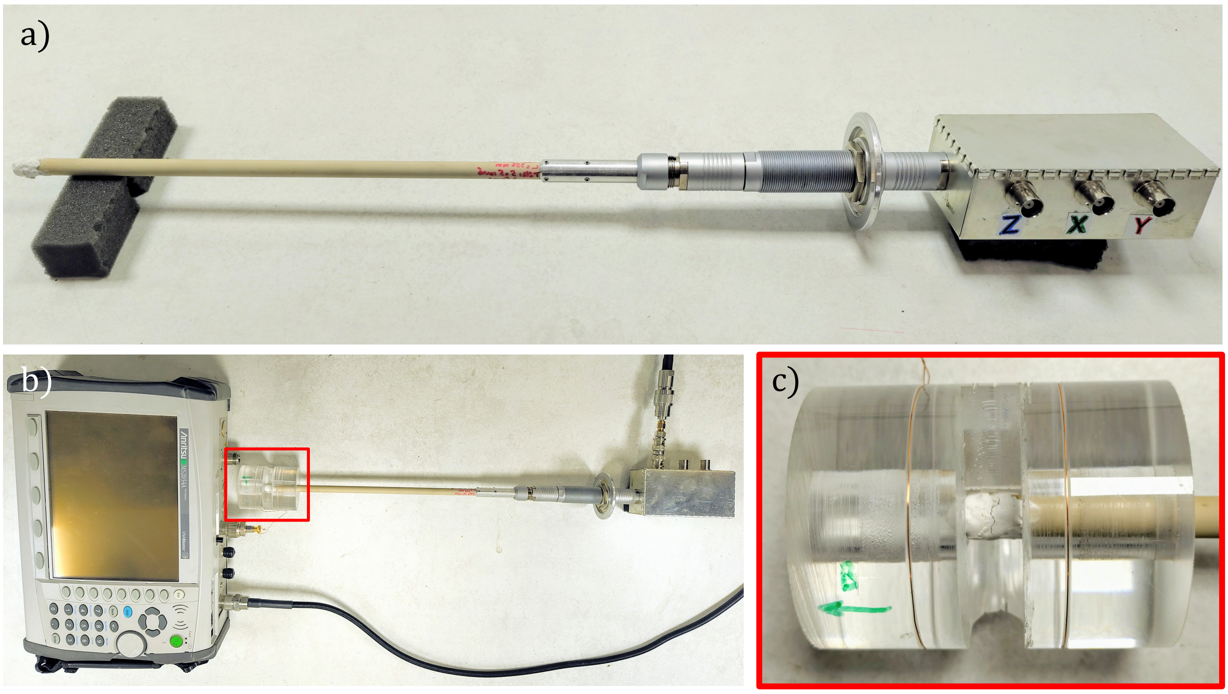

FIGURE I.14 – *a)* Assembled B-dot probe. *b)* Calibration circuit for the probe coil along B_z. *c)* Zoom on the probe head inserted in the Helmholtz coils. The magnetic field direction is indicated.

represent a negligible impedance $|Z_c| \ll |Z_0 + i\omega L|$. A naive expression of the sensitivity would be written as

$$\beta_{naive}(\omega) = N\mathcal{A}\frac{Z_0}{Z_0 + i\omega L} \tag{I.49}$$

The sensitivity of the probe should drop as a first-order lowpass filter above a cut-off frequency f_{cut}. In the present case, L is expected to be about 0.4 μH which would result in a cut-off frequency

$$f_{cut} = \frac{Z_0}{2\pi L} \simeq 20 \text{ MHz} \tag{I.50}$$

Nonetheless the total impedance of the system can be more complex. This is particularly true at frequencies beyond 10 MHz, where non-ideal behaviours of the electric components may reveal unexpected resonances [Gar99]. Additionally, wave resonance might appear in the transmission cables depending on their lengths and their impedance, as it introduces parasitic capacitances and inductances [Mes+06 ; Dém14]. It can be limited by matching the output impedances to the cable impedance, hence setting the oscilloscope impedance at 50 Ω, although it is accompanied by a halved output signal [Pol+17]. For all these reasons it is strongly suggested to complete a wide range frequency scan of the B-dot sensitivity.

Calibration technique: The frequency response of the probe is calibrated according to the method detailed in [Mes+06]. It is achieved by exciting the B-dot probe with a well-known external magnetic field source and analysing the reflected and transmitted powers through the system using the VNA (see figure I.14b)).

In order to excite the B-dot probe, a 1-loop Helmholtz coils have been designed using a 0.2 mm thick copper wire wrapped around a plexiglas core of $R = 2.5$ cm radius. Both loops are separated by a distance $d = R$ in order to obtain a homogeneous magnetic field at the coil center (see figure

I.14c)). The generated magnetic field B_{helm} is proportional to the DC current supplied I with a proportional coefficient α_{helm}, derived theoretically [Pol+17]:

$$B_{helm} = \alpha_{helm} I \quad \text{with} \quad \alpha_{helm} = \frac{8}{5^{3/2}} \frac{\mu_0 N_{helm}}{R} \tag{I.51}$$

with μ_0 the vacuum permeability and $N_{helm} = 1$ the number of turns of the Helmholtz coils.

The results show a fair agreement with the theory as B_{helm} is proportional to I with an experimental proportionality factor $\alpha_{helm} = 0.356 \pm 0.003\ \mathrm{G \cdot A^{-1}}$, close to the theoretical value of $0.360\ \mathrm{G \cdot A^{-1}}$.

Then the frequency response of the system is measured using the VNA. As represented in figure I.15a), the quadrupole under test is composed of the Helmholtz coils coupled to the B-dot probe. They are both modelled using a simple non-ideal coil model that account for unexpected resonances at high frequencies [Gar99]. This schematics does not include transmission lines such as the twisted pairs between the output port and the Helmholtz coils, or the transmission lines displayed in figure I.13b). Yet they are present and are taken into account by the VNA measurements. These transmission lines partly explain the unexpected high-frequency resonances.

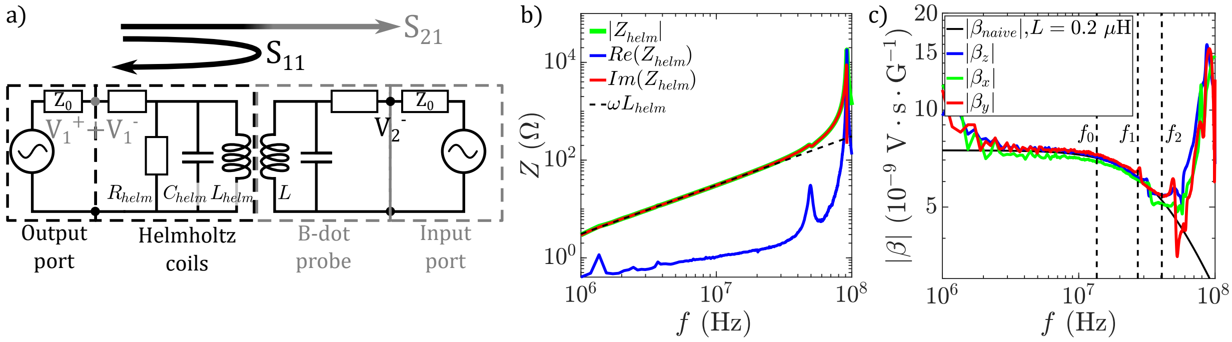

FIGURE I.15 – *a)* Electrical circuit. *b)* Impedance measurement of the Helmholtz coils. *c)* Calibration results for the three coils of the B-dot. $f_0 = 13.56$ MHz and the two first harmonics f_1 and f_2 are shown with the black dashed lines.

The voltage amplitude and phase emitted by a port are described with V_i^+, i being 1 or 2 for the output port and the input port respectively. The input port emits no signal, meaning that $V_2^+ = 0$. On the other hand, the incident voltage amplitude and phase at a port entry are noted

$$V_i^- = S_{ij} V_j^+ \tag{I.52}$$

So S_{11} and S_{21} are complex numbers that encapsulate the electrical response of both elements over the frequency range spanned by the VNA. One can fully understand the electrical behaviour of the quadrupole by performing two successive measurements:

1. Analyse the power reflected at the Helmholtz coils (black dashed box in figure I.15a)) in absence of the B-dot probe and the input port (gray dashed box). It enables to fully calibrate the Helmholtz coils electrical response.
2. Analyse the power transmitted from the Helmholtz coils to the B-dot probe. The fine calibration of the Helmholtz coil impedance is used to deduce the electrical response of the B-dot probe.

The two experiments are carried out successively by spanning the frequency range 1 MHz - 100 MHz. The impedance of the Helmholtz coils is computed from the S_{11} values resulting from the first experiment via the following formula:

$$Z_{helm} = Z_0 \frac{1+S_{11}}{1-S_{11}} \tag{I.53}$$

This formula relies on the fair assumption that there is a negligible phase shift along the 10-cm long transmission lines between the output port and the Helmholtz coils. The non-ideal coil is modelled as an RLC component to account for unexpected high-frequency resonances [Gar99; Mes+06], as can be seen in the electrical circuit in figure I.15a). The combination of stray capacitances C_{helm} with the coils inductance L_{helm} creates a resonance at high frequency. Because of the finite impedance at resonance, an empirical parallel resistance R_{helm} is introduced as well. The electrical frequency response of the Helmholtz coils enable to measure the values of R_{helm}, C_{helm} and L_{helm}.

The real and imaginary parts of the impedance (respectively the blue and red solid lines) and the absolute impedance value (green solid line) are shown in figure I.15b). The black dotted line shows the best fit for the imaginary impedance in the linear regime, indicating the measured inductance of the Helmholtz coils $L_{helm} = 0.49\ \mu\mathrm{H}$, which is close to the $L_{helm} = 0.36\ \mu\mathrm{H}$ theoretical value. The difference can be explained by the presence of stray inductances, whose linear values in coaxial cables are typically $0.25\ \mu\mathrm{H} \cdot \mathrm{m}^{-1}$. The LC resonance occurring at 92.1 MHz enables to measure the capacitance $C_{helm} = 6.1$ pF. The impedance saturation at resonance leads to a resistance value of $R_{helm} = 18\ \mathrm{k}\Omega$. The other resistive and radiative parts of the impedance can be modelled as well but are negligible, so they are not detailed here [Mes+06]. Small unexpected deviations due to non-ideal behaviours at high frequencies are visible around 50 MHz but are hard to account for in the model.

Once the Helmholtz coils are modelled accurately with these components values, the sensitivity of the probe can be computed using S_{21} measurements with the formula

$$\beta_j(f) = Z_0 \frac{S_{21}}{2\pi i f \alpha\,(1-S_{11})} \tag{I.54}$$

The absolute sensitivity values are showed in figure I.15c) and compared to the naive formula I.49. L is set at $0.2\ \mu\mathrm{H}$, which is half of the expected value but displays an excellent agreement with $|\beta_x|$, $|\beta_y|$, $|\beta_z|$ at first order. This closeness supports the reliability of the calibration method. The fundamental f_0 and its first two harmonics f_1 and f_2 are highlighted with the dashed black lines. The difference in sensitivities at f_0, f_1 and f_2 emphasize the importance of the frequency calibration of each B-dot probe. On the other hand, the sensitivity beyond 50 MHz exhibit strange peaks that are most certainly due to resonances in the cables or deviations to the model.

Note that no calibration of the cross-talking between the three coils due to the non-orthogonality of the probe head has been conducted. This effect has been assessed to be negligible though. For future probe design, a relevant improvement would be to connect the three coils to shielded 50 Ω impedance cable to diminish electrostatic pick-up.

Experimental routine: The B-dot has been designed to be used on the vertical translator placed at $z = 49$ cm. The probe is oriented such that B_z points downwards, B_y points to the antenna and B_x points to the side, the three directions forming a right-handed cartesian coordinate system. Acquisitions are done with an automated Agilent DSO-X 3014A oscilloscope triggered by a 5 V pulse generated at the plasma shot end. The sampling rates vary from 100 MS/s to 1 GS/s with 2 ms to 0.2 ms samples, thus ensuring a fine acquisition at f_0 in accordance with Shannon's criterion.

I.3.5 High-speed camera imaging

I.3.5.1 Light emission in a low-pressure cold plasma

The light radiated by a low-pressure cold plasma results from non-trivial interactions between particles and quantum processes. Let us consider a low-pressure cold plasma constituted of electrons, neutral (Ar) and ionised (Ar^+) argon atoms. The system being out of equilibrium and low density, the main radiation mechanism is the emission of a photon due to the spontaneous decay of excited species (neutral argon atoms or ions) from a high energy to a lower energy quantum state. Indeed, the transition from an excited state at energy E_β to a lower energy state at energy E_α leads to the emission of a single photon at a specific frequency $\nu_{\beta\to\alpha}$ according to the Planck relation

$$(E_\beta - E_\alpha) = h\nu_{\beta\to\alpha} \tag{I.55}$$

with h the Planck constant. Consequently, the plasma light spectrum is composed of well-defined emission lines, corresponding to transitions between discrete energy levels. These emission lines experience collisional, Doppler or Zeeman broadening for instance, which can be exploited for spectroscopy measurements. Spectroscopy has not been conducted in this PhD, and it will not be detailed here. In the case of argon, one can mention a few major emission lines presented in table I.5.

Emission line	Upper energy level	Lower energy level	Species
487.99 nm	$3s^23p^4(^3\mathrm{P})4p \quad ^2\mathrm{D}^\circ \quad 5/2$	$3s^23p^4(^3\mathrm{P})4s \quad ^2\mathrm{P} \quad 3/2$	Ar^+
750.39 nm	$3s^23p^5(^2\mathrm{P}^\circ_{1/2})4p \quad ^2[1/2] \quad 0$	$3s^23p^5(^2\mathrm{P}^\circ_{1/2})4s \quad ^2[1/2]^\circ \quad 1$	Ar
751.47 nm	$3s^23p^5(^2\mathrm{P}^\circ_{3/2})4p \quad ^2[1/2] \quad 0$	$3s^23p^5(^2\mathrm{P}^\circ_{3/2})4s \quad ^2[3/2]^\circ \quad 1$	Ar
810.36 nm	$3s^23p^5(^2\mathrm{P}^\circ_{3/2})4p \quad ^2[3/2] \quad 1$	$3s^23p^5(^2\mathrm{P}^\circ_{1/2})4s \quad ^2[1/2]^\circ \quad 1$	Ar
811.53 nm	$3s^23p^5(^2\mathrm{P}^\circ_{3/2})4p \quad ^2[1/2] \quad 0$	$3s^23p^5(^2\mathrm{P}^\circ_{3/2})4s \quad ^2[3/2]^\circ \quad 2$	Ar

Table I.5 – Dominant emission lines commonly used for spectroscopy diagnostics for cold argon plasma characterization. Each emission line corresponds to the transition of an upper to a lower energy level. Energy levels are expressed with the complete electronic configuration, the term series and the total angular momentum number J. They originate from the NIST database [Kra+23].

In the case of cold plasmas, excited argon states are populated solely due to high energy electrons since $T_e \gg T_i$. The transition from a state α to an excited state β occurs at an excitation frequency $\nu_{exc}^{\beta\to\alpha}(T_e)$ and an excitation rate $K_{exc}^{\beta\to\alpha}(T_e)$. They can be computed following the calculation detailed in subsection I.2.3 by considering the cross-section relevant to each excitation process. For instance, the excitation cross-section shown in figure I.4a) is specific to the lowest energy electron-neutral excitation process, with an energy barrier estimated at $E_{exc} = 12.1$ eV [Lie+05]. The typical order of magnitude of the excitation processes ν_{exc} are about 10 kHz for the VKP-ICP case.

Apart from complex metastable states and transitions, the typical timescale for spontaneous decay is often of the order of 1 ns to 1 μs. At low density and low temperature, it means that the decay from a state β to a state α $\tau_{\beta\to\alpha}$ is small before the typical excitation timescale $1/\nu_{exc}$. Hence, the excited atoms are assumed to transit back to the ground state before reaching a higher energy level, and emit a photon. In the so-called Corona model, relevant for cold low-density plasma [Fan06], the light emission is mainly attributed to the transition from an excited state to the ground state. The light radiated for the emission line associated to the decay from a β state to the α ground state thus reads

$$I_{cam}^{\beta\rightarrow\alpha} \propto n_e n_\alpha K_{exc}^{\beta\rightarrow\alpha}(T_e) \tag{I.56}$$

with n_α the density of argon atoms in the ground state. $n_e n_\alpha$ corresponds to the number of pairs of electrons and argon in ground state, thus the encountering probability of these two particles. One can infer simply that n_α is proportional to the neutral density n_n or the ion density n_i depending on the species considered.

The Corona model is valid for electron temperatures of a few eV and plasma densities up to 10^{19} m^{-3}. Plasmas with higher temperatures or densities may reach thermodynamic equilibrium, which requires more advanced models to fully understand plasma radiation, such as the collisional radiative model [Fan06].

If one assumes the electron temperature to be homogeneous in space and time, the light emission of a plasma is a good proxy for plasma density or neutral density measurements [Old+10 ; Cal+11 ; Gon+20]. However, the influence of electron temperature fluctuations on light emission should be considered carefully. Its understanding enables a deeper quantitative analysis of the plasma properties [Vin+22]. Besides, high-speed camera imaging of the light radiated is particularly relevant for the investigation of wave propagation and interactions. It provides a versatile and non-intrusive method for wave front tracking and mode identification [Tha+14 ; Vin+23].

I.3.5.2 Experimental application

Light fluctuations in the helicon plasma are investigated using a Phantom v2511 high-speed camera. It faces the plasma column ending with a borosilicate window. Two mirrors are placed to extend the optical path up to 4 m in order to reduce parallax errors (see figure I.16a)). The focus is set approximatively at the probe measurement port, *i.e.* $z = 49$ cm. The lens used has a focal length of $f = 150$ mm and a $f/4$ aperture. By considering a circle of confusion of the pixel size (13.5 μm), the depth of field is assessed at $DoF \simeq 7$ cm. Light interferometric filter can be added before the lens to study various lines of emission of argon. The one used by default is a 750 nm filter with a 8 nm Full Half Width Maximum (FHWM), in order to investigate the light emission from neutral argon. Note that raw images are in grayscale, and a colormap is applied in the data analysis phase.

The light collected by the camera results from the integration of the radiated light over the whole plasma column. Since the plasma is confined by the external magnetic field, T_e and n adopt the same geometry than B. As shown in figure I.2, the magnetic field is distorted, especially at the measurement port at $z = 49$ cm. Hence, the light seen from the camera is unfaithful to the true light emission profile of the plasma at a given position z. That is why the coordinates x^* and y^* from the camera recording are denoted with a star to avoid any confusion with probe measurements. A thorough analysis of the effect of the magnetic field distortion and the camera parallax can be found in previous PhD work [Vin21].

Each film is recorded at 200000 fps, with an exposure time of 4.5 μs for each frame, for a total duration of 60 ms. The camera resolution is 256 × 192 px^2, corresponding to a 15 cm wide field of view. The acquisition is done with an external trigger that occurs at the end of the plasma shot. High-frequency noise presumably due to the camera shutter may appear beyond 60000 fps. When no high-frequency coherent mode was identified, films were corrected with a lowpass filter at a 50 kHz cut-off frequency. The average image for a helicon plasma generated at 860 G, 0.13 Pa and 1 kW is exhibited in figure I.16b). The standard deviation for each pixel is also shown in figure I.16c). It highlights the highly-focused light intensity profile, and the coexistence of multiple instabilities at various radial positions of the plasma column ($y^* = 0.5$ and 4 cm in the present case). A deeper investigation of the existing low-frequency fluctuations will be conducted in chapter V.

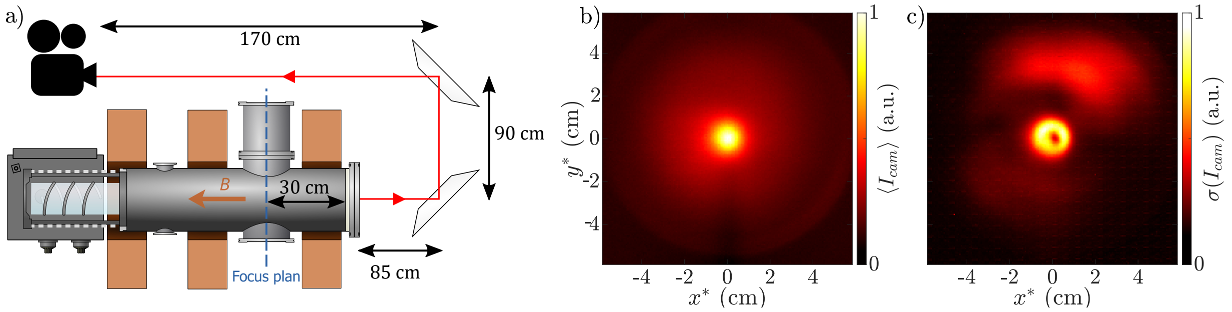

FIGURE I.16 – *a)* Camera optical set-up. *b)* Mean and *c)* standard deviation of the light intensity profile for a helicon plasma observed at 750 nm.

In order to investigate the light fluctuations, a few steps are applied to improve the signal-to-noise ratio. Firstly, a gaussian filter of 1 pixel FHWM is applied in order to smooth noise. Then, the mean background image is computed and subtracted to each frame. Finally, the light fluctuations are normalised by the standard deviation for each pixel. Despite no supplementary effect on the signal-to-noise ratio, this last step guarantees an enhanced contrast for the eye. Overall, the light fluctuations are processed according to the following transformation

$$\tilde{I}_{cam} = \frac{I_{cam} - \langle I_{cam} \rangle}{\sigma(I_{cam})} \tag{I.57}$$

I.3.5.3 Two-dimension Fourier transform

Light fluctuations can be decomposed on an orthogonal basis in order to identify predominant coherent structures. A modal decomposition technique enables to identify the most energetic modes, their properties and their interactions. The most common decomposition technique is the Fourier transform. In the present case, the two-dimension Fourier transform, (abbreviated 2D-FT) is of particular interest to investigate the azimuthal waves properties.

Let us consider a signal $f(t)$. The Fourier transform assumes the existence of an orthonormal basis of functions $\{e^{i\omega t}; \omega \in \mathbb{R}\}$ relevant to decompose any function $f(t)$ in the infinite time domain $[-\infty; +\infty]$. Hence, f can be written as a sum of harmonic functions, where each spectral component is written as $\hat{f}(\omega) = \int_{-\infty}^{+\infty} f(t) e^{-i\omega t} \, \mathrm{d}t$. In the case of spatio-temporal data, the Fourier transform can be applied independently to both dimensions $\hat{f}(k, \omega) = \iint_{-\infty}^{+\infty} f(t) e^{-i(\omega t + kx)} \, \mathrm{d}t\mathrm{d}x$.

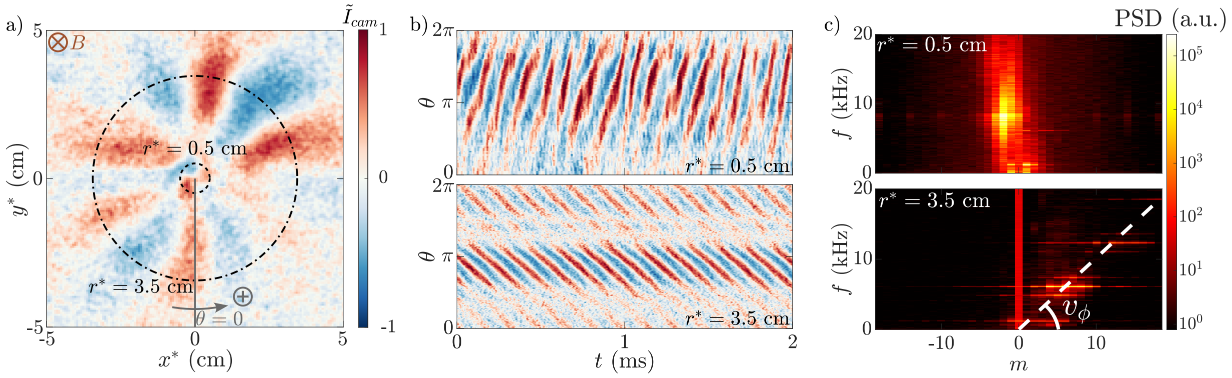

FIGURE I.17 – *a)* Light fluctuations for a 900 G, 0.13 Pa, 0.9 kW helicon plasma. *b)* Spatiotemporal graphs of the light fluctuations at $r^* = 0.5$ cm (top) and $r^* = 3.5$ cm. *c)* Spectrum in the (m, f) plan of the $r^* = 0.5$ and 3.5 cm light intensity profile.

The 2D-FT technique applied to the high-speed imaging data consists in conducting Fourier transform on the temporal domain t and the azimuthal dimension θ. The center of the plasma column ($x^* = 0$, $y^* = 0$) is found as the location of the maximal intensity of the mean light emission profile. The light fluctuations for a helicon plasma generated at 900 G, 0.13 Pa and 0.9 kW for a given instant t are pictured in figure I.17a). Blue pixels (respectively red pixels) correspond to a light emission less intense (resp. more intense) than the mean background image. For each circle of radius r^*, the light emission profile is converted in cylindrical coordinates (r^*,θ), with θ being divided in 800 points and defined as positive in the trigonometric direction. Two black dotted lines at $r^* = 0.5$ and 3.5 cm are represented, and their resulting spatiotemporal light fluctuations profiles are shown in figure I.17b). One can see two distinct counter-rotating coherent and very stable modes for both radii.

Then, the 2D-FT technique is applied on these light intensity profiles. The azimuthal wavenumber can be written as $k_\theta = \frac{2\pi}{\lambda} = \frac{m}{r^*}$, with $m \in \mathbb{Z}$ the azimuthal mode number. The Fourier transform reads

$$\hat{I}_{cam}(r^*, k_\theta, \omega) = \iint \tilde{I}_{cam}(r^*, \theta, t) e^{-i(\omega t + m\theta)} \, \mathrm{d}\theta \mathrm{d}t \tag{I.58}$$

Positive m numbers are associated to a clockwise rotation. The two-dimension spectrum is displayed in the plan (m,f), with f the frequency in Hz corresponding to ω, like in figure I.17c). The colormap is in logarithmic scale, main spectral components are highlighted in bright colours. 2D-FT technique is usually displayed in the range $m \in [-18; 18]$, but the full computation covers the 800 m modes. The rotation in opposite directions at $r^* = 0.5$ and 3.5 cm appears unambiguously in the 2D-FT spectra. Note that the $m = 0$ mode presents an unexpected and artificial white noise. The wave phase velocity is defined as $v_\phi = \frac{\omega}{k_\theta} = \frac{2\pi f r^*}{m}$. Hence, this type of graph enables a clear calculation of v_ϕ, since it appears in the two-dimension spectrum as the slope of the white dashed line visible in figure I.17c).

The cylindrical 2D-FT technique is well suitable for the present high-speed imaging data, and represents a powerful tool. It describes finely the harmonic modes that may arise from data containing a cylindrical symmetry like here. Furthermore, it gives access to the spatial modes and their temporal phase, which are rich properties for the investigation of wave interactions for instance. Its main drawback is a long computation time and a limited interested for transient regimes and non-symmetric results, as can be seen in chapter V.

I.3.5.4 Proper orthogonal decomposition

Proper orthogonal decomposition (abbreviated POD) is a powerful image analysis technique. Its goal is to decompose a signal on an optimal orthonormal basis. Contrarily to the Fourier transform, which assumes a pre-defined orthonormal basis, the POD technique relies on the identification of non-trivial predominant eigenmodes on its own orthonormal basis. In other words, the main naturalw coherent structures are identified on a specific basis that arise from the data set itself. This technique is of particular interest for the study of complex and chaotic structures, hence it has been exploited in the case of turbulent flows for instance [Lum67]. The working principle of POD will be briefly detailed in the current subsection, as well as its practical implementation and interpretation. A curious reader may read reference articles [Ber+93; Smi+05] and detailed experimental studies [Vin21] for a thorough description.

The decomposition of the high-speed camera imaging data on a N-size orthonormal basis can be written as

$$\tilde{I}_{cam}(x, y, t) = \sum_{i=1}^{N} \sigma_i a_i(t) \Psi_i(x, y) \tag{I.59}$$

where σ_i is the i-th eigenvalue corresponding to the eigenmode $\Psi_i(x, y)$, and $a_i(t)$ is the temporal variation of this mode. The extension of N to infinity ensures an exhaustive decomposition of the signal, similarly to the Fourier transform.

The goal of POD is to identify the most optimal basis. Quantitatively, it means that the norm $\sum_i^N \sigma_i^2$ of the projection of $\tilde{I}_{cam}$ on the N-size basis, constituted of the eigenmodes $(\Psi_i)_{i\in[1;N]}$, is maximal for any number N. Hence, a reduced set of the orthonormal basis is still an efficient modal decomposition.

Let us define the scalar product of two functions u and v as (u, v), the norm $\|u\|^2 = (u, u)$ and the ensemble average on all time domain $\langle\cdot\rangle_{t_j}$. In practice, spatial eigenmodes are successively identified as the mode that resembles most to the original data at a given instant, and averaged on the complete time domain. Then, the research for the predominant eigenmode can be written this way

$$\max_{\Psi_1}\left(\frac{\langle|(\tilde{I}_{cam}(t_j), \Psi_1)|^2\rangle_{t_j}}{\|\Psi_1\|^2}\right) \tag{I.60}$$

Then the eigenmode i should be orthogonal to the previous ones $(\Psi_i)_{i\in[1;i-1]}$. All in all, the calculation of Ψ_i is computed according to the following general formula

$$\max_{\Psi_i\perp(\Psi_k)_{k\in[1;i-1]}}\left(\frac{\langle|(\tilde{I}_{cam}(t_j), \Psi_i)|^2\rangle_{t_j}}{\|\Psi_i\|^2}\right) \tag{I.61}$$

Since the computation of eigenmodes is prioritising the most resembling mode, the singular values σ_i are sorted in a descending order, until the newly calculated singular values are low enough to be considered negligible. In the present PhD, the number of eigenmodes were limited to 20, which has been found to fully describe even fine structures.

The POD decomposition in eigenmodes is equivalent to a singular value decomposition (SVD) problem and the research of the associated eigenvalues. For a one-dimension signal $I_{cam}(x)$ covering the interval $[0; L]$, The calculation of the first POD mode that relies on I.60 consists in solving the following eigenvalue problem

$$\int_0^L \langle\tilde{I}_{cam}(x)\tilde{I}_{cam}(x')\rangle_{t_j}\Psi_1(x')\,\mathrm{d}x' = \sigma_1\Psi_1(x) \tag{I.62}$$

This equation comes down the computation of the two-point auto-correlation function $R(x, x') = \langle u(x)u(x')\rangle_{t_j}$ and a variational principle with respect to the eigenmode of interest $\Psi_1(x)$. The definition can then be expanded to two-dimension data.

POD does not require any symmetry in the original data, which is a strong advantage to analyse any data set, even in complex experimental configurations. Besides, the limitation to the few most energetic eigenmodes enable an optimised and quick calculation time. However, the physical interpretation of POD may be challenging and convoluted. The σ_i^2 terms may carry physical meaning when the decomposed signal is adapted. When applied to flow velocity fields for instance, σ_i^2 is related to kinetic energy. In the frame of light fluctuations investigation $\tilde{I}_{cam}$, which can be seen as a proxy of plasma density fluctuations $\tilde{n}$ at constant electron temperature, the physical meaning σ_i^2 is not straightforward.

The data for a helicon plasma generated at 900 G, 0.13 Pa and 0.9 kW, already analysed using 2D-FT, is treated using POD. The normalised eigenvalues of the first 15 modes are visible in figure I.18. Three types of modes arise: the first three ones which focus a major part of the energy, the modes 4 to 7 which are close to one another, and the higher number remaining modes.

The spatial structures, the temporal evolutions and their temporal Fourier transform of the first eight eigenmodes are displayed in figure I.19. Spatial structures are very informative. Three

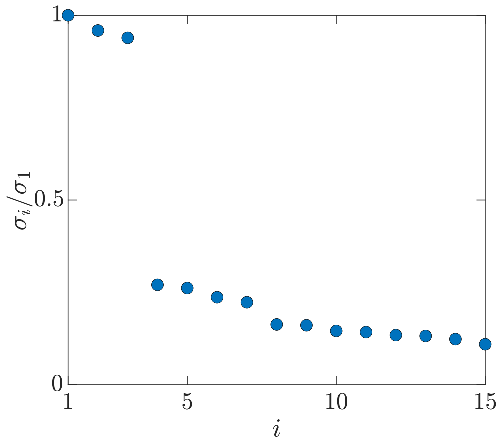

FIGURE I.18 – Normalised eigenvalues of the first 15 modes associated to the POD decomposition for a 900 G, 0.13 Pa, 0.9 kW helicon plasma.

main groups of modes appears naturally, namely the modes 1 to 3, 4 to 7 and the mode 8 and beyond, which is consistent with the singular values calculation. Indeed, Ψ_1 to Ψ_3 are relevant to describe the $m = 6$ edge mode, while the modes Ψ_4 to Ψ_7 describe accurately the $m = -2$ core mode. Ψ_8 conveys less energy, but is related to the $m = 12$ edge mode. So it appears as the first harmonics of the Ψ_2 mode.

The spatial structures being fixed in time, the association of a couple of eigenmodes phase-shifted by $\pi/2$ in space lead to rotating structures, and may correspond to the harmonic modes found with the 2D-FT. For instance, the modes Ψ_2 and Ψ_3 look alike, and their temporal evolutions a_2 and a_3 show a remarkable time correlation with a phase shift close to $\pi/2$. Hence their temporal Fourier transforms are very similar. These couples may be completed by complementary modes such as Ψ_1 that account for inhomogeneities of the spatial pattern. Modes Ψ_4 to Ψ_7 are also strongly correlated and depicts accurately the core light fluctuations. Core and edge fluctuations coupling may also appear from this visualisation, as modes Ψ_6 and Ψ_7 seem to influence to some extent the plasma around $y^* = 3$ cm.

Overall, the axisymmetry being a strong experimental feature, the 2D-FT often prevails and carries a stronger physical meaning. It is used primarily, while POD is explored to investigate more complex structures.

I.3.6 Protocol of operation

The plasma is operated during shots of about 5 s, spaced by 60 s resting periods due to thermal constraints. The whole device is air-cooled. Each plasma regime is matched during its stationary phase with a $< 1\%$ reflected power before conducting a series of measurements.

The full automation of the experimental set-up is made possible by a National Instruments PXIe-1062Q chassis. This equipment ensures the software-hardware communication. Then the experimental device is operated via a LabView interface. The PXI chassis can be supplemented by pluggable DAQ acquisition cards of variable characteristics. The two main DAQ cards used during my PhD are the PXIe-6368 16 analogical inputs 2 MS/s card, used for temporally-resolved acquisitions, and the PXIe-4139 source measurement unit (SMU), used for Langmuir probe scans. Electrostatic probes are inserted through the access ports located at $z = 49$ cm (see figure I.1a)). They are placed either on an automated radial translators or a longitudinal rail placed inside the cylindrical chamber, in order to conduct spatially-resolved measurement at a 0.1-mm precision. Electrical signals are transmitted from the probe to the acquisition card through Fischer hermetic

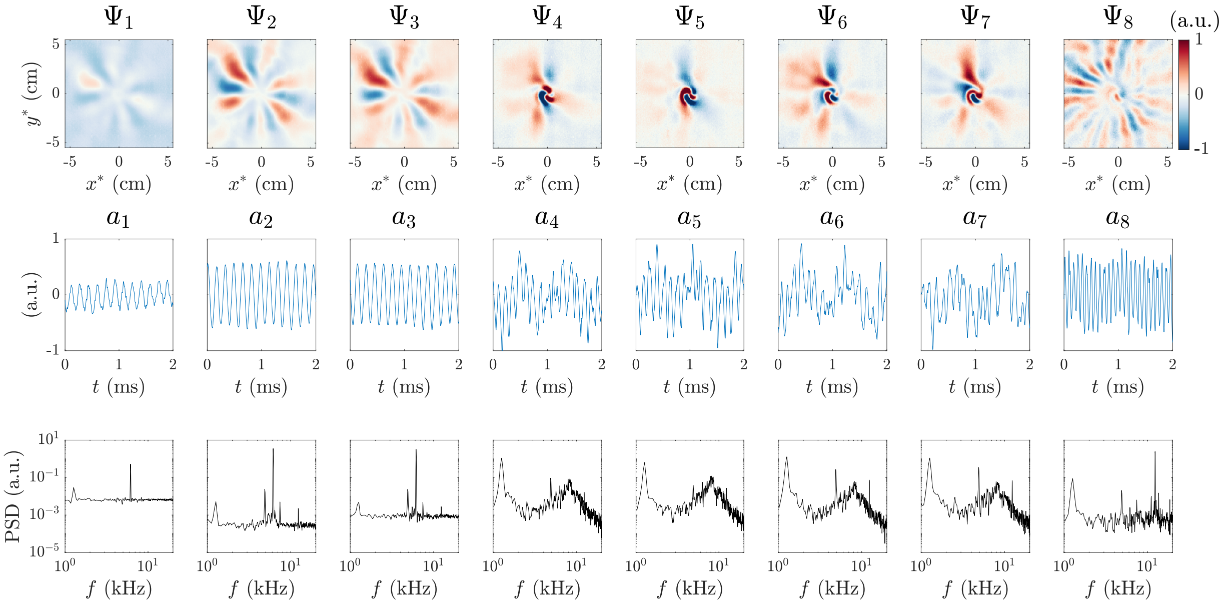

FIGURE I.19 – POD decomposition of the light fluctuations in a 900 G, 0.13 Pa, 0.9 kW helicon plasma. First row are spatial eigenmodes, second row are their associated temporal evolution and third row are the resulting temporal Fourier transforms.

electrical feedthroughs, which grant an excellent electrical contact and a high-quality vacuum.

A typical plasma shot is represented in figure I.20. Firstly, the plasma is ignited with a smooth input power 1 s ramp in presence of a 170 G external magnetic field. This initial magnetic field value is optimised to generate a preliminary inductive plasma instead of a capacitive plasma. Indeed, a magnetic field lower than 30 G would not confine the electrons enough, meaning that the high-energy electrons would be lost at the device walls. A tenuous capacitive plasma discharge would diffuse in the cylindrical chamber. On the other hand, a magnetic field higher than 300 G would induce a strong electron magnetisation, and thus a limited radial diffusion of electrons. The plasma is formed in a thin skin depth at the vicinity of the borosilicate tube, and the plasma discharge remains capacitive. The 170 G is optimised to sustain an inductive plasma discharge given the device and the antenna geometries, and the matching box characteristics. Note that this protocol was optimised for inductively-coupled plasma discharges, but has been applied on helicon plasmas as well.

Once the plasma is ignited after the power ramp and a 0.5 s transient phase, the magnetic field is adjusted to the particular value of interest (540 G in the experiment presented in figure I.20). If used, the cathode bias V_b, which was left floating thus far, is fixed at a constant value for the rest of the plasma shot ($V_b = -40$ V herein, see yellow curve from figure I.20).

The last phase of the plasma shot lasts 1 to 3 s and is dedicated to various measurements. In figure I.20, the green curve shows a temporally-resolved floating potential measurement using an emissive probe at the plasma core. The purple curve is a Langmuir bias sweep from -60 V to 10 V. It is divided in three sections to gain accuracy from an optimal acquisition range of the PXIe-4139 SMU card. The light blue pulse is generated by an external analogical output, and is used for camera or oscilloscope triggering. The two latter measurements are always conducted at the end of the plasma shot so that a stationary state is reached.

Plasma shots display a high shot to shot reproducibility, as ion saturation current measurements using a Langmuir probe report a variability of $\pm 0.6\%$ over 40 shots, with a standard deviation of 0.2% [Dés+21]. Each plasma shot corresponds to a single plasma property measurement at a given probe location. During a radial or a longitudinal scan, probes are displaced during the resting period via the automated translators.

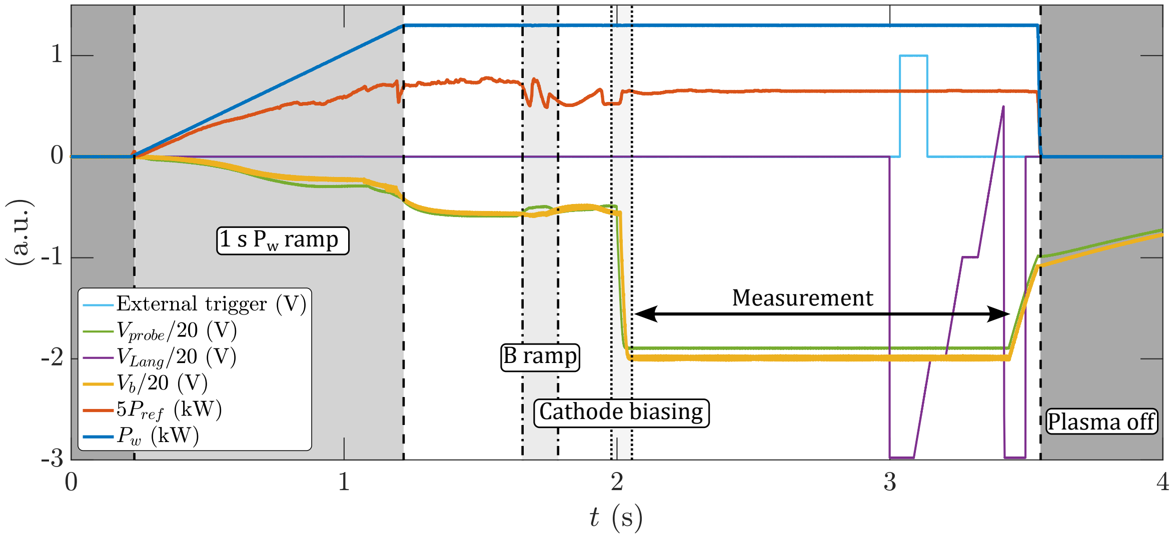

FIGURE I.20 – Typical plasma shot operation.

I.3.7 Mean profiles of plasma parameters

Radial scans of densities, electron temperatures and plasma potentials are displayed in figure I.21. P_w is set at 1 kW, while B and p_0 varies for two different regimes: 240 G and 0.26 Pa, and 340 G and 0.13 Pa. Plasma density and electron temperature measurements are conducted with the 5-tips probe while the plasma potential is obtained using an emissive probe. The pale areas represent the error estimation for n and T_e while being the standard deviation of the fluctuations for ϕ_p.

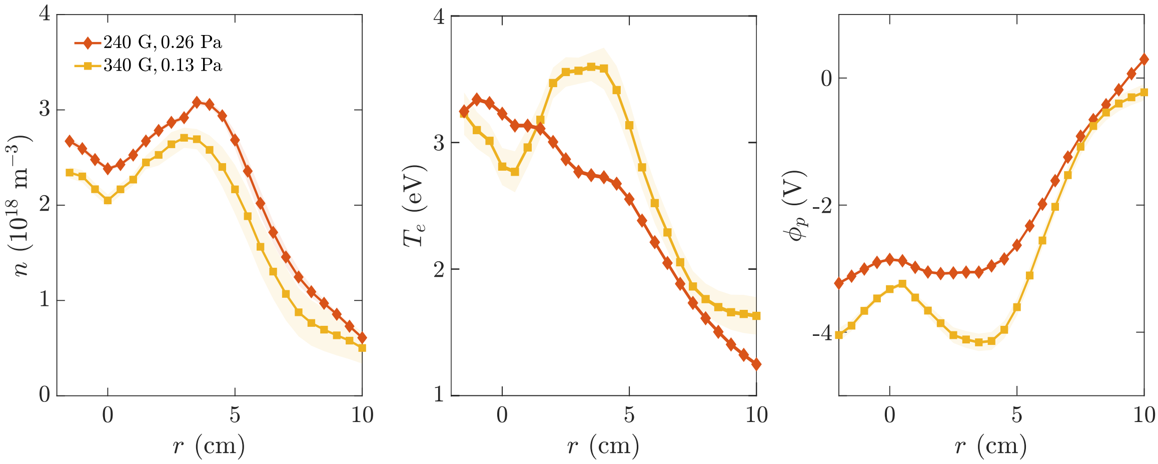

FIGURE I.21 – Plasma density, electron temperature and plasma potential measurements for two different regimes. Pale areas represent the error estimation for n and T_e while it is the standard deviation during a plasma shot for ϕ_p.

Measurements are consistent with experiments reported previously [Vin21]. Plasma density increases with B due to an enhanced confinement that reduces the cross-field plasma transport and the particle flux at the walls. Additionally, an increase in pressure causes higher collision rates, resulting in a plasma density increase and an electron temperature decrease. The electrons transfer indeed more energy to the surrounding ions and neutrals through elastic and ionising collisions. One can notice that n and T_e peak between 3.5 cm and 5 cm. It is most certainly a signature of the inductive heating occurring in the skin layer at the vicinity of the source tube of inner radius 5.5 cm. All in all, the plasma density and electron temperature are close to the values predicted by the simple energy and particle balance 0D model (see subsection I.2.7).

The plasma potential measurements show a non-monotonic profile with a minimum located around 4.5 cm, while the ground at the wall is well recovered. A lower plasma potential at the center of the plasma column is a common feature reported in other magnetised linear devices [Gra+04 ; Jin+19]. The non-trivial plasma potential profiles arise spontaneously from the complex particles transport at the walls and cannot be easily predicted. Collisions and waves play a major role in their shape. In the case of an unmagnetised plasma, ϕ_p is expected to be larger in the plasma core. It is due to the predominance of the electron flux at the wall compared to the ion flux ($J_e \gg J_i$). The application of an external magnetic field and a weak magnetisation inverts this ordering, resulting in an inward radial electric field, as observed here.

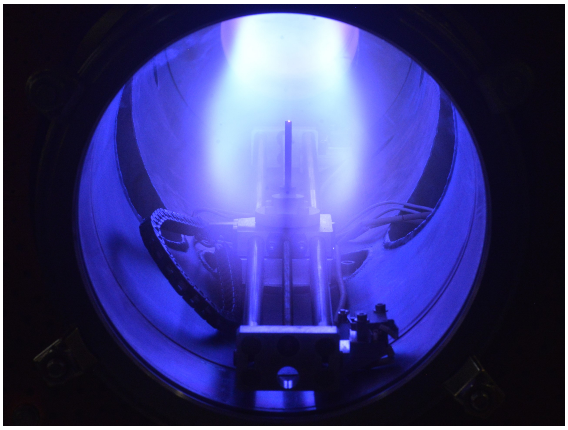

FIGURE I.22 – Emissive probe operating on the longitudinal translator.

Besides, a longitudinal rail has been engineered over the course of this PhD during the supervision of a Bachelor internship conducted by Till Person (see figure I.22). The goal is to investigate the axial properties of the plasma column. The metallic structure is grounded and placed at the bottom of the cylindrical plasma chamber ($r > 7$ cm). It breaks the axisymmetric design of the experiment, but it is placed at the plasma edge. It should disturb the plasma to a lesser extent. An automated stepper motor drives a worm screw to displace the probe holder longitudinally. The emissive or uncompensated Langmuir probe is placed on a 2 cm high ceramic base. The signal is transmitted by a 1-m long shielded coaxial cable placed inside a retractable track. The importance of using a shielded cable to reduce electrostatic pick-up has been shown over the course of this internship. The new automated translator opens the way to longitudinal wave structure measurements, which is of particular interest for low-frequency waves identification [Vin21] or helicon waves investigation [Lig+95].

Longitudinal plasma density, electron temperature and plasma potential profiles are reported in figure I.23. The density decreases from the source to the vacuum chamber end. It is no surprise since the plasma is generated at $z = 0$ cm and is progressively recombined at the walls as z increases. Besides, this effect is diminished when the magnetic confinement is improved. A satisfying degree of homogeneity is observed at $B = 510$ G. The longitudinal gradient length

$L_{grad} = \langle n \rangle_z / |\partial n / \partial z|$ is always superior to 1 m, ensuring a satisfying longitudinal homogeneity. Electron temperature is overall homogeneous along the plasma column despite fluctuations allegedly attributed to RF fluctuations and the use of an uncompensated Langmuir probe. However, the plasma potential presents inhomogeneities, especially near the antenna and the end of the plasma column. ϕ_p fluctuations are more pronounced as B is increased, especially around $z = 49$ cm. It is perhaps a consequence of the inhomogeneity in B at this location (see figure I.2).

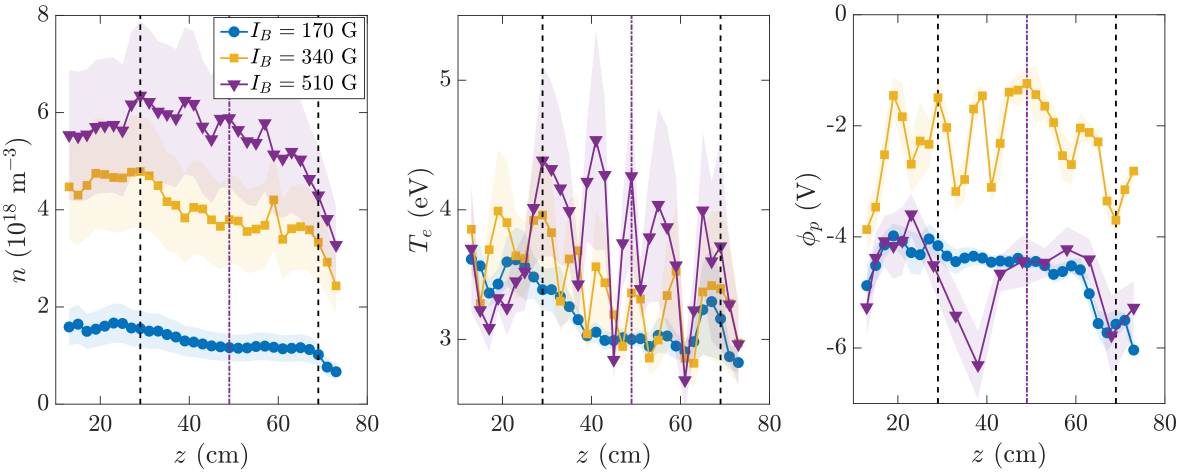

FIGURE I.23 – Plasma density, electron temperature and plasma potential longitudinal measurements for $B = 170$ G, 340 G and 510 G. Dashed black lines represent the coils positions and the purple dotted line is the probe access port.

CHAPITRE

II

EMISSIVE CATHODE OPERATION AND PLASMA-CATHODE INTERACTIONS

L'émission thermoionique générée par une cathode émissive de tungstène plongée dans une colonne de plasma magnétisée est étudiée expérimentalement et numériquement. Un modèle thermodynamique détaillé reproduit fidèlement les mesures de température de la cathode. Le calcul des transferts thermiques lors de l'émission thermoionique permet de comprendre finement l'existence de profils de température fortement hétérogènes et l'utilisation pratique de la cathode émissive. Ce chapitre a fait l'objet d'une publication dans le journal *Plasma Sources, Science & Technology* [Pag+23].

II.1 Role of emissive cathodes in plasma physics

II.1.1 Versatility of emissive cathodes

Heating of an electrode leads to thermionic electron emission as mentioned in subsection I.3.3. This effect has been routinely used as a source of primary electrons to ionize a plasma since the pioneering works of Edison, as reported by Preece [Pre85], and of Fleming on vacuum tubes [Fle04]. In 1928, the importance of thermionic emission in technological applications was underlined by the award of the Nobel Prize award to Richardson *"for his work on the thermionic phenomenon and especially for the discovery of the law named after him"*.

The use of hot cathodes is not limited to vacuum tubes, but was and still is widely used for primary electron production in plasma sources, both at high [Ben08] and at low pressure [Bos+86 ; Gre+93 ; Gek+16]. The high-pressure plasma regime ($\sim 10^{23}$ m^{-3}) strongly couples the cathode temperature distribution and the plasma properties, resulting in various emission modes that have been extensively studied, both experimentally and theoretically [Ben98 ; Ben14]. On the other hand, in the context of glow discharges in the presence of hot cathodes, several regimes of operation have been reported [Arn+96 ; H P+02]. Transitions, oscillations and multistability between these different regimes are understood from the complex interactions between the plasma and the cathode. In low-pressure plasma discharges, modelling the interaction between the plasma and emissive cathodes remains an active research topic [Cam+17 ; Ped+15 ; Mor+23].

In the context of plasma transport control in tokamaks, biasing experiments using emissive cathodes demonstrated improved confinement and the emergence of a transport barrier by current injection, more than 40 years ago [Tay+89]. Edge biasing using emissive surfaces is still an active line of research in the fusion community, leading to improved confinement [Sil+04] or the control of runaway electrons [Gha+12]. The behaviour of thermionic emissive plasma-facing components has several potential advantages [Tol+20]. A first potential application is the operation of emissive divertor in the presence of an inverse sheath (an electron-rich sheath), that favours plasma detachment and low target plasma temperatures [Cam20]. A second advantage of thermionic emission lies in the cooling of components in contact with the plasma. This effect is due to both radiation and cooling by the emitted electrons, which carry away the potential barrier energy associated to the emission [Kom+17]. Cooling from thermionic emission has also been proposed for the atmospheric re-entry of spacecrafts, known in this context as electron transpiration cooling [Uri+15 ; Han+17].

II.1.2 A new parameter control

There has been a recent surge of interest in the study of plasma flow induced by the interaction of large current emitted by hot cathodes with an already existing magnetised plasma. It shed new light on transport and plasma turbulence in magnetised plasma columns [DuB+14 ; Gil+15], plasma flow generation [Dés+21 ; Jin+19], or the dynamic of interacting plasma filaments [Syd+19 ; Kar+22]. The control of electric fields perpendicular to the ambient magnetic field is also crucial for a number of applications of $E \times B$ configurations [Kag+20], and among them, high-throughput plasma mass separation [Gue+18 ; Zwe+18]. The control of the plasma potential and of the plasma rotation using current injection from emissive cathode has recently been the subject of experimental investigations [Liz+21b] and of theoretical modelling [Tro+22 ; Pou19], which require a precise description of the cathode behaviour in the presence of a plasma.

This brief review shows that there are still a number of cutting-edge technological applications involving thermionic cathode immersed in a pre-existing plasma. Most of the understanding of their functioning relies on established physical properties (see for the instance the review [Her+49] or the recent review on oxides and borides emissive materials [Gao+20 ; Tar+09]) and extensive thermophysical properties dataset [Kaw22]. Nevertheless, the operation of a hot cathode immersed in a pre-existing plasma requires a careful modelling of the interaction between a low-pressure plasma and a large emissive cathode. In this present chapter, we report an experimental study and a detailed modelling of the operation of a hot tungsten cathode immersed in a low-pressure magnetised plasma column conducted throughout the course of this PhD. Spatially and temporally resolved temperature measurements allow to precisely predict the cathode current, and a thermal budget is developed.

II.2 Operation of a tungsten emissive cathode

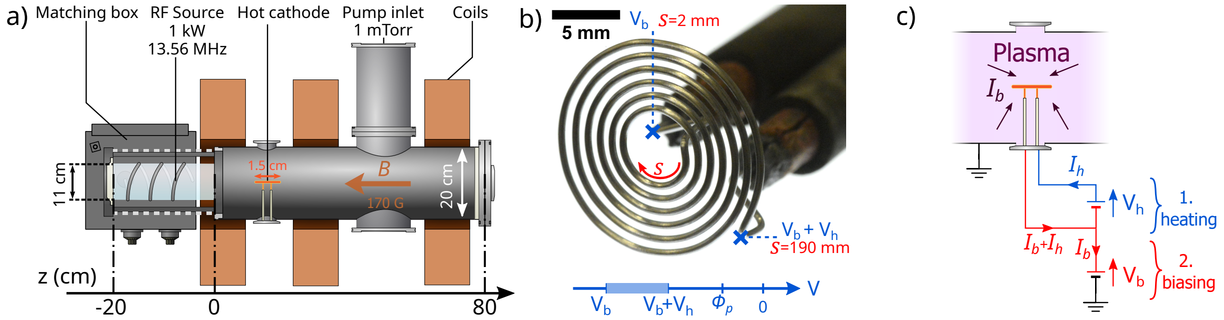

FIGURE II.1 – *a)* Sketch of the experimental setup. *b)* Photograph of the tungsten emissive cathode. *c)* Electrical circuit of the electrode.

A hot emissive cathode is inserted in the VKP-ICP setup from the lateral port located at $z = 16$ cm (see figure II.1a)). It consists in a 6-turns spiral-shaped filament of pure polycristalline tungsten of radius $r_W = 253$ μm, and total length $l_W = 198$ mm [Dés+21] (see figure II.1b)). The filaments are spaced by a 440 μm gap. The filament experiences a minor thermal expansion as it is heated up to 3000 K. This effect is accounted for in the thermophysical properties presented in section II.5, which require a high degree of accuracy, but the variation of the cathode surface is neglected for the Richardson current or ion saturation current, as it should vary up to 1%. The outer diameter of the spiral is 1.52 cm. The curvilinear coordinate s is defined with $s = 2$ mm at the centre of the spiral and $s = 190$ mm at the outer end (note the mounting base of the filaments that are not in the spiral plane). Electrical contact is ensured by two 4-mm thick and 35-cm long copper rods clamping the ends of the cathode and insulated by two alumina 6-mm thick tubes. They are connected to two electrical hermetic feedthroughs across a stainless steel DN 50 ISO-K flange. The distance from the DN 50 ISO-K access port to the hot cathode is about 10.3 cm so that the cathode is placed at the plasma column center. Both alumina tubes are aligned horizontally to perturb the plasma as little as possible. The cathode is operated using two independent electrical DC power supplies (see figure II.1c)):

1. The tungsten filament is Joule heated by a given heating current I_h, with no constraints on the voltage drop V_h. The DC power supply used is a EA-PS 9080-50, reaching up to 50 A ;
2. Strong thermionic emission is achieved setting a negative bias V_b, below the plasma potential. The DC power supply used is a EA-PS 9200-70, reaching up to 70 A. However, the total cathode current I_b is hard-ware limited to 15 A to avoid damaging the cathode. Note that, for the sake of simplicity, the convention is such that $I_b > 0$ when electrons are emitted from the cathode.

V_h and I_b are measured using two differential probes (Metrix MX 9030, 1/20 gain) at the ends of the copper rods outside of the electrical feedthroughs. The data are digitized via the 16-channels NI PXIe-6368 acquisition card at a sampling rate of 200 kS/s. A simple calculation of the copper rods resistance gives a 0.01 mΩ estimation, thus it is neglected. However, a poor electrical contact between the copper rods and the clamped ends causes a non-zero contact resistance R_{con}. Its value was assessed using a 4-wire ohmmetre Fluke 8846A by comparing the cathode resistance at the cathode legs and at the clamping ends of the copper rods. The order of magnitude of R_{con} was evaluated at about 10 ± 3 mΩ, typically 1% of the cathode resistance $R_h = U_h/I_h$, which is significant enough to be considered. The contact resistance depends on the mechanical clamping of the cathode ends by the copper rods. It may vary when the cathode is heated, displaced or replaced, hence the important deviation in R_{con}. This value is hardly controllable, but it remains low enough to impact moderately the cathode behaviour.

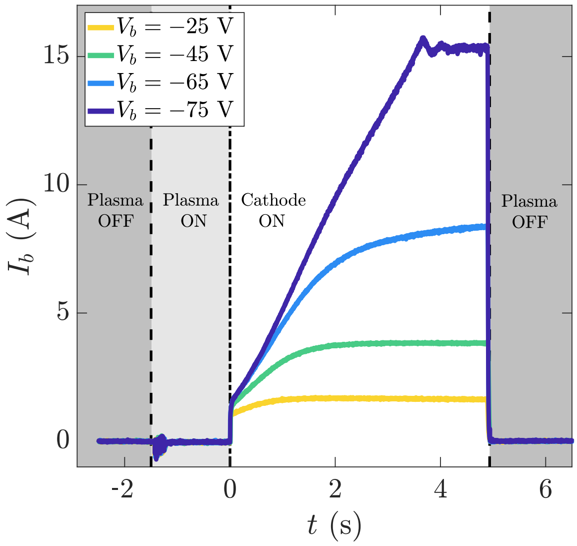

FIGURE II.2 – Time evolution of the emitted current I_b for a given heating current I_h and various values of the cathode bias V_b.

The plasma-cathode interactions are investigated for a plasma generated at 0.13 Pa, 170 G and 1 kW. Typical time series of the current I_b during plasma shots are shown in figure II.2. The cathode is continuously heated, whether the radio-frequency plasma is ignited or not, and the cathode bias is left floating initially. The plasma is ignited at $t = -1$ s and the cathode is negatively biased at V_b at $t = 0$ s. A strong cathode current I_b is then emitted starting at time $t = 0$ s, until the plasma is turned off ($t = 5$ s for the shots shown in figure II.2). Note that the bias voltage V_b is referenced to ground and feeds the center of the spiral (see figure II.2), and that the heating current I_h is set constant whether the plasma is ignited or not (here $I_h = 17$ A).

A naive interpretation of the above-described protocol is the following: the cathode temperature is set by the heating power supply, independently of the cathode bias. Since, for a given cathode material, thermionic emission is controlled by the cathode temperature, this should allow independent control of the injected current and potential. However, as observed in figure II.2, the more negative the voltage bias, the higher the injected current. As shown later, this current increase is linked to an inhomogeneous increase of the cathode temperature due to plasma-cathode interactions, as the bias becomes increasingly negative. The goal of this section is to provide precise estimates of the cathode current from detailed measurements of the cathode temperature profile and its modelling. Steady-state regimes are reached after a 2 s transient regime for weak bias voltages ($V_b = -25$ V and -45 V in figure II.2) and divergent regimes, with runaway evolution of I_b are observed at stronger bias voltage ($V_b = -75$ V in figure II.2). Yet the model developed in section II.5 shows that, when $V_b = -75$ V, the cathode experiences an unbounded temperature growth leading to current divergence.

A video showing the effect of thermionic emission on the plasma column is available online [1]. It is a side view of the inside of the plasma chamber at 1 mTorr, 170 G and 1 kW. A drawing of the setup is displayed at the beginning: the RF source is at the left end, while the cathode faces the plasma at the other end of the chamber. First the plasma is ignited using the RF source on the left side, resulting in a 10-cm wide plasma column while the cathode is hot and floating. Then the cathode is negatively biased and emits primary electrons from the right end, creating a denser 2-cm wide plasma core. The strong emission at the cathode is sustained for a few seconds, and finally the power of the RF source is shut down.

The upper bound for thermionic emission, the Richardson current, has already been introduced in equation I.45. The cathode surface is $\mathcal{S} = 314$ mm^2. Richardson current is assumed to be unaffected by the external magnetic field and the specific cathode geometry. Both effects could induce a returning electron flux to the cathode but it is expected to be low at a $10^{18} - 10^{19}$ m^{-3} density [Cam+15]. Furthermore, λ_D is 10 to 50 times smaller than the spacing between the filaments, allowing them to emit thermionic electrons independently.

A subtlety to be discussed is the temperature dependence of the work function W with regards to the temperature. We assume herein W to be independent of T_W, despite a lack of consensus in the literature [Dur+01; Kaw08]. The evolution of W is bounded by 15 meV between 2500 K and 3000 K, which is a first-order correction. Ultimately we chose $W = 4.54$ eV, which is the value commonly used in the literature [Gao+20] that lies within the range recommended by the most recent and comprehensive study [Kaw22]. Besides, there are a few sources of discrepancies from the Richardson current, the two most probable will be addressed now.

The Schottky effect might modify the Richardson current in the presence of a strong electric field at the metal surface [Her+49]. The electric field from the plasma to the cathode may provide a beneficial source of work to extract electrons from the metal. By considering an homogeneous electric field E facing the metal surface, the order of magnitude for the modified work function in presence of the Schottky effect is $W' = W - \sqrt{eE/4\pi\epsilon_0}$. In our case, the electric field is estimated at about a 10 V potential drop over $10\lambda_D$, so the Schottky effect correction reaches up to a few tens of meV. Its relative effect on W' is of the order of 1%, it is a first-order correction which will also be neglected.

Then, the Richardson current is reached only if the extraction of electrons is not impeded by the existence of a virtual cathode [Ye+00; Pou19]. Indeed, thermionic electrons have a low kinetic energy and could easily be repelled by a small potential barrier. However, an important outward thermionic emission may not be balanced by an inward ion flux from the plasma, resulting in the formation of a virtual cathode at the metal surface. The zone would be negatively charged by the incoming flux of thermionic electrons, thus creating a dip in potential. The Richardson current can no longer be reached, and this is called space-charge limited effects. The formation of a virtual cathode depends on the cathode bias V_b and the plasma density. Unless mentioned, we consider a strong cathode bias and a high plasma density so that the Richardson current is effectively reached. This assumption will be discussed in section II.6.

The other major contributions to the current at the cathode are the ion saturation and the electron currents flowing from the plasma to the cathode. One could refine this analysis by considering the secondary-electron emission at the cathode induced by ion bombardment. However, it is expected to be low before I_{is} given the low incident energy of ions [Kon92; Tol14], so it is neglected. The current I_b delivered by the bias power supply is the sum of the emitted current I_{em}, the ion saturation current I_{is} and the electron current I_e collected by the cathode at potential V_b

---

[1] https://youtu.be/FSkBuWGV62I

$$I_b = I_{em} + I_{is} - I_e \tag{II.1}$$

$$I_{em} = A_g \mathcal{S} T_W^2 \exp\left(-\frac{eW}{k_B T_W}\right) \propto T_W^2 \exp\left(-\frac{eW}{k_B T_W}\right) \tag{II.2}$$

$$I_{is} = en\mathcal{S}\alpha u_B \propto n\sqrt{T_e} \tag{II.3}$$

$$I_e = I_{es} \exp\left(\frac{V_b - \phi_p}{T_e}\right) \tag{II.4}$$

The plasma density and electron temperature facing the cathode are assumed to be homogeneous.

II.3 Experimental measurements of the cathode temperature

Since the amplitude of the emitted current is set by the value of the temperature profile $T_W(s)$ of the cathode, precise temperature estimates are essential. Then, the equation II.2 can be integrated over the measured temperature profile to compute finely the thermionic current emitted at the cathode. Two experimental methods of cathode temperature measurements are investigated and compared in this section.

II.3.1 Effective temperature estimate from global electrical resistance measurement

Temperature estimates from measurements of the filaments' resistance is a widely spread method, which relies on the temperature evolution of the resistivity of the materials. The temperature evolution of pure Tungsten resistivity ρ_W, corrected for thermal expansion, is accurately known [Des+84 ; Whi+97], with a best power-law fit in the range [1800 K ; 3200 K]:

$$\rho_W = 5.31 \times 10^{-11} T_W^{1.222} - 1.56 \times 10^{-9}\ \Omega \cdot \mathrm{m} \tag{II.5}$$

A direct measurement of the cathode resistance $R_h = V_h/I_h$, in the absence of emitted current, thus provides an estimate of an effective cathode temperature $\overline{T_W}$ as:

$$\overline{T_W} = \left[\left(\frac{\pi r_W^2}{l_W} R_h + 1.56 \times 10^{-9}\right) \frac{10^{11}}{5.31}\right]^{1/1.222} \tag{II.6}$$

The main uncertainty factor is a $\Delta r_W = \pm 1\ \mu$m error estimation in the cathode radius. The resulting error bar on $\overline{T_W}$ is about 1%. This method is particularly suited for cases where the temperature is uniform along the filament. In the case of current emission, I_b flows from the cathode to the plasma. Since the total current flowing through the cathode filament evolves along the curvilinear abscissa s, the resistance computation is not trivial. The estimate II.6 is only possible before or at the end of the plasma shot, where $I_b = 0$ A, and is not suitable for time-resolved measurements. Moreover, we will show that in the case of strongly inhomogeneous temperature profiles, the estimate of the current using $\overline{T_W}$ is inaccurate.

The main source of error of the electrical method for temperature measurement is the uncertainty in the cathode geometry, especially the radius r_W. An attempt to overcome this issue was to conduct a relative measurement, where the resistance of the filament at room temperature is compared to the resistance at high temperature. Even though this method proved to be inaccurate, its principle is detailed here.

The cathode resistance $R_{h,amb}$ at room temperature T_{amb} and the contact resistance are measured using a 4-wire ohmmetre. Then, the cathode is put under vacuum and the resistance at high

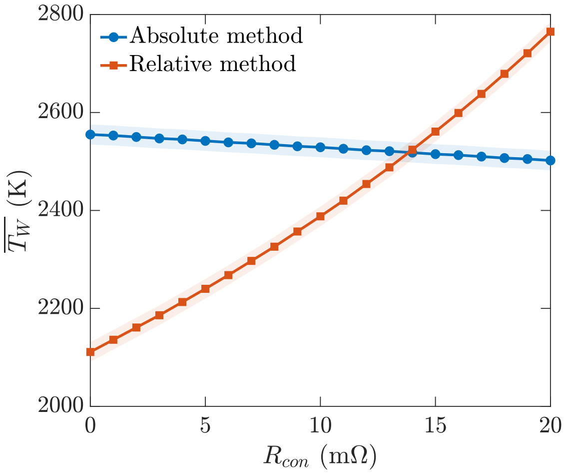

FIGURE II.3 – Cathode temperature measurement from the absolute resistivity (blue circles and equation II.6) and the relative resistivity (orange squares and equation II.7) measurements.

temperature R_h is measured likewise. Given that the tungsten resistivity equation II.5 is corrected for thermal expansion, the dimensions of the cathode are cancelled out in the ratio $R_h/R_{h,amb}$:

$$\frac{R_h}{R_{h,amb}} = \frac{\rho_W\left(\overline{T_W}\right)}{\rho_W\left(T_{amb}\right)} \quad \Leftrightarrow \quad \overline{T_W} = \left[\left(\frac{R_h}{R_{h,amb}}\rho_W\left(T_{amb}\right) + 1.56\times10^{-9}\right)\frac{10^{11}}{5.31}\right]^{1/1.222} \tag{II.7}$$

The results for the absolute and the relative resistivity measurements as a function of the hypothetical contact resistance R_{con} are shown in figure II.3. The absolute method (equation II.6) is displayed in circle blue while the relative method (equation II.7) is in square orange. The blue and orange pale areas are the error bars, which are respectively due to the error estimation on r_W and the variation in room temperature $\Delta T_{amb} = \pm 2$ K.

The major caveat of the relative method is the large contact resistance ($R_{con} \simeq 10$ mΩ) with respect to the resistance at room temperature ($R_{h,amb} = 60$ mΩ). A slight error in R_{con} causes a strong variation in $\overline{T_W}$, as can be seen in figure II.3. The empirical contact resistance of 10 mΩ would mean a 140 K discrepancy between the two methods. As the relative method gives a high degree of uncertainty as a function of R_{con}, resulting in significantly lower temperature estimates compared to the absolute method, it was discarded.

II.3.2 Temperature measurements via an optical method

Measurement of the filament temperature using an intensity comparison pyrometer is a powerful alternative method. The principle of operation relies on the comparison of the intensity of the infrared radiation at a given wavelength, between a grey-body under test and a precisely calibrated reference filament. I used a Keller ITS Mikro PV 11 pyrometer, based on the measurement of the radiation at 650 nm. The pyrometer is located 2.30 m away from the cathode and images the cathode through a borosilicate window. The pyrometer output was shot using a Nikon D610 camera with a minimal resolution of 1920 × 1080 pixels, at a framerate of 30 fps with fixed camera settings. Typical snapshots of the cathode intensity at 650 nm are shown in figure II.4, before plasma ignition (*i.e.* $t < -1$ s) and at the end of a plasma shot. The bottom panels of figure II.4 shows the evolution of the light intensity, which depends upon the local temperature T_W, along the curvilinear coordinate of the spiral. The cathode temperature profile is clearly inhomogeneous after being biased in the plasma.

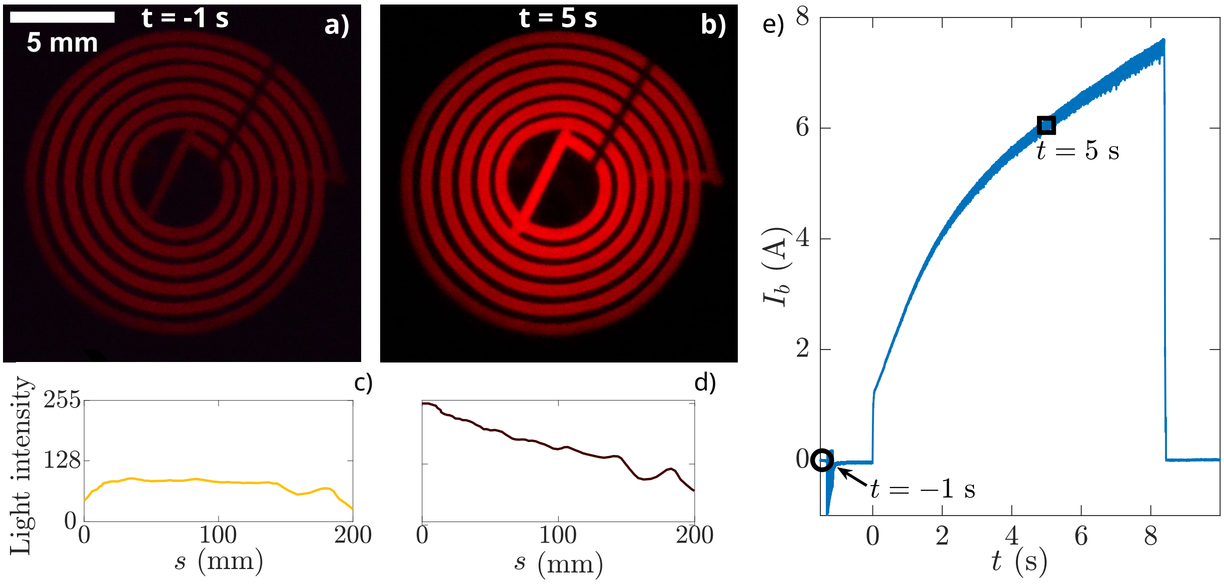

FIGURE II.4 – Hot cathode ($I_h = 16.3$ A) observed through the pyrometer at 650 nm *a)* without plasma and *b)* in presence of plasma ($V_b = -61$ V, $I_b = 8$ A). The reference grey body is the darker line in the right upper corner. *c)-d)* Corresponding light intensity profiles along the cathode. *e)* Current at the cathode I_b as a function of time. Timestamps $t = -1$ s and $t = 5$ s are highlighted.

The quantitative interpretation of the radiation intensity relies on Stefan-Boltzmann law, corrected by a material-dependent emissivity factor ϵ that depends on wavelength λ and T_W:

$$P_{\sigma,\lambda} = \sigma \mathcal{A} \epsilon(\lambda, T_W) T_W^4 \tag{II.8}$$

with $\sigma = 5.7 \times 10^{-8}$ W/(m^2 K^4) the Stefan-Boltzmann constant. The pyrometer principle exploits equation II.8 by matching the cathode light intensity at 650 nm to the one from a reference grey body of tunable emissivity $\epsilon(\lambda = 650\ \text{nm}, T_W)$.

Its operation requires the exact knowledge of the material emissivity. Polycristalline tungsten emissivity at 650 nm decreases with temperature T_W, from $\epsilon_W(\lambda = 650\ \text{nm}, T_W = 2200\ \text{K}) = 0.44$ to $\epsilon_W(\lambda = 650\ \text{nm}, T_W = 2800\ \text{K}) = 0.425$ [Cez+96; De 54]. Moreover, the cathode is imaged through a borosilicate window, whose transmittance τ_g at 650 nm needs to be measured. It has been quantified from relative measurements following the following protocol:

1. The cathode is put under vacuum in front of an unspecified borosilicate window and heated at a fixed heating current I_h. Its apparent temperature T_W^a is measured at a given emissivity ϵ_a, which takes into account the emissivity of the cathode and the transmittance of the unspecified window.
2. Then the borosilicate window used for the experiment presented in section II.2 is added outside of the vacuum chamber between the pyrometer and the cathode. The emissivity parameter of the pyrometer is adjusted to ϵ' in order to recover the measured temperature T_W^a obtained at step 1. This relative measurement provides the transmittance τ_g of the borosilicate window as the ratio ϵ'/ϵ_a.
3. The experiment is repeated for various values of I_h and ϵ_a to ensure reproducibility.

The real emissivity ϵ used in the experiment in section II.2 is then $\epsilon = \epsilon_W \tau_g$, with ϵ_W the tungsten emissivity. The correction factor τ_g is displayed in figure II.5 for two different initial values of ϵ_a as a function of I_h. Dark blue (respectively light orange) solid lines represent the mean values of the dark blue circles (resp. light orange squares) markers, pale areas represent the standard deviation for each dataset. The final value of the glass transmittance has been assessed at 80 ±4 %.

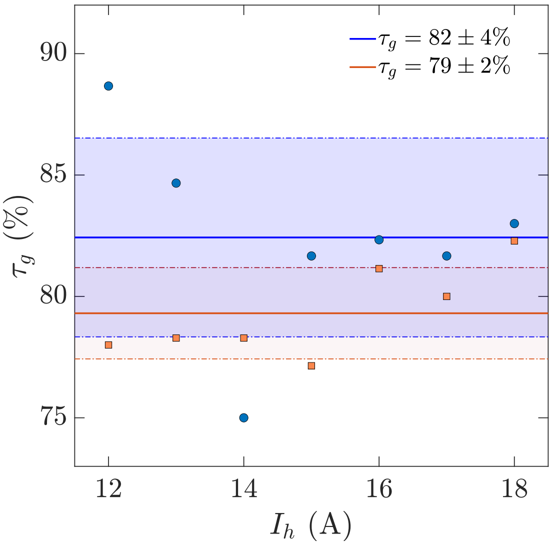

FIGURE II.5 – Transmittance of the glass window between the pyrometer and the cathode for $\lambda = 650$ nm for two different scans in I_h for $\epsilon_a = 0.3$ (blue circles) and $\epsilon_a = 0.35$ (orange squares).

Eventually we chose a linear evolution of ϵ from 0.35 at 2000 K to 0.325 at 3000 K, accounting for the glass transmittance and the tungsten emissivity dependence on T_W. A conversion factor from pixel intensity to local temperature of the tungsten filament is then computed using these physical parameters in equation II.8. This conversion has been calibrated in the 2270 K - 2700 K range accessible with the pyrometer, and was extrapolated up to 3000 K. An error $\Delta T = \pm 10$ K is considered for T_W below 2700 K and $\Delta T = \pm 25$ K above 2700 K. In the absence of a plasma, these values provide temperature in agreement with the electrical measurement of $\overline{T_W}$ within 30 K as will be shown later.

Note that only the spiral shape of the tungsten filament can be studied directly by the pyrometer. Indeed, this part faces the pyrometer and it is clearly visible from the pyrometer perspective. On the other hand, both ends of the filament are parallel to the observation direction and are not visible from the pyrometer. The temperature of the cathode at both ends, *i.e.* $s < 10$ mm and $s > 190$ mm, is computed by extrapolating linearly the temperature profiles measured at 10 mm $< s <$ 20 mm and 180 mm $< s <$ 190 mm.

II.4 Current emitted by a heterogeneously heated filament

In this section, we provide a detailed experimental characterization of a divergent regime, whose temporal evolution of the current I_b is shown in the top panel of figure II.6. The temporal evolution of the emitted current and voltage drop across the tungsten filament are reconstructed from spatially and temporally resolved measurements of the cathode temperature. These results are detailed in the section below, and exhibit an excellent agreement with empirical observations.

II.4.1 Spatially and temporally resolved temperature measurements

The cathode temperature profile is investigated during thermionic emission using the pyrometer. The plasma is operated at 170 G, 0.13 Pa and 1 kW. The spatial evolution of the tungsten

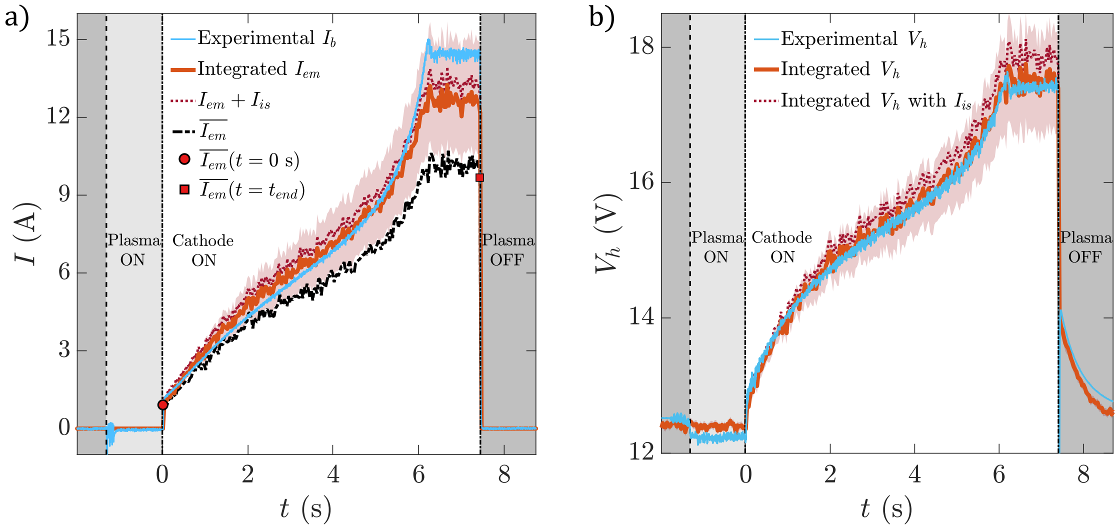

FIGURE II.6 – *a)* Time evolution of the emitted current during a divergent regime ($I_h = 16.2$ A, $V_b = -62$ V): experimentally measured current I_b (solid blue line), integrated thermionic emission I_{em} from temperature measurements (solid red line), sum of I_{em} and ion current saturation I_{is} (purple dotted line) and effective thermionic emission $\overline{I_{em}}$ assuming a homogeneous temperature profile (solid black line). *b)* Time evolution of the potential drop across the cathode: experimentally measured voltage V_h (solid blue line), integrated voltage taking into account temperature inhomogeneities (solid red line) and ion saturation current (purple dotted line) according to II.11 (red). Red shaded areas correspond to error bars for the solid red lines.

filament temperature T_W along the curvilinear abscissa s is displayed in figure II.7 at various time during the shot. As previously observed in figure II.4, a nearly homogeneous temperature profile at $t = 0$ s quickly evolves to a strongly inhomogeneous profile, where the center of the spiral ($s = 0$ mm) is hotter than the outer part of the spiral ($s = 200$ mm). An homogeneous profile is quickly recovered once the plasma is turned off, but is not shown in figure II.7.

A supplementary video available online[2] shows simultaneously the raw pyrometer measurements associated to the figure II.7. The temporally-resolved temperature profile along the cathode and the emitted current I_b are shown during the plasma shot.

The balance between the various thermal processes is detailed in section II.5, but a rough sketch of the instability mechanism can be given. Thermionic electrons leave progressively the cathode from the center of the spiral to the outer edge, leading to a decrease of the current flowing through the filament and inducing an excess of Joule heating in the central part. The non-linear evolution of the Richardson current with T_W enhances the inhomogeneous heating, possibly leading to unstable divergent regimes, as in figure II.6. For the sake of illustration of the importance of spatially resolved temperature measurements, the value of the effective temperature $\overline{T_W}$ inferred from the experimental electrical resistance, is shown for $t = 0$ s and $t = t_{\text{end}} = 7.4$ s. The corresponding Richardson currents for the homogeneously heated cathode are shown in figure II.6 with a red circle and square. While an excellent agreement is observed with an homogeneous temperature profile, prior to thermionic emission, the electric current run-away behaviour cannot be captured because of temperature inhomogeneity.

---

[2] http://tinyurl.com/4tcjvhax

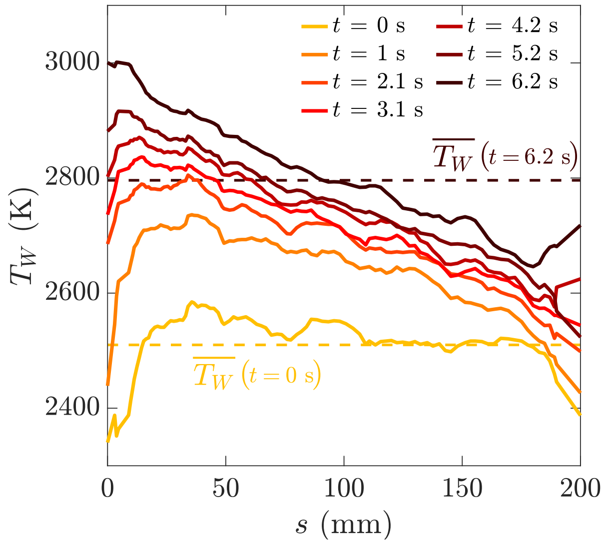

FIGURE II.7 – Temperature profile of the cathode along its curvilinear abscissa, from the center to the edge during the divergent regime ($I_h = 16.2$ A, $V_b = -62$ V) shown in figure II.6.

II.4.2 Estimate of thermionic emission from temperature measurements

The total thermionic emission can be efficiently computed when plugging the spatio-temporal evolution of the cathode temperature T_W into equation II.2. Assuming no space-charge limited effects, the total thermionic emission reads

$$I_{em}(t) = \int_0^{l_W} i_{em}(x,t)\,\mathrm{d}x = \int_0^{l_W} A_G 2\pi r_W T_W(x,t)^2 \mathrm{e}^{-\dfrac{eW}{k_B T_W(x,t)}}\,\mathrm{d}x \tag{II.9}$$

where the notation i_x denotes current per unit length. The time trace of $I_{em}(t)$ is shown in figure II.6a), solid red line. The shaded red area represents the error bar for I_{em} due to the error on the estimate of $T_W(s,t)$. A very good agreement is observed between the integrated thermionic emission $I_{em}(t)$ and the cathode current I_b delivered by the bias power-supply. While I_b always remains in the error bar margin of I_{em}, there is still a slight overestimation of I_b at the beginning of the shot and a mild underestimation of I_b during the current saturation. The initial overestimation of I_b may be due to small measurement inaccuracies. The underestimation at the end of the plasma shot is most certainly due to the calibration range, that is reliable up to 2700 K, while the maximum temperature value is 3000 K.

The potential drop V_h across the cathode is also computed from a similar integration, using the evolution of the resistivity $\rho_W(T_W)$ with T_W. The current $I_c(s,t)$ flowing in the cathode at position s is the sum of the constant heating current I_h and of the thermionic current emitted between position s and the outer end of the cathode:

$$I_c(s,t) = I_h + \int_s^{l_W} i_b(x,t)\,\mathrm{d}x \tag{II.10}$$

with $i_b = i_{em}$. The incorporation of the 10 mΩ contact resistance with the copper rods R_{con} leads to:

$$V_h(t) = \int_0^{l_W} \rho_W\left(T_W(x,t)\right) I_c(x,t) \frac{\mathrm{d}x}{\pi r_W^2} + R_{con}\left(I_h + \frac{I_b(t)}{2}\right) \tag{II.11}$$

The contribution of the Hall effect to V_h is negligible, as the carrier density in the metal is particularly high and the external magnetic field remains weak. Therefore it is not considered.

The heating potential drop V_h time traces of the experimental measurements and of the computation using spatially resolved cathode temperature profiles are shown in figure II.6b). The inhomogeneous heating of the cathode and the addition of the current I_b result in a 42 % increase of the cathode voltage drop V_h during the plasma shot, which is extremely well captured by the computation using the spatially and temporally resolved temperature measurement. Once the plasma is off, I_b is set to 0 A so the persistence in the increased filament resistance is solely due to the heterogeneous heating of the filament during thermionic emission.

A refinement is incorporated by taking into account the ion saturation current I_{is} in the current flowing through the negatively biased cathode. Note here that this correction is small since I_{em}/I_{is} lies in the range [5;16]. Due to the large primary injection from the cathode, the plasma density increases with thermionic emission. Following the experimental observations, a linear evolution of the plasma density with the emitted current is considered here $n = 10^{18} + 3 \times 10^{17} I_{em}$, and the Bohm velocity is assumed constant. This linear variation appears to be logical, as the increase in density is proportional to the power injected into the plasma, as presented in subsection I.2.7. The validity of this linear variation will be discussed later, in subsection II.5.4. We assume no plasma electron current flowing to the cathode since the cathode potential is at least $10T_e$ lower than ϕ_p. The small correction on the emitted current is displayed in figure II.6 (purple dotted line) for the cathode current and the voltage drop (for which $i_b(x,t) = i_{em}(x,t) + i_{is}$ in equation II.10).

Finally, we stress the failure of using an effective temperature $\overline{T_W}$ from resistance measurement for the prediction of the cathode current, which relies on the assumption of an homogeneous temperature profile. While the experimental estimate of $\overline{T_W}$ is only possible at the beginning and at the end of the shot, it is possible to infer an effective average temperature from the spatio-temporal temperature profiles, using the average electrical resistance value $\overline{R_h} = \int_0^{l_W} \rho_W \left(T_W(x,t)\right) \frac{\mathrm{d}x}{\pi r_W^2}$ in equation II.6. An effective emitted current $\overline{I_{em}}$ is then computed using this value of the effective temperature in equation II.2. The results are shown in figure II.6a) (dotted black line). The experimental values using the experimentally measured values of $\overline{T_W}$ are shown as red-filled black symbols at $t = 0$ s and $t = t_{end}$. This method clearly underestimates the emitted current especially at strong emission, by up to 30%.

II.5 Thermionic emission and plasma-cathode interactions modelling

II.5.1 Cathode thermal budget

The previous section demonstrated that the knowledge of the spatiotemporal variations of the cathode temperature T_W allows to precisely reconstruct the current I_b drawn at the cathode. The goal of this section is to efficiently predict the temperature profile of the cathode by solving the local enthalpy budget equation leading to a partial integro-differential equation for the temperature $T_W(s,t)$. We provide below a model that accurately predicts the spatio-temporal evolution of the cathode temperature during the divergent regime shown in figure II.6, which thus applies both to stationary and unsteady regimes. In the remaining of this section, the notation $\dot{X}(s,t)$ refers to the time derivative per unit length $\mathrm{d}s$ of the scalar X, *i.e.* $\dot{X}(s,t) = \frac{\partial X(s,t)}{\partial t \, \mathrm{d}s}$.

The enthalpy budget of the cathode is given by

$$\dot{H} = \dot{Q}_\Omega + \dot{Q}_c + \dot{Q}_i + \dot{Q}_{\sigma,in} - \dot{Q}_{\sigma,out} - \dot{Q}_e, \tag{II.12}$$

where H is the enthalpy of the cathode, and $\dot{Q}_X$ refer to powers per unit length. $\dot{Q}_\Omega$ is the ohmic heating term, $\dot{Q}_c$ the thermal conduction term, $\dot{Q}_i$ the heating term due to ion bombardment, $\dot{Q}_{\sigma,in}$

the radiative incoming term, $\dot{Q}_{\sigma,out}$ the radiative outgoing term and $\dot{Q}_e$ the thermionic cooling term (or electron transpiration cooling term). Each of these terms are now discussed in details, and require the knowledge of the physical parameters of tungsten with temperature. The evolution with temperature were extracted from previous studies for the electrical resistivity $\rho_W(T_W)$ [Des+84; Whi+97], the specific heat $C_p(T_W)$ [Whi+97], the thermal conductivity $\lambda_W(T_W)$ [Whi+97], and the total effective emissivity $\epsilon_{eff}(T_W)$ [Mat+99].

The temperature-dependent thermophysical properties for tungsten are displayed in II.8: thermal conductivity λ_W [Whi+97; Des+84], electrical resistivity ρ_W [Whi+97; Des+84], specific heat C_p [Whi+97; Des+84] and hemispherical total emissivity ϵ_{eff} [Mat+99] from top left to bottom right. The first three quantities are fits based on experimental data in the range [1800 K; 3200 K] while the last one is the best fit according to the works of Matsumoto *et al.* [Mat+99] in the range [2000 K; 3400 K].

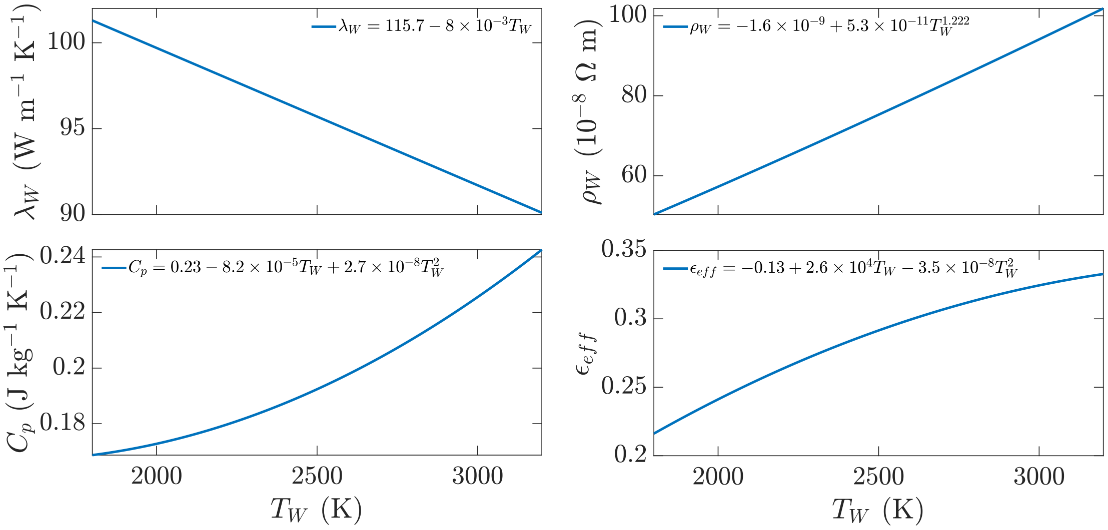

FIGURE II.8 – Thermophysical properties of tungsten as a function of temperature.

II.5.1.1 Detailed budget

The evolution of the enthalpy is given by

$$\dot{H}(s,t) = C_p(T_W)\rho\pi r_W^2 \frac{\partial\, T_W(s,t)}{\partial\, t}, \tag{II.13}$$

where ρ is the volumic mass of tungsten.

The main heat source for the filament is ohmic heating, which depends upon the local current $I_c(s,t)$ flowing through the cathode at location s, given by equation II.10:

$$\dot{Q}_\Omega(s,t) = \frac{\rho_W(T_W)}{\pi r_W^2}\left(I_h + \int_s^{l_W} i_b(x,t)\,\mathrm{d}x\right)^2, \tag{II.14}$$

with $i_b(x,t) = i_{em}(x,t) + i_{is}$. Since i_{em} is set by the temperature T_W from Richardson's law, the ohmic heating term leads to an integral term in T_W.

Since the cathode is under vacuum, one can neglect the convection losses. Nonetheless heat diffuses along the filament via thermal conduction as:

$$\dot{Q}_c(s,t) = \lambda_W(T_W)\pi r_W^2 \frac{\partial^2\, T_W(s,t)}{\partial\, s^2} \tag{II.15}$$

Let us now discuss the radiative terms, and focus first on losses. The cathode is considered as a grey-body of hemispherical total emissivity $\epsilon_{eff}(T_W)$, which is the total effective emissivity of tungsten along the complete spectrum of radiation, and the emitted radiative power per unit length reads:

$$\dot{Q}_{\sigma,out}(s,t) = \sigma 2\pi r \epsilon_{eff}(T_W) T_W(s,t)^4 \tag{II.16}$$

The incoming radiative flux is mainly due to self-heating by the radiation from neighbouring parts of the filament because of the spiral shape. The radiative inward flux from the environment and the low-density plasma are neglected, the vessel and the argon neutrals being close to room temperature. The winding of the spiral leads to an inward flux at a given location s, on turn N, emitted by the cathode at location s_{N-1} on turn $N-1$ and location s_{N+1} on turn $N+1$, as sketched in figure II.9. A fraction C_1 of the radiative power per unit length $\dot{Q}_{\sigma,out}(s_{N-1},t)$ emitted at location s_{N-1} is intercepted by the filament at location s. The value of C_1 is approximately given by the value of the solid angle $\delta\theta$ seen by each filament, as $C_1 \simeq \delta\theta/2\pi \simeq 0.1$. Assuming that the absorbance of the filament at T_W is $\epsilon_{eff}(T_W)$, the radiative inward term at position s reads:

$$\dot{Q}_{\sigma,in}(s,t) = C_1 \epsilon_{eff}(T_W) \left(\dot{Q}_{\sigma,out}(s_{N-1},t) + \dot{Q}_{\sigma,out}(s_{N+1},t) \right) \tag{II.17}$$

Some locations have only one or none neighbouring filament. For instance, it is the case for the filament at s_{N-1} or s_{N+1} in figure II.9. In that case, the incoming radiative flux from the neighbouring filament is equated at 0. In order to assess the exact C_1 value, the temperature of the cathode in absence of plasma has been measured experimentally and compared to numerical results. The evolution of the homogeneous temperature T_W as a function of I_h is shown in figure II.9b). The numerical value solves the heat budget equation and assumes no plasma, *i.e.* $I_b = 0$ A, $Q_i = 0$ and $Q_e = 0$. The numerical temperature obtained at $s = 100$ mm is retained to be compared with experimental values. The optimal value of the parameter C_1 is inferred from the best agreement between the experimental values and the numerical solution of the model. The case $C_1 = 0$ (black dotted line) underestimates T_W by 50 K to 75 K. An excellent agreement is observed for $C_1 = 0.15$ (black dashed line) over the whole range of I_h, and is close to the previous 0.1 estimate. This latter value was retained for all numerical simulations.

The last heating source for the cathode is due to plasma-cathode interactions, namely ion bombardment, since interactions with plasma electrons and neutrals will be ignored. No secondary electron emission is taken into account as mentioned previously [Kon92; Tol14]. The energy of ions transferred to the cathode is the sum of the potential energy $e\left(\mathcal{E}_i - W\right)$ due to the ion-electron recombination, with $\mathcal{E}_i$ the ionization energy in eV, and the kinetic energy $C_2 e \left(V_c(s,t) - \phi_p(t)\right)$ [Ker+01], where C_2 is a numerical factor to account for the elastic collision and dissipative phenomena during the energy transfer to the lattice, and V_c the local potential of the tungsten filament. C_2 is expected to lie between 0.5 and 1 [Ker+94]. The ion-bombardment term thus reads:

$$\dot{Q}_i = \frac{i_{is}}{e} e \left[\mathcal{E}_i - W + C_2 \left(V_c(s,t) - \phi_p(t) \right) \right] \tag{II.18}$$

Finally, thermionic electrons extract heat from the material as they leave the cathode [Her+49; Han+17]. Assuming a Maxwell energy distribution at temperature T_W for the emitted electrons, the cooling term reads:

$$\dot{Q}_e = \frac{i_{em}}{e} \left(eW + 2k_B T_W \right) \tag{II.19}$$

In summary, the only adjustable parameter of the numerical model is C_2, and its importance will be discussed in subsection II.5.5.

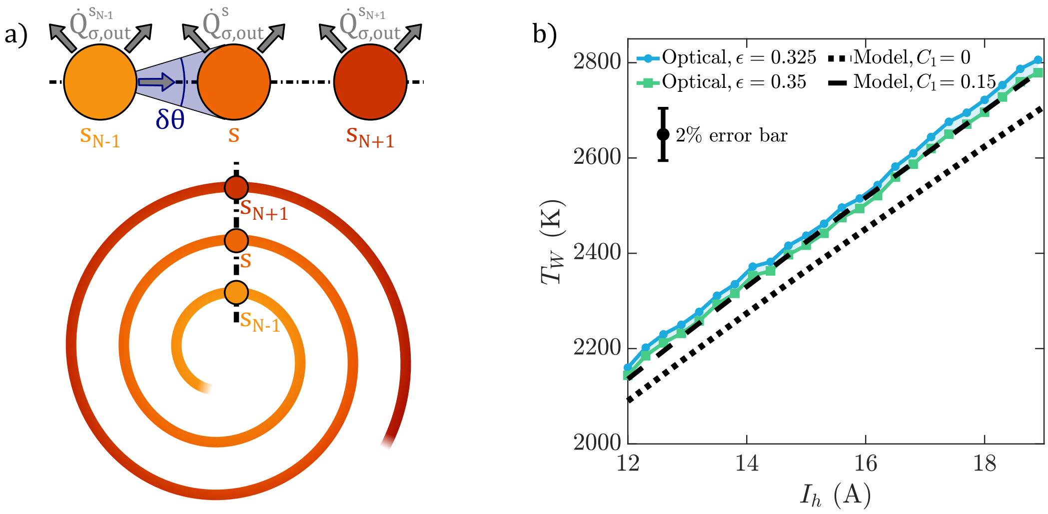

FIGURE II.9 – *a)* Cross-sectional (top) and upper (bottom) views of the cathode. The solid angle $\delta\theta$ is shown in light blue and gives an estimation of the parameter C_1. *b)* Comparison of optical measurements (solid lines) and numerical results (black lines) of T_W for different values of I_h in absence of plasma. The error bar represents the margin of error for optical measurements.

II.5.1.2 Boundary conditions

Boundary conditions are set to prescribe heat fluxes at both ends. The cathode is clamped to copper rods of thermal conductivity λ_{Cu}, length $l_{Cu} = 35$ cm, radius $r_{Cu} = 2$ mm which are kept at ambient temperature at the other end. Thermal conduction along the large copper rods being assumed to be the only flux term, the spatial derivatives of temperature T_W at the boundaries are imposed:

$$\begin{cases} \left.\dfrac{\partial\, T_W}{\partial\, s}\right|_{s=0} = \dfrac{\lambda_{Cu} r_{Cu}^2}{\lambda_W(T_W(0,t))r_W^2} \dfrac{T_W(0,t) - T_{amb}}{l_{Cu}} \\ \left.\dfrac{\partial\, T_W}{\partial\, s}\right|_{s=l_W} = -\dfrac{\lambda_{Cu} r_{Cu}^2}{\lambda_W(T_W(l_W,t))r_W^2} \dfrac{T_W(l_W,t) - T_{amb}}{l_{Cu}} \end{cases} \tag{II.20}$$

The poor thermal contact between tungsten and copper is taken into account by setting λ_{Cu} at 40 $\mathrm{W} \cdot (\mathrm{m\,K})^{-1}$, one order of magnitude below the common values for λ_{Cu} [Whi+97]. The influence of this value is discussed in subsection II.5.6.

II.5.2 Computation of the cathode current

The current flowing through the cathode or from the cathode to the plasma is crucial for the ohmic heating $\dot{Q}_\Omega$, the heating due to ion bombardment $\dot{Q}_i$ and the thermionic cooling $\dot{Q}_e$. This paragraph clarifies the current computed at the cathode in order to compute the heat transfer terms mentioned.

The temporal evolution of the cathode temperature profile $T_W(s,t)$ is computed from the numerical integration of the integro-differential equation for T_W, equation II.12. In case of weak biasing or low plasma density, the space-charged limited solution is implemented according to the model from Ye and Takamura [Ye+00] and bounds the thermionic current (see section II.2). Otherwise, the cathode current is computed as the Richardson current using the spatio-temporal evolution of T_W in equation II.9. The ion saturation current I_{is} is considered homogeneous along the filament as well. I_e is neglected since the biasing is assumed to be strong. In this study, W was set at 4.54 eV to model a tungsten cathode, but this could be modified at will to study other materials.

II.5.3 Plasma potential decrease with thermionic emission

As shown by the experimental results displayed in figure II.2, the dynamical evolution of the cathode current is very sensitive to the cathode bias through the plasma-cathode interactions. Hence the prediction of the cathode temperature profile depends upon the evolution of the plasma density and plasma potential with the cathode current. It is important to provide a precise picture of the evolution of plasma parameters with the cathode current.

Firstly, let us focus on the plasma potential. Its dependency on the current I_b requires to be taken into consideration for the ion bombardment term $\dot{Q}_i$. Despite the recent development of analytical models for the evolution of the plasma potential in the presence of emitted current [Tro+22; Pou19], these models do not provide a direct and reliable comparison with experimental observations at very large current emission yet (see section III). Measurements of ϕ_p at the plasma core as a function of I_b are shown in II.10a) for three different experiments (blue solid lines), and the best power law fit is presented (black dotted line). Hence the retained power law to model numerically the evolution of ϕ_p is:

$$\phi_p = \phi_{p,0} + \gamma I_b^{1/p}, \tag{II.21}$$

where $\phi_{p,0} = -1$ V is the plasma potential at zero thermionic emission and $\gamma = -6.6$ and $p = 3$ are empirical constants.

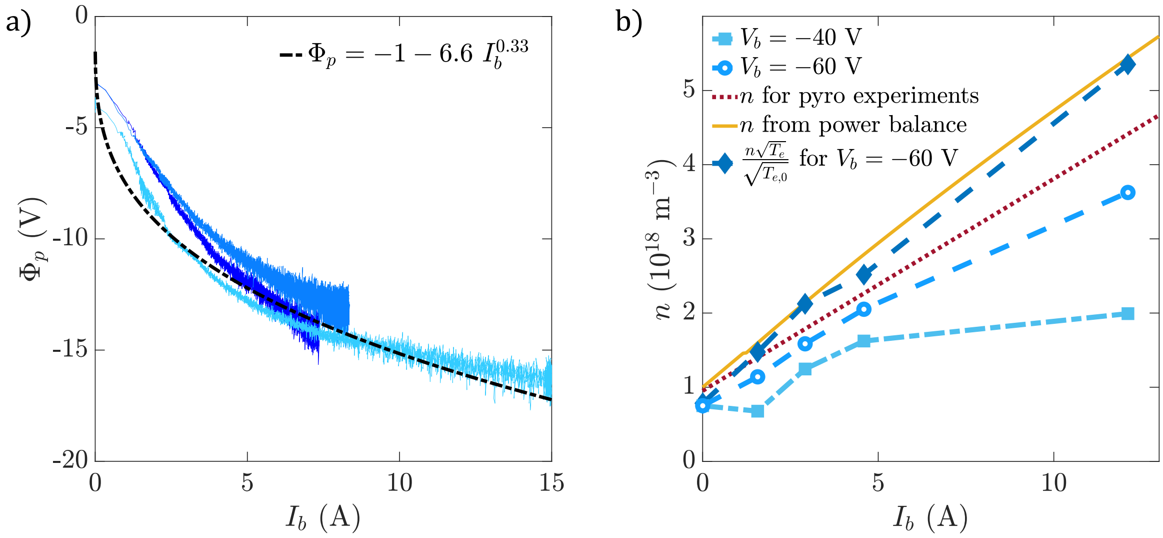

FIGURE II.10 – *a)* ϕ_p measurements as a function of I_b. The black dotted line represents the best power law fit for the light blue curve. *b)* Density at the plasma core as a function of current through the cathode I_b for $V_b = -40$ V and $V_b = -60$ V. The empirical (dotted line) and numerical (solid line) values used to compute I_{is} at $T_{e,0} = 4.5$ eV, respectively used for subsections II.4.2 and II.5.1.1, are displayed. The density corrected by the experimental electron temperature for $V_b = -60$ V is also displayed.

II.5.4 Plasma density increase with thermionic emission

Secondly, the modelling of the evolution of the plasma density with the cathode current is essential. The power supplied by the cathode to the plasma contributes to ionization and heating in addition to the RF antenna, as shown in figure II.11 for $V_b = -60$ V and various I_b values. It results in a broad density increase along the plasma radius, and a localized increase of the electron temperature at the core. The most striking effect is the 5-fold density increase at $r = 0$ cm, while the average electron temperature at the core increases from 5 eV to 10 eV. The plasma density n and electron temperature T_e are averaged between $r = -0.5$ cm and $r = 0.5$ cm. The dependency of n on the parameter I_b is shown in II.10b) for two different biases of the cathode: hollow circles for $V_b = -60$ V, plain squares for $V_b = -40$ V. The linear evolution considered in subsection II.4.2 is shown as a dashed red line ($n = 10^{18} + 3 \times 10^{17} I_{em}$) and reproduces qualitatively the density increase for $V_b = -60$ V with an error up to 20 %. Since the contribution of the ion saturation current on the total cathode current is minor in regards with thermionic emission, we consider that our linear modelling is accurate enough for the computation of the current emitted at the cathode $I_b = I_{em} + I_{is}$ as computed in subsection II.4.2.

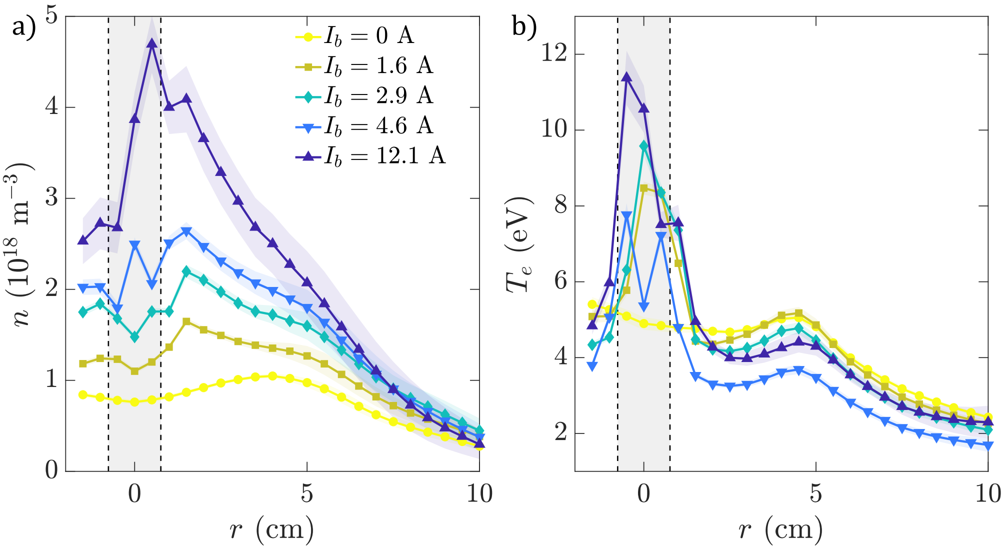

FIGURE II.11 – Radial evolution of *a)* the plasma density and *b)* the electron temperature for various currents I_b. The grey areas represent the location of the cathode.

A simplified power balance model has been used to reproduce numerically the plasma density increase as a function of the power deposited by the emissive cathode [Lie+05; Cha+11]. Before examining this topic, one can mention that the electron temperature increase could be computed by considering the particles balance as well. However, it is challenging to model the ionization from high-energy primary electrons. Besides, the effect of electron temperature on the cathode thermal budget is minor as it only affects the ion saturation current to the square root. This is why T_e is kept constant at $T_{e,0} = 4.5$ eV in the numerical model. Nonetheless, its influence on I_{is} is assessed in II.10b) for $V_b = -60$ V, where $n\sqrt{T_e}/\sqrt{T_{e,0}}$ is shown as full diamond. Its effect is significant and an accurate resolution of the particles balance would be a good refinement of the numerical model. In its absence, it still provides a confidence range for the plasma density computation.

The calculus principle of the power model is a refined version of the 0D calculation presented in subsection I.2.7 as it accounts for the scale separation between the large plasma column and the smaller dense plasma core due to thermionic emission. When the cathode is left floating or cold (*i.e.* $I_b = 0$), the plasma density n_0 is sustained by the RF antenna alone and is assumed to be homogeneous in a cylinder of radius $R = 5$ cm. The density increase due to the cathode emission is assumed to be linear from the edge of the plasma (5 cm) to the core (0 cm) accordingly to the experimental measurements (see figure II.11) and the plasma density is modelled as $n(r) = n_0 + \Delta n\,(1 - r/R)$.

The total power absorbed by the plasma is the $P_w = 1$ kW RF power and the power input from the cathode to the plasma provided by thermionic electrons P_{cath}. On the other hand, the global model assumes stationarity, *i.e.* the excess in absorbed power P_{cath} is balanced by an excess in power losses at the ends of the plasma column. The supplementary losses are caused by the recombination of each electron-ion pair that releases $E_T = 75$ eV. The additional losses δP_{losses} at both ends is obtained after the integration from $r = 0$ cm to R. Ultimately, the new power terms yield:

$$P_{cath} = \int_0^{l_W} I_{em}(x)(\phi_p - V_c(x))\,\mathrm{d}x \quad \text{and} \quad \delta P_{losses} = \frac{\Delta n}{3} h_l 2\pi R^2 \sqrt{eT_{e,0}/m_i} e E_T \tag{II.22}$$

with h_l the dimensionless ratio of the bulk density to the pre-sheath density. This factor can be estimated of the order of 0.5 in our low pressure plasma [Lie+05]. Then the density at the core ($r = 0$ cm) reads:

$$n = n_0 + \frac{3P_{cath}}{\pi R^2 \sqrt{eT_e/m_i} e E_T} \tag{II.23}$$

which is shown as the solid yellow line in II.10b) for $V_b = -60$ V and reproduces well the experimental data corrected in T_e.

II.5.5 Simulation of the temporal dynamics of diverging regimes

Finally, the model described above is numerically solved for the conditions of the dynamics shown in figure II.6 and II.7. The numerical simulation solves an integro-differential heat equation. The time step is 10^{-3} s and the spatial step is 1 mm. This resolution verifies the Courant-Friedrich-Levy condition for the heat equation

$$\frac{\lambda_W}{\rho C_p} \frac{\mathrm{d}t}{\mathrm{d}x^2} \sim 2.5 \times 10^{-2} \leq 1 \tag{II.24}$$

For the computation of iteration N, the integral term is computed manually from the temperatures at N-1. The equation is solved numerically using the function `pdesolver` from MATLAB. The initial temperature profile of the cathode is obtained from an initially homogeneous profile, then freely evolving in absence of plasma for 5 seconds.

The parameter C_2 (the ratio of energy transfer considered for the ion bombardment term) is the only free parameter of the model, whose value is set to match the experimental temperature profiles. This results in the temporal evolution of the spatial profiles of the cathode temperature shown in figure II.12a), which very accurately reproduces the experimental measurements with $I_h = 16.2$ A, $V_b = -62$ V and C_2 set at 1.01[3]. The slow heterogeneous growth in T_W during the first part of the shot is well captured. Then, when the regime diverges rapidly, the numerical profiles are slightly warmer than the experimental profiles for $s < 50$ mm, and slightly cooler for $s > 100$ mm. We stress that the discrepancy between the experimental and numerical profiles at $s \simeq 10$ mm might originate from an underestimated experimental temperature due to the pyrometer calibration, as mentioned in section II.3.2. The inset of figure II.12a) shows that the simulation of the total cathode current is in excellent agreement with the experimental value. The limitations of the model are further discussed in subsection II.5.6.

The influence of the parameter C_2 is illustrated in II.12b) as one can see temperature profiles obtained for C_2 values ranging from 0.5 to 1.01. The insert shows the temporal evolution of I_b for three values of C_2. One clearly sees the influence of C_2 on the temporal evolution of the cathode temperature profile due to ion bombardment. The best agreement with the experimental data for I_b is observed for $C_2 = 1.01$.

---

[3] Video available at: http://tinyurl.com/24zzwk2m

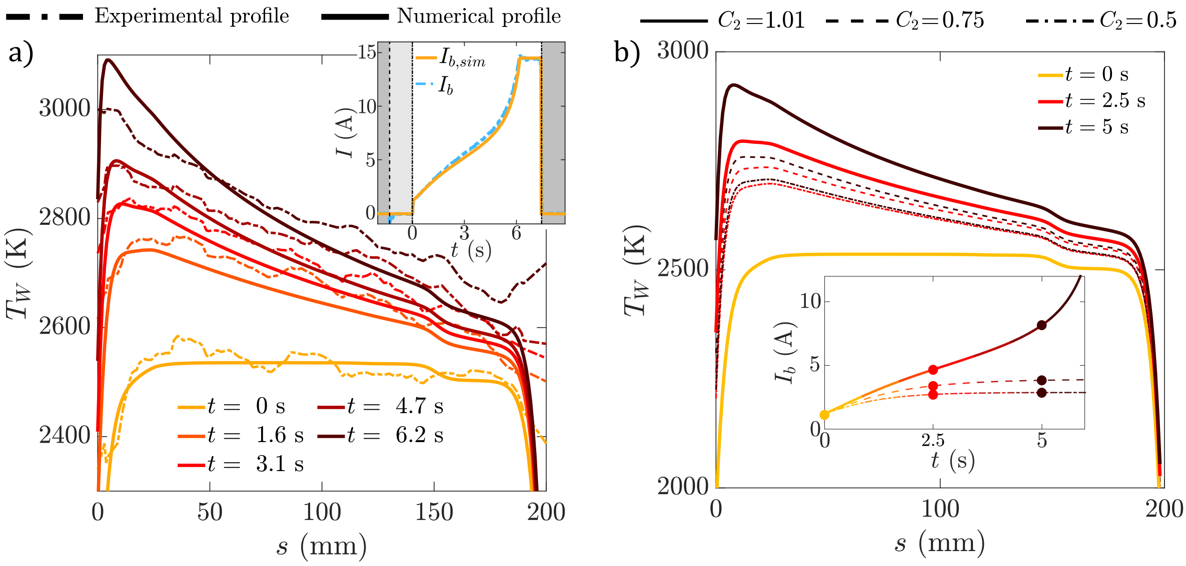

FIGURE II.12 – *a)* Comparison of experimental and numerical T_W during a divergent regime ($I_h = 16.2$ A, $V_b = -62$ V). Dashed lines are for experimental profiles, solid lines are for numerical profiles. The same colors correspond to identical timestamps. Insert represents the current I_b over time obtained experimentally and numerically. *b)* Temperature profiles of the cathode at $I_h = 16.2$ A and $V_b = -60$ V for $C_2 = 0.5$ (dotted lines), $C_2 = 0.75$ (dashed lines) and $C_2 = 1.01$ (solid lines). Insert: I_b over time for the three cases.

II.5.6 Limits of the model

Firstly, the influence of the boundary conditions and the copper conductivity λ_{Cu} on the temperature profile is shown in figure II.13. λ_{Cu} covers the range [20 W · (m K)$^{-1}$; 80 W · (m K)$^{-1}$]. The blue area represents the spans of T_W and I_b for higher values of λ_{Cu} up to 80 W · (m K)$^{-1}$ while the red one represents T_W and I_b for lower λ_{Cu} down to 20 W · (m K)$^{-1}$.

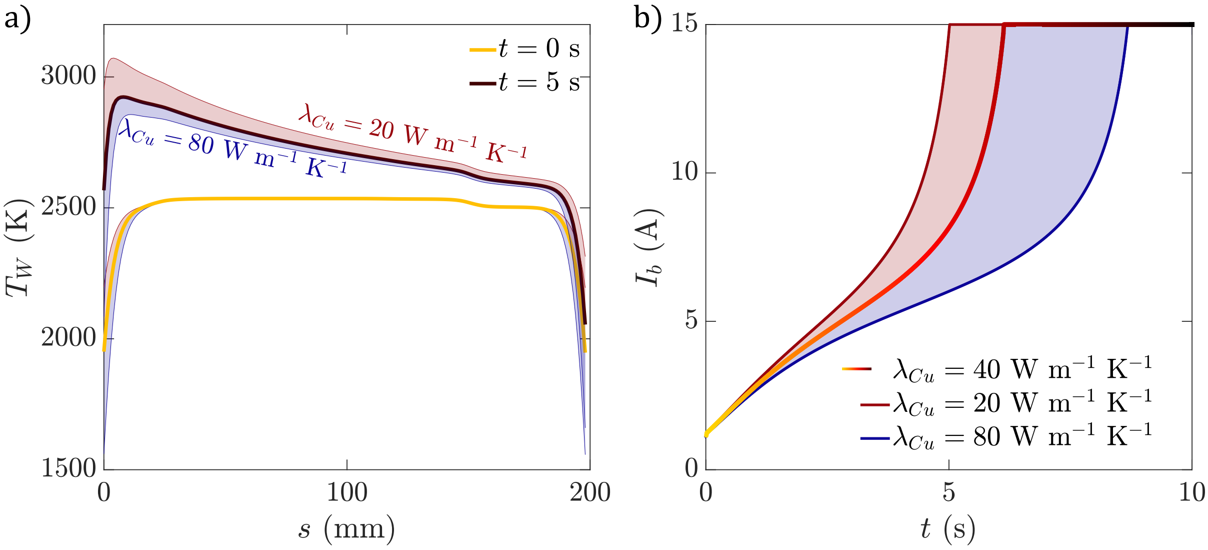

FIGURE II.13 – *a)* Temperature profile along the cathode. *b)* Currents I_b for 3 different values of λ_{Cu}.

One can see that the initial temperature profile along the cathode is not modified except at the 15-mm extremities, where a significant difference is observed. It results in similar I_b trends which differ progressively because of the small variations in initial conditions and the different losses at the boundaries. Yet this effect remains minor and was not thoroughly investigated.

Overall, while the model reproduces the experimental data with high fidelity, it still presents some limitations. The first refinement would be to include heating from electron bombardment, which would be important when the outer end of the spiral is at a potential close to the plasma potential, *i.e.* when $\phi_p - (V_b + V_h)$ is lower than $\sim 3\ T_e$. This correction would likely explain the difference between the simulation and the experiments for $s > 100$ mm. In addition, the cathode properties might change during a strongly emissive regime. Firstly, the surface state of the cathode might be altered by impurities. Scanning electron microscope (abbreviated SEM) imaging revealed for instance an altered surface of state for cathodes that underwent particularly strong heating (thousand shots and hundred divergent regimes, see figure II.14a)), which will impact most certainly the work function. Then, tungsten sputtering is not taken into account, which could reduce the filament thickness. SEM showed that the filament thickness is smaller between $s = 0$ mm and 25 mm after a few hundreds plasma shots, with a shrinkage up to 2 % located at $s \simeq 10$ mm (see figure II.14b)). Tungsten evaporation would add a new cooling term in the energy budget equation and the decrease of r_W would modify the energy budget equation. The absent cooling term associated to tungsten evaporation could be another factor that may explain the discrepancy between numerical and experimental temperatures at $s = 10$ mm, as it is more prominent when T_W increases [Goe+07].

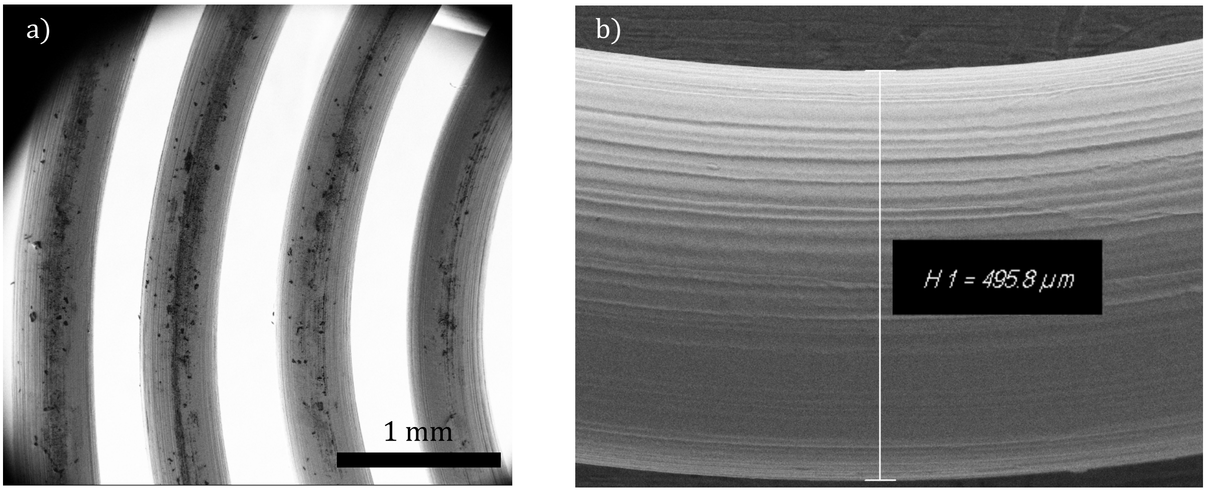

FIGURE II.14 – *a)* Scanning electron microscope image of an altered cathode after strong heating and hundreds of divergent regime. Black spots are impurities at the tungsten surface. *b)* Zoom on the cathode at $s = 20$ mm, the thickness of the filament is measured at 495.8 μm.

Finally, note that the precise tuning of C_2 could slightly depend upon the base plasma parameters n_0 and $T_{e,0}$ and thus upon base pressure, magnetic field, RF power and geometry of the plasma device.

II.6 Insights on plasma-surface interactions from modelling

II.6.1 Prediction of the operating parameters and of stable regime limits

The model described in the previous section allows to predict whether a steady-state regime or a time-divergent regime is reached for cathode operation. For given values of the background plasma parameters, a set of simulations were run for heating current $I_h \in [14.5\text{ A}; 17.5\text{ A}]$ and bias voltage $V_b \in [-100\text{ V}; -45\text{ V}]$. The values of the cathode current I_b obtained after 30-seconds simulations are reported in figure II.15a). Diverging regimes are defined as the cathode exceeding 25 A, and lie below the red curve in figure II.15a), *i.e.* the black portion of the parameter map at high heating current and strong voltage bias. Stable regimes at moderate emission are observed for low heating current or weak voltage bias. The V_b dependency of I_b highlighted in figure II.2 is thus correctly captured by the model. A high emission would cause severe damage to the cathode due to tungsten sputtering, and is therefore undesirable, but could be predicted by this model. Note that stable regimes at strong emission are observed for moderate bias and strong heating in the upper right part of the parameter space ($I_b \in [15\text{ A}; 25\text{ A}]$) because of space-charge limited emission ; this should be interpreted with caution as I_e can no longer be ignored since $(V_b + V_h - \phi_p)/T_e$ is below 3.

The inset highlights the sensitivity to $\dot{Q}_i$ and $\dot{Q}_e$ and displays the frontiers between stable and divergent regimes for four cases: $\dot{Q}_i = 0$ (yellow up triangles), $\dot{Q}_i/2$ (orange down triangles), $\dot{Q}_e = 0$ (black squares) and $\dot{Q}_e/2$ (brown diamonds). One can see notably the stabilizing effect of strong thermionic cooling and most importantly the prominent role of ion bombardment in the dependence on V_b of the divergent regime. This latter instability, called the "cathode-sheath instability" by Benilov [Ben14], has already been reported in high-pressure arc discharges. However, for these high-pressure arc discharges, where the plasma density is of the order of 10^{23} m^{-3}, the term $\dot{Q}_i$ is greater than $\dot{Q}_{\sigma,out}$ and $\dot{Q}_\Omega$ by a few orders of magnitude [Ben08], which is in sharp contrast with the ordering of the various terms discussed below in section II.6.3, where $\dot{Q}_{\sigma,out} \sim \dot{Q}_\Omega \sim 10\dot{Q}_i$.

The experimental data confirm the extreme sensitivity with the control parameters, but no quantitative data can be furnished for a comparison with the numerical values of the figure II.15a). The divergent regimes around ($I_h = -16.2$ A, $V_b = -62$ V) were witnessed, as well as the non-existence of a divergent regime at $V_b > -40$ V for any value of I_h. Sharp transitions from stable to unstable regimes at $V_b < -80$ V and $I_h \sim 15.5$ A have also been observed.

II.6.2 Correction of current emission computed using the effective cathode temperature from electrical measurements

As already mentioned, thermionic electron emission is clearly underestimated when using the effective cathode temperature $\overline{T_W}$ from electrical measurements (see figure II.6a)). However, the simple implementation of this electrical diagnostic makes it very attractive. Using the complete thermal modelling of the cathode presented in section II.5, we are able to compute a correction factor for the thermionic emission computed as $I_{em,sim}/\overline{I_{em,sim}}$, as shown in figure II.15b). The correction factor ranges between 1.2 and 1.5 for most of the operational parameters, but may reach values up to 2 for emitted current superior than 15 A.

The evolution of this correction factor with the current injected I_b is displayed in figure II.16. Each line corresponds to a scan in the cathode bias V_b at fixed heating current I_h, *i.e.* a vertical sweep in the phase diagram in figure II.15b) from top to bottom, until the unstable regime occurs. The ratio $I_{em,sim}/\overline{I_{em,sim}}$ for each I_h value is accurately fitted with a linear fit, hence the linear trends shown in figure II.16. The mean correction factor used for further computation of I_{em} is the thicker $I_h = 16$ A line. The black dashed lines represent the extent of $I_{em,sim}/\overline{I_{em,sim}}$ variability depending

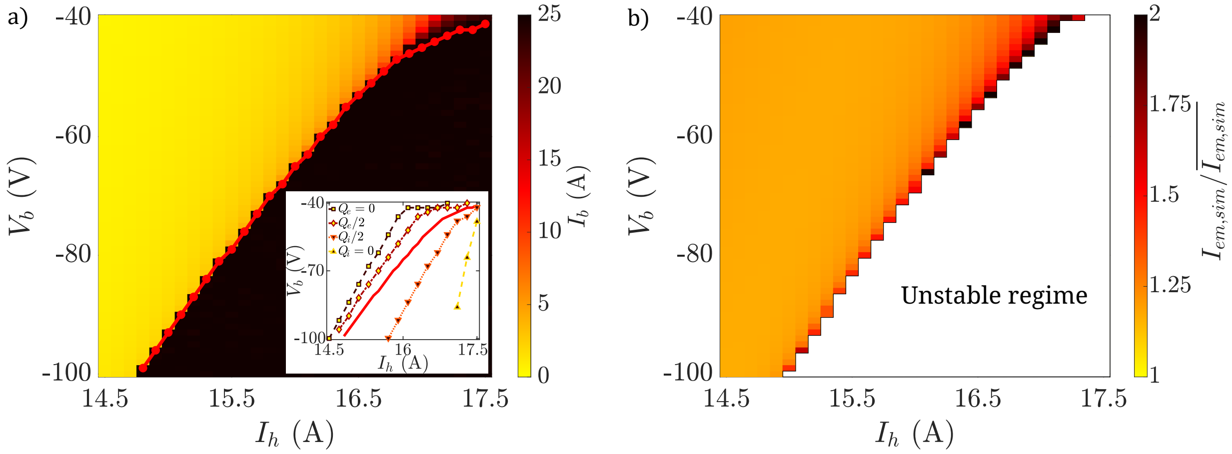

FIGURE II.15 – *a)* I_b as a function of experimental parameters V_b and I_h after 30 s of simulation. Simulations are bounded at 25 A maximum. The red line splits the diagram in two domains whether $I_b = 25$ A is reached or not. Inset: frontiers between the stable and divergent regimes for different values of $\dot{Q}_i$ and $\dot{Q}_e$. *b)* Corresponding ratio $I_{em,sim}/I_{em,elec}$ after 5 s of simulation.

on I_h. The use of this correction factor and its error estimation are extremely important for the estimate of the Richardson current, which is essential to understand how current injection affects the potential profile (see section III and works from Trotabas and Gueroult [Tro+22]).

The measurement of the cathode temperature via the electrical resistance given by equation II.6, coupled to the correction factor estimation for temperature heterogeneity above-mentioned, is used for I_{em} computation in chapter III. Ensuing error bars for I_{em} primarily accounts for a $\Delta r_W = \pm 1$ μm variation in cathode radius. Additionally, a realistic 6% error in the correction factor, as observed in figure II.16, is considered.

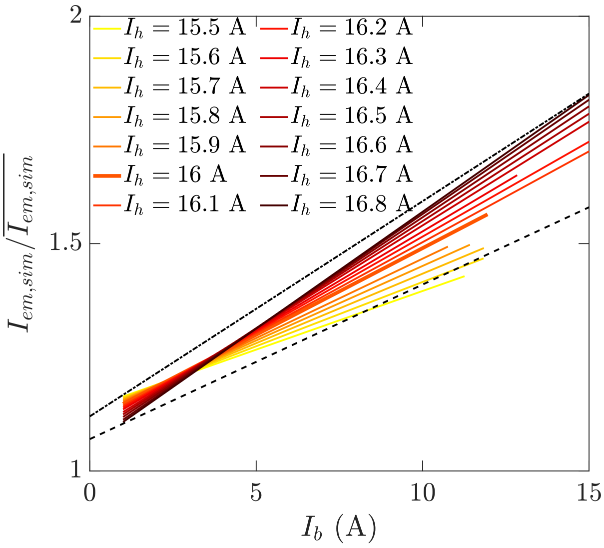

FIGURE II.16 – Correction factor $I_{em,sim}/\overline{I_{em,sim}}$ as a function of I_b for various heating current I_h. Black dashed lines represent the variability of the correction factor.

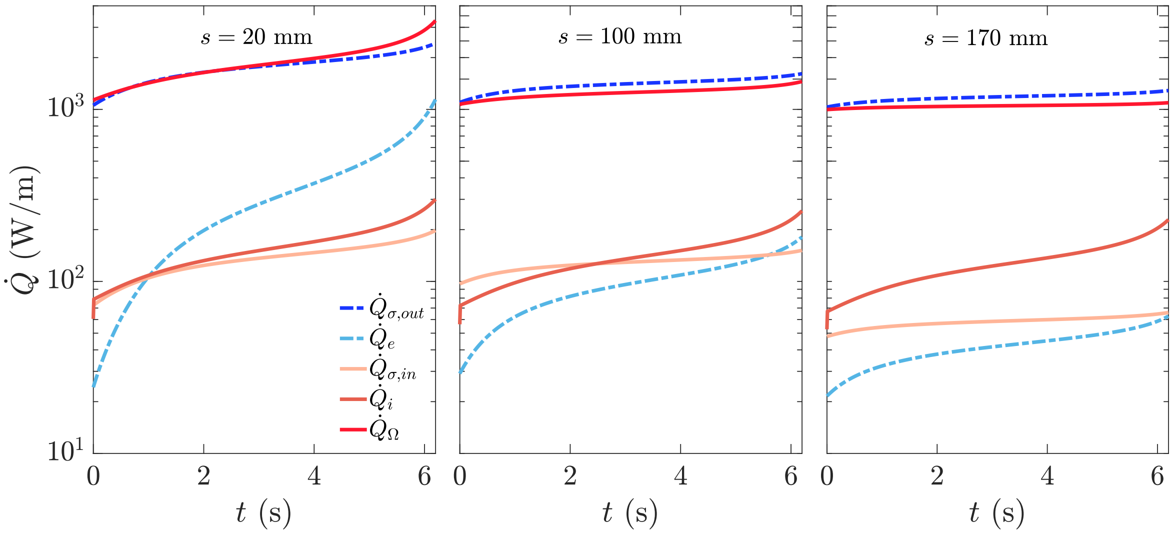

FIGURE II.17 – Power per meter provided to the filament over time at $s = 20$ mm, $s = 100$ mm and $s = 170$ mm. Red solid lines are the heating terms, blue dashed lines are the cooling terms. Conduction is not represented here.

II.6.3 Relative contributions of heat transfer mechanisms

The simulation enables to compute the various heat sources and sinks, and to assess the importance of each of them separately. Hence the heating mechanisms at play are displayed in figure II.17 at three different locations along the cathode over time. Conduction is subdominant, except near the extremities, and is not displayed here for clarity. A video illustrating time evolution of the various terms is available online [4].

Heating mechanisms are represented by solid red lines, cooling mechanisms by dashed blue lines. One can see that $\dot{Q}_\Omega$ and $\dot{Q}_{\sigma,out}$ are an order of magnitude greater than the other terms and account for the main dynamics of T_W. $\dot{Q}_\Omega$ increases with electron emission as can be seen in equation II.14, leading to a T_W instability at $s = 20$ mm. On the other hand, $\dot{Q}_i$ and $\dot{Q}_{\sigma,in}$ are rather homogeneous heating terms along the cathode length. The latter presents almost no variations over time, illustrating its weak effect on the runaway behaviour. $\dot{Q}_i$ causes a supplementary heating at $t = 0$ s that depends on V_b and n, which might be enough to trigger the runaway behaviourthrough the cathode-sheath instability, as explained in subsection II.6.1. Finally, $\dot{Q}_e$ being proportional to $T_W^2 \exp\left(-eW/k_B T_W\right)$, its heterogeneity is important and it provides an essential stabilizing effect, especially at the center of the cathode (around $s = 20$ mm), where the cathode temperature is the highest. This is particularly important at strong emission.

II.7 Conclusion

In conclusion, the regime of operation, and in particular the cathode current of a highly emissive cathode in a pre-existing plasma is shown to be accurately predicted from the knowledge of the temperature profile along the cathode. Spatially and temporally resolved temperature profiles have been obtained using an intensity comparison pyrometer, and the computation of the emitted current using Richardson's law is in excellent agreement with the measurements. The experimental results are also predicted as the solution of a detailed thermal balance, resulting in

---

[4] http://tinyurl.com/3p9n5xut

an integro-differential equation for the temperature field. It was found that, when immersed in a high density argon plasma column, the cathode experiences strong temperature heterogeneities mainly due to the inhomogeneous ohmic heating from thermionic current. This causes the emission current not only to be driven by the initial temperature of the cathode, but also by the bias of the cathode and the plasma properties. The original thermal model developed along the course of this PhD shows that the regime of operation is highly sensitive to the cathode heating from ion bombardment.

The operation in a stable low-emission regime depends on many positive or negative feedback loops. Here is a brief summary of the main destabilizing phenomena:

- Thermionic emission leads to more current flowing through the cathode, resulting in an enhanced heating at the cathode center (biased at the lowest potential V_b), which causes a higher thermionic emission and a heterogeneous temperature profile. This effect is more pronounced with a thinner filament.
- The density of the plasma grows with thermionic emission, resulting in a stronger ion bombardment and thus more heating. This is also true to a smaller extent with an increased electron temperature, since ion bombardment is proportional to $n\sqrt{T_e}$. This effect increases with a thicker filament as ion bombardment is proportional to the cathode surface.

On the other hand, the stabilizing feedback loops are the following:

- Dissipative radiation is the main source of heat losses for the cathode. As it grows with T_W^4, a rise in T_W results in a much stronger dissipation.
- Thermionic cooling may become an important cooling term at high emission, since this stabilizing effect is proportional to the thermionic current.
- The plasma potential decreases with thermionic emission, resulting in weaker ion bombardment. Even though it is a minor effect, it can modify slightly the frontier of the stability regime.
- Space-charge limited regimes may also reduce emission when $(V_b - \phi_p)/T_e$ is of order unity. For instance, this prevents the divergence of the emitted current at $V_b > -40$ V as I_b saturates for any value of I_h

The deep understanding of this simple cathode design opens the path to a wider use of cathodes as control tools in pre-existing plasmas at a minor cost. However the work reported herein found a limitation in the operational regime intrinsic to the cathode design in order to avoid damaging the tungsten filament. Although this design is an interesting alternative to costly and complex oxide cathodes at low emission, systematic studies at very large emission require the development of advanced cathodes, such as LaB_6. Their primordial advantage is a very low work function $W = 2.68$ eV [Gao+20], hence a strong emission at low temperature ($T_W = 1750$ K). The design of a LaB_6 cathode is a promising perspective, and is under reflection.

Finally a few first-order refinements of the numerical simulations have been suggested along the chapter presented herein. A github repository[5] containing the source codes for the simulation is available. Its goal is to share the new model with the plasma community and potentially improve it.

---

[5] https://github.com/FrancisPagaud/Emissive-Cathode-Model.git

CHAPITRE

III

PLASMA POTENTIAL CONTROL USING THERMIONIC EMISSION IN A MAGNETISED PLASMA

Le dispositif expérimental VKP-ICP est associé à l'utilisation de la cathode émissive afin d'étudier l'effet de l'injection d'électrons sur les propriétés plasma. L'accent est mis sur le contrôle du potentiel plasma, et une comparaison approfondie avec le modèle de Trotabas et Gueroult [Tro+22] est menée. Bien que ce modèle apporte une compréhension qualitative pertinente, les prédictions quantitatives sont un ordre de grandeur plus faibles que les variations observées du potentiel plasma. Des pistes d'amélioration sont discutées, telles que la modélisation de la gaine anodique ou des fluctuations basse-fréquences, présentant ainsi de nouvelles perspectives afin d'améliorer le modèle existant.

III.1 Cathode operation for plasma control

III.1.1 Rotation of a cold plasma column

In linear devices, strong drifts may arise and govern the plasma flow at a global scale [Rax05]. The electric $\mathbf{E} \times \mathbf{B}$ drift (see subsection I.2.4) or the diamagnetic drift, which originates in the plasma non-uniformity, may drive primarily the particles flow. Besides, magnetic drifts may occur for a non-uniform external magnetic field. For instance, the gradient or the curvature of the magnetic field lead to supplementary drifts. It is all the more likely to impact significantly the plasma flow for large or complex plasma devices, like tokamaks or stellarators. In the VKP-ICP case, such drifts will be neglected since the relative variations in magnetic field over the device is lower than a few percent. Besides, plasma non-uniformities also induce a diamagnetic drift that may affect the plasma flow. Note that except for the $\mathbf{E} \times \mathbf{B}$ drift, these motions are opposite for electrons and ions, often leading to the polarisation of the plasma and the generation of a supplementary electric field. All these contributions may influence the rotation of the plasma column, and a brief analysis in the present case will be drawn here.

The VKP-ICP plasma is approximated by a two-fluid model in cylindrical coordinates (r, θ, z). The global momentum of the plasma being mostly governed by the ions, their momentum equation will be studied for a preliminary analysis. An external electric field $\mathbf{E}$ and a magnetic field $\mathbf{B}$ along $\mathbf{z}$ are applied. Under the stationary assumption and in absence of collisions, the simplified momentum equation reads

$$\mathbf{0} = -e\nabla\left(nT_i\right) + ne\mathbf{E} + ne\mathbf{v_i} \times \mathbf{B} \tag{III.1}$$

The ion temperature is assumed to be homogeneous, and the crossed product with $\mathbf{B}$ is applied to equation III.1. Then, one can derive the ion velocity along the azimuthal direction $v_{i,\theta}$

$$v_{i,\theta} = \frac{E}{B} - \frac{T_i}{n}\frac{\partial n/\partial r}{B} = v_{\mathbf{E}\times\mathbf{B}} + v_{d,i} \tag{III.2}$$

with $v_{d,i}$ the ion diamagnetic velocity. This model could be refined by including the effect exerted by the drag on ions, *i.e.* the effect of collisions with neutrals and ionisation. It would only result in a reduced ion velocity by a factor $1/K = 1/\left(1 + \left(\nu_{in} + \nu_{iz}\right)^2/\omega_{c,i}^2\right)$ [Dés+21].

For typical values of $E \simeq 50\ \mathrm{V\cdot m^{-1}}$, $B \simeq 200$ G, $T_i \simeq 0.2$ eV, $n \simeq 2\times10^{18}\ \mathrm{m^{-3}}$ and a radial gradient $\nabla n \simeq 4\times10^{19}\ \mathrm{m^{-4}}$, the orders of magnitude for $\mathbf{v}_{\mathbf{E}\times\mathbf{B}}$ and $\mathbf{v}_{d,i}$ are the following

$$v_{\mathbf{E}\times\mathbf{B}} \simeq 2500\ \mathrm{m\cdot s^{-1}} \quad \text{and} \quad v_{d,i} \simeq 200\ \mathrm{m\cdot s^{-1}} \tag{III.3}$$

Overall, the $\mathbf{E} \times \mathbf{B}$ governs the rotation of the plasma column in the VKP-ICP case. The ordering $v_{\mathbf{E}\times\mathbf{B}} \gg \mathbf{v}_{d,i}$ can be generalized to many cold magnetised linear plasma devices since T_i is weak. That is why a fine control of the local electric field allows to tune the plasma flow. The acute control of the magnetised plasma medium being at the core of industrial applications, the stakes of plasma potential tailoring are huge. Such a perspective is far-reaching and has been a major topic of interest.

III.1.2 Plasma potential profile tailoring using biased end-rings

The effective control of plasma potential profile was already addressed a few decades ago using biased cold electrodes. It has been of prime interest in fusion devices, where electrodes were found to create a sharp transport barrier at the plasma edge [Tay+89]. Using this technique, an efficient transition from the low-density L-mode to the high-density H-mode was observed. H-mode enables an enhanced particles and energy confinement at the plasma core, which is essential

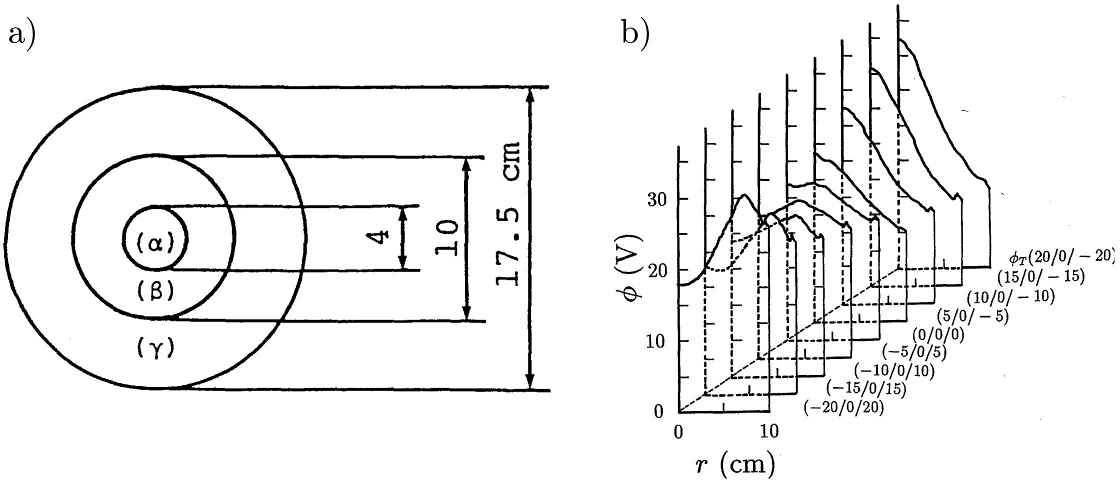

FIGURE III.1 – *a)* Biased-end concentric rings implemented in a linear device. *b)* Resulting plasma potential profiles depending on the rings bias. Taken from [Tsu+91].

for reaching ignition. The transport barrier originates in the development of a strong **E** × **B** shear layer at the plasma outer edge. This shear prevents the large-scale growth of turbulent eddies, stabilizing turbulence and reducing particles transport to the wall [Bur97; Oos+03].

In linear devices, biased-end rings have been found to tailor plasma potential (see figure III.1), but the knowledge of the physical underlying mechanisms remained elusive at the time [Tsu+91; Yos+99].

Simple theoretical models were derived to predict the modification of ϕ_p using a positively biased electrode [Baa+20] or a negatively-biased electrode [Liz+20], *i.e.* a cathode. The interpretation relies on the computation of the incoming charge fluxes at the cathode and the grounded walls. Then the core plasma potential depends on the electrode bias, the plasma properties and the electrode dimension (see figure III.2a) and reference [Tro+22]). As the ion saturation current at the cathode increases, the plasma potential is modified significantly by the voltage bias V_b. This dependency is captured by the non-dimensional parameter χ, which will be presented in subsection III.2.1. The local Ohm's law can be used for a complete mapping of the plasma potential distribution [Gue+19], as shown in figure III.2b). Indeed, the local electric field can be computed for various ratios of the anisotropic electrical resistivities $\eta_\perp/\eta_\parallel$ (see subsections I.2.5 and III.2.1). The topic gained recent interest through the derivation of new analytical models aiming at a quantitative prediction of the plasma potential using cold electrode [Liz+20], complemented by extensive experimental measurements [Gue+24] and in-depth numerical investigations [Tro22].

Actually, the consequences of biased-end electrodes on the plasma behaviour are more complex than a mere effect on the local electric field. Applying a particle flux to the electrode and influencing the plasma potential distribution affects all the plasma properties and its global stability as well [Des+16]. The plasma confinement and the development of transport barriers have been enhanced using positively-biased electrodes in linear devices for instance [Sak+93; Shi+02]. The low-frequency fluctuations are affected too: the increased radial electric field often leads to a stronger radial shear [Tsu+91], exciting flute modes [Yos+99], drift waves [Sak+93; Yos+99; DuB+12] or Kelvin-Helmholtz instability [Tho+03]. Hence, the mentioned instabilities can be suppressed by using appropriate end-biased electrodes [Tho+05], leading to an improved plasma control.

This fine plasma flow control is required to design advanced mass separation technologies [Leh73; Zwe+18] for nuclear spent fuel reprocessing and rare earth recycling [Gue+18; Liz+21a]. This technological advance would provide a versatile and efficient recycling technique. Finally, basic laboratory plasmas would benefit greatly from an improved plasma flow control. The past studies on the plasma rotation on low-frequency instabilities [Vin+22; Agg+23] and turbulence [Tha+14] could be extended to new regimes.

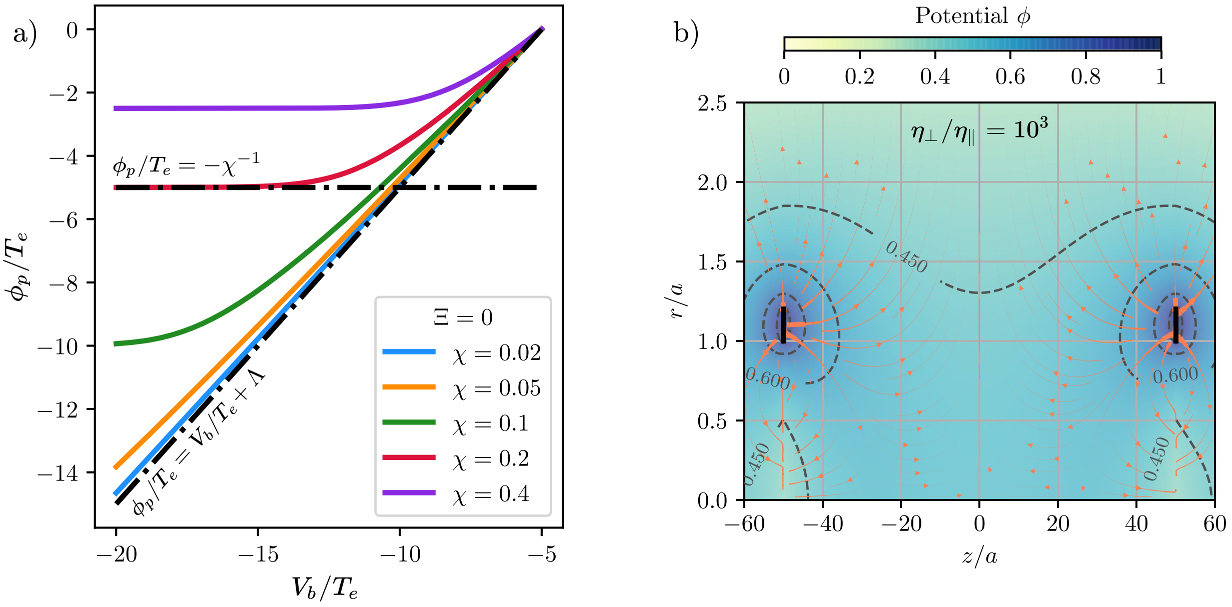

FIGURE III.2 – *a)* Plasma potential as a function of the cathode potential for various plasma parameters in absence of emission ($\Xi = 0$). Taken from [Tro+22]. *b)* Plasma potential distribution map from positively biased ring without emission. Coral lines represent current density streamlines. Taken from [Gue+19].

III.1.3 An innovative approach to enhanced plasma control

A limitation of cold cathodes is the saturation of the collected ion current. Once saturation occurs, the plasma properties are no longer modified by a lower bias at the cathode. An advanced step in plasma control is the use of emissive cathodes. The ion saturation current is then supplemented by an important thermionic electron flux from the cathode to the plasma. Therefore, the impact of cathodes on the plasma behaviour is significantly improved, thus extending greatly its field of application. The incoming ions and the emitted electrons at the cathode result in an inward charge flux from the cathode perspective.

A recent increasing interest of emissive cathodes has been observed because of its high effectiveness on plasma control. The empirical control of the plasma flow [Dés+21], the shaping of the plasma potential profile [Jin+19; Liz+21c] and plasma properties [Van+19] via emissive cathodes have been evidenced lately. Moreover, promising analytical [Tro+22] and numerical [Pou19] models emphasize the significant capability of plasma control using emissive cathodes. The implications on the waves and instabilities are wide, as the plasma potential profile and the plasma density gradients are both modified at strong emission. Intensification of electron-ion hybrid instability [DuB+14], spoke generation [Vin21], drift-Alfvén modes induced turbulence [Kar+22] or even Kelvin-Helmholtz suppression [Vin21] were shown to occur in strongly-emissive regimes.

In summary, the use of an emissive cathode as a new external control parameter is a recent and promising topic of interest. However, the lack of fundamental understanding of plasma potential control using an emissive cathode hinders the wide-spreading of such a powerful tool. Recent studies successfully tackled this issue in a low-emission regime in the LAPD experiment, which is ignited by a thermionic discharge [Jin+19; Van+19]. The extension to a radio-frequency magnetised linear device at high emission would be a significant contribution to the plasma community.

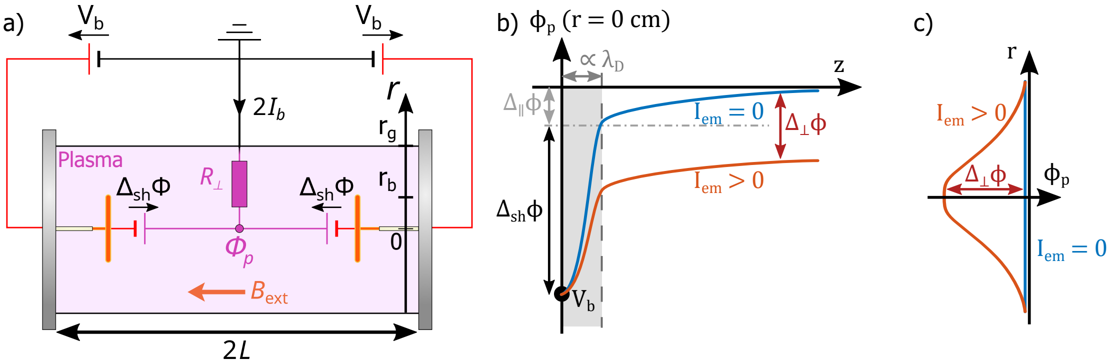

FIGURE III.3 – *a)* Geometry of the model and of the equivalent electrical circuit. *b)* Schematic longitudinal and *c)* radial potential drops for a cold and a hot biased cathode.

The following chapter aims at investigating the effect of strongly-emissive cathodes on high-density weakly magnetised plasma columns by combining an analytical and an experimental approaches on VKP-ICP. The main goal is to provide a robust physical interpretation and a quantitative predictive tool for plasma potential control using an emissive cathode. Firstly, the discharge model of the plasma in interaction with an emissive cathode described by Trotabas and Gueroult [Tro+22] is presented in section III.2. Secondly, a detailed experimental investigation and an in-depth confrontation with the analytical model are shown in section III.3. It is found that the modelling provides robust physical arguments to interpret and forecast qualitatively the behaviour of the obtained results, while not being accurate enough for quantitative predictions. Sources of discrepancies between the model and the experiments are addressed in section III.4, which provides material for future improvements.

The following chapter results from a collaboration with Renaud Gueroult and Baptiste Trotabas, whose contributions were highly valuable for understanding and adapting the plasma potential control model, as well as analysing the experimental results.

III.2 Analytical model for plasma potential control via electron injection

III.2.1 Impact of cathodes on a cold magnetised plasma column

The goal of using a cathode in a magnetised radio-frequency plasma is to tailor finely the plasma potential spatial distribution despite the above-mentioned challenges. In the present chapter, I focus on the quantitative comparison of a plasma potential control model to experimental measurements using an emissive cathode. The analytical model will be presented thoroughly in the following section.

The model configuration is a symmetrical cylinder of length $2L$, with full disks cathodes at both bases of the cylinder, as shown in figure III.3a), and described in detail in the works of Trotabas and Gueroult [Tro+22]. The cathodes of radius r_b and surface $\mathcal{S}$ are negatively biased at V_b (noted ϕ_e in reference [Tro+22]). The external cylindrical vessel of radius r_g is grounded, while the end caps are insulating for $r_b < r < r_g$. Therefore, the ion current I_i collected at the cathode is balanced by an electron current collected at the vacuum vessel walls. In the case of hot cathodes, the supplementary thermionic current injected I_{em} is balanced by an increased electron flux at the walls. As a reminder, the total current flowing from the cathode to the plasma I_b is the sum of the thermionic emission and the electron and ion contributions:

$$I_b = I_{em} + I_i - I_e \tag{III.4}$$

All in all, the current I_b is an experimental parameter that drives the charge fluxes in the plasma. The model aims at computing the spatial distribution of the resulting plasma potential by solving the local Ohm's law, given the anisotropic electrical conductivities and the imposed electron and ion fluxes at the cathodes [Gue+19].

As mentioned in subsection I.2.5 for the VKP-ICP case, the perpendicular conductivity is mainly due to ion-neutral collisions, while the parallel conductivity is attributed to magnetised electrons. The general expression for plasma conductivities is complex, but the combination of the collision rates from equation I.11 and the resistivities I.22 yields an order of magnitude:

$$\eta_\parallel = \frac{m_e}{e^2}\left(\langle v_e \sigma_{ei}\rangle + \langle v_e \sigma_{en}\rangle \frac{n_n}{n}\right) \quad \text{and} \quad \eta_\perp = \frac{1}{n m_i \langle \sigma_{in} v_i\rangle}\frac{B^2}{n_n} \tag{III.5}$$

leading to the ratio $\eta_\perp/\eta_\parallel$ which is an essential parameter of the model. Note that even though the ratio $\eta_\perp/\eta_\parallel$ from equation III.5 yields a relevant order of magnitude, detailed formulas for the classical resistivities $\eta_{\perp,comp}$ and $\eta_{\parallel,comp}$ (not shown here) that take into account all types of particle collisions [Son+01 ; Rax+19] are used for the accurate computation of the local Ohm's law.

For clarity, let us address schematically the plasma potential distribution arising from a cathode immersed in a plasma [Gue+19 ; Tro22] (see figures III.3b) and c)). The plasma potential in presence of the floating electrodes is assumed to be homogeneous and equals to $\phi_{p,0} = 0$ V as a first approximation. When the electrode is biased, a sheath surrounds the cathode and screens the cathode potential over a few Debye lengths. The sheath potential drop is noted $\Delta_{sh}\phi$. Then, the enforced inward charge flux due to thermionic emission, *i.e.* $I_{em} > 0$, leads to a radial potential drop $\Delta_\perp\phi$. Because of the magnetically-induced anisotropy in transport properties, the longitudinal potential drop $\Delta_\parallel\phi$ differs largely from $\Delta_\perp\phi$. In magnetised regimes where $\eta_\perp/\eta_\parallel \gg 1$, the anisotropy leads to a small longitudinal potential drop with respect to the other potential drops $\Delta_\parallel\phi \ll \Delta_{sh}\phi, \Delta_\perp\phi$. Hence, $\Delta_\parallel\phi$ will be considered negligible from now on. However, note that in strongly emissive regimes, $\Delta_\parallel\phi$ can become predominant, questioning the assumption of plasma potential homogeneity along the magnetic field lines [Tro+22]. In the works reported herein, thermionic emission is not high enough for this effect to be significant. Ultimately, the model comes down to the simple circuit model shown in figure III.3. The applied bias V_b is equal to the plasma potential ϕ_p minus the voltage drop across the sheath $\Delta_{sh}\phi$. A detailed ordering of the three potential drops $\Delta_{sh}\phi$, $\Delta_\parallel\phi$ and $\Delta_\perp\phi$ in the VKP-ICP experimental configuration will be provided in subsection III.3.1.

The role of the cathode is to impose an inward charge flux ($I_b > 0$), *i.e.* an outward radial electron flux or an inward ion flux across the plasma column. Since electrons are magnetised, the cross-field transport is mainly ensured by ions. Therefore, if one imposes a radial current I_b flowing from the plasma core to the wall, the resulting plasma potential drop is computed as $\Delta_\perp\phi = R_\perp^{(model)} I_b$, where

$$R_\perp^{(model)} = \int_{r_b}^{r_g} \frac{\eta_{\perp,comp}(r)\mathrm{d}r}{2\pi L r} \tag{III.6}$$

is the perpendicular resistance between the external electrode radius and the grounded wall over the plasma length L.

In the case of strongly-biased cold cathodes, I_{em} and I_e fall to 0 and the total current I_b reaches the ion saturation current I_{is}. I_b depends on the plasma properties n and T_e, and the cathode radius r_b. A larger cathode would result in a much more important incoming ion flux, and ultimately a significant modification of the plasma potential. Hence, the potential drop at the plasma core normalised by the electron temperature T_e reads $R_\perp^{(model)} I_{is}/T_e \propto r_b^2 \ln\left(r_g/r_b\right)$. This quantity is defined as $1/\chi$ in reference [Tro+22]. Then the maximal potential drop would be reached for $r_b = e^{-0.5} r_g$, meaning that the electrode needs to be large for an efficient plasma potential control. That is why large concentric biased-end rings are often used to achieve plasma potential tailoring in linear devices [Tsu+91 ; Gue+24]. However, large sizes could be intrusive and represent a practical issue for designing and operating such electrodes.

In the case of emissive cathodes, the ion saturation current I_{is} is supplemented by the injected current I_{em}. Then, the current crossing the plasma radius increases from I_{is} to $I_{em} + I_{is}$, and the normalised potential drop at the plasma core increases to $R_{\perp}^{(model)} \left(I_{is} + I_{em}\right)/T_e$. One can introduce the non-dimensional parameter $\Xi = I_{em}/I_{is}$, which is essential to assess the role of the cathode emissivity. So in comparison with the cold cathode case, a significant potential drop can be induced using a small cathode, enabling an efficient and local plasma potential control.

In summary, the model relies on four major assumptions:

- The plasma column is magnetised, *i.e.* $\eta_{\perp}/\eta_{\parallel} \gg 1$;
- With a floating electrode, the plasma is quiescent and its potential is homogeneous in space at a value $\phi_{p,0}$ assumed to be 0 V ;
- The plasma potential is primarily driven by the imposed cross-field current I_b. It yields a potential drop $R_{\perp}^{(model)} I_b$ while the thin cathode sheath is adjusted to match ϕ_p and V_b ;
- No secondary electron emission is considered, which is often valid in low-temperature cold argon plasmas [Tol14 ; Kon92].

Although this model has only been applied to a plasma homogeneous in density and temperature so far [Tro+22], it can be extended to the non-homogeneous case via equation III.6, as done in the work presented herein.

Three dimensionless parameters allow to infer the regime of operation [Tro+22]. For given geometry and plasma parameters, two dimensionless control parameters are set by the properties of the biased electrode: the voltage bias normalised to the electron temperature V_b/T_e, and the normalised thermionic emission $\Xi = I_{em}/I_{is}$, which is controlled by the electrode temperature. Then, the already mentioned χ parameter depends mainly on the cathode and plasma device geometry.

III.2.2 Effective plasma potential control using an emissive electrode

The model underlines three regimes of operation depending on the dimensionless parameters presented in figure III.3a).

Non-saturated regime: This regime is observed for a non-zero electron current originating from the plasma and collected at the cathode, *i.e.* at a weak cathode bias. Since $V_b < \phi_p$, the ion current is assumed to be the ion saturation current I_{is}. Besides, in absence of virtual cathode, the thermionic current can be computed using Richardson current. Overall, we have $I_b = I_{is} + I_{em} - I_e < I_{is} + I_{em}$. In this regime, the plasma potential ϕ_p follows the applied bias to the cathode shifted by a factor ΛT_e, with Λ the sheath parameter $\Lambda = \ln\left(\sqrt{2m_i/(\pi m_e)}\right)$ previously introduced in subsection I.2.1. The plasma potential then reads $\phi_p = V_b + \Lambda T_e$.

Saturated regime: It is observed at stronger cathode bias, when the current I_b reaches $I_{is} + I_{em}$. Then, the potential drop across the plasma column $\Delta_{\perp}\phi$ should be equal to $R_{\perp}^{(model)} I_b$ for any cathode bias V_b. In other words, the radial plasma potential drop is

$$\Delta_{\perp}\phi = \phi_p^{sat} = -R_{\perp}^{(model)} I_b = -(1+\Xi) R_{\perp}^{(model)} I_{is} \qquad \text{(III.7)}$$

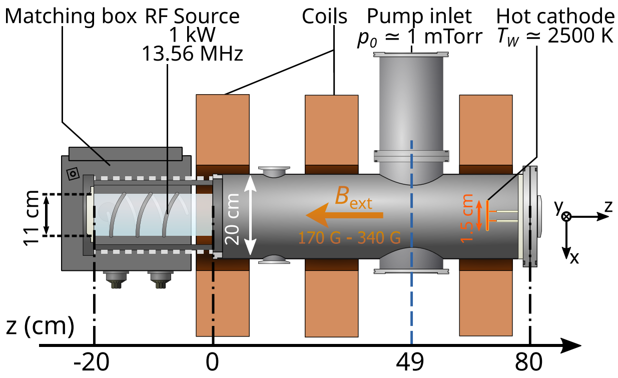

FIGURE III.4 – Experimental arrangement for the present chapter.

To be more accurate, this regime occurs at $V_b < \phi_p^{sat} - \Lambda T_e$ [Tro+22]. A cathode voltage bias V_b below the critical value $\phi_p^{sat} - \Lambda T_e$ would only increase the sheath voltage drop $\Delta_{sh}\phi$. This regime is of particular interest because it sets the plasma potential value through the experimental parameter Ξ. The most important feature of the model is that thermionic emission offers a larger range of attainable plasma potential values.

Virtual cathode: A third regime is reached past a critical value of thermionic emission, when a virtual cathode forms in front of the cathode (see section II.2 and references [Ye+00; Pou19]). This is expected to occur for values of Ξ of the order of 100 or at weak cathode bias, as discussed in subsection II.6.1.

If one considers a homogeneous plasma column and experiments where $1 \ll \Xi \ll 100$, the saturated value of the plasma potential scales as

$$\phi_p^{sat} \propto \frac{-1}{\sqrt{T_i m_i}} \frac{B^2}{n_n} \frac{I_{em}}{n} \tag{III.8}$$

The purpose of the present chapter is to confront the above predictions with the extensive experimental observations I conducted on the VKP-ICP experiment.

III.3 Experimental plasma potential control via thermionic emission

III.3.1 Experimental configuration

The tungsten emissive cathode, presented in section II, is placed at the center of the plasma column at the opposite end relative to the source, *i.e.* at $z = 70$ cm (see figure III.4). The two copper rods are inserted through a 40 mm large hole in a DN 200 ISO-K flange covered by a insulating BN disk of 197 mm in diameter. The operation principle is the same as the one presented in subsection II.2.

Thermionic emission I_{em} is estimated using the averaged temperature $\overline{T_W}$ from the measurement of the cathode resistance $V_h/I_h = \rho_W l_W/(\pi r_W^2)$, corrected in temperature homogeneity (see subsection II.6.2). The cathode temperature increasing because of plasma-cathode interactions, $\overline{T_W}$ was always measured at the end of the plasma shot.

The corrected cathode temperature allows to compute the maximum emitted current I_{em} from Richardson's law. We consider that I_{em} is a correct estimate of the emitted current as long as no virtual cathode is present, as discussed in subsections II.5.2 and II.6.1.

Configuration	I	II	III
Magnetic field B (G)	170	240	340
RF power P_w (kW)	1	1	1
Neutral pressure p_0 (Pa)	0.13	0.26	0.13
B^2/n_n (vs config. I)	1	1	2
V_b/T_e	10 & 15	13 & 20	13 & 20
$\chi = T_e/(R_\perp^{(model)} I_{is})$	750	650	160
$\Xi = I_{em}/I_{is}$	[1 ;30]	[1 ;30]	[1 ;30]

TABLE III.1 – Control parameters for the three investigated configurations.

The experimental set-up is considered as a simple approximation of one half of the symmetrical model. A non-uniform plasma created by the RF source, which is not considered in the analytical model, fills the cylindrical volume. The dependency on the intensity of the magnetic field B, the neutral density n_n (or equivalently the neutral pressure), and the thermionic current I_{em} indicated by equation III.8 was investigated experimentally by studying the three configurations described in table III.1. The high χ values ensure that the operation is in the saturated regime when $V_b < \phi_p - \Lambda T_e \simeq -40$ V. For each configuration, the influence of thermionic intensity on the plasma parameters profiles was assessed for two values of the voltage bias, namely $V_b = -40$ V and $V_b = -60$ V.

As discussed in subsection I.2.5, the $\eta_\perp/\eta_\parallel$ ratio ranges between 10^2 and 10^3. The assumption $\eta_\perp/\eta_\parallel \gg 1$ is guaranteed in the present experiment. Besides, the values of the magnetic field were chosen below 400 G such that the plasma remains essentially quiescent [Vin21], while the electrons are strongly magnetised. Given the orders of magnitude at stake, the radial potential drop $\Delta_\perp\phi$ is expected to be about a few volts, meaning that the model forecasts the ordering $\Delta_\parallel\phi \ll \Delta_\perp\phi \ll \Delta_{sh}\phi$.

Finally, the non-uniformity of the plasma density and temperature with regards to electron injection were measured and considered for a relevant comparison to the analytical model. Realistic plasma properties profiles, highly dependent on I_{em}, were used for numerical computation and comparison to the analytical model.

III.3.2 Drive of the plasma potential in strongly emissive cases

The evolution of the plasma potential ϕ_p as a function of the electrode bias V_b, for a cold and a hot cathode is shown in figure III.5a) for configuration III (1 mTorr, 340 G). The plasma potential at the center of the plasma column, $\phi_p(x = 0)$, and at the outer edge, $\phi_p(x = r_g = 10\text{ cm})$, are displayed. No evolution of the plasma potential with the voltage bias is observed when the cathode is cold, *i.e.* a stronger electrode bias leads to an equal increase of the voltage drop across the cathode sheath $\Delta_{sh}\phi$. It corresponds to the saturated regime. Note that in this configuration, the plasma potential at the outer edge of the plasma column is close to ground. In contrast, when the thermionic cathode is strongly emissive, the plasma potential can be efficiently controlled by the electrode bias V_b, up to typically -45 V, before reaching a plateau. Surprisingly, both $\phi_p(x = 0)$, and $\phi_p(x = r_g)$ are affected by the electrode voltage bias V_b, and a large anode sheath of a few T_e is observed at the outer edge of the plasma column.

One may notice a radial voltage drop in absence of thermionic emission. This spontaneous

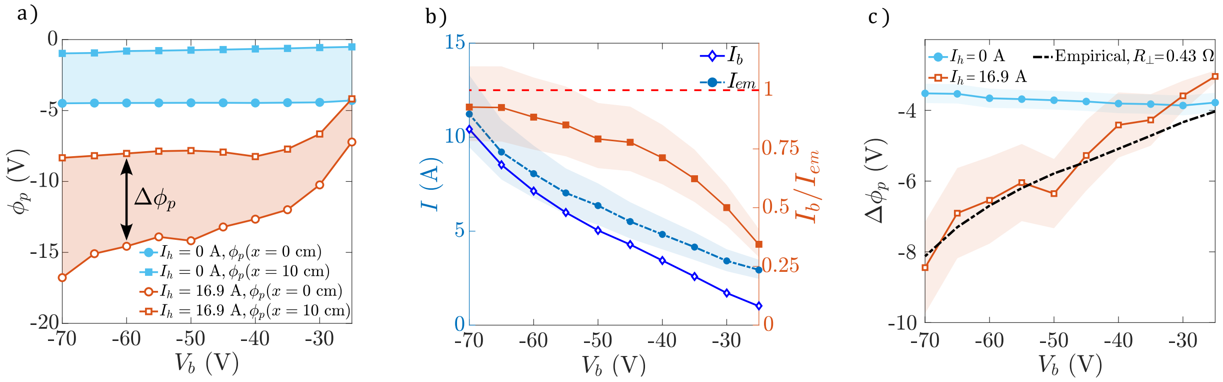

FIGURE III.5 – *(a)* Evolution of the plasma potential in configuration III as a function of the electrode bias V_b for a cold (blue) and a hot highly emissive cathode (red) at the center of the plasma column (open circles) and at the outer edge, $x = 10$ cm (full squares). *(b)* Evolution of the current at the cathode I_b (blue diamonds) and the thermionic current I_{em} (blue circles) as a function of V_b. The ratio I_b/I_{em} is in red squares (right axis). *(c)* $\Delta\phi_p$ for the cold cathode (blue circles) and the hot cathode (red squares) cases as functions of V_b. The dotted black line is the empirical potential drop $R_\perp I_b$.

plasma potential distribution is caused by the device geometry and the experimental conditions (see subsection I.3.7). But it is not considered by the simple analytical model that assumes a homogeneous initial plasma potential distribution. From now on, the apparition of a radial potential drop driven by the current I_b will be considered as a linear effect that is superimposed to the initial plasma potential profile ($I_b = 0$ A) for a relevant model-experiment comparison.

Then, let us describe the main features of the anode sheath. Its spatial structure was probed inserting an emissive probe along the vertical axis y, with a home-made grounded aluminium flange filling the DN 100 access port at $y = -r_g$, and is shown in figure III.6a) for configuration III. This scan exhibits a high level of reproducibility, and shows that the anode sheath thickness seems lower than a few hundreds of microns. No accurate measurement can be provided as the emissive probe is accurate up to 500 μm. Moreover, the probe shaft is strongly intrusive and could affect the bulk plasma potential outside the sheath. The error bars for ϕ_p represent the standard deviation, and they are enhanced at the wall vicinity. The power spectral density (PSD) for ϕ_p (see figure III.6b)) reveals indeed that the plasma potential kHz fluctuations in the plasma bulk increase at the wall.

In the remainder of this chapter, we will use the notation $\phi_p(x = r_g)$ to describe the value of the plasma potential at the exit of the anode sheath, *i.e.* the value defined over $-9.95 < y \leq -9.8$ cm in figure III.6a). The anode sheath is not considered by the analytical model drawn in section III.2 [Tro+22], and its characteristics will be discussed in subsection III.4.2. Since the model does not account for the existence of an anode sheath, a new notation $\Delta\phi_p = \phi_p(x = r_g) - \phi_p(x = r_b)$ will be used from now on. $\Delta\phi_p$ is a good indicator of the radial potential drop due to the current I_b, and its analysis will be conducted in the rest of the chapter.

$\Delta\phi_p$ is analysed as the voltage drop $R_\perp^{(model)} I_b$ accordingly to the analytical model. The increase of the cathode current I_b with the absolute value of the cathode bias $|V_b|$ is shown in figure III.5b), and is mainly due to an increase of the cathode temperature. Indeed, as shown in subsection II.6.1, the cathode temperature depends on V_b through plasma-cathode interactions. For each value of V_b, the Richardson current I_{em} is computed using the corrected $\overline{T_W}$ value as explained in subsection III.3.1, and shown in figure III.5b).

The evolution of I_b/I_{em} is displayed in figure III.5b) (rightmost scale) and is a reasonable proxy

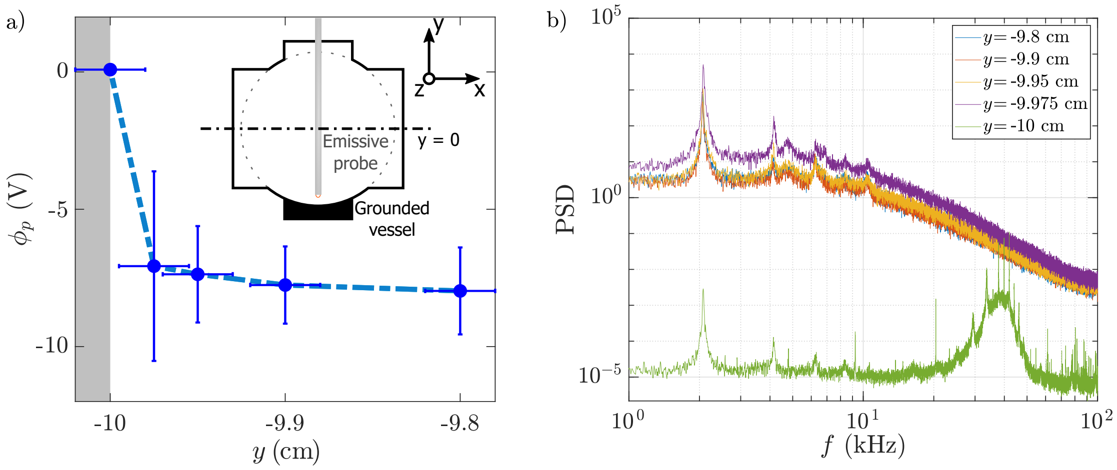

FIGURE III.6 – *a)* ϕ_p at the wall in configuration III, $V_b = -45$ V and $I_b = 4.2$ A. The wall is symbolised by the grey zone at $y < -10$ cm. *b)* Power spectral density (PSD) of the ϕ_p fluctuation spectra.

of the nature of the regime. When $I_b/I_{em} < 1$, the regime is non-saturated,*i.e.* a strong electron current is drawn from the plasma. The saturated regime should correspond to $I_b/I_{em} = 1 + 1/\Xi \simeq 1$. For the present experiment, a saturated regime is observed for voltage biases below -50 V. The transition from a non-saturated to a saturated regime with V_b is readily observed on the evolution of the plasma potential. Nonetheless, as proven in chapter II, the cathode temperature increase with the voltage bias $|V_b|$ results in an increase of Ξ, therefore a direct comparison with the model predictions is not straightforward. As V_b and I_b are not independent, the saturated regime is not directly associated to a constant plasma potential regardless of V_b, contrarily to the ideal analytical model [Tro+22].

A refined Ξ calculation, accounting for the density and electron temperature increase with I_b, previously discussed in subsection II.5.4, has been conducted. The ion saturation current is measured in configuration III in the cold and floating cathode case ($V_b = -16$ V). The core plasma density and electron temperature were measured for the three following cases: $V_b = -16$ V and $I_b = 0$ A, $V_b = -40$ V and $I_b = 5$ A, $V_b = -60$ V and $I_b = 8$ A. It enabled to compute the evolution of the factor $n\sqrt{T_e}$ along the scan in V_b presented in figure III.5. It allowed to quantify the I_{is} growth according to the ion saturation current equation II.3, represented with black squares in figure III.7 (magnified 10 times for clarity). A second order polynomial fit is applied on these experimental values to compute I_{is} empirically for any cathode bias in the range $[-70\text{ V}; -16\text{ V}]$ (black dashed line). In addition, the thermionic current I_{em}, already discussed previously, is shown in blue circles. The I_{is} calculation leads to the estimate of $\Xi = I_{em}/I_{is}$, displayed in orange diamonds in figure III.7 (associated to the right scale), with an error margin of about 20%. Ξ lies between 10 and 30 in the present experiment, ensuring $\Xi \gg 1$.

Finally, the evolution of $\Delta\phi_p$ with V_b is shown in figure III.5c) for the cold and hot cathode cases. Error bars account for ϕ_p standard deviation. As previously mentioned, $\Delta\phi_p$ remains constant in the cold cathode case, while it strongly increases with $|V_b|$ for the emissive case. This latter situation is compatible with a voltage drop $R_\perp I_b$, with an empirical value $R_\perp = 0.43\ \Omega$ resulting from the best linear fit. The expected value for $R_\perp$ ranging from 0.1 Ω to 1 Ω, this empirical approach apparently yields a positive preliminary result.

The non-uniformity of the plasma properties and the dependence on experimental parameters such as B and p_0 are key parameters to assess the relevance of the model. Their influence will be

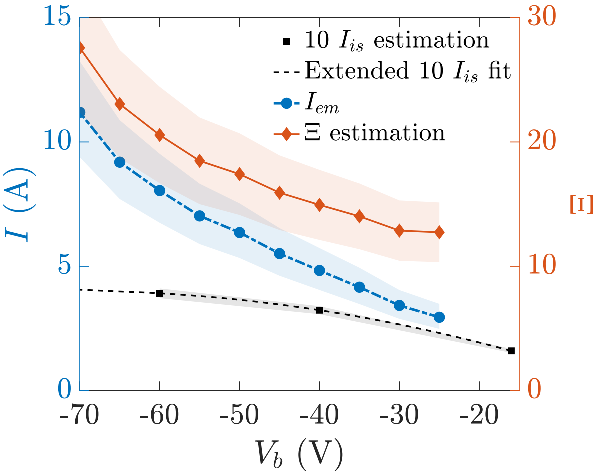

FIGURE III.7 – Left scale: I_{em} and I_{is} (magnified 10 times) estimations as a function of V_b for the experiment reported in figure III.5. Right scale: estimation of the Ξ factor as a function of V_b.

measured and discussed in the following subsections.

III.3.3 Spatially-resolved plasma parameters

A systematic approach is adopted for spatially-resolved measurements. Single measurements are conducted for each plasma configuration and probe position, and data are collected during the last second of the plasma shot. The spatial evolutions of the plasma parameters in configuration II along the x axis, for increasing values of the cathode temperature (and thus increasing values of the emitted current) are shown in figure III.8. The grey area corresponds to the location of the cathode at the plasma core.

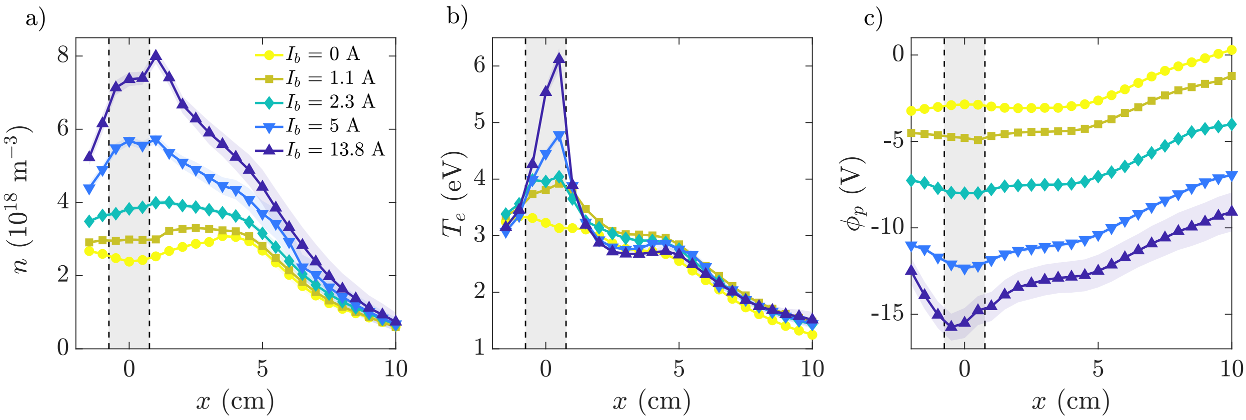

FIGURE III.8 – Plasma properties in configuration II and V_b = -60 V for various values of I_b. The grey area represents the shadow the emissive cathode.

The emitted current has a strong influence on the plasma density profile and a minor influence on electron temperature, as previously discussed for configuration I in figure II.11. The plasma density increase is due to the presence of energetic primary electrons accelerated through the cathode sheath $\Delta_{sh}\phi = |\phi_p - V_b|$, which is larger than the ionization energy for argon $\mathcal{E}_i = 15.8$ eV. The broader density profile is presumably due to ambipolar diffusion. On the other hand, hot primary electrons are strongly confined in the cathode shadow. Collisional heating between the energetic emitted electrons and electrons from the ambient plasma causes a quick thermalization at $|r| < 1$ cm.

A clear influence of electron emission is also observed on the plasma potential ϕ_p, similarly to figure III.5. However, V_b is set constant here, contrarily to figure III.5, while the injected current I_b is variable. Once again, most of the plasma potential drop is observed at the edge of the plasma column, with the creation of a large anode sheath, that reaches $3T_e \approx 10$ V. A closer investigation of the plasma potential profile also reveals that the voltage drop across the plasma column $\Delta\phi_p$ increases with cathode emission. The radial profile of the plasma potential profile is also strongly affected, and in particular the sign of $\partial\phi_p/\partial r$ at $r \leq 2$ cm reverses when thermionic emission increases, leading to a reversal of the plasma rotation [Dés+21].

The analysis of the electron temperature increase is supported by $I - V$ uncompensated Langmuir scans performed at the plasma core for configuration I and $V_b = -60$ V (see figure III.9). The top left a) panel exhibits measurements bounded between -60 V and 10 V, while the top right panel b) focuses on voltages V_{Lang} ranging from -100 V to -10 V. The electron current in logarithmic scale and the electron temperature linear fits are displayed in the bottom left panel c). The resulting electron temperature as a function of I_b are shown in the bottom right panel d).

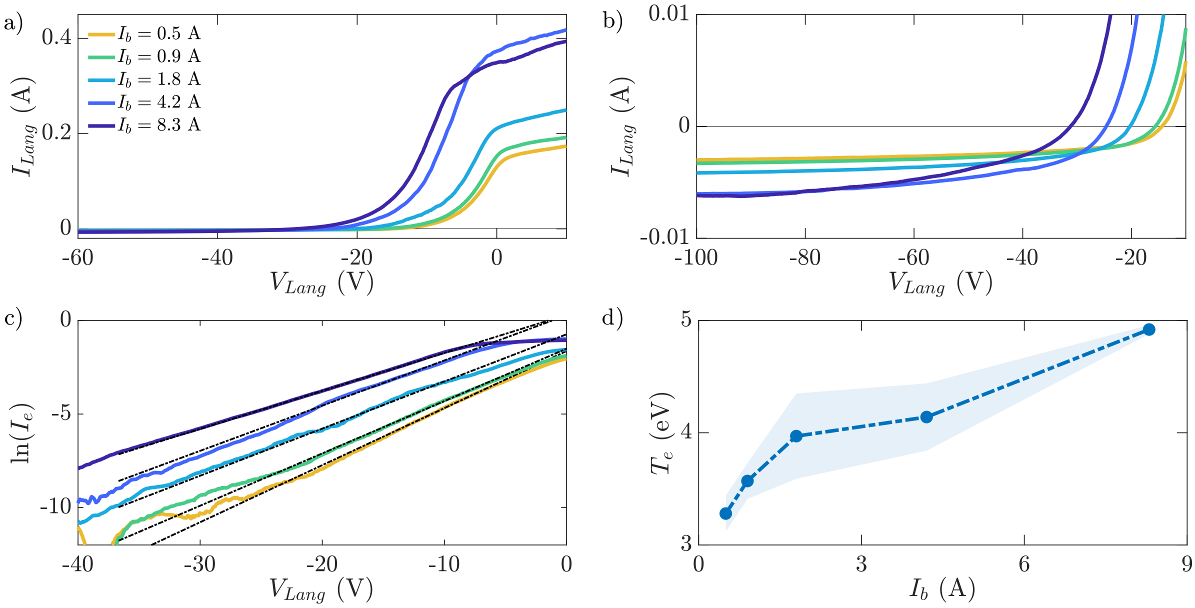

FIGURE III.9 – *a)* Langmuir scans for configuration I and $V_b = -60$ V at $r = 0$ cm for various electron injection. *b)* Langmuir scan measurements at very low voltage for the same experimental parameters. *c)* Fits of the electron current and *d)*resulting electron temperatures as a function of I_b.

Surprisingly, the $I - V$ characteristics does not exhibit a clear variation in the $[-60$ V; -40 V$]$ range. A naive assumption would be that the primary electrons are emitted at such potential, and should appear distinctively. Instead, the electrons seem to be thermalised at an increased electron temperature with I_b, like in figure III.10. This result is explained by the following analysis. The primary electrons are injected with a peaked energy distribution at $T_{e,prim} = \Delta_{sh}\phi > T_{e,0}$ due to the acceleration from the cathode sheath. Then, thermalisation between electrons occurs at a time-scale of the order of $1/\nu_{ee} \simeq 1/\nu_{ei} = 60$ ns [Bel06; Fun+07]. The thermalisation length of the injected beam with the surrounding plasma is

$$l_{th} = \frac{v_{e,prim}}{\nu_{ee}} \quad \text{with} \quad v_{e,prim} = \sqrt{\frac{2e\Delta_{sh}\phi}{m_e}} \tag{III.9}$$

A numerical application with $\Delta_{sh}\phi = 45$ V yields $l_{th} \sim 20$ cm. The two electron populations are thermalised before reaching the Langmuir probe placed 20 cm away from the cathode.

Transient regimes can be analysed using the 5-tips probe. The temporally-resolved measurements allow to compute ϕ_f, n and T_e as thermionic emission increases. Three divergent regimes are investigated in figure III.10 with 5-tips probe measurements conducted at $r = 0$ cm (yellow line), $r = 4$ cm (green line) and $r = 8$ cm (blue line). Data were low-pass filtered at 200 Hz for clarity. The emitted current I_b displays a high shot-to-shot reproducibility regardless of the position of the probe. The experiment was conducted in configuration I, with a cathode bias $V_b = -75$ V, for which the divergent regime is reached, consistently with the results presented in chapter II.

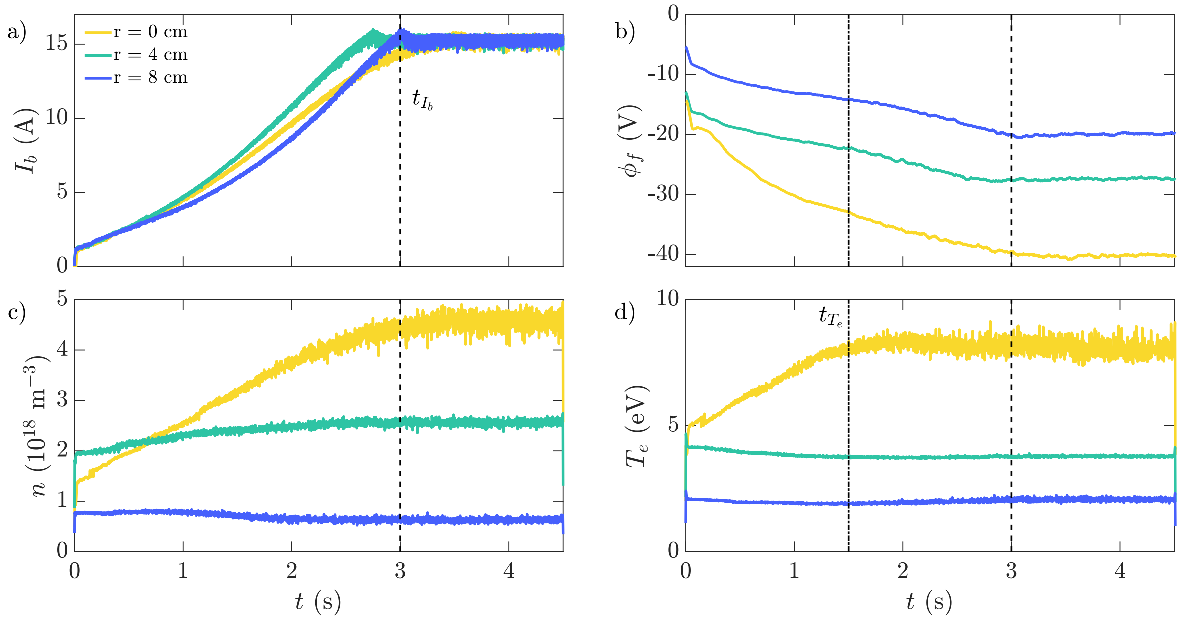

FIGURE III.10 – Strongly emissive regimes in configuration I at $V_b = -75$ V. Temporally-resolved *a)* I_b, *b)* ϕ_f, *c)* n and *d)* T_e measurements from 5-tips probe at $r = 0$ cm, $r = 4$ cm and $r = 8$ cm. Typical characteristic times t_{I_b} and t_{T_e} are highlighted.

The decrease in floating potential across the whole plasma column corroborates with the increase in injected current I_b, until the saturation of I_b occurs at t_{I_b}. $\phi_f(x = 0\text{ cm})$ exhibits a significant lowering during thermionic injection, especially at the early injection phase. Besides, in accordance with figure III.8, plasma density strongly increases at the plasma core, following closely the dynamics of I_b. Furthermore, the plasma is less modified far from the cathode, enhancing the radial density gradient, as can be seen from the comparison between the densities at $r = 0$, 4 and 8 cm. Electron temperature soars very rapidly at the plasma core until a typical timescale t_{T_e}. The physical reason behind the difference between t_{I_b} and t_{T_e} is unclear yet. An hypothesis is that the decrease of the plasma potential at the core means that the cathode sheath potential drop is reduced. Injected electrons are less energetic, causing the electron temperature to saturate earlier. Meanwhile, no significant variation in T_e is observed outside of the plasma core. It confirms the very local heating of electrons in the shadow of the emissive cathode. Yet, transient regimes are complex and their interpretation is challenging.

III.3.4 Influence of neutral pressure and magnetic field

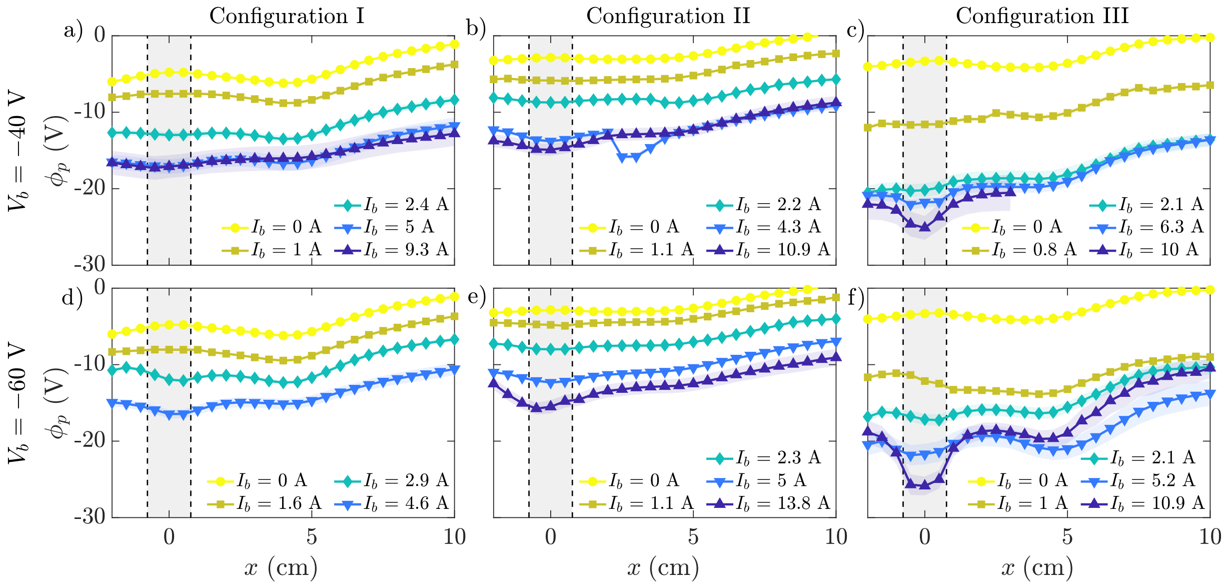

FIGURE III.11 – Plasma potential versus x for configuration I (*a), d)*), configuration II (*b), e)*) and configuration III (*c), f)*), at $V_b = -40$ V (*a)-c)*) and $V_b = -60$ V (*d)-f)*). I_b is modulated by a variable heating current I_h.

Let us now focus on ϕ_p. The plasma potential profile evolution for the three configurations and the two values of voltage bias are reported in figure III.11. Each row corresponds to a given bias ($V_b = -40$ V at the top, and -60 V at the bottom) and each column to a specific configuration (configurations I to III from left to right).

Keep in mind that emissive probe measurements are challenging. This is why some radial scans may be incomplete (configuration III, $V_b = -40$ V, $I_b = 10$ A), exhibit outliers (configuration II, $V_b = -40$ V, $I_b = 4.3$ A) or questionable behaviours (crossing of $I_b = 5.2$ and 10.9 A profiles in configuration III, $V_b = -60$ V). Yet it represents a rich dataset relevant for a comprehensive comparison with the analytical model. One also may notice that the plasma potential fluctuations are important in some cases. This feature is most probably due to the excitation of large-scale unstable modes, and will be discussed in subsection III.4.1.

The overall trends are similar to the ones previously discussed. The importance of the χ control parameter through the influence of B^2/n_n (see equation III.8) is clearly observed, while the role of the voltage bias is marginal. Increasing B at constant p_0 enables a more efficient drive of the plasma potential for a given current I_b. Besides, similar plasma potential behaviours are observed for configurations I and II, for which B^2/n_n is kept constant, although n, T_i and T_e are modified. Detailed plasma density and electron temperature profiles can be found in appendix.

III.3.5 Potential drop across the plasma column

Let us now focus here on the potential drop across the plasma column $\Delta\phi_p = \phi_p(r_g) - \phi_p(r_b)$, discarding both the influence of the cathode sheath $\Delta_{sh}\phi$ and the anode sheath at the outer edge $\phi_p(x = r_g)$. A strong assumption is that the model assumes no potential drop across the plasma column at zero emitted current. In other words, a flat plasma potential profile is expected at $I_b = 0$ A. This linear approximation assumes that the radial voltage drop is the sum of a constant voltage drop due to the pre-existing plasma, and of a voltage drop caused by thermionic emission. It is a

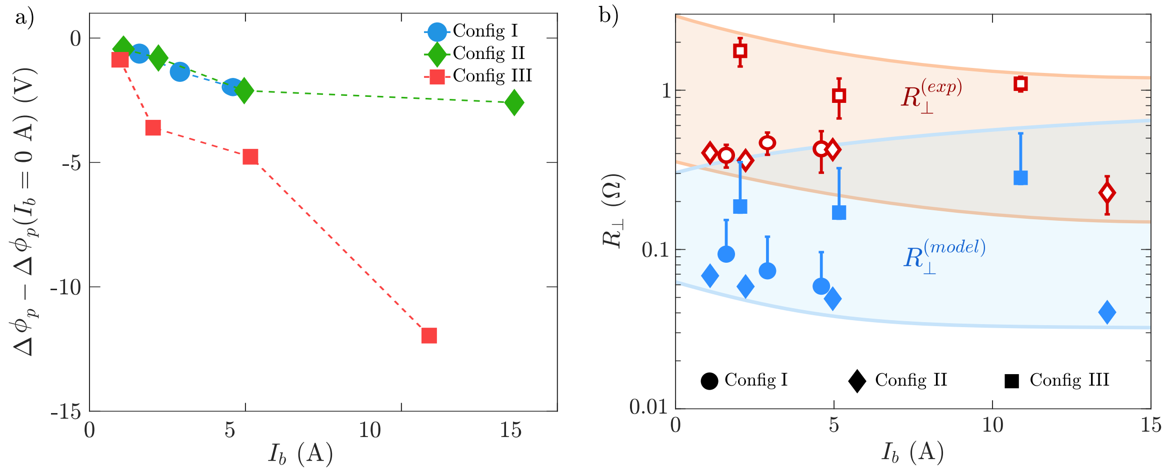

FIGURE III.12 – *a)* $\Delta\phi_p(I_b) - \Delta\phi_p(I_b = 0)$ as a function of I_b at $V_b = -60$ V. *b)* Perpendicular resistance values at $V_b = -60$ V. Circles correspond to configuration I, diamonds to configuration II and squares to configuration III. Blue markers are the analytical values and red ones the experimental values. Coloured areas are only a guide for the eye.

strong assumption that is likely to fail at large thermionic emission, for which the plasma density and electron temperature profiles are significantly modified (see figure III.8), and instabilities may arise (see subsection III.4.1). Therefore, the natural potential drop measured in the experiment in the absence of thermionic emission $\Delta\phi_p(I_b = 0)$ will be subtracted to the potential drop $\Delta\phi_p(I_b)$ measured in the presence of an emitted current I_b.

The experimental perpendicular resistance $R_\perp^{(exp)}$ is computed as

$$R_\perp^{(exp)} = \frac{\Delta\phi_p(I_b) - \Delta\phi_p(I_b = 0)}{I_b}. \tag{III.10}$$

$R_\perp^{(exp)}$ will be compared to the theoretical $R_\perp^{(model)}$ value. This latter quantity is computed using the experimental plasma density and electron temperature profiles according to the equation III.6. The cross-section for ion-neutral collisions is 1.3×10^{-18} m^2 (see subsection I.2.3), and T_i are respectively set at 0.2, 0.28 and 0.45 eV for configuration I, II and III [Dés18]. One should keep in mind that T_i is certainly underestimated for configuration II, since the 0.28 eV value has been measured at 0.13 Pa instead of 0.26 Pa. $\Delta\phi_p(I_b) - \Delta\phi_p(I_b = 0)$ as a function of I_b for $V_b = -60$ V is shown in figure III.12a). Their evolution seems to be linear in the investigated I_b range, which is consistent with a fully saturated regime.

The values of $R_\perp^{(exp)}$ and $R_\perp^{(model)}$ are displayed in figure III.12b) for all configurations at $V_b = -60$ V. The first observation is that values computed according to the model are about one order of magnitude lower than the experimental ones. The second observation is that, as expected from theoretical arguments, the perpendicular resistance in configuration I and II are very close, and the perpendicular resistance in configuration III is higher than that of configuration I, within a ratio close to the theoretical ratio of 4. Note that shaded areas bound the obtained values and are only a guide for the eye. Besides, the constant values obtained for $R_\perp^{(exp)}$ regardless of I_b are possible evidence of a weakly perturbed plasma. This observation supports the assumption that electron injection is a linear effect that is superimposed to a moderately-altered background plasma.

The estimate of $R_\perp^{(model)}$ is extremely sensitive to the value of the neutral density n_n, for which we assumed a neutral gas temperature of 400 ± 100 K, and the absence of neutral depletion [Fru17]. For a 50% homogeneous neutral depletion, the perpendicular resistivities would be increased by a factor 2, hence the upper error bars for $R_{\perp}^{(model)}$ which take this probable 50% neutral depletion into account. An important experimental refinement would be the measurement of radial neutral density profile. Besides, radial scans at another location in the plasma column could be an interesting improvement, as it would enable to assess the longitudinal homogeneity of the plasma potential.

III.4 Limits of the model and possible refinements

III.4.1 The quiescent plasma assumption

One essential assumption is the quiescence of the plasma. Its purpose is to assume a uniform classical cross-field transport. Large-scale coherent modes, waves and instabilities could induce a non-trivial radial and longitudinal transport, questioning the relevancy of the analytical model presented. Although the experimental conditions were chosen such that the plasma is quiescent in absence of thermionic emission, the electron injection could affect the plasma flow at a macroscopic scale [Dés+21], which may trigger current-driven instabilities [DuB+14 ; Vin21]. The quiescent application will be discussed further now.

As can be seen in figure III.11, the standard deviation of ϕ_p increases with electron injection. The PSD of ϕ_p for the three configurations, at $r = 0$ cm and $V_b = -60$ V, are displayed in figure III.13. They are obtained following Welch's method on 20 ms segments over 1 s samples.

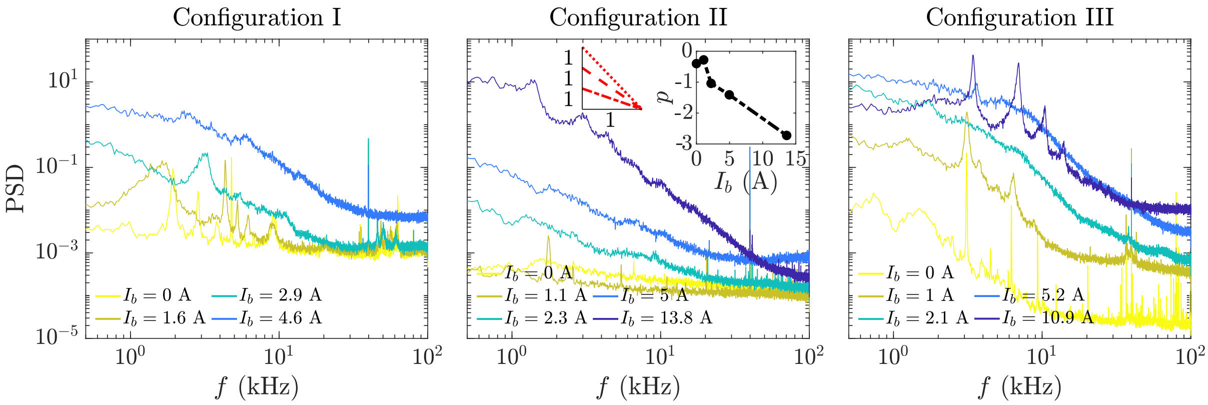

FIGURE III.13 – Power spectral density (PSD) of ϕ_p for the three configurations at $r = 0$ cm and $V_b = -60$ V. Insert in the middle panel shows the logarithmic slope of the PSD as a function of I_b.

Firstly, one can see that the initial plasma configurations at $I_b = 0$ A exhibit a low level of fluctuations, especially in configuration II. The fluctuations are dominated by a strong localized peak at 40 kHz, which is certainly an aliasing artifact from the $f_0 = 13.56$ MHz radio-frequency fluctuations sampled at 200 kS/s.

The electron injection alters significantly the fluctuations observed. The sharp coherent oscillations in the kHz range at $I_b = 0$ A in configurations I and III are dampened with I_b, while low-frequency broadband fluctuations become dominant when I_b exceeds 5 A. These broadband fluctuations present a plateau at $f < 1$ kHz and a seemingly linear slope from 1 kHz to 30 kHz in the log-log plots presented here. The PSD slopes, estimated from a linear fit in the range [1 kHz; 30 kHz] for configuration II, are shown in insert of the middle panel as a function of I_b. A linear variation of p with respect to I_b is witnessed.

Besides, new or enhanced instabilities are witnessed at strong emission in configuration III. Such instabilities were briefly investigated using high-speed imaging on VKP-ICP [Vin21]. Large rotating spokes were reported, which was thought to be excited by the Simon-Hoh instability.

Indeed, the common criterion for the Simon-Hoh instability to be excited is $\mathbf{E} \cdot \nabla n > 0$, but more detailed calculations can be found in [Smo+16; Har+22]. As shown in figure III.8, the plasma density and potential profiles are in accordance with the excitation of the Simon-Hoh. This is a suitable explanation for the emergence of the 3.4 kHz peak in configuration III at $I_b = 10.9$ A and its corresponding harmonics. However, a deeper and cautious analysis is required for a confident instability identification.

To summarize, electron injection induces broadband low-frequency fluctuations for the three configurations investigated, and a strong coherent large-scale oscillation in configuration III at strong emission. Overall, the quiescent plasma assumption remains verified over the experiences conducted. The density fluctuations $\tilde{n}/\langle n \rangle$ remain below 17% for configuration I and 10% for configuration II for any current I_b. The density fluctuations reach a maximum value of 48% for configuration III, $I_b = 10.9$ A. Such unstable configurations could experience an increased anomalous cross-field transport, hence a reduced value of $R_\perp^{(exp)}$. However, no significant decrease of $R_\perp^{(exp)}$ with I_b is visible in figure III.12b). It supports the assumption of a quiescent plasma.

III.4.2 The existence of an anode sheath

A major refinement of the analytical model would be the description of the observed anode sheath. Spatial measurements of the anode sheath are scarce and challenging, and revealed a thin sheath. An accurate study of its properties was not extensively conducted, but the large dataset provides the access to ϕ_p and ϕ_f values at $x = 10$ cm. Although the probe is progressively withdrawn through a lateral recess and does not crosses the anode sheath at $x = 10$ cm, a preliminary analysis of the anode sheath properties can be performed using $\phi_p(x = 10\text{ cm})$.

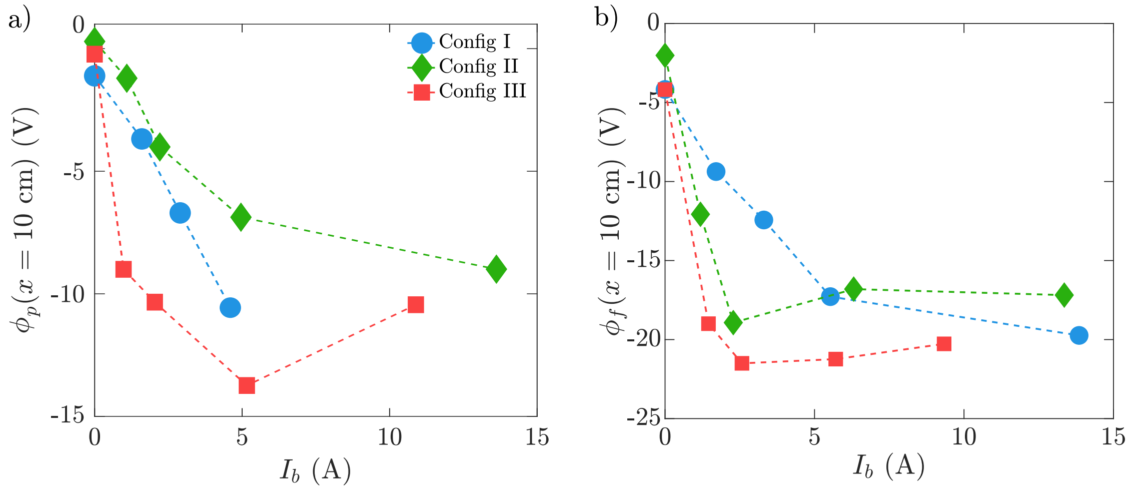

FIGURE III.14 – *a)* ϕ_p and *b)* ϕ_f at $x = 10$ cm as a function of I_b for $V_b = -60$ V.

The values of $\phi_p(x = 10\text{ cm})$ from emissive probe measurements, and $\phi_f(x = 10\text{ cm})$ from 5-tips probe measurements as a function of I_b are shown in figure III.14 for the three configurations investigated at $V_b = -60$ V. Both trends are consistent with each other, except for a few outliers like $\phi_p(x = 10\text{ cm})$ in configuration III and $I_b \simeq 5$ A. As discussed previously, it is presumably due to challenging emissive probe measurements. The anode sheath potential drop is greater than the potential drop across the plasma column $\Delta\phi_p(I_b) - \Delta\phi_p(I_b = 0)$ (see figure III.12a)). The anode sheath potential follows an ordering similar with respect to the three configurations to the one observed in figure III.12a). Besides, the evolution is non-linear and saturates at strong thermionic emission. It is in accordance with figure III.5a), where $\phi_p(x = 10\text{ cm})$ saturates for $V_b < -40$ V and $I_b > 5$ A in configuration III. The anode sheath saturation occurs at different values of I_b depending on the experimental configuration. So, if one models the anode sheath potential drop as the apparition of a new perpendicular resistance $R_\perp^{(anode)} > R_\perp^{(model)}$ according to the analytical model, its value would display a complex behaviour and a strong dependence on I_b.

This anode sheath repels ions back to the plasma while enhancing electron flux at the wall, so it is consistent with the inward charge flux enforced by the cathode. However, the origin of this sheath is non-trivial. The literature on magnetised plasma sheaths is broad. Here is a short review of the physical phenomena at play in order to understand the origin of the anode sheath.

The application of a magnetic field oblique to a floating wall induces the creation of a magnetic pre-sheath. This pre-sheath is added to the more classical quasi-neutral collisional pre-sheath and the non-neutral sheath (see subsection I.2.1). Pioneer works from Chodura [Cho82] introduced a collisionless analytical model for the computation of large magnetic pre-sheaths, often called the Chodura sheath. This sheath scales as the ion Larmor radius in the collisionless case. Yet, the case of a magnetic field parallel to the wall is a singularity, since the outward charge flux is null in absence of collisions. Advanced models extended the previous works to magnetic field parallel to the wall in weakly and strongly magnetised plasmas [Mor+16]. Inverse magnetic pre-sheaths ranging from a few Debye lengths to a few ion Larmor radii depending on magnetisation were reported. More quantitatively, the wall potential was found to be higher than the bulk plasma potential by a few T_i in some cases.

Further improvements have been carried out by considering anomalous transport at the magnetised pre-sheath [The+89], or taking into account the effect of collisions [Mor+18]. Such refinements show the possibility of complex sheaths structures, with non-monotonous potential profiles. The potential drop may reach up to a few T_e, especially as the magnetic field has a grazing incidence [Mor+19]. In the VKP-ICP case without cathode, no reliable signature of a significant magnetic pre-sheath has been evidenced yet.

More importantly, the case of variable electron-to-ion fluxes ratio in the context of a magnetic field parallel [Bei+97] or oblique to the wall [Bei+98] was addressed. Potential drops of a few T_e were reported in the weakly magnetised and high incoming electron flux scenario. This scenario is particularly relevant for the VKP-ICP case in presence of a cathode, since a change in I_b increases the electron-to-ion fluxes ratio at the wall. The resulting pre-sheath width ranges between 0.1 to 0.01 ρ_i, which could match the thin sheath measurements shown in figure III.6. Besides, a limitation of the potential drop with the incoming electron flux is evidenced, which is also consistent with the results displayed in figure III.14.

To that magnetic pre-sheath should be added the effect of the non-neutral sheath. Given the enforced outward electron flux and inward ion flux at the grounded wall, a ion-depleted region should appear at the wall vicinity. This could be a supplementary effect explaining the existence of the anode sheath. Plus, the perpendicular conductivity being assumed to be mainly driven by ions, a ion-depleted zone would lead to a diminished perpendicular conductivity, hence the apparition of a stronger potential drop at the wall. However, a quantitative analysis requires the resolution of the sheath extension and potential drop, which is a vast project that requires further investigation.

As a summary, a deeper analysis of the magnetised sheath structure under the application of an enhanced incoming electron flux to the wall should be conducted for a more reliable and quantitative interpretation. An extensive experimental investigation of the control parameters effects on $\phi_p(x = 10 \text{ cm})$ could provide further insight into the anode sheath origin. The model drawn in section III.2.2 would benefit greatly from such an analysis, which would be upgraded to a quantitative and predictive tool for plasma potential control.

III.5 Conclusion

To conclude, the analytical cross-field ion transport model for plasma potential control using electron injection has been confronted to an extensive dataset of plasma density, electron temperature and plasma potential measurements.

A qualitative agreement was found between the model and the measurements:

- The plasma potential control is directly proportional to electron injection ;
- The predicted ordering in plasma potential control efficiency between the three configurations was confirmed experimentally ;
- $R_\perp^{(model)}$ and $R_\perp^{(exp)}$ are less than one order of magnitude apart.

However, this model includes a few gaps that need to be addressed, and the experiments could be completed:

- The unexpected existence of an anode sheath prevents the analytical model to be fully predictive on the exact bulk plasma potential value ;
- The model assumes a linear contribution of electron injection superimposed to an unperturbed background plasma. The inclusion of non-quiescent experimental configurations in a wider self-consistent model would be a very ambitious yet highly valuable upgrade ;
- Spatially-resolved neutral density profiles and finer ion temperature profiles are lacking for an accurate quantitative prediction of plasma potential control.

In summary, this first experimental investigation of the pre-established analytical model is encouraging. The study of the anode sheath properties is an exciting prospect that could be further explored experimentally and theoretically.

Finally, the design of a highly emissive LaB_6 cathode could extend the works presented herein to a higher range of electron injection. Besides, its simpler design would enable homogeneous thermionic emission and voltage bias distributions over the surface of the LaB_6 cathode. It would ensure an improved independence of V_b and I_b, which would be very profitable for numerical models.

PART II:

HELICON PLASMA OPERATION

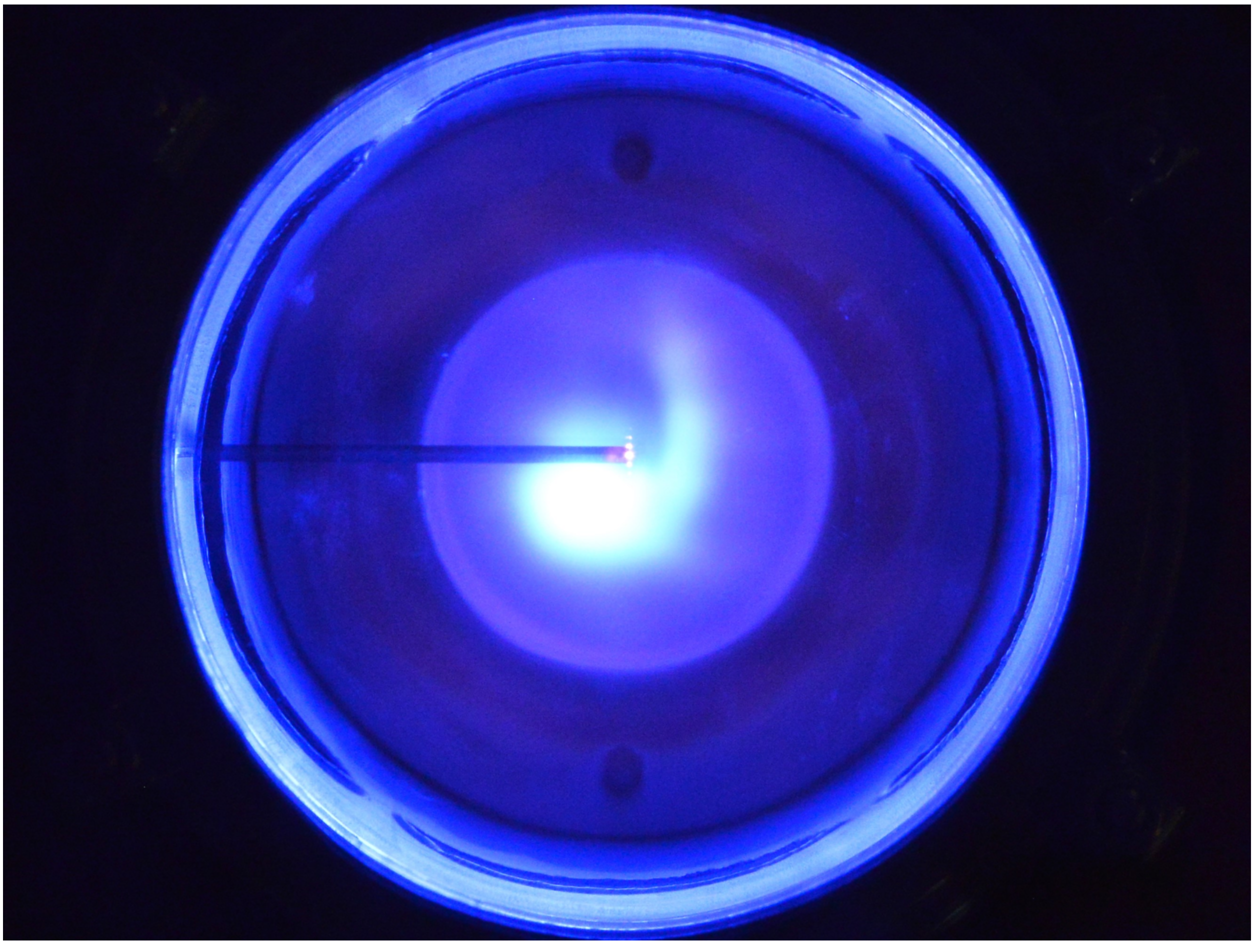

CHAPITRE

IV

HELICON PLASMA UPGRADE AND PHENOMENOLOGY

Ce chapitre présente l'amélioration Von-Kármán Plasma - Helicon Source, abréviée VKP-HS1. Le plasma est généré via un couplage avec une onde radio-fréquence dite hélicon, excitée par une antenne semi-hélicale d'hélicité droite. Une fois l'expérience VKP-HS1 présentée, les propriétés expérimentales de ce plasma sont comparées à la littérature. Enfin, l'influence d'une cathode émissive sur les propriétés du plasma hélicon est brièvement étudiée.

IV.1 State of the art of helicon plasmas

IV.1.1 Historical review

Helicon plasmas are cutting-edge high-density magnetised plasma discharges. They belong to the category of wave-heated plasma, *i.e.* the plasma discharge is sustained by an energy transfer from an electromagnetic wave to the plasma via absorption. In the case of helicon plasmas, the energy transfer is ensured by the so-called whistler waves, resulting in a highly efficient plasma heating. Their first mathematical formalism was introduced in solid state physics in the 1960s [Bow+61 ; Ros+62] and was extended to gaseous plasmas a few years later [Leh+65 ; Klo+65]. For the first time, the dispersion relation, the wave structure and the attenuation lengths of a helicon wave in a uniform cylindrical plasma were presented. It was soon followed by the first proof of concept of a helicon plasma discharge in 1970 with the pioneer work from Rod Boswell [Bos70]. Unique helicon plasma features were already observed, such as the tightly condensed high plasma density profile and the propagation of specific electromagnetic whistler waves. However, the understanding of the power deposition from the wave to the plasma was incomplete at the time.

As a brief historical review, the development of helicon antennas and helicon plasmas occurred during the 1980s and 1990s. Firstly, the investigation of the fundamental underlying mechanisms of helicon plasma generation were addressed. The heating mechanisms were investigated thoroughly, and a consensus on helicon plasma generation seemingly emerged over the 2010s decade. Major efforts have also been invested in optimal antenna design up to that day, and advanced helicon discharges topics are still an active domain of research.

Many advantages can be found in helicon plasmas. For instance, they can be generated over a large range of frequencies [Shi22]. This versatility is an advantage compared to Electron Cyclotron Resonance antennas for instance, which relies on the excitation of a resonance at the specific electron cyclotron frequency. Then, new plasma conditions are of great interest for basic laboratory plasmas. Such high-density plasmas arouse promising application perspectives. Unique plasma regimes are reached, permitting innovative fundamental investigations on high-density low-pressure plasma physics [Jac+23 ; Fil+23]. Highly homogeneous helicon plasmas are also considered for the next generation of small linear particle accelerator. For example, the plasma wakefield accelerator AWAKE aims at accelerating particles up to a 100 GeV energy over 100 m using multiple helicon antennas [But+18 ; Gsc+22]. This original experiment could replace immense and expensive particle colliders such as the Large Hadron Collider (LHC) facility in the coming decades. New plasma propulsion devices relying on helicon plasma antennas have also been emerging recently, with models such as the helicon double-layer thruster (HDLT) or the variable specific impulse magnetoplasma rocket (VASIMR) [Cha09]. It provides modular solutions and wide operating regimes, holding the promise of an efficient and long life-time electrodeless design [Tak+14a ; Jim+23]. Helicon plasmas are also of particular interest for plasma-assisted chemical vapor deposition, utilised for dielectric thin films synthesis [Cot+99], enhanced metal etching [Tak+14b] or efficient plasma mass separation techniques [Zwe+18]. Finally, high-density helicon plasmas are relevant for nuclear fusion. For instance, the fusion-relevant plasma-material interactions in hydrogen or deuterium plasmas are studied using helicon plasmas in the MPEX facility [Lum+20]. Besides, whistler waves for current drive heating in fusion reactors using traveling wave antennas show encouraging results in DIII-D or KSTAR tokamaks [Pin+18 ; Lee+23]. Such a technology is considered for reaching the fusion ignition threshold in the future ITER tokamak.

IV.1.2 Whistler waves propagation

The goal here is to define the main properties of the electromagnetic waves used for helicon plasma discharges. Whistler waves in a plasma may exist only in presence of an external magnetic field, and they propagate along its direction. Their name originate from their propagation characteristics. The plasma is a dispersive medium, meaning that the propagation velocity of a wave depends on its frequency. In particular, the high-frequency components of the whistler waves propagate faster than the low frequencies. Consequently, the signal coming from a whistler wave gives a specific chirp signal, whose frequency decreases over time, hence their denomination "whistler" waves. Dispersion relations of the electromagnetic waves propagating in a magnetised plasma can be derived from Maxwell equations. The magnetically-induced anisotropy and the multi-species plasma formalism lead to several electromagnetic waves structures, dispersion, absorption and resonances. The purpose of this subsection is not to draw a comprehensive picture of wave propagation in a magnetised plasma, but rather to understand the basic theory of whistler wave propagation. Complete calculations can be found in specialised textbooks [Lie+05; Rax05].

Let us consider a transverse wave, *i.e.* the electric field $\mathbf{E}_{wave}$ is perpendicular to the wave vector $\mathbf{k}$. If the propagation direction of the wave is along the magnetic field direction, *i.e.* $\mathbf{k}\|\mathbf{B}$, the eigenmodes propagating in the magnetised plasma are the left-handed and the right-handed polarisations with respect to $\mathbf{B}$, respectively noted L and R. The magnetic field induces a chirality, resulting in dissimilar wave propagation. For instance, the difference in phase velocity for the L and R waves is at the origin of the Faraday rotation, namely the rotation of the polarisation plane of a transverse wave through a magnetised plasma depending on the frequency of the wave. One can derive their dispersion relation using a simplified model of the plasma and Maxwell equations.

The assumptions are the following:

- The plasma is homogeneous, weakly magnetised, and its resistivity is considered null.
- Maxwell equations are linearised.
- The inertia of the electrons is neglected.

The first approximation implies many consequences. The weak magnetisation means that electrons are confined along the magnetic field, while ions are not. Then, the plasma current is only conveyed by electrons along the $\mathbf{E} \times \mathbf{B}$ drift guiding center, while ions do not carry a significant current. Besides, if one assumes that the wave frequency ω_0 is higher than the ion cyclotron and lower hybrid frequencies [Rax05; Bel06], the ions can be considered immobile. As a reminder, the lower hybrid frequency corresponds to a resonant mode of a coupled electron and ion dynamic in a magnetised plasma. In summary, it implies the following ordering of the typical plasma frequencies

$$\omega_{c,i} \ll \omega_{LH} < \omega_0 \ll \omega_{p,i} \ll \omega_{c,e} \ll \omega_{p,e} \quad \text{with} \quad \omega_{LH} \simeq \sqrt{\omega_{c,e}\omega_{c,i}} \tag{IV.1}$$

Under these assumptions, and by neglecting the displacement current in Maxwell-Ampere equation, the relevant set of equations is

$$\nabla \cdot \mathbf{j}_{wave} = 0 \tag{IV.2}$$

$$\nabla \times \mathbf{E}_{wave} = -\frac{\partial \mathbf{B}_{wave}}{\partial t} \tag{IV.3}$$

$$\nabla \cdot \mathbf{B}_{wave} = 0 \tag{IV.4}$$

$$\nabla \times \mathbf{B}_{wave} = \mu_0 \mathbf{j}_{wave} \tag{IV.5}$$

$$\mathbf{E}_{wave} = \frac{\mathbf{j}_{wave} \times \mathbf{B}}{ne} \tag{IV.6}$$

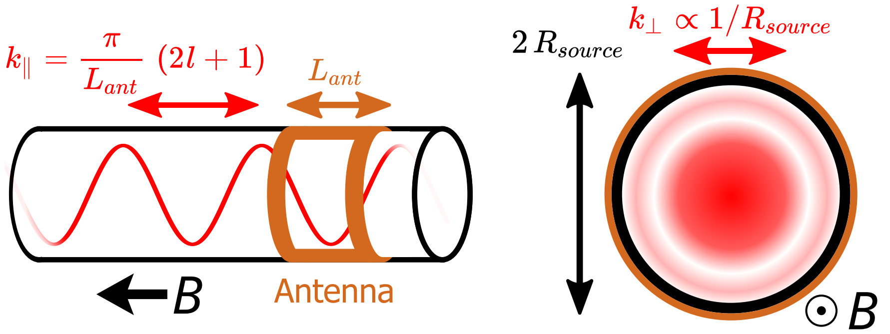

FIGURE IV.1 – Schematics of $k_\parallel$ and $k_\perp$, imposed respectively by the antenna length L_{ant} and the antenna radius R_{source}. The red sine wave on the left represents the whistler wave for $l = 0$, and the red concentric circles on the right is the intensity distribution of the whistler wave across a section of the cylinder for $N_r = 2$.

with $\mathbf{E}_{wave}$ and $\mathbf{B}_{wave}$ the electric and magnetic wave components, $\mathbf{j}_{wave}$ the current driven by the electromagnetic wave, and $\mathbf{B}$ the externally applied magnetic field. One can compute the dispersion relation for a progressive harmonic plane wave. The wave vector $\mathbf{k}$ can be decomposed in two components, $k_\parallel$ being along $\mathbf{B}$ and $k_\perp$ the component orthogonal to $\mathbf{B}$, so that $k = \sqrt{k_\perp^2 + k_\parallel^2}$. For this ensemble of assumptions, the set of equations leads to the dispersion relation of both R and L whistler waves

$$\frac{\omega_0}{k} = \frac{Bk_\parallel}{ne\mu_0} \tag{IV.7}$$

This dispersion relation could be refined by considering collisions or particles inertia. The full relation dispersion is represented in figure 1 of the review [Shi18]. These waves have been studied experimentally in unbounded magnetised plasmas [Ste+15]. They can be excited by very simple loop antennas [Urr+14], or more advanced loop arrays [Ste+14] in order to excite specific wave structures and complex whistler waves. Such studies can be expanded to the context of fusion plasmas, where whistler waves are not bounded longitudinally.

Whistler waves present a complex three-dimensional structure. In the case of a linear magnetised plasma device, the wave structure complexity is described by the wave numbers $k_\parallel$ and $k_\perp$. As can be seen from the dispersion relation (IV.7), they play an important role in the wave propagation. A schematics is presented in figure IV.1 for clarity. The shape of the antenna is essential to select specific whistler waves. The antenna can excite an odd number of half-wavelengths along its length L_{ant}, so that the wavelength of the whistler wave is $L_{ant}/\,(2l+1)$, with $l \in \mathbb{N}$. On the other hand, the radius of the antenna R_{source} dictates the radial wavelength. Across a section of the linear device, an integer number of modes N_r may exist. Overall, $k_\perp$ scales as $\propto 1/R_{source}$.

The azimuthal dimension is an important feature of the whistler wave. The wave can be written under the form of a progressive harmonic plane wave in cylindrical coordinates (r, θ, z)

$$\mathbf{E}_{wave} = \mathbf{E}_0(r)\mathrm{e}^{i\left(m\theta + k_\parallel z - \omega_0 t\right)} \quad \text{and} \quad \mathbf{B}_{wave} = \mathbf{B}_0(r)\mathrm{e}^{i\left(m\theta + k_\parallel z - \omega_0 t\right)} \tag{IV.8}$$

with $\mathbf{E}_0(r) = E_r(r)\mathbf{e}_r + E_\theta(r)\mathbf{e}_\theta + E_z(r)\mathbf{e}_z$ and $(\mathbf{e}_r, \mathbf{e}_\theta, \mathbf{e}_z)$ are the unitary vectors of the cylindrical vector basis, $\mathbf{B}_0(r) = B_r(r)\mathbf{e}_r + B_\theta(r)\mathbf{e}_\theta + B_z(r)\mathbf{e}_z$, and m the integer azimuthal mode number. m gives the polarisation of the whistler wave. Indeed, $m = +1$ is right-handed polarised with respect to the external magnetic field, while $m = -1$ is left-handed polarised, so they correspond respectively to the R and L waves. The spatial electric field pattern of the $m = +1$ whistler wave in a uniform infinite plasma is drawn in figure IV.2a). The two electric field patterns for the $m = +1$

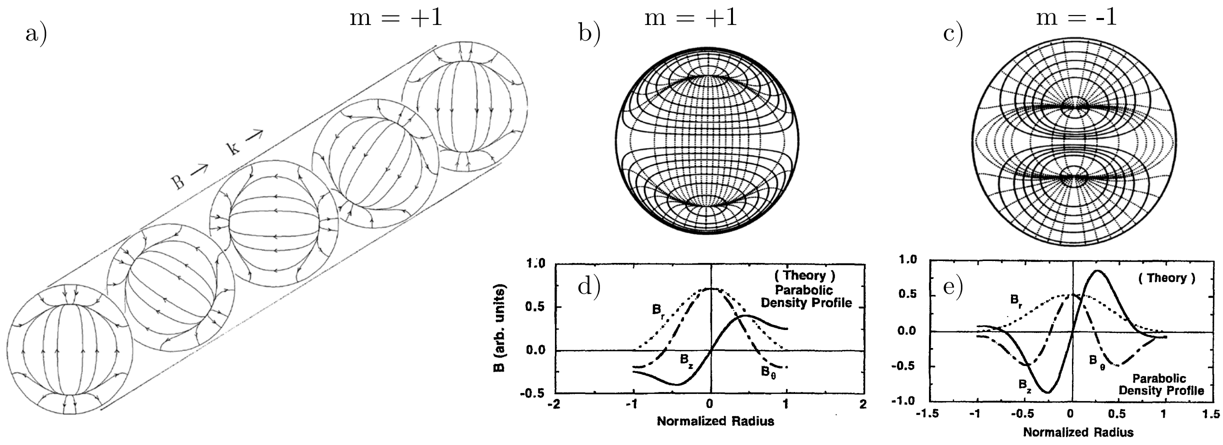

FIGURE IV.2 – *a)* Spatial electric field pattern of a $m = +1$ mode in a uniform cylindrical plasma. *b-c)* Electric field structures of the $m = +1$ and $m = -1$ modes. The three graphs are taken from [Che91]. *d-e)* Radial magnetic field structures for the $m = +1$ and $m = -1$ modes in a parabolic plasma density profile. These two graphs are taken from [Shi+96].

l	$k_\parallel$ (m^{-1})	$k_\perp$ (m^{-1})	k (m^{-1})	n (10^{18} m^{-3})
0	15.7	65.4	67.3	1.11
1	47.1	58.5	75.1	3.72
2	78.5	55.8	96.3	7.94
3	110	54.7	123	14.2
4	141	54.2	151	22.4

TABLE IV.1 – Characteristics of the longitudinal whistler modes l for $B = 180$ G, $R_{source} = 5.5$ cm, $f_0 = 13.56$ MHz, $m = 1$ and $N_r = 1$.

and $m = -1$ modes are displayed in figure IV.2b-c) and exhibit distinct structures. This chirality is due to the external magnetic field and the ordering $\omega_{c,i} \ll \omega_0 \ll \omega_{c,e}$. Indeed, the electrons and ions responses under the application of an oscillating magnetic field at a frequency ω_0 is different, hence the asymmetry in $m = +1$ and $m = -1$ modes.

The calculation of $k_\perp$ in a cylinder requires the computation of the following equation

$$mkJ_m\left(k_\perp R_{source}\right) + k_\parallel J'_m\left(k_\perp R_{source}\right) = 0 \tag{IV.9}$$

where J_m is the m-th Bessel function of the first kind, and J'_m its derivative. In the case of $m \neq 0$, it couples $k_\parallel$ to $k_\perp$. Taking into account these considerations of antenna size and azimuthal wave number, the ratio ω_0/k is fixed by the antenna. Besides, B is an experimental control parameter, meaning that the plasma density is the only free parameter of the dispersion relation. Consequently, the propagation of a helicon wave at a given ratio ω_0/k and magnetic field B is associated to a specific plasma density n, hence there is an intrinsic coupling between the plasma properties and the whistler wave. An estimation of the plasma density for a given helicon mode is given in table IV.1. The antenna is 20 cm long and the excitation frequency f_0 is set at 13.56 MHz. The magnetic field is assumed to be 180 G, the inner source tube has a radius R_{source} of 5.5 cm. Equation IV.9 on $k_\perp$ is solved for $m = +1$ and $N_r = 1$, while the longitudinal mode varies from $l = 0$ to 4. The plasma density at the core lies between 1.6×10^{18} and 26×10^{18} m^{-3}, that is to say between a 5% and a 80% ionisation rate at 0.13 Pa.

IV.1.3 Plasma-helicon wave coupling

In the context of finite size experimental devices, the whistler waves are called helicon waves, and the plasma discharge is often called helicon plasma. In the case of a linear device, the radial and the longitudinal wave magnetic field cancel respectively at the cylinder lateral and base walls. A standing wave constrained both radially and longitudinally arises, and it results in a strong coupling between the helicon wave and the plasma cavity. In other words, the antenna excites a multiplicity of waves, but the resonance with the cavity enables a high selectivity, resulting in the establishment of a predominant standing helicon wave in the whole plasma device. One may refer to valuable articles from Chi *et al.* [Chi+99] and more recently Zhang *et al.* [Zha+24], which present clearly the cavity resonance on the existence of specific helicon modes.

Besides, the generation of helicon plasmas results from a strong plasma-wave coupling. The helicon mode can be generated only if a plasma density threshold is reached first. At low power P_w, the plasma density is not large enough for the helicon wave to propagate, and the helicon plasma cannot be sustained. The helicon wave excited close to the antenna at the low-density plasma edge is strongly damped, and does not penetrate up to the plasma core. Once the plasma density reaches a critical threshold, the helicon wave propagates in the whole plasma device. It allows an efficient power deposition at the plasma core, and a new plasma heating source is provided. The underlying heating mechanism from the helicon wave was a major topic in the early development of helicon plasmas [Shi22]. One can mention three important processes:

- Collisional damping of the wave was firstly considered to explain the energy transfer from the wave to the plasma. However, it revealed to be insufficient to explain the strong ionisation rate of helicon plasmas [Bos70].
- Then, Landau damping, initially proposed by Chen in 1991 as the main heating mechanism [Che91], plays a major role in heating the plasma. Electrons can be locked in phase with the travelling helicon wave and accelerated up to high energies ($10 \text{ eV} < T_e < 100 \text{ eV}$). It leads to ionising collisions with neutrals. However, it was also evidenced to be insufficient to account for the high plasma density in various experimental devices.
- Ultimately, the heating from the Trivelpiece-Gould mode, abbreviated TG mode, has been identified as another essential heating mechanism in helicon plasma by Shinohara in the early 2000s [Sha+01]. The TG mode is a short wavelength plasma wave absorbed at the antenna vicinity. It provides a strong heating source at the plasma edge, allowing a sufficient plasma density for the helicon wave to penetrate up to the plasma core. Then, the helicon wave can propagate, establish a standing wave in the cavity and transfer its energy, so that the high-density helicon plasma mode is triggered. These TG modes were reported in various helicon plasma discharges [Bla+02 ; Vir+03], and were successfully compared to theoretical predictions.

The role of each of these mechanisms depend on the device geometry and the experimental conditions. No unified theory exists for the predominant heating sources of helicon plasmas, and it is often a debatable issue within the helicon plasma community [Tsa+22]. Eventually, spatially-resolved measurements of the helicon waves using B-dot probes were reported and allowed a finer estimation of the power deposited by the helicon wave to the plasma [Nie+08]. One can mention that contrarily to the inductively-coupled plasma, the bulk ionisation of the plasma occurs along the whole symmetry axis of the linear device instead of being limited to the antenna location. Note also that even if a single helicon mode is supposed to set the plasma density, the coexistence of multiple radial and longitudinal helicon modes [Lig+95], various heating phenomena like Landau damping and the TG mode [Bla+02], and the non-uniformity of the plasma properties [Gra+23] are multiple causes for deviations between the analytical and the experimental plasma density.

IV.1.4 Antenna design for helicon wave generation

In practice, the helicon wave is sustained via a radio-frequency antenna. The excitation of the various helicon modes depends heavily on the antenna design. As a reminder, for a stationary observer, the $m = +1$ mode is the R wave with respect to $\mathbf{B}$, while the $m = -1$ mode is the L wave. The power deposited to the plasma being inherent to the helicon wave structure, the accurate knowledge of the propagating helicon modes is required to fully capture the wave-plasma coupling. A confident identification of the $m = +1$ and $m = -1$ modes relies on the measurement of the magnetic field radial wave structure using B-dot probes, whose respective analytical profiles are shown in figure IV.2d-e). One can emphasize that the $m = -1$ mode presents a much narrower profile and a stronger B_z component.

Schematics of the common helicon antenna designs are presented in figure IV.3a) [Shi18]. One can mention three wide-spread designs, namely the Boswell antenna 1., whose symmetric configuration enables the simultaneous excitation of $m = +1$ and $m = -1$ modes, the double saddle antenna 2. also used for $m = +1$ and $m = -1$ modes excitation, and the half-helical antenna 3. which presents a high degree of selectivity of $m = +1$ or $m = -1$ modes depending on the external magnetic field. Innovative designs presenting their own advantages are still under investigation [Gui+21].

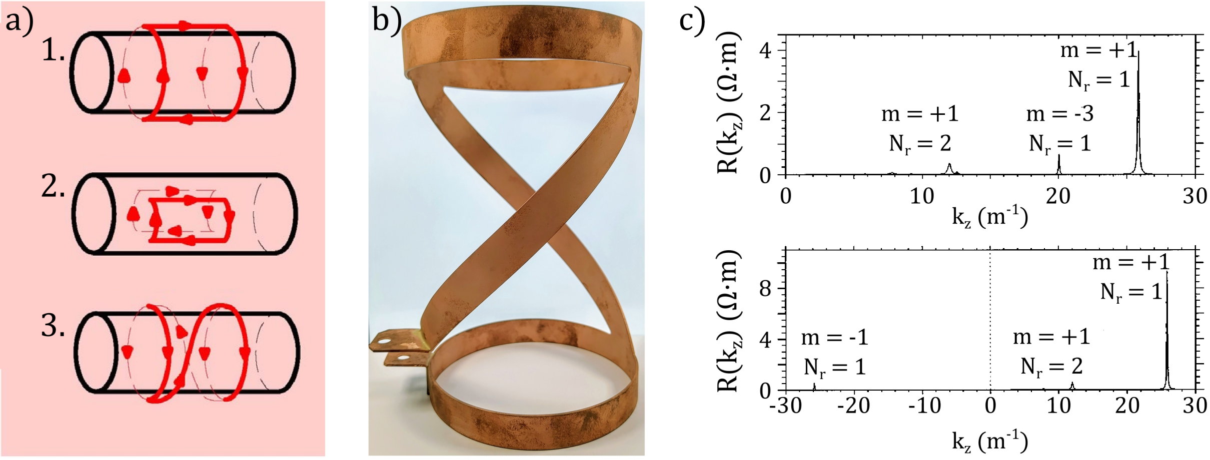

FIGURE IV.3 – *a)* Various antenna designs. From top to bottom: 1. the Boswell antenna ($m = \pm1$ modes), 2. the double saddle antenna ($m = \pm1$ modes) and 3. the left-handed half-helical antenna ($m = +1$ or $m = -1$ modes). Taken from [Shi18]. *b)* 20 cm long right-handed half-helical antenna used for the VKP-HS1 set-up. *c)* Impedance of the double saddle antenna (top) and the half-helical antenna (bottom). m designates the azimuthal mode, and N_r the radial mode. Taken from [Kam+96].

The antenna used for the VKP-HS1 experiment is a 20 cm long right-handed half-helical antenna, with the power supply feed located at one side of the antenna (see figure IV.3b)). The goal is to achieve an optimal conversion to a single helicon mode.

Each antenna design exhibits a different excitation spectrum for the helicon waves. The total impedance of the antenna can be computed numerically using a finite elements method applied to the plasma-antenna system [Kam+96]. Then, one can see that the excitation spectrum is complex, as can be noticed from figure IV.3c) for the double saddle (top row) and the half-helical spectra (bottom row). The azimuthal and radial modes are denoted with the m and N_r notations. The half-helical excitation spectrum displays a high selectivity, as can be seen from the slight $m = -1$ mode excitation at $k_z = -25\ \mathrm{m}^{-1}$ in figure IV.3c).

IV.1.5 Major helicon plasma features

Helicon plasmas in linear devices demonstrate multiple typical features. A signature of argon helicon plasma is the observation of a bright blue core, associated to a high ionisation rate [Tha+15]. Besides, plasma density profile is parabolic and tightly condensed, contrarily to capacitively and inductively-coupled plasmas, while electron temperature remains rather low.

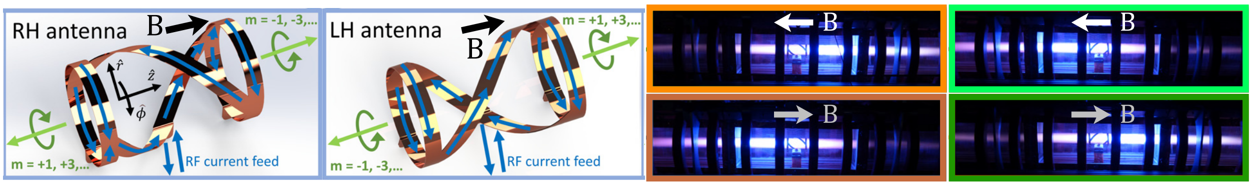

FIGURE IV.4 – *Left panel:* right-handed and left-handed half-helical antennas in a rightward magnetic field. The positive and negative m modes are indicated. *Right panel:* Right-handed (pictures on the left) and left-handed (pictures on the right) half-helical antennas in a rightward (top) and leftward (bottom) magnetic field. Taken from [Gra+23].

Due to a strong plasma-wave coupling, the ionisation by the helicon wave depends primarily on the nature of the excited helicon wave. Since the wave structures of the various azimuthal helicon modes are different, the corresponding deposited power to the plasma differ. For instance, $m = +1$ was evidenced to be highly efficient for ionisation, while the $m = -1$ mode does not propagate and is inefficient to trigger the W mode [Yas+94 ; Shi+96 ; Mil+98b] [1]. The origin of this poor efficiency lies in the strong damping of $m = -1$ mode in a radially non-uniform plasma column [Krä99]. Hence, the magnetic field direction causes a chirality in the helicon wave propagation, which has been well documented at the MAP experiment [Gra+23]. In figure IV.4, one can see the right-handed and left-handed half-helical antennas being implemented on a symmetric linear device. The design of this linear device is such that no asymmetry in B and no boundary may influence the plasma. For each antenna and $\mathbf{B}$ direction, the $m = +1$ mode is predominantly generated on one side, while the $m = -1$ mode is generated on the other side. One can notice unequivocally that the helicon blue core is located on the $m = +1$ side of the antenna. This location is flipped with the direction of $\mathbf{B}$ and the antenna helicity. A comprehensive numerical simulation of the helicon wave energy deposition to the plasma shows a strong disparity between the $m = +1$ and $m = -1$ modes. Whereas the $m = +1$ mode propagates up to 1 m, the $m = -1$ mode is damped over 25 cm and does not heat the plasma beyond this distance. The plasma density in the $m = -1$ mode decays rapidly along the longitudinal axis, with a threefold reduction in n compared to the $m = +1$ mode.

Another major helicon plasma feature is the existence of multiple plasma-wave coupling modes, as mentioned in subsection IV.1.2. An increase in input power at the antenna results in successive helicon plasma modes, from the low-power capacitive and inductive couplings, respectively noted E and H modes, to the helicon plasma coupling W. The W modes being numerous depending on the exact nature of the helicon waves, many transitions to the n-th helicon mode W_n can be witnessed. The resulting E-H-W transitions are well documented, as can be seen in figure IV.5a) [Chi+99 ; Fra+03]. The E-H-W transitions have been documented theoretically in a 0D model, by computing the power deposited from the helicon wave to the plasma, as can be seen in figure IV.5b) [Cha+11]. It is the extension of the power balance model presented in subsection I.2.7 to the case of helicon plasmas. However, since the energy transfer from helicon waves to the plasma is complex, this calculation is far from trivial. This multiple stability is accompanied by an hysteresis in input power, as shown in figure IV.5c). Indeed, the excitation of the helicon mode enables

---

[1] Note that the $m = +1$ and $m = -1$ convention is inverted in the works from Yasaka and Hara.

to reach a high-density plasma, hence allowing the helicon wave to propagate more efficiently at lower power. In other words, the high-density helicon plasma is a stabilising feedback loop for the propagation of helicon waves.

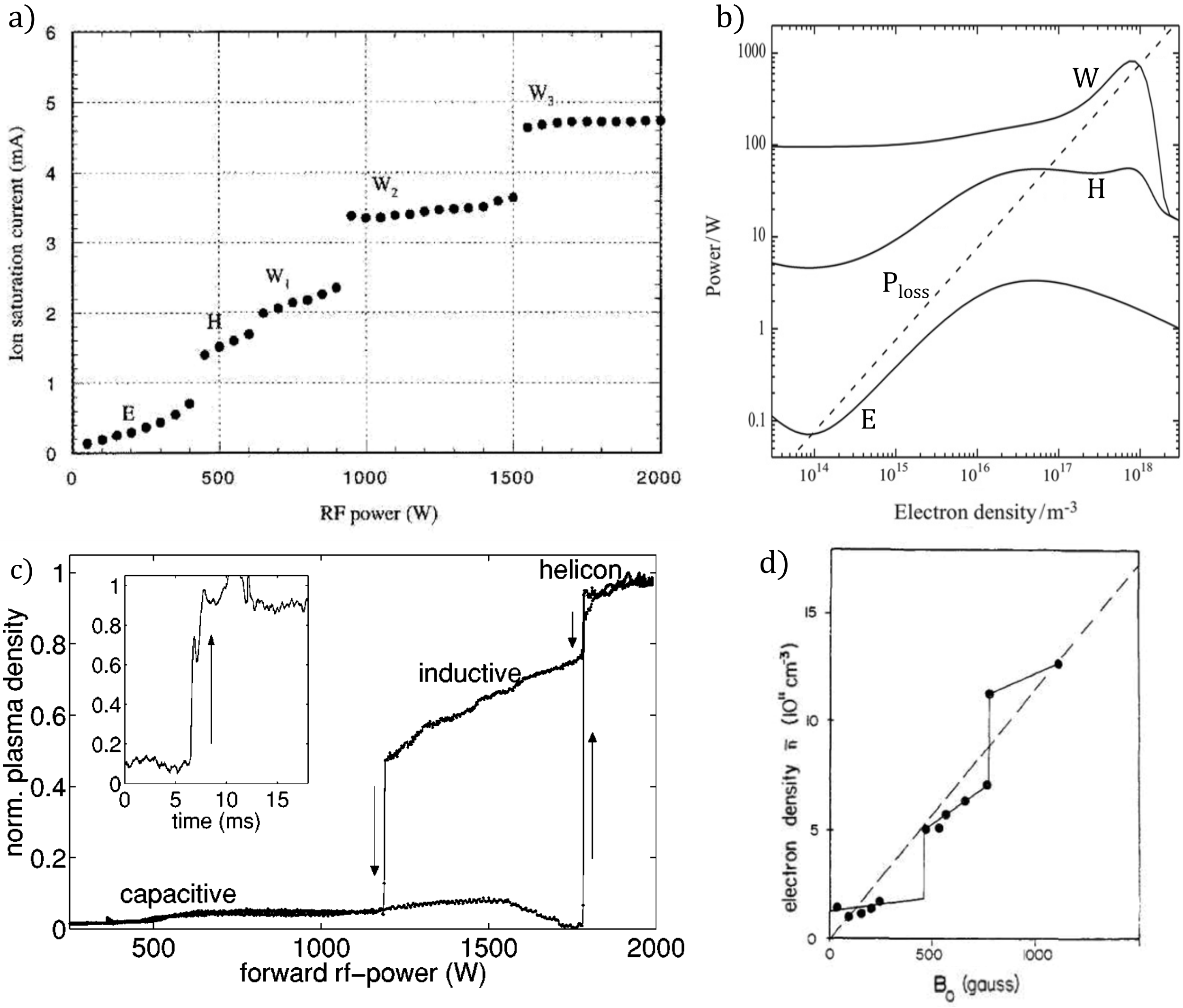

FIGURE IV.5 – *a)* Plasma density as a function of the radio-frequency power. Sudden mode transitions are highlighted. Taken from [Chi+99]. *b)* Power balance model for the E-H-W transition. Taken from [Cha+11]. *c)* Hysteresis in the E-H-W transition. Taken from [Fra+03]. *d)* Plasma density as a function of the external magnetic field. Taken from [Bos84].

Furthermore, it is expected from the dispersion relation IV.7 that the plasma density is directly proportional to the external magnetic field for a given helicon mode. This global trend is observed empirically [Bos84], yet brutal increases in plasma density with the external magnetic are observed too (see figure IV.5b)). This effect arises from sudden W-W transitions, as new helicon modes may become predominant when plasma properties are modified with B.

Finally, longitudinal variations of the helicon waves can be observed as a result of the coexistence of multiple longitudinal helicon modes [Lig+95]. The small difference in $k_{\parallel}$ causes a beat and may induce a longitudinal modulation in plasma density [Jac+23].

The high ionisation rate and the strong radial plasma density gradient provoke a unique helicon plasmas phenomenology. For instance, characteristic H-W oscillations are commonly observed, *i.e.* milliseconds oscillations between an inductively-coupled and a helicon plasma [Deg+99a ;

Deg+99b]. The main cause of this phenomenon was proven to be neutral depletion. Indeed, the neutrals are quickly depleted by a high ionisation rate at the plasma core. Then, with an insufficient neutral refill, the ionisation is not enough and the plasma density drops below the plasma density threshold for the helicon mode. The helicon mode decays, a transition back to the inductive mode is observed, and the neutral depletion decreases. The diffusive refilling of neutrals occurs until the helicon mode can be sustained again. Besides, the high density and the heterogeneous plasma properties are favourable to the emergence of drift waves [Sch+05; Bur+05], Rayleigh-Taylor [Tha+14] and Kelvin-Helmholtz [Lig+01] instabilities, which might be detrimental to the operation and stability of helicon plasmas. This last aspect will be detailed in chapter V.

IV.2 Experimental set-up upgrade

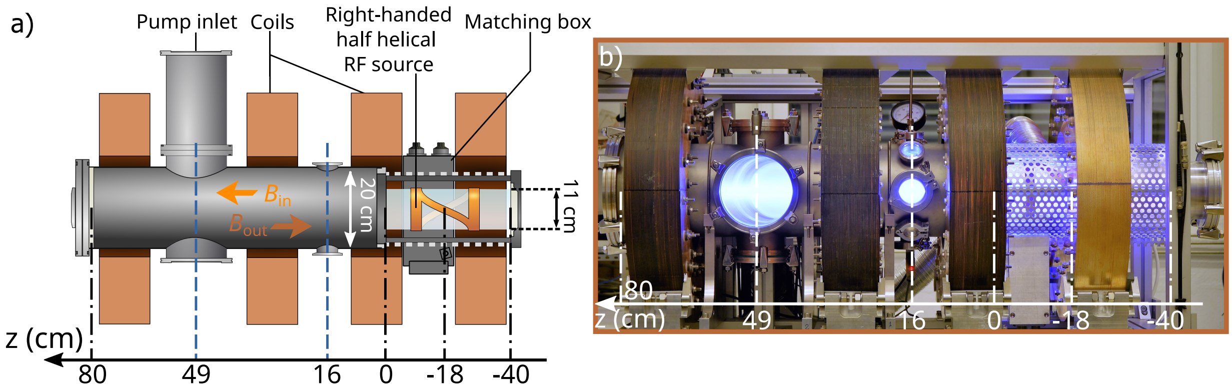

FIGURE IV.6 – *a)* Drawing of the Von-Kármán Plasma experiment with a right-handed half-helical radio-frequency source (VKP-HS1). Both ends of the plasma chamber are electrically insulated, the stainless steel vessel is grounded. *b)* Picture of the VKP-HS1 set-up operating with argon and the B_{out} magnetic configuration. The right-handed half-helical plasma source is visible at $z = -18$ cm.

The VKP-ICP set-up was upgraded to the Von-Kármán Plasma - Helicon Source set-up, abbreviated VKP-HS1, in order to generate high-density helicon plasmas. The source tube was replaced for a longer one, namely a 40 cm long and 11 cm wide borosilicate tube. A 20 cm long right-handed half-helical antenna, pictured in figure IV.3b), was placed at $z = -18$ cm. The matching box was renewed for a compact manual L-type matching box. The capacitors C_{load} and C_{tune} remained identical though, with capacitances ranging respectively up to 500 pF and 1000 pF. Finally, a bitter coil, identical to the previous ones, was added at $z = -23$ cm. A drawing of the upgraded experimental device, and a picture of the operating set-up is shown in figure IV.6. B-dot, emissive and Langmuir probe measurements are carried out on the lateral access ports located at $z = 49$ cm, similarly to the measurements on VKP-ICP presented in the previous chapters.

As mentioned in subsection IV.1.4, the use of a half-helical antenna associated to a possible reversal of the external magnetic field direction enables to switch from a predominant excitation of the $m = +1$ mode to the $m = -1$ mode. The B_{out} magnetic field configuration corresponds to a magnetic field directed from the plasma diffusion chamber to the plasma source, while the B_{in} configuration is the opposite. Because of the right-handed helicon antenna, the B_{out} configuration should generate primarily the efficient $m = +1$ mode, while the B_{in} configuration should mostly excite the poorly efficient $m = -1$ mode. This assumption on the plasma production efficiency will be addressed in section IV.3.

Since the external magnetic field is essential for helicon wave propagation, the addition of a new coil aims at generating a homogeneous magnetic field at the antenna location. A numerical computation of the magnetic field distribution similar to the one presented in section I.1.2 can be found in figure IV.7. The right-handed antenna is represented by the red solid line. A fairly homogeneous B profile is obtained all along the vacuum chamber. This numerical computation allows to adjust the conversion factor from the current flowing through the coils I_B and the amplitude of the magnetic field B, previously evaluated at $\langle B/I_B \rangle = 1.70\ \mathrm{G} \cdot \mathrm{A}^{-1}$ for the VKP-ICP configuration. The VKP-HS1 set-up has a mean magnetic field value along the symmetry axis $\langle B/I_B \rangle = 1.80\ \mathrm{G} \cdot \mathrm{A}^{-1}$ between $z = 0$ and 80 cm.

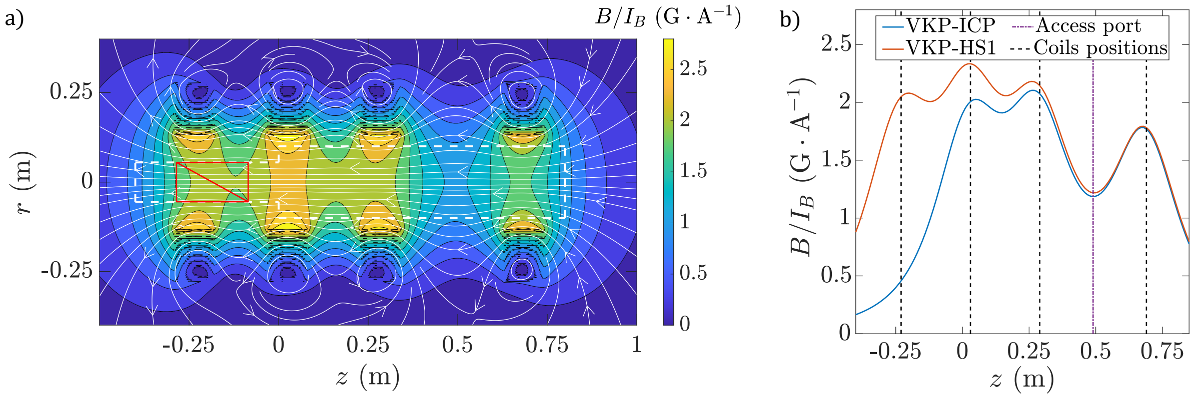

FIGURE IV.7 – *a)* Numerically computed magnetic field for the VKP-HS1 set-up. Magnetic field values are normalised by the current intensity I_B going through the coils. The white dashed lines represent the vacuum chamber and the red solid line the radio-frequency antenna. Note that the z axis is rightward. *b)* Magnetic field normalised by I_B along the symmetry axis of the device.

IV.3 Helicon plasma experimental phenomenology

IV.3.1 Observation of helicon plasma features

The above-mentioned major helicon plasma features are observed in the VKP-HS1 set-up. In the present subsection, some of them are reported and compared to the expectations from the literature review presented in section IV.1. Note that since helicon plasmas in linear devices result from a coupling between a helicon wave and a cavity, the introduction of an electrostatic probe at the plasma core might be detrimental to the W mode transition. Consequently, the probes are more intrusive than in the VKP-ICP case. It often results with a P_w threshold for W mode transition shifted up to 100 W depending on the probe size.

IV.3.1.1 Influence of the magnetic field configuration

The effect of the magnetic field direction on the helicon plasma generation was investigated. The configurations B_{out} and B_{in} were applied for various pressure, magnetic field and power. The magnetically-induced chirality was observed, as can be seen in figure IV.8. In order to minimize the effect of the dielectric end close to the helicon antenna, the source tube is exceptionally prolonged with a 25 cm long and 11 cm wide grounded stainless steel extension, which ends with a borosilicate window. Lateral access ports enable to place a DN-50 borosilicate window on the side as well. The magnetic field being divergent at this location, the plasma is in direct contact with the ground. Hence, losses at the walls are increased, and the magnetic field is non-uniform on this side. Yet, this modification allows to observe qualitatively the effect of the magnetic field direction, similarly to the above-mentioned figure IV.4.

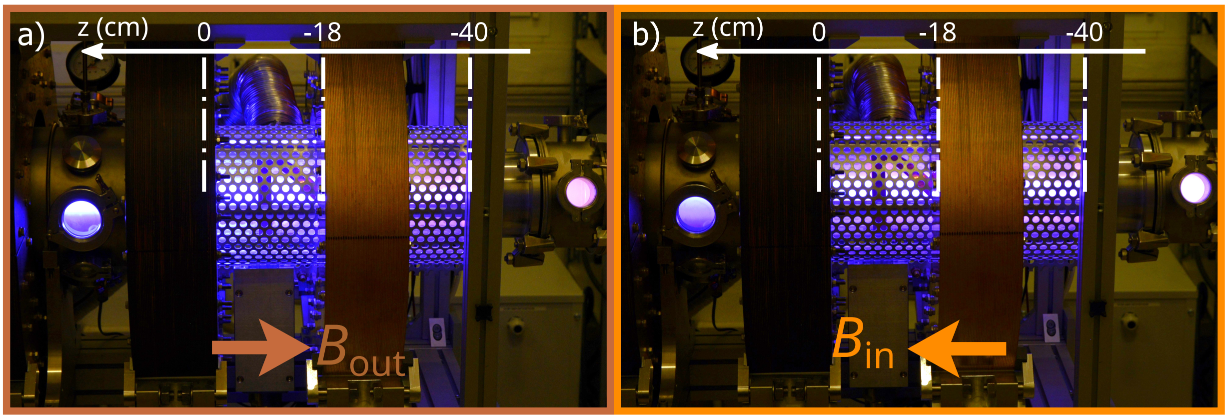

FIGURE IV.8 – Pictures of the right-handed half-helical antenna operating in the *a)* B_{out} configuration and the *b)* B_{in} configuration.

The experimental parameters are $p_0 = 0.13$ Pa, $B = 900$ G and 1.4 kW. The left picture corresponds to the B_{out} configuration, while the right picture is the B_{in} configuration. Both pictures are shot with the same camera placed on a tripod, with identical exposure time, shutter speed and ISO parameters. The helicon antenna is located at $z = -18$ cm, and is visible through the Faraday cage. Lateral windows placed on both sides enable to observe the plasma core in both directions. The left picture IV.8a) displays a striking contrast between the left and the right sides. The left side, which should be associated to a predominant $m = +1$ mode excitation, presents a bright blue core, while the plasma colour on the right side is pale pink. On the other hand, the right picture IV.8b) shows less disparity. Both sides are luminous and exhibit a blue colour. Comparatively to the B_{out} configuration, the plasma diffusion chamber side is darker, which is consistent with the major excitation of the $m = -1$ azimuthal mode. The extension side , which is associated to the $m = +1$ mode, is brighter than in the B_{out} case. However, no clear blue core is observed there, allegedly because of important losses at the walls and the weaker divergent magnetic field.

These observations are in accordance with the asymmetric $m = +1$ and $m = -1$ helicon modes excitation using a half-helical antenna [Gra+23]. Surprisingly, a bright plasma core is still observed in the plasma diffusion chamber in the B_{in} configuration, despite the presumed excitation of a poorly efficient $m = -1$ azimuthal mode.

IV.3.1.2 E-H-W transition

A major feature of the helicon plasma is the E-H-W transition illustrated in figure IV.5a). This signature was investigated for B_{out} and B_{in} configurations in absence of the source tube extension. A Langmuir probe is placed at the plasma core and biased at -60 V using a DC battery. The ion saturation current $I_{is} \leq 10$ mA is collected and measured with a shunt resistor of 20 Ω. The plasma was operated at 360 G with a 5 s ramp up in input power up to 1.75 kW, then followed by a 5 s ramp down. The matching box capacitors were left constant for all the experiments conducted, and the reflected power was always lower than 10% during the plasma shot. A more optimal coupling to the plasma could be reached with an automated matchbox [Chi+99]. The effect of neutral pressure and the magnetic field direction on the E-H-W transition were explored. The ion saturation current as a function of the forward power is shown in figure IV.9a). The electron temperature at the plasma core ranging between 3 to 5 eV (see the following subsection IV.4.1), its influence is weak on I_{is}. By assuming that I_{is} is directly proportional to the plasma density n, the ion saturation is a reasonable proxy for plasma density measurement.

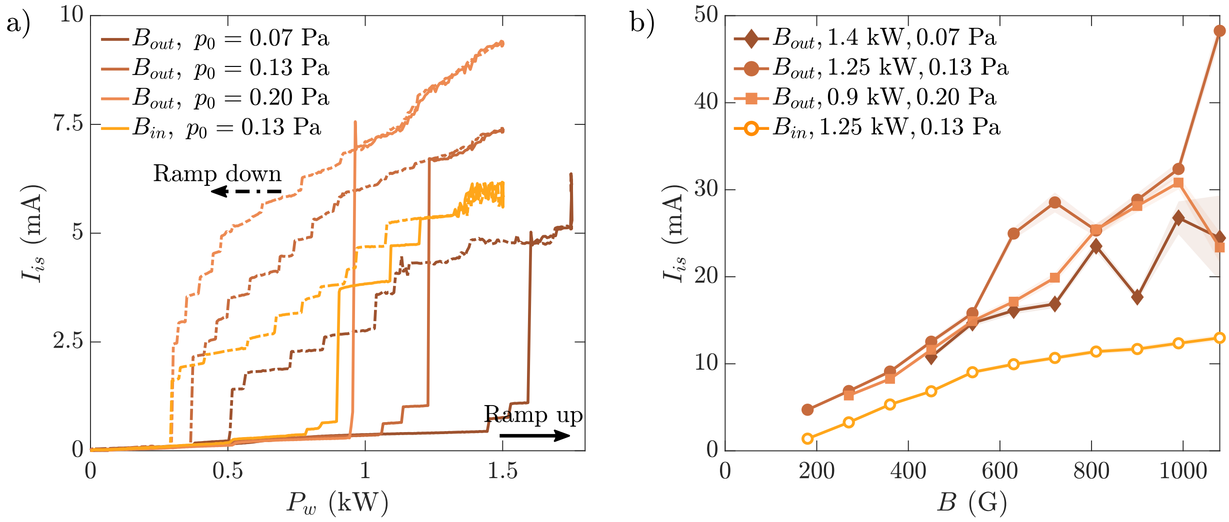

FIGURE IV.9 – *a)* Plasma density as a function of the input power for $B = 360$ G. Solid lines represent the power ramp up, dashed lines the power ramp down. *b)* Plasma density as a function of the external magnetic field for both magnetic configurations.

One can observe the sharp H-W transition at $P_w \geq 1$ kW. Similarly to the VKP-ICP case, an increase in pressure results in an increase in plasma density. During the power ramp down, the plasma discharge is sustained in this W mode before experiencing multiple transitions until $P_w \leq 0.5$ kW, where the high density W mode is lost. A strong hysteresis in the plasma density with respect to P_w is witnessed. It is caused by the centrally-peaked high plasma density of the W mode, which is favourable to the propagation of helicon waves. Consequently, the transition to a W mode is a stabilising feedback loop. Besides, the W mode exhibits multiple discontinuities in I_{is}, evidencing the existence of W-W transitions. These successive transitions appear unambiguously at low pressure, while they are less significant at higher pressures. This observation was previously reported in other experiments [Chi+99]. Indeed, a lower collisionality means that the damping of the helicon wave is reduced, so the standing helicon wave exists in the whole cavity. An excellent coupling between the helicon wave and the plasma cavity can be achieved. It results in a high selectivity of the standing helicon wave, thus in very stable W modes and significant transitions between W modes. One can also remark that the B_{in} configuration shows such E-H-W transitions, in spite of the major excitation of the poorly efficient $m = -1$ mode.

IV.3.1.3 Effect of the magnetic field intensity

The ion saturation current evolution at the plasma core in helicon mode depending on B was studied as well with the same experimental set-up. Both magnetic field configurations and the effect of the neutral pressure were investigated. The results are presented in figure IV.9b). The pale areas represent the standard deviation on I_{is} due to plasma density and electron temperature fluctuations.

The expected increase in plasma density with the magnetic field is highlighted here. The linear dependence of n with regard to B for a given helicon mode predicted from equation IV.7 is a fair approximation, particularly for the B_{in} configuration. However, deviations to this trend are observed, for instance at 630 G for the B_{out} and 0.13 Pa case. This is commonly attributed to the excitation of another helicon mode, hence to a brutal change in n. This argument is once again supported by the smoother evolution at higher pressure. As a high collisionality impedes a strong coupling with the plasma cavity, less mode transitions are witnessed and the linear evolution of n as a function of B is more robust.

Besides, the plasma density deviates from this linear evolution at high magnetic field. This is attributed to the growth of various instabilities, which are revealed by the strong standard deviation at $B > 900$ G and 0.07 Pa for instance. This feature was observed in other helicon discharges [Lig+01]. It is most certainly due to an increased radial anomalous transport and enhanced losses at the vessel walls, thus a reduced core plasma density. These instabilities will be addressed in chapter V. One can also mention that a strong neutral depletion could also cause the plasma density saturation at high magnetic field [Mil+98a].

No longitudinal measurements were conducted with the helicon plasma. The axial homogeneity of the plasma properties and the propagation of helicon waves were not assessed. However, the axial non-uniformity of helicon plasma depending on $m = +1$ and $m = -1$ modes has been proven many times [Che+95 ; Gra+23]. An interesting perspective would be to document this further using Langmuir, emissive and B-dot probes on the longitudinal translator.

IV.3.2 Operation diagram

IV.3.2.1 Direction of the magnetic field

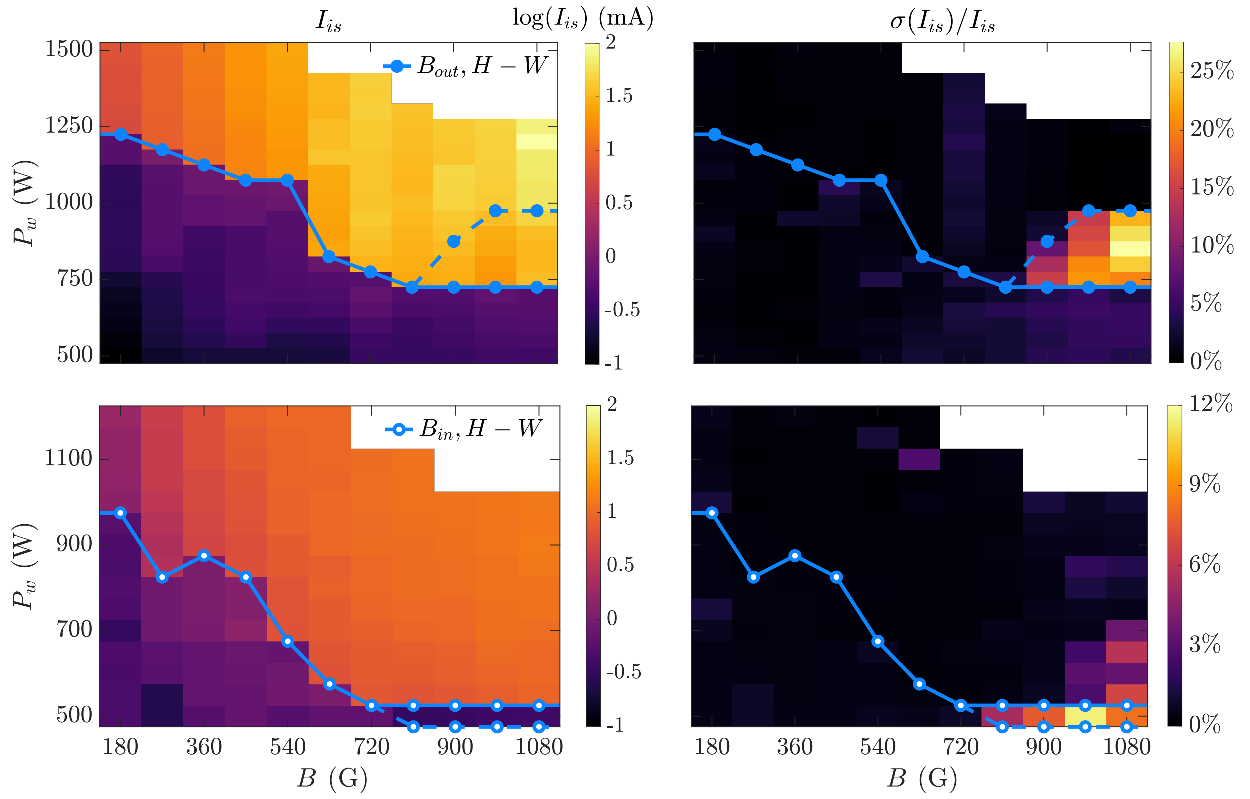

FIGURE IV.10 – *Left column:* Ion saturation current at the plasma core in logarithmic scale as a function of P_w and B for $p_0 = 0.13$ Pa in the B_{out} (*top row*) and B_{in} (*bottom row*) configurations. *Right column:* Relative standard deviation of the corresponding ion saturation current. The solid lines represent the H-W transition, the dashed lines highlight strong fluctuations domains at the H-W transition.

An extensive documentation of the helicon plasma operation regime was conducted using a negatively biased Langmuir probe at the plasma core. The experiment is similar to the one presented previously. The influence of the input power P_w, the external magnetic field B, the neutral pressure p_0 and the magnetic field configuration B_{in} or B_{out} were explored. B lies between 180 G and the maximal hard-ware limited value 1080 G. P_w was limited to 1.6 kW to avoid damaging the probe, and the pressure was set between 0.07 and 0.20 Pa.

The ion saturation current I_{is} at $p_0 = 0.13$ Pa in both magnetic field configurations is displayed in the left panel of figure IV.10. The blank areas were not explored. Note that the colourmap corresponds to the logarithmic value of I_{is}. The right panel shows the normalised fluctuations of the ion saturation current $\sigma\left(I_{is}\right)/\langle I_{is}\rangle$ expressed in percentage, presumably attributed to plasma density fluctuations.

The solid line highlights the sharp H-W transition, with at least a tenfold increase in I_{is}. The W mode transition occurs at a lower power when B is increased. It seems counter-intuitive since the plasma density increases dramatically with the magnetic field (see figure IV.9), so one may expect the power required for the H-W transition to increase with B. On the other hand, the plasma density profile is much more condensed at high magnetic field. At fixed power and increasing magnetic field, the energy of the plasma is condensed at its core, but the overall volume integration of the plasma energy remains similar. So, the focusing of the plasma core balances the higher plasma density. Furthermore, an unstable domain at high magnetic field and low power is identified. The instability domain delimited by the dashed lines is associated to a fast blinking of the blue core and strong fluctuations in I_{is} up to 30%. The influence of the neutral pressure will be discussed in the following subsection, and the existence of these instabilities will be addressed in chapter V.

Similarly, the plasma operation regime in the B_{in} configuration is mapped in the bottom row of figure IV.10. For a relevant comparison, the bottom left panel displays the ion saturation current with the same logarithmic scale applied for the top left panel. The right panel shows the relative fluctuations in I_{is}. The plasma density jump is less important, yet a clear H-W transition is observed. It occurs at a lower power input compared to the B_{out} configuration, but the I_{is} values in the W mode are reduced. On the other hand, the I_{is} fluctuations are three times smaller, and the unstable domain is narrower. Instabilities were rare or not observed at other neutral pressures. It confirms once again the effect of the $m = -1$ and $m = +1$ helicon modes in the generation of a high density helicon discharge, but the unexpected stability and the lower required power in the B_{in} configuration are valuable experimental features.

IV.3.2.2 Influence of pressure

The influence of pressure on the H-W transition in configuration B_{out} is shown in figure IV.11. The top row corresponds to $p_0 = 0.20$ Pa pressure, , the middle row to $p_0 = 0.13$ Pa and the bottom row to $p_0 = 0.07$ Pa. Solid and dashed lines are used to identify respectively the H-W transition and the instability domain as previously. The middle row enables a direct comparison of these domains on the same graph. No significant instability were witnessed above $p_0 = 0.20$ Pa. Higher pressures were not explored to avoid strong thermal constraints on the experimental device. The helicon mode was hardly achievable at pressures below 0.07 Pa.

The power required for the H-W transition is lowered when the neutral pressure is increased. This latter effect is consistent with previous studies [Chi+99]. It could be explained by a higher plasma density at high pressure in the E and H modes, thus enabling to reach the plasma density threshold for helicon wave propagation sooner. Besides, the instability domain is highly sensitive on p_0. The instability is particularly intense and its domain is wider at 0.13 Pa. The increase in pressure seems to reduce that effect, since the fluctuations are smaller and the instability domain is translated to lower power and higher magnetic field values. On the other hand, a reduced pressure induces stronger fluctuations, reaching up to 35% (bottom right panel in figure IV.11). Yet the instability domain is reduced, but most certainly because of the H-W transition that requires higher power and magnetic field.

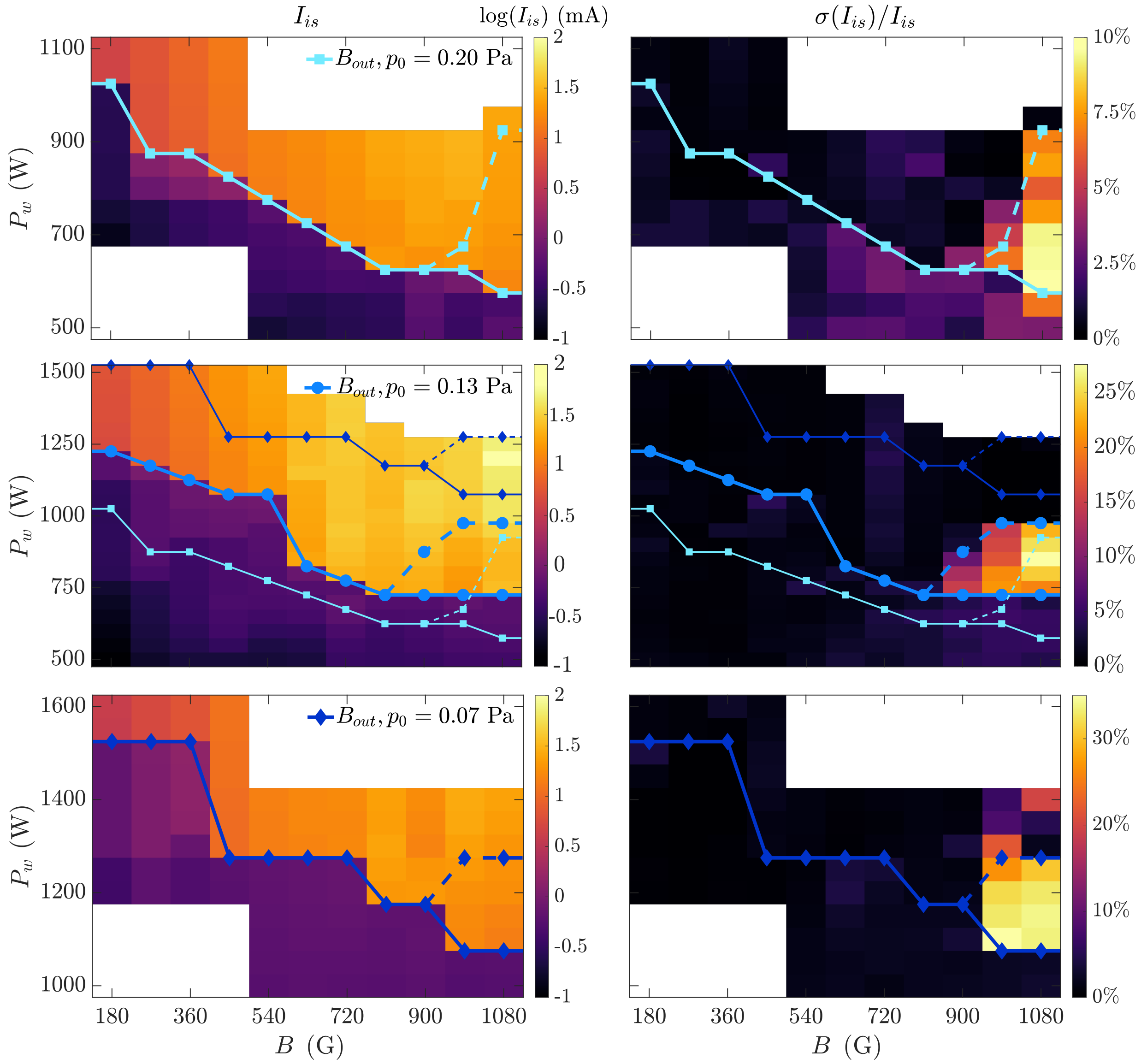

FIGURE IV.11 – *Left column:* Ion saturation current at the plasma core in logarithmic scale as a function of P_w and B for $p_0 = 0.20$ Pa (*top row*), $p_0 = 0.13$ Pa (*middle row*) and $p_0 = 0.07$ Pa (*bottom row*) in the B_{out} configuration. *Right column:* Relative standard deviation of the corresponding ion saturation current. The solid lines represent the H-W transition, the dashed lines highlight strong fluctuations domains at the H-W transition.

IV.4 Helicon mode characterization

IV.4.1 Mean profiles of plasma properties

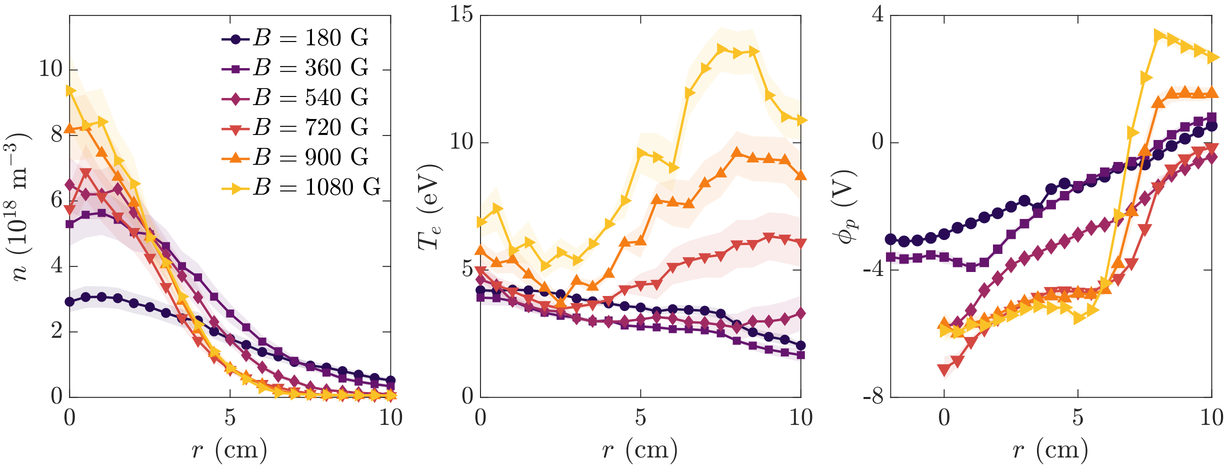

FIGURE IV.12 – Plasma properties in the helicon mode depending on the magnetic field, for the B_{out} configuration at $p_0 = 0.13$ Pa.

The mean radial profiles of the helicon plasma properties were measured using a compensated Langmuir probe and an emissive probe. For any value of the magnetic field B, powers were such that measurements were conducted in the W mode, close to the H-W transition. As discussed previously, the probes inserted may be intrusive and displace the transition to the helicon mode up to 100 W. Hence, the power P_w required for the H-W transition may differ slightly for a Langmuir or an emissive probe measurement. Here, the plasma properties are assumed to be the same between the Langmuir and the emissive probe measurements, and their results will be confronted directly. The typical powers used extend from 0.8 to 1.4 kW depending on B.

The plasma properties in configuration B_{out} for a pressure $p_0 = 0.13$ Pa are shown in figure IV.12. The rise in density with the magnetic field appears clearly. Besides, the helicon blue core tight focusing is evidenced as well, as the parabolic density profiles becomes narrower with B. The Full Width at Half Maximum (FWHM) is reduced from 4 cm to 2.5 cm with B. The absolute values evidence a high ionisation rate. In absence of plasma, the neutral density at 0.13 Pa is estimated at 3.2×10^{19} m^{-3}. However, the ionisation and the heating of the neutrals from collisions with ions cause the neutral density to drop of a few tens of percent [Hou+12; Fru17]. Then, the maximal plasma density at the center is expected to be about 1.5×10^{19} m^{-3}, meaning that the ionisation degree at the core reaches more than 50%.

Electron temperature exhibit a high degree of reproducibility and appear to be reliable. The fits realised for electron temperature measurements lead to accurate measurements and low error bars, especially when $n \gtrsim 5 \times 10^{18}$ m^{-3}. It confirms the discussion on the compensated Langmuir probe efficiency introduced in subsection I.3.1.1. Radio-frequency fluctuations grow with B, preventing a good estimation of T_e at the plasma edge for $B > 720$ G. Another reason might be the growth of the kHz fluctuations that are investigated in chapter V, which are not compensated by the probe design. T_e beyond 5 eV seem unreasonable and should be interpreted with caution. Overall, the electron temperatures exhibit consistent values, ranging from 4 eV at the plasma core to 2 eV at the edge. The radial decrease of T_e is rather linear, and no longer indicates the local heating at $r \simeq 5$ cm seen in the VKP-ICP case. This observation cannot be extended for $B > 720$ G however because of questionable T_e values.

Plasma potential profiles are linear from $r = 0$ to 10 cm for $B \leq 540$ G. The radial electric field is homogeneous and grows with B. For higher magnetic fields, a steep increase of a few volts over 1 to 2 cm appears at the plasma edge. A potential well may form at $r = 5$ cm for very high magnetic fields. It results in a non-uniform radial electric field, and thus a strong radial shear due to a heterogeneous $\mathbf{E} \times \mathbf{B}$ drift. As will be shown in chapter V, this strong electric field correlates with the existence of low-frequency oscillations, which could be consistent with Rayleigh-Taylor or Kelvin-Helmholtz instabilities. Fluctuations of ~ 1 V amplitude in ϕ_p are measured. Besides, the effect of the power on plasma potential profiles is briefly discussed in appendix figure C.4. The potential well at $r \simeq 5$ cm appears to be slightly modified, but the sparse data set cannot allow a rigorous discussion on that matter.

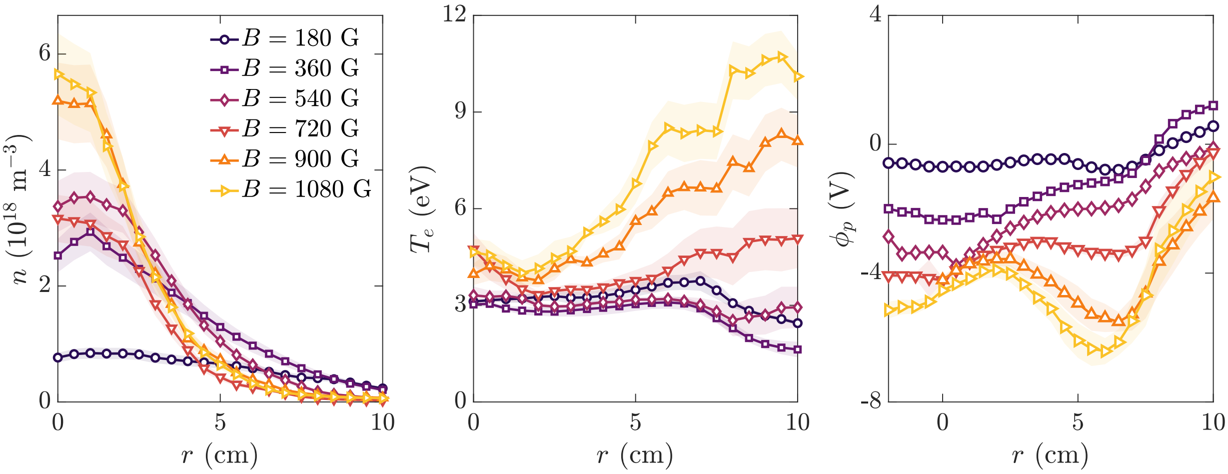

FIGURE IV.13 – Plasma properties in the helicon mode depending on the magnetic field, for the B_{in} configuration at $p_0 = 0.13$ Pa.

The plasma properties measured in the B_{in} configuration are displayed in figure IV.13. The global shapes of the plasma density profiles are very similar, except for the low magnetic field $B = 180$ G which is more homogeneous. Once again, the plasma density profile is narrower at higher magnetic field. Indeed, the FWHM decreases from $r = 4.5$ to 2.5 cm when B increases. But plasma densities are about twice smaller than for the B_{out} configuration. The powers applied for the B_{in} configuration match the ones used for the B_{out} configuration with less than 100 W difference (figure IV.12). So, even though the density profiles in the B_{in} configuration suggests the existence of an helicon mode, it hints at a more optimal ionisation in the B_{out} configuration. The efficiency of the B_{in} configuration for helicon plasma discharges remains surprisingly high, since it is expected to be unfavourable to excite the W mode, as mentioned in subsections IV.1.5 and IV.3.1.

The electron temperatures reported are homogeneous across the plasma column at approximately 3 eV, which is about 1 eV smaller than the B_{out} case. Once again, exceptionally high temperatures are observed at the plasma edge for $B \geq 720$ G. This is allegedly caused by an insufficient RF compensation of the Langmuir probe. Consequently, the rise in T_e at the plasma core up to 4.5 eV for $B \geq 720$ G should be interpreted with vigilance.

Plasma potential is lowered when B is increased. More importantly, it exhibits a transition from a monotonous to a non-monotonous profile at $B = 720$ G, with the appearance of a deep potential well at $r \simeq 5$ cm. This magnetic field value correlates with the growth of strong plasma potential fluctuations, as shown by the large extension of the shaded areas for high magnetic field values. Like the B_{out} case, the high radial electric field and its important gradient may trigger low-frequency instabilities, which will be discussed in chapter V.

The effect of pressure on plasma potential profiles is presented in figure IV.14 for the B_{out} confi-

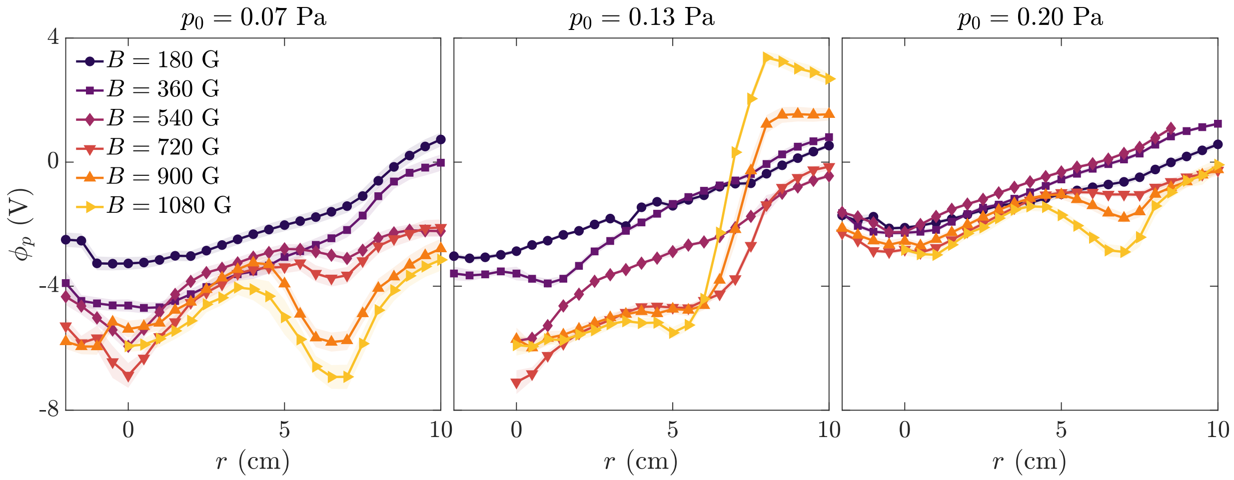

FIGURE IV.14 – Plasma potential profiles for various magnetic field B and neutral pressure p_0 for the B_{out} configuration.

guration. The overall behaviours of ϕ_p with respect to B are similar for all pressures. A significant potential well appears at the plasma edge, while the plasma potential at the core is lowered with B. The increase of p_0 induces more homogeneous plasma potential profiles. Indeed, the extent of ϕ_p variations with regard to B is reduced, the appearance of the potential well requires a more intense magnetic field, and the gradients are damped. One plausible explanation is that particles transport due to collisions is more important, so that the radial transport is enhanced and the plasma is less confined. The effect of the electric field on particles transport is less prominent, hence the smaller variations in ϕ_p. Besides, fluctuations are mitigated at high pressures. These concurrent findings support the hypothesis of low-frequency oscillations excitation due to a $\mathbf{E} \times \mathbf{B}$ induced radial shear.

IV.4.2 Helicon wave structure identification

The above-mentioned phenomenology and the mean profiles of plasma properties suggest a clear W mode in the B_{out} configuration, but also an unexpected W mode in the B_{in} configuration, which should favour the poorly efficient $m = -1$ mode (see subsection IV.1.5). A deeper investigation of the helicon wave was conducted by studying the helicon magnetic wave structure using a B-dot probe.

B-dot radial scans were performed for various experimental conditions. The Fourier transform of the measured magnetic field is shown in figure IV.15a) for a quiescent helicon plasma regime (180 G, 0.13 Pa and 1.8 kW). The signal component is observed primarily at $f_0 = 13.56$ MHz, and secondarily at the f_0 harmonics. The signal-to-noise ratio lies between 10 and 100. Amplitude modulation of the 13.56 MHz signal may emerge as a signature of low-frequency instabilities, resulting in secondary peaks around the f_0 central peak. However, the goal of the B-dot probe is not to study thoroughly these oscillations, hence no deeper investigation will be dedicated to this particular matter. The signal were band pass filtered around f_0 with a 2 MHz bandwidth frequency. The amplitude of the helicon wave components is computed using the standard deviation of the signal.

The polarisation and the amplitude of the helicon wave were analysed. As a reminder, the magnetic field is decomposed as such: $\mathbf{B}_0(r) = B_r(r)\mathbf{e}_r + B_\theta(r)\mathbf{e}_\theta + B_z(r)\mathbf{e}_z$. B_θ is noted positive for a right-handed polarisation with respect to $\mathbf{B}$ by convention. As a reminder, the $m = +1$ helicon mode is right-handed polarised at the plasma core. (B_r, B_θ, B_z) amplitudes for the B_{out} and

B_{in} configurations at 180 G, 0.13 Pa and respectively 1.8 kW and 1.9 kW are displayed in figure IV.15b) and IV.15c). High powers were used to trigger unambiguously the W mode. They can be compared to the expected wave field structure previously presented in figure IV.2.

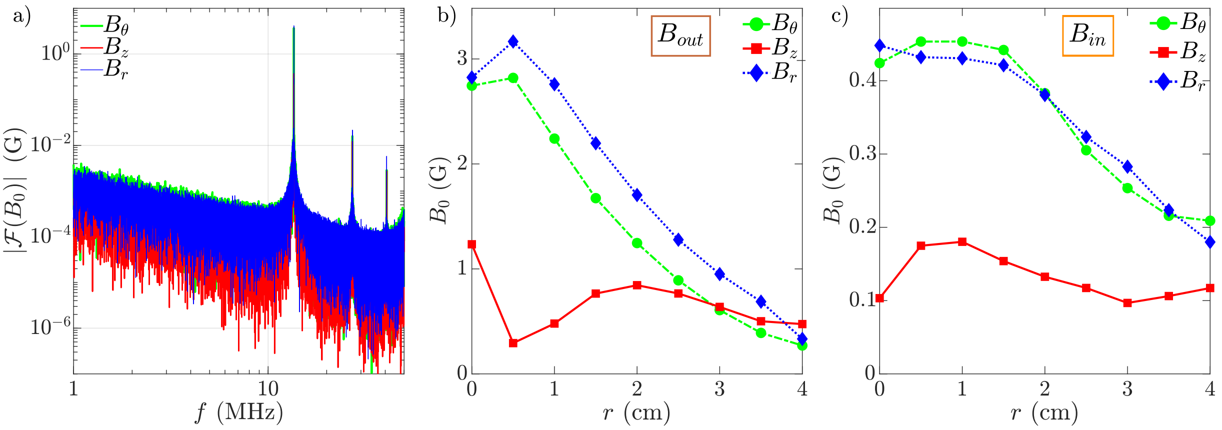

FIGURE IV.15 – *a)* Fourier transform of the acquired magnetic field at the plasma core for the B_{out} configuration. $B = 180$ G, $P_w = 1.8$ kW and $p_0 = 0.13$ Pa. *b)* Magnetic helicon wave structure for the B_{out} configuration, at 180 G, 1.8 kW and 0.13 Pa. *c)* B_{in} configuration, at 180 G, 1.9 kW and 0.13 Pa.

Notice that the helicon wave amplitude is one order of magnitude greater in the B_{out} configuration than in the B_{in} configuration. The B_{out} case exhibits a helicon structure close to the analytical profile for $m = +1$. Indeed, B_r and B_θ are alike, with a slight predominance of B_r. B_z has a much smaller amplitude and peaks at the blue core periphery. Moreover, the polarisation is right-handed at the plasma core as expected. The helicon wave is successfully identified as a $m = +1$ mode.

On the other hand, the B_{in} configuration reveals a more complex wave structure. The amplitude profiles are wider, which is usually associated to a $m = +1$ helicon mode. Once again, the ordering in the magnetic field amplitudes are similar, namely $B_r, B_\theta > B_z$. However, B_z seems to be more centrally-peaked, contrarily to the previous case. Eventually, $B_\theta > 0$, meaning that the polarisation with respect to $\mathbf{B}$ remains right-handed, hinting at a $m = +1$ mode propagation.

The strong signature of a $m = +1$ mode in the B_{out} configuration is conform to the expectations. It is consistent with the use of a selective half-helical antenna, and explains the high-density W mode documented in figure IV.10. However, the B_{in} case is surprising. While a $m = -1$ mode is expected, a right-handed polarised wave is observed. The wave structure differs from the analytical profiles, especially at magnetic fields higher than 700 G (see figure C.6 in appendix). Besides, a lower plasma density is reached in the B_{in} case, which is consistent with previous articles [Yas+94 ; Shi+96] [2]. The privileged explanation for this unexpected $m = +1$ helicon mode in the B_{in} configuration is a stronger axial damping of the $m = -1$ mode compared to the $m = +1$ mode [Shi+96 ; Gra+23]. Hence, the excited $m = -1$ mode may decay before reaching the B-dot probe situated 70 cm away from the antenna. Then, the slight $m = +1$ excitation [Kam+96] due to an asymmetry in the antenna design for instance propagates further along the plasma column. Consequently, the measured helicon mode at the probe location appears to be the $m = +1$ mode. This assumption could be tested by investigating the helicon wave propagation along the longitudinal axis of the plasma in both magnetic configurations, and the corresponding axial plasma density profiles.

A few remarks can be added. Firstly, the helicon wave propagation investigation in the inductive mode revealed to be unfruitful. Even though the polarisation hints at $m = +1$ modes in any experimental configuration, the wave structures are far from the analytical profiles. Secondly, the

---

[2] Reminder: the $m = +1$ and $m = -1$ convention is inverted in the works from Yasaka and Hara.

dielectric end at the source tube certainly influences the helicon plasma generation. The helicon wave reflected at the dielectric end near the antenna has already been reported to affect the helicon plasma density for instance [Che15]. Finally, the B-dot probe is 5 mm wide and is rather intrusive. Since the signal-to-noise ratio is high, a smaller B-dot could be designed in order to perturb less the helicon plasma.

IV.5 Plasma potential control using an emissive cathode

The role of an emissive cathode on the plasma potential of a helicon plasma was briefly investigated. The project was conducted by Vassili Desages during a a Master internship I co-supervised. The main goal of this short project was to verify the influence of an emissive cathode on the helicon plasma properties.

The experimental arrangement is the same than the one used in chapter III. The cathode was placed at the end of the column, facing the radio-frequency source. The plasma was generated at $p_0 = 0.13$ Pa, $B = 180$ G and $P_w = 1.3$ kW in the B_{out} configuration. The voltage bias of the cathode was set at $V_b = -60$ V, while the heating current was modified to control the injected current I_b. Radial profiles of the plasma properties were acquired using a compensated Langmuir probe and an emissive probe.

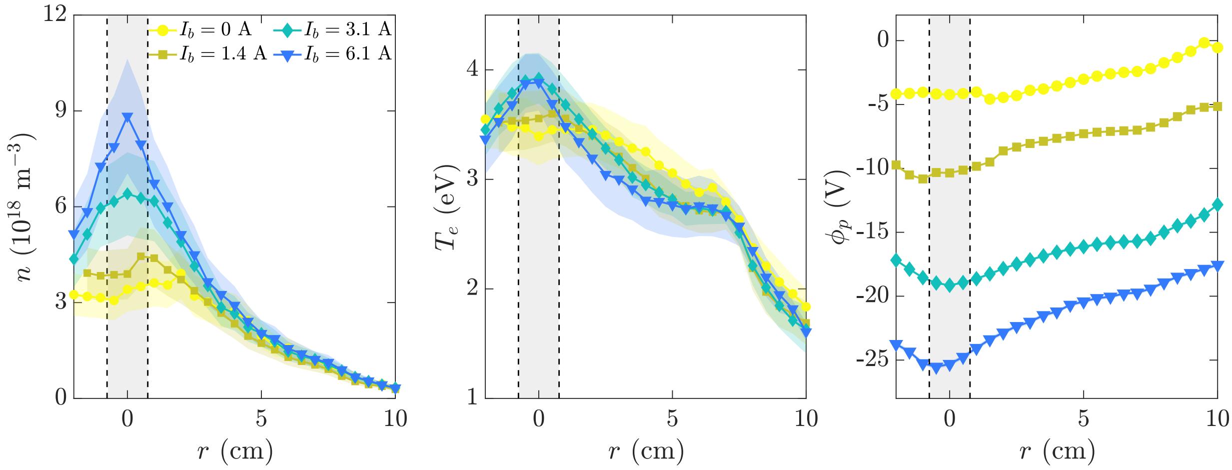

FIGURE IV.16 – Plasma properties profiles for a helicon plasma in the B_{out} configuration and an injected current I_b from the cathode. The cathode location is indicated via the grey area. The experimental parameters are $p_0 = 0.13$ Pa, $B = 180$ G, $P_w = 1.3$ kW and $V_b = -60$ V. *a)* Plasma density and *b)* electron temperature from compensated Langmuir probe measurements. *c)* Plasma potential from emissive probe measurements.

As observed with the inductive source, the plasma density at the center is increased three times with an injected current $I_b = 6.1$ A. The plasma diffuses up to $r \simeq 4$ cm, and no significant variation of n is witnessed beyond. Besides, electron temperature is not modified except at the cathode location, where a slight increase from $T_e = 3.5$ eV to 4 eV is observed. The trends observed are similar to the ones presented in chapter III. However, the increase of T_e at the plasma core is minor. The results presented here are computed from the full $I - V$ characteristics, and are more reliable than the 5-tips probe measurements, which may explain the difference with the data presented in figure III.8 for the VKP-ICP device.

Concerning plasma potential, the main features observed in chapter III are also reported here with the helicon source. $\phi_p(x = 10 \text{ cm})$ shows that a large anode sheath grows and appears to saturate with I_b. The radial potential drop $\Delta\phi_p = \phi_p(x = 10 \text{ cm}) - \phi_p(x = 0.75 \text{ cm})$ increases from 4 V to 7 V. A more extensive data set of floating potential profiles ϕ_f is available in appendix figure C.5. It suggests once again a more efficient plasma potential drive with higher B and lower p_0. Figure IV.16 can be directly compared to figure B.2, where n, T_e and ϕ_p are shown for the VKP-ICP set-up operated under similar experimental conditions. In the case of the helicon plasma, the anode sheath is strongly increased. On the other hand, $\Delta\phi_p$ is of the same order of magnitude. This latter result is not surprising, since plasma properties are not far from the ones in the VKP-ICP case. However, the differences in plasma density profiles modify the local perpendicular resistivity (see equation III.5), and should influence the plasma potential distribution resulting from the injection of electrons.

CHAPITRE

V

LOW-FREQUENCY FLUCTUATIONS INVESTIGATION

Les fluctuations basse-fréquences dans l'expérience VKP-HS1 sont étudiées. Après une courte revue des ondes et instabilités au sein des plasmas hélicons, une étude expérimentale basée sur l'exploitation d'imagerie rapide et de mesure de sondes a été réalisée. Des oscillations de relaxation H-W et W-W ont été observées. De plus, des oscillations basse-fréquences ont été étudiées à des champs magnétiques supérieurs à 720 G. Une instabilité de Kelvin-Helmholtz en périphérie du cœur bleu hélicon, ainsi qu'une instabilité de Rayleigh-Taylor en périphérie du plasma sont identifiées. Enfin, l'existence d'une forte instabilité de cœur à $B = 1080$ G est analysée.

V.1 Instabilities in helicon plasmas

V.1.1 Effect on global plasma dynamics

Instabilities are of prime interest for understanding plasma confinement and energy transport. The phenomenology of plasma waves and instabilities is broad, and a comprehensive review of the low-frequency (LF) oscillations in plasmas is not intended here. However, a brief context and summary of relevant LF oscillations is drawn in this section.

LF oscillations are highly sensitive to experimental parameters, so the exact plasma properties need to be specified. Let us consider first fusion plasmas. The multi-scale nature of hot fusion plasmas lead to a wide variety of oscillations. One can mention Edge Localized Modes (ELMs) which grow at the pedestal, *i.e.* the transition region from the hot plasma core to the cold plasma edge [Zoh96]. ELMs can be considered as LF oscillations, meaning that $\omega \ll \omega_{c,i}$. The emergence of coherent modes increases the radial outward transport, which can be detrimental to the stability of the high confinement H mode in tokamaks. Furthermore, the shear induced by strong LF oscillations can generate vortices and a transition to turbulence [Bur+05 ; Tyn+09]. The resulting turbulent transport causes an efficient diffusion of the plasma core energy to the walls [Doy+07 ; Zwe+07]. Hence, the plasma confinement is degraded and the H mode can no longer be sustained. Properties of the turbulent transport has been widely investigated [Con+94 ; Gar+03] but is still an active domain of research. One of the main difficulty is the non-linear coupling between the multiple instabilities. For instance, the drift wave induced turbulence was evidenced to trigger multiple supplementary instabilities [Hor99] or zonal flows [Dia+05]. In the latter case, these zonal flows form transport barriers, which limit the turbulent transport. Another complex example is the enhanced confinement of the plasma core via the formation of a transport barrier by applying a strong peripheral $\mathbf{E} \times \mathbf{B}$ shear [Bur97]. The shear excites a Kelvin-Helmholtz instability which breaks the large size turbulent vortices. Hence, the turbulence-driven transport is significantly reduced. Similar experimental documentation of the transition from a low confinement L mode to the H mode using a turbulence-driven shear flow to create a transport barrier can be found in recent experimental studies [Yan+14].

A much simpler configuration for the investigation of LF oscillations is the linear device. The magnetic field curvature generates magnetically-induced drifts, which may trigger various instabilities in toroidal devices. Its absence in a linear experiment simplifies the instability phenomenology. However, the use of linear devices is highly relevant for many fundamental investigations concerning plasma stability and transport at the cold edge of fusion plasmas. The non-uniformity of plasma properties generate plasma density gradients, which are prone to excite drift waves (DW). Similarly to tokamaks, linear plasmas experience a significant $\mathbf{E} \times \mathbf{B}$ drift, which results in the rotation of the plasma column. The induced centrifugal force may be responsible for instabilities. A mechanism similar to the Rayleigh-Taylor (RT) instability has been reported and extensively studied. Moreover, the non-uniformity of the plasma rotation induces a differential shear, which may excite a Kelvin-Helmholtz (KH) instability. The complete phenomenology of instabilities in a linear device is wide, and each LF oscillation requires a dedicated study for a confident identification.

The origin of LF oscillations is determined by measuring several quantitative criteria. The computation of growth rates, the analysis of the phase velocity, the specific scale and location of the oscillations, the intensity of the plasma density or potential fluctuations are multiple evidence for the oscillations characterisation. A comprehensive review will not be provided here, but a physical explanation and a short summary of several relevant instabilities will be presented. Three instabilities will be addressed, namely the drift waves, the KH instability and the RT instability. A thorough discussion can be found in dedicated works [Jas72 ; Tha+14 ; Vin21].

V.1.2 Review of LF oscillations

V.1.2.1 Drift waves

Drift waves arise from the plasma pressure gradients, and are ubiquitous in plasma physics. It is a topic that has been extensively addressed [Hor99 ; Tyn+09]. To understand the physical origin, let us assume a non-uniform collisionless plasma, of equilibrium plasma density n and homogeneous electron temperature T_e. According to Maxwell-Boltzmann equation, the local density of the plasma reads

$$n(x) = n \exp\left(\frac{\phi(x)}{T_e}\right) \tag{V.1}$$

If one assumes an equilibrium plasma potential $\phi = 0$ and small perturbations of the plasma density $\tilde{n}$ and potential $\tilde{\phi}$, $n(x)$ and $\phi(x)$ can be written $n + \tilde{n}$ and $\tilde{\phi}$. Consequently, the linearisation of equation V.1 yields

$$\frac{\tilde{n}}{n} \simeq \frac{\tilde{\phi}}{T_e} \tag{V.2}$$

Hence, the existence of a plasma density fluctuation leads to a plasma potential fluctuation. In magnetised plasmas, a resultant $\mathbf{E} \times \mathbf{B}$ drift arises. A schematics is drawn in figure V.1a), with a density gradient along $\mathbf{x}$ and a magnetic field along $\mathbf{z}$. Suppose the existence of a local density fluctuation, represented by the "+" sign in figure V.1a). As shown in equation V.2, it is accompanied by an outward electric field. It gives rise to a local rotational motion due to the resulting $\mathbf{E} \times \mathbf{B}$ drift. Moreover, since plasma density decreases with x, the net particles transport in the upper direction is smaller than the downward particles transport. Then, the initial local density anomaly is displaced along $+\mathbf{y}$. In conclusion, the drift wave propagates to the right. However, since the density and potential fluctuations are in phase, the computed growth rate of the drift waves is null. Besides, no net radial transport is driven. Indeed, the radial transport reads $\Gamma = \langle \tilde{n}\tilde{v}_r \rangle$, and $\tilde{v}_r$ is assumed to be governed by the $\mathbf{E}_\theta \times \mathbf{B}$ drift. Note that these DW can be driven by temperature fluctuations as well.

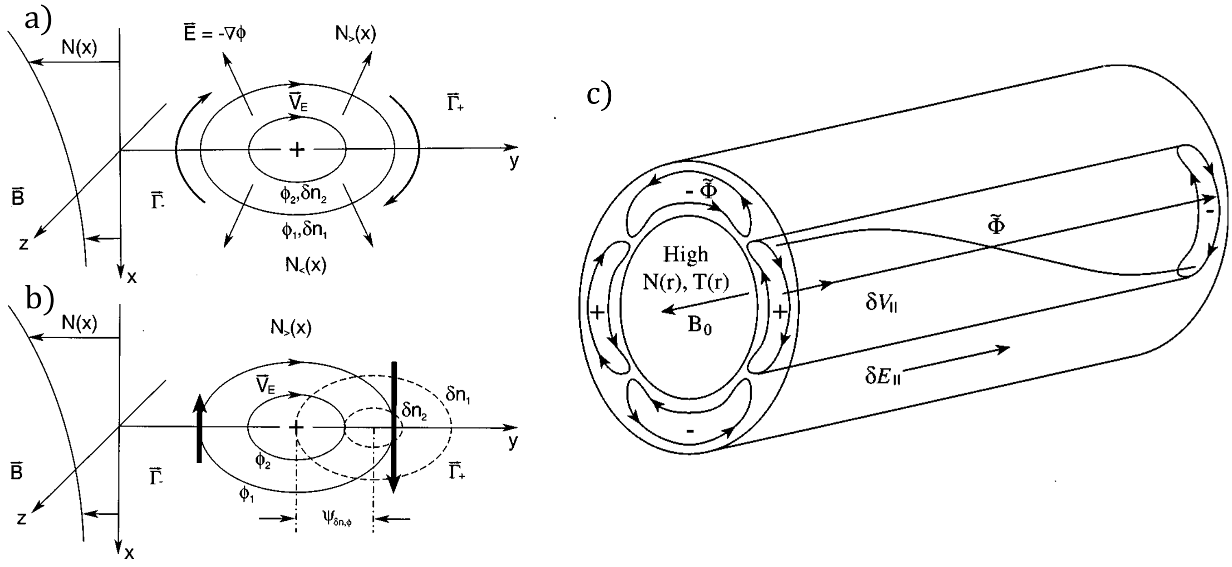

FIGURE V.1 – Schematics of the drift waves mechanism for the *a)* colisionless case and the *b)* resistive case. *c)* Schematics of a $m = 2$ DW mode across a plasma column. Taken from [Hor99].

Now, if one considers collisions, the drift wave becomes resistive. A delay exists between the density and the potential fluctuations, so that equation V.2 is modified as such

$$\frac{\tilde{n}}{n} \simeq \frac{\tilde{\phi}}{T_e}\left(1 + i\delta\right) \tag{V.3}$$

with $\delta \neq 0$ depending on the plasma collisionality. A net transport arises from the non-zero cross-phase shift $\xi\left(\tilde{n}, \tilde{\phi}\right)$ down the density gradient. A sketch of the resistive drift wave is presented in figure V.1b), where the downward net transport is emphasized.

Specific characteristics are typically observed with resistive drift waves [Hor99 ; Bel06 ; Tyn+09]. In the case of linear devices, DW are driven by the electron pressure gradient. Hence, DW propagate in the electron diamagnetic drift velocity, *i.e.* along $\nabla p \times \mathbf{B}$. Moreover, the computation of growth rates indicates the need for a cross-phase shift $\xi(\tilde{n}, \tilde{\phi})$ lower than $\pi/4$, and an optimal parallel wavelength $\lambda_{\parallel} = 2L$. Considering $k_\theta = m/r$, with m the azimuthal mode number, no constraints on m exists. Typical m modes reported in linear devices are usually lower than 5. The typical scale $\rho_S = u_B/\omega_{c,i} = \sqrt{T_e m_i/e}/B$ drives the DW, and a maximal growth rate is found for $k_\theta \rho_S \simeq 1$. Hence, the azimuthal number should be modified accordingly, with a m increase with magnetic field for instance. Drift wave turbulence has been evidenced to be mainly excited at such a scale [Tyn+06 ; Tha+14], and to drive multiple instabilities through non-linear interactions [Doy+07]. A sketch of the $m = 2$ drift wave mode across a plasma column can be found in figure V.1c), where one can notice the longitudinal wavelength $\lambda_{\parallel} = 2L$.

V.1.2.2 Kelvin-Helmholtz instability

The Kelvin-Helmholtz instability is a well-known fluid instability that finds its origin in the existence of a velocity shear. In magnetised plasma devices, a non-trivial electric field arises in the bulk plasma. Since plasma rotation is mostly driven by $\mathbf{E} \times \mathbf{B}$ drift, it results in a non-uniform rotation and a radial shear. Such instability might generate flute modes or convective cells, and thus impact significantly particles transport. The instability has been characterized extensively in plasmas, taking into account the effect of density gradients, finite Larmor radius, collisionality and interactions with other instabilities. Interested readers could refer to some reference articles [Ken+69 ; Jas72 ; Hor+87].

A few key features can be highlighted. The effect of the plasma density gradient on KH instability is found to be negligible. Long longitudinal wavelengths are favourable to the development of the KH instability, meaning that one should observe mainly $k_{\parallel} \simeq 0$. Besides, there is no restriction on the azimuthal wave number m. KH instability was found to excite a wide multiplicity of modes, but a predominant resonant mode, related to the extension of the shear layer, will emerge primarily. The larger is the shear layer, the lower is the azimuthal mode m [Jas72].

V.1.2.3 Rayleigh-Taylor instability

The Rayleigh-Taylor instability has been widely documented in fluid mechanics. This instability arises from the superposition of a heavier fluid on top of a lighter one. Any perturbation of the interface will lead to the growth of an instability and the interchange of the two fluids.

In rotating plasmas, the centrifugal force plays the role of the effective gravity $g_{eff} = v_\theta^2/r$. Moreover, the plasma core is denser and is ejected at the less dense plasma edge. Then, the mechanism appears to be similar to the common RT instability. However, magnetised plasmas being subject to various drifts, the description of the RT instability is more complex than for classical fluid mechanics [Bel06]. In toroidal devices, the magnetic curvature and its corresponding drift contribute to the triggering of the instability. In linear devices, the centrifugal force results in a gravitational drift, which will trigger the instability. Very much like the classical RT instability, the

Properties	Drift waves	Kelvin-Helmholtz	Rayleigh-Taylor
Localisation	Max($v_{d,e}$)	Max(v_θ)	Max($\left(\mathrm{d}n/\mathrm{d}r\right)/n$)
Phase velocity v_ϕ	$\frac{1}{1+k_\theta^2\rho_S^2}v_{d,e}+v_\theta$	$(0.1-0.4)\ \mathrm{Max}(v_\theta)$	v_θ
Growth rate γ	$\omega_{d,e}^2/\varsigma_\parallel$	$\frac{r}{2}\frac{\mathrm{d}}{\mathrm{d}r}\frac{v_\theta}{r}$	$\frac{\lvert v_\theta\rvert}{\sqrt{r}}\left(-\frac{\partial_r n}{n}-\frac{m^2}{4r}\right)^{1/2}$
$\left\lvert\frac{\tilde{\phi}_p}{T_e}\right\rvert / \left\lvert\frac{\tilde{n}}{n}\right\rvert$	$\lesssim 1$	$\gg 1$	$\gtrsim 1$
Cross-shift $\xi\left(\tilde{n},\tilde{\phi}_p\right)$	$[0;\pi/4]$	$[\pi/2;\pi]$	$[\pi/4;\pi/2]$
Parallel wave vector	$k_\parallel \simeq \frac{\pi}{L}$	$k_\parallel = 0$	$k_\parallel = 0$

TABLE V.1 – Main characteristics of the above-mentioned instabilities.

denser fluid is mixed with the lighter fluid. These types of instabilities were reported to drive flute modes [Bro+05] or oscillations with high azimuthal wave numbers [Tha+14]. Note that the instability is static in the frame of the plasma, meaning that the phase velocity is the plasma rotation velocity. A specificity of the RT instability lies in the low parallel wave vector $k_\parallel \simeq 0$. Besides, it mixes the effect of a strong rotation and a strong density gradient, and thus presents an interplay with DW and KH instability [Jas72].

V.1.2.4 Main characteristics

A summary of the main characteristics of the above-mentioned instabilities, inspired by multiple articles [Jas72 ; Tha+14 ; Vin21], is presented in table V.1. $v_{d,e}$ is the electron diamagnetic velocity in the azimuthal direction, which reads

$$v_{d,e} = \frac{T_e}{n}\frac{\lvert\nabla n \times \mathbf{B}\rvert}{B^2} = \frac{T_e}{n}\frac{\partial n/\partial r}{B} \tag{V.4}$$

Concerning the growth rate of DW, two new factors are introduced: $\omega_{d,e} = v_{d,e}k_\theta$ and $\varsigma_\parallel = \frac{k_\parallel^2}{k_\theta^2}\omega_{c,i}\omega_{c,e}/\nu_{ei}$. The free energy sources for each of these mechanisms are different, namely a density gradient for DW, a radial shear for KH instability, and a fast rotation coupled to a high density gradient for RT instability.

V.1.3 Case of helicon plasmas

V.1.3.1 Reported instabilities

Helicon plasmas in linear devices present notably strong radial density and potential gradients, hence they are particularly prone to excite LF instabilities. However, the literature on LF instabilities in helicon plasmas is scarce. A short review can be found in the textbook from Shinohara [Shi22]. Most probably because of the high density gradients, multiple works reported drift-wave dominated regimes. DW were positively identified in CSDX [Bur+05], HELIX [Sun+05] and VINETA [Sch+05 ; Gru+07] for instance. These waves were also seen to drive or to be coupled to other instabilities [Tha+14 ; Des+16]. DW-induced fluctuations were observed to drive zonal flows in LMD-U [Ara+16] or turbulence in CSDX [Tyn+06]. KH instability has also been commonly reported in various devices, such as HelCat [Des+16] or the helicon linear device operated by Light, Chen and Colestock at Los Alamos [Lig+01 ; Lig+02]. Yet it often presents complex behaviours and a strong interplay with drift waves. Similarly, the RT instability has been identified in a few other devices such as CSDX [Tha+14] or LEAD [Liu+23].

The effect of these instabilities on the global plasma equilibrium is of prime interest. The coincident observation of plasma density saturation and the growth of LF fluctuations was reported for magnetic fields superior to 600 G [Lig+01]. The enhanced anomalous transport resulting from the existence of large-scale coherent modes in the helicon device is presumably responsible for an increased particles flux at the wall [Lig+02]. The losses at the walls being enhanced, the helicon plasma density no longer increases with B and saturates. The effect of the RT instability in a helicon device on radial transport was also investigated [Liu+23] and exhibited an unexpected inward particle transport. In summary, a fine mapping of the instabilities involved is required for a complete understanding of the global plasma stability.

V.1.3.2 H-W oscillations

Another kind of LF oscillations are the H-W relaxation oscillations, which are specific to helicon plasmas. The operation in a given W mode requires a minimal plasma density, as mentioned in subsection IV.1.3. The transition from a low-density H mode to a high-density W mode causes an increased pressure and a high degree of ionisation at the plasma core. If the neutrals are sufficiently depleted so that the W mode can no longer be sustained, the plasma will experience a transition back to the H mode. Diffusion will slowly replenish the neutrals at the center, enabling the transition back to the W mode once again. Such H-W relaxation oscillations were witnessed and modelled for the first time by Degeling *et al.* [Deg+99a ; Deg+99b].

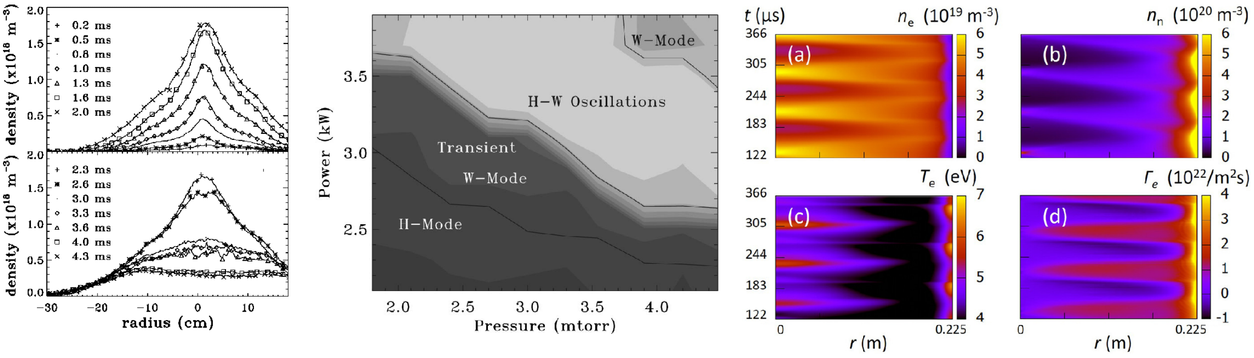

FIGURE V.2 – *(Left panel)* Plasma density profile during a H-W relaxation oscillation. *(Middle panel)* Phase diagram of the H-W oscillations at 120 G, the colourmap codes for the plasma density. Both graphs are taken from [Deg+99a]. *(Right panel)* Spatio-temporal profiles of the plasma density (a), neutral density (b), electron temperature (c) and inward electron flux (d). Taken from [Isa+19].

The typical frequency of these oscillations lie between 100 Hz and a few kHz. It is scaled on the diffusion coefficients and the size of the plasma chamber. These type of oscillations have been observed experimentally elsewhere [Zhu+23], emphasizing the essential role of the neutral density profile. Advanced numerical computations analysed the spatio-temporal plasma and neutral density profiles, and evidenced the existence of such H-W oscillations [Isa+19]. Consequently, these oscillations are very sensitive to the experimental parameters [Deg+99b]. An increased neutral pressure will ensure an enhanced neutral diffusion, and prevent the occurrence of these relaxation oscillations. An increased antenna power will provide a stable W mode. Numerical computation of the neutrals dynamic showed that in that case, the hollow density profile of the H mode is important enough to force a strong inward flux of neutrals [Isa+19]. Thus, neutral depletion is balanced by an increased neutral flux at the plasma core, so that the W mode is sustained. Ultimately, an increased magnetic field could trigger the H-W oscillations. Indeed, since n is proportional to B (equation IV.7), an increased magnetic field leads to an increase in ionisation at the plasma core, and consequently to a higher neutral depletion. However, since the helicon wave-plasma coupling is a complex multi-mode phenomenon, it should be noted that changing B might modify the helicon mode, so that this dependency is not straightforward.

V.2 Observation of low-frequency oscillations

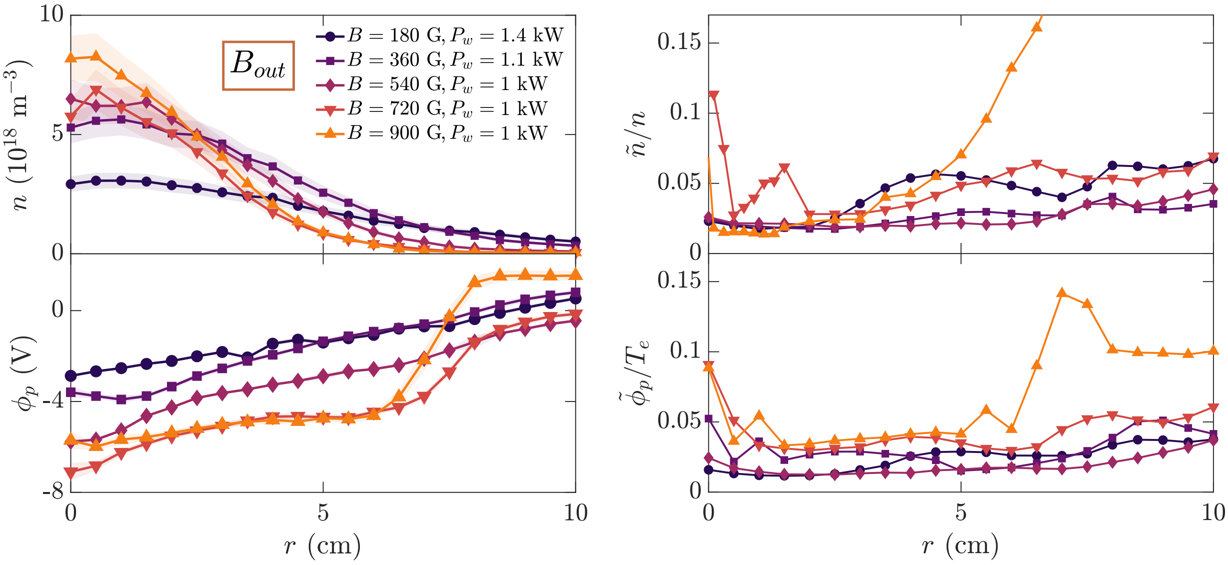

FIGURE V.3 – Mean plasma properties profiles *(left column)* and relative density and potential fluctuations *(right column)* for the B_{out} configuration, with a plasma operated in W mode at 0.13 Pa.

The following sections aims at describing and investigating the various LF oscillations observed in the VKP-HS1 set-up. A comprehensive understanding of the instabilities occurring in the helicon plasma is demanding and time-consuming. Note that the works presented herein focus on specific experimental regimes, and do not fully document the parameters phase. The main data set covers the instabilities observed for various magnetic fields in the B_{out} configuration, at 0.13 Pa and in the W-mode close to the H-W transition. The effect of the magnetic field direction and the pressure will be briefly discussed.

V.2.1 Mean and fluctuation profiles

The radial profiles of the mean density and plasma potential, already presented in figure IV.12, are displayed in the left column of figure V.3 for increasing values of the magnetic field. LF oscillations can be easily evidenced by analysing temporally-resolved probe measurements of the plasma parameters. 5-tips probe and emissive probe measurements are used for radial scans of the ion saturation current and the plasma potential, respectively. The data set of the 5-tips probe is limited to the B_{out} configuration at $p_0 = 0.13$ Pa, with B ranging from 180 G to 900 G because of technical issues that arose at larger magnetic field values. The power is adjusted so that the plasma operates in W mode, close to the H-W transition. The relative density and potential fluctuations $\tilde{n}/n$ and $\tilde{\phi}_p/T_e$ are displayed in the right column of figure V.3.

One can notice that the fluctuations are below 5% for any experiment at $B \leq 540$ G. The helicon plasma is quiescent in these low magnetic field regimes, and it has been confirmed using high-speed imaging. Significant fluctuations appear at 720 G, with density fluctuations at the plasma core $r \leq 2$ cm, and density and potential fluctuations at the plasma edge $r \geq 5$ cm. The edge fluctuations increase remarkably at $B = 900$ G in both density and potential. However, note that the 5-tips probe was damaged at 900 G, so that the important edge density fluctuations measured up to 50% are not fully reliable. This is why the graph is cropped beyond 15%. Fluctuations of the order of 10-20% were measured using negatively-biased Langmuir probes under these experimental conditions.

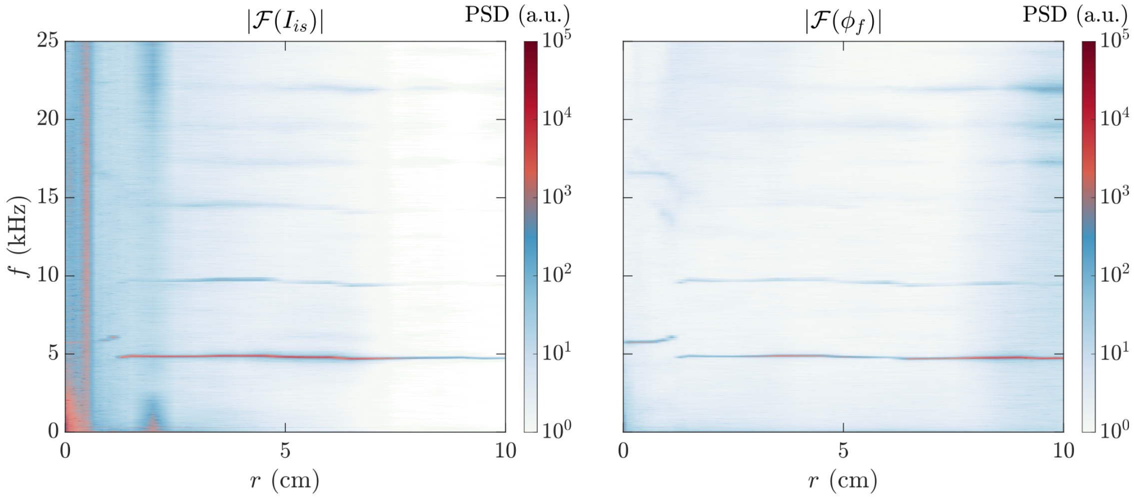

FIGURE V.4 – Fourier transform of ion saturation current *(left panel)* and floating potential *(right panel)* from the 5-tips probe measurements for B_{out}, 810 G, 0.13 Pa and 1 kW.

The important fluctuations at 810 G were analysed by conducting Fourier transforms in the low-frequency regime on the I_{is} and ϕ_f signals resulting from the 5-tips probe measurements V.4. The ion cyclotron frequency at this magnetic field is $\omega_{c,i} = 31$ kHz. The horizontal axis represents the radial position of the probe. This graph highlights the existence of coherent density and potential fluctuations across the whole plasma column centred at 5 kHz, and its first and second harmonics. Moreover, while not being discernible for ion saturation fluctuations, weak potential fluctuations around 22 kHz and located at $r > 8$ cm are also reported. This signal grows significantly at higher magnetic fields and antenna powers. One can also observe multiple peaks shifted regularly by about 2.5 kHz, at 17 kHz and 19.5 kHz. This is the evidence of a weakly non-linear interaction with a 2.5 kHz oscillation. Further investigation using bicoherence would be required for a confident analysis.

Fourier transforms of the emissive probe ϕ_p data for 810 G, 0.13 Pa and 1 kW across the plasma column are reported as well in figure V.5. The high-quality emissive probe measurements allow a good accuracy and a significant data set, resulting in accurate data analysis. The low-frequency and the high-frequency ranges are respectively displayed in the left and right panels. Again, strong and coherent potential fluctuations are reported across the plasma column at 5 kHz, with a striking increase at the plasma edge ($r = 7$ cm). The two first harmonics are reported as well. The 22 kHz edge fluctuations is more pronounced, along with the multiple ripples spaced by 2.5 kHz. Besides, the high-frequency range reveals the existence of additional oscillations. A 30 kHz oscillation at the plasma core appears ($r < 2$ cm), which coincides with $\omega_{c,i}$. Despite being faint, this oscillation is clearly observed with high-speed imaging, as will be reported in the next subsection. Eventually, mild high-frequency fluctuations arise with increased B values across the whole plasma column. 100 kHz oscillations and multiple ripples spaced of 5 kHz are observed at 810 G and strengthened at higher magnetic fields. However, these fast oscillations were not successfully documented enough to conduct a complete analysis of their properties.

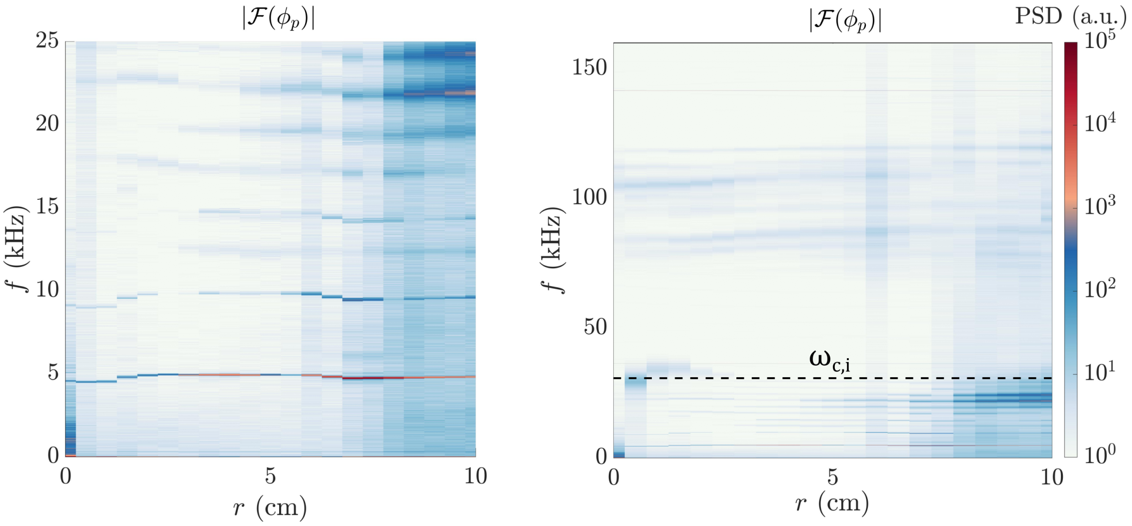

FIGURE V.5 – Fourier transform of the plasma potential in the low-frequency *(left panel)* and high-frequency range *(right panel)* for B_{out}, 810 G, 0.13 Pa and 1 kW. The black dashed line highlights the ion cyclotron frequency.

V.2.2 High-speed imaging of light fluctuations

High-speed imaging is a powerful tool for LF oscillations investigation. The experimental routine and analysis was already described in subsection I.3.5. It enables a non-intrusive tracking method of the oscillations wave front and azimuthal number m. These measurements being quick and easy to conduct, the high-speed imaging data set covers a wide range of the experimental parameters. The plasma always appears to be quiescent at $B \leq 540$ G so that high-speed imaging experiments were focused on $B \geq 720$ G. Raw images of the light fluctuations observed at 900 G, 0.13 Pa and 1 kW are reported in figure V.6. An apparent separation of scale is evidenced between a counter-clockwise core and a clockwise outer wave propagation. This observation is emphasized by the two black arrows visible in the first image at t_0. A $m = -2$ mode is seen at the plasma center, and a $m = 6$ mode is observed at the periphery of the helicon blue core. The $m = -2$ mode is irregular, with occasional quick transitions to the $m = -1$ mode, while the $m = 6$ mode is very robust. However, this latter instability is modulated along the θ dimension. One can see that the light fluctuations present a good signal-to-noise ratio at the top and bottom of the images, while being poor at the left and right sides. Figure I.17b) supports this observation. This

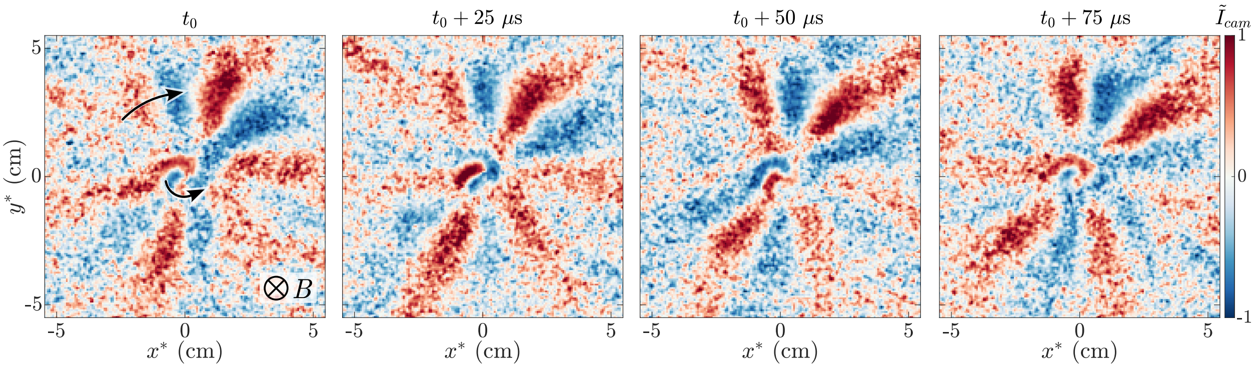

FIGURE V.6 – Light fluctuations for the B_{out} configuration at 900 G, 0.13 Pa and 1 kW. Each frame is spaced by 25 μs. The two black arrows in the first frame indicate the rotation direction.

feature was observed in every experiment, and is most probably related to the half-helical antenna design. Furthermore, the observed light fluctuations in the upper corners of the second and third images hint at the existence of a third LF oscillation beyond $r^* = 5$ cm. Although being hardly distinguishable in the frames displayed here, this supplementary oscillation will be documented more extensively in subsection V.3.2.3.

V.3 Identification of the LF fluctuations

Three main types of LF fluctuations were reported in the W mode in the VKP-HS1 set-up. For a pedagogical presentation, the high density fluctuations regions from the operation diagram displayed in figure IV.10 are highlighted in figure V.7. The B_{out} configuration is displayed in the left panel, while the B_{in} configuration is in the right panel. Note that this graph concerns only the ion saturation current at the plasma core, and is not a comprehensive review of all the LF oscillations in VKP-HS1.

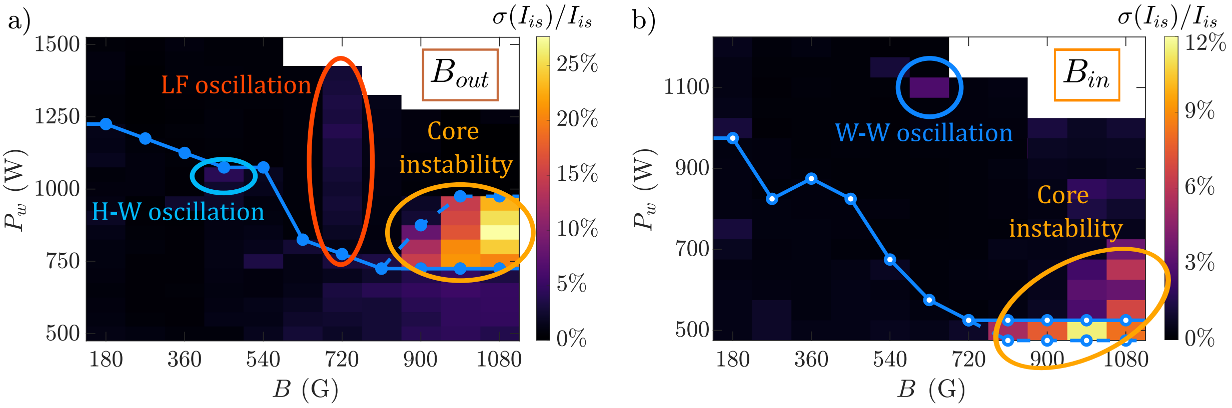

FIGURE V.7 – Relative ion saturation fluctuations in the operation diagram at 0.13 Pa, reproduced from figure IV.10. Various LF fluctuations domains are highlighted for both *a)* B_{out} and *b)* B_{in} configurations. The solid blue line is the H-W transition, while the dotted line bounds the core instability strong fluctuations domain.

The first type of oscillation is the H-W or the W-W oscillation. The identification of H-W oscillations is straightforward since they are located at the frontier of the W domain. In the case of W-W oscillations, the mechanism is similar to H-W oscillations (see subsection V.1.3.2), but occurs between two different W modes within the W domain. These oscillations are well located in the operation diagram, for a short range of pressure, power and magnetic field. Their specific features will be discussed in subsection V.3.1. Then, a broader class of LF oscillations, introduced in subsection V.1.2, can be observed over wide ranges of experimental parameters. For instance, high coherent LF oscillations are reported in the B_{out} configuration at $B = 720$ G for a large span of input power. They will be addressed in subsection V.3.2 and beyond. Ultimately, an unexpected domain of large fluctuations is observed at the H-W transition at high B values. These fluctuations, described here as "core instability", are much more complex and will be described in section V.3.3.

V.3.1 Mode relaxation oscillations

V.3.1.1 B_{in} configuration

The existence of H-W and W-W oscillations is reported here. For now, the focus will be set on the B_{in} configuration. Oscillations similar to the H-W relaxation oscillations were positively identified at 180 G, 0.13 Pa and 1.75 kW. The images captured are displayed in figure V.8, and highlight the existence of two main light emission structures. The left image is a low density mode, with a quasi-uniform light emission profile, while the right image is a tightly focused mode, comparable to a W mode. It should be noted that the left mode is not exactly a H mode. Given the 1.75 kW power, the plasma should operate in the W domain. However, the H-W transition is not sharp at 180 G in the B_{in} configuration, and this specific mode could be a hybrid mode between a W and a H mode. The temporally-resolved normalised light intensity I_{cam} at the plasma center is shown in the top right graph, while its Fourier transform is displayed in the bottom right graph. One can see sharp and regular transitions between two different states of different life times. This oscillation is characterized by a main 290 Hz component, and multiple harmonics.

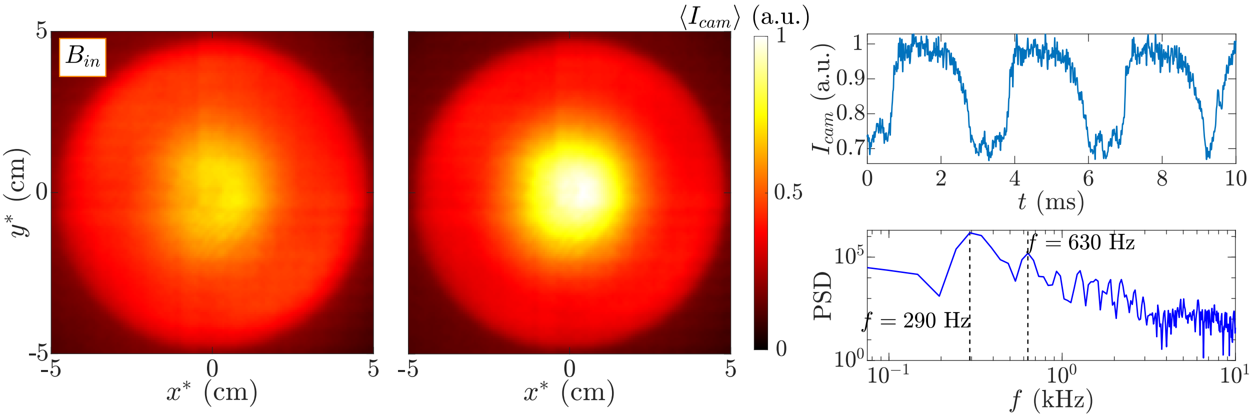

FIGURE V.8 – *(Left panels)* Two main light emission structures observed during a relaxation oscillation in the B_{in} configuration at 180 G, 0.13 Pa and 1.75 kW. *(Right panels)* Temporally-resolved light intensity of the plasma core *(top)* and its corresponding Fourier transform *(bottom)*.

A simple model provides an estimation of the H-W oscillation frequency [Deg+99a]. It relies on the calculation of the neutral depletion and refilling timescales. The transition to the W mode corresponds to a significant increase in plasma density. For an electron temperature $T_e = 3$ eV, the reaction rate K_{iz} for argon is approximately evaluated at 10^{-15} $\mathrm{m^3 \cdot s^{-1}}$ [Lie+05]. The typical neutral depletion timescale thus reads $\tau_{iz} = 1/\left(nK_{iz}\right) \simeq 1$ ms. Here, the neutral depletion timescale is assumed to be driven by ionisation instead of momentum exchange from the ions, but the model could be refined to include them, which would result in a similar timescale. On the other hand, the refilling of the neutral density in the source tube is ensured by a flux of neutrals from the plasma diffusion chamber to the source tube. The typical timescale is $\tau_{fill} = 4L_{source}/v_{th,n}$. With $L_{source} = 40$ cm and $v_{th,n} \simeq 500$ $\mathrm{m \cdot s^{-1}}$, τ_{fill} is assessed at 3 ms. These orders of magnitude are typical of helicon plasmas, so that the frequency of the H-W relaxation oscillations ranges between 100 Hz and 1000 Hz.

Other relaxation oscillations were witnessed in the W domain. High-speed imaging reported the existence of relaxation oscillations at 720 G, 0.20 Pa and 1.4 kW, where two different tightly-focused helicon modes oscillating at 300 Hz were observed. Their observation can be found in appendix figure D.7. This phenomenon being unambiguously in the W domain and well located in the operation diagram, it hints at W-W oscillations. This kind of dynamics was also measured using negatively-biased Langmuir probe at the plasma core at 630 G, 0.13 Pa and 1.1 kW. Ion saturation current is represented in figure V.9, along with its Fourier transform. Typical 420 Hz fluctuations are reported, and disappear with a slight change of experimental conditions. Despite the absence of two clearly distinguishable ion saturation levels, both arguments are in favour of a W-W relaxation oscillation.

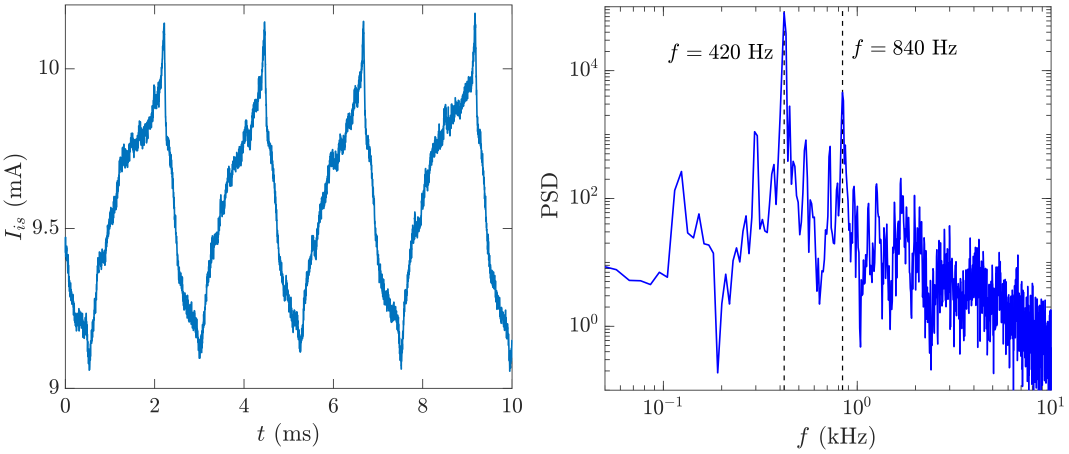

FIGURE V.9 – LF oscillations in ion saturation current *(left)* and its corresponding Fourier transform *(right)* in the B_{in} configuration at 630 G, 0.13 Pa and 1.1 kW.

V.3.1.2 B_{out} configuration

This type of oscillations were also reported in the B_{out} configuration, but with a rarer occurrence. They were investigated using negatively-biased Langmuir probe placed at the plasma center. For instance, H-W oscillations were reported at 450 G, 0.13 Pa and 1.05 kW. The temporal evolution of I_{is} and its spectral decomposition can be found in appendix figure D.8. They are identified unambiguously, as their dynamics is below 1 kHz due to the typical ionisation and diffusion timescales. Moreover, their occurrence is sharply located at the H-W transition in the operation diagram. However, no evidence of W-W relaxation oscillations has been found.

V.3.2 LF oscillations

V.3.2.1 Estimate of the azimuthal plasma flow

Now, the focus will be set on LF oscillations. High-speed imaging revealed a rich phenomenology of instabilities in the W mode. These observations were complemented by 5-tips, emissive and compensated Langmuir probe measurements. The density and potential profiles allow to compute the azimuthal flow $v_\theta = v_{i,\theta}$. The plasma flow is an essential feature of the apparition of LF oscillations. As mentioned in subsection III.1.1, the main contributions to the column rotation is the $\mathbf{E} \times \mathbf{B}$ and the ion diamagnetic drifts. This simple model can be refined by considering the drag caused by ion-neutrals collisions, with a frequency ν_{in}, and ionisation with a typical frequency ν_{iz} [Dés+21]. The azimuthal ion speed then reads

$$v_{i,\theta} = \frac{1}{K}\left(v_{\mathbf{E}\times\mathbf{B}} + v_{d,i}\right) \quad \text{with} \quad K = \frac{1}{1 + \left[\left(\nu_{in} + \nu_{iz}\right)/\omega_{c,i}\right]^2} \tag{V.5}$$

The W mode close to the H-W transition at $p_0 = 0.13$ Pa in both B_{out} and B_{in} configurations over the range [180 G; 1080 G] was investigated. The value of the term $\nu_{in} + \nu_{iz}$ does not vary significantly with B, ranging between 30 kHz and 75 kHz, while $\omega_{c,i}$ is proportional to B and increases significantly with B. A rough estimation of $\nu_{in} + \nu_{iz} = 50$ kHz is set for the numerical computation, so that K ranges from 2.34 to 1.04 over the B range. Past experiments in the VKP-ICP set-up showed that higher K values are observed at low magnetic field, with K reaching up to 9 at 120 G [Dés+21]. But the higher is B, the more robust is the K estimation. Reliable K values below 2 were measured at $B > 500$ G. In summary, the K values used here are most probably underestimated at $B \leq 360$ G, but rather robust beyond.

Furthermore, the computation of the ion diamagnetic drift requires the knowledge of the ion temperature. Laser induced fluorescence applied to ion temperature measurement was conducted on VKP-ICP, but has not been implemented on VKP-HS1 yet. The exact T_i value is then unknown. However, one can mention that T_i was found to be proportional to B in VKP-ICP [Dés18] and other linear devices [Sci+07]. In order to calculate $v_{d,i}$, a rough estimation of $T_i = 0.15$ eV at 180 G and a linear relation $T_i \propto B$ was used, which is close to the VKP-ICP values. T_i affects mildly ν_{in}, hence the variation of $\nu_{in} + \nu_{iz}$ above-mentioned, and more significantly $v_{d,i}$, which is actually lower than $v_{\mathbf{E}\times\mathbf{B}}$. In summary, T_i has a limited impact on $v_{i,\theta}$, which depends mostly on $v_{\mathbf{E}\times\mathbf{B}}$. That is why the reliability of the plasma potential measurements is essential.

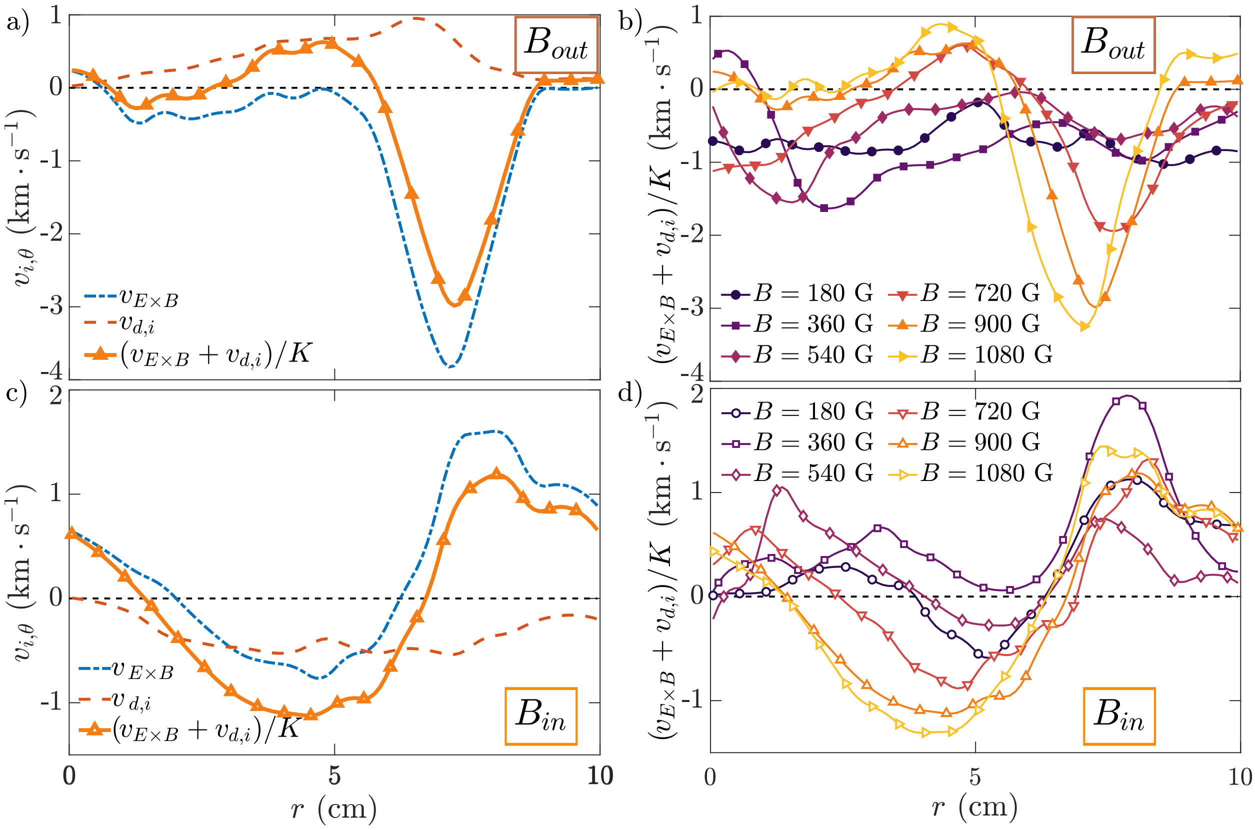

FIGURE V.10 – *a)* Azimuthal flow in the W mode at 900 G, 0.13 Pa for the B_{out} configuration. *b)* Comparison between different B values in the B_{out} configuration. Similar profiles are shown for *c)* the B_{in} configuration at 900 G and 0.13 Pa, and *d)* for various B values in the B_{in} configuration.

The radial profiles of $v_{\mathbf{E}\times\mathbf{B}}$, $v_{d,i}$ and $v_{i,\theta}$ for the B_{out} and B_{in} configurations at 900 G are respectively shown in figure V.10a) and c). The inversion of the **B** direction results in the global inversion of the azimuthal flow. In the B_{out} case, the strong potential barrier observed in figure V.3 generates a fast rotation localised at $r = 7$ cm. On the other hand, the B_{in} case develops a wider and less intense potential well centred at $r = 7$ cm (see figure IV.13), causing a broader and weaker azimuthal flow. Note the difference in vertical scale, with a threefold increase of $v_{i,\theta}$ from the B_{in} to the B_{out} configuration.

The azimuthal velocities for numerous B values are displayed in the B_{out} (figure V.10b)) and the B_{in} configuration (figure V.10d)). In both cases, the increase in B results in a more intense shear at $r = 6$ cm and velocity extrema at $r = 7$ cm. Furthermore, the B_{in} case exhibits a minimum at $r = 4.5$ cm. Overall, the increase in B induces a faster and non-uniform rotation of the plasma column.

V.3.2.2 Growth rates computation

The growth rates can be computed using the experimental plasma properties and azimuthal flow profiles, and the analytical formulas provided in table V.1. Keep in mind that these growth rates should be discussed cautiously since they are derived in a slab geometry under a variety of simplifying assumptions. Yet, it provides insightful evidence for the identification of LF oscillations.

Growth rates of the DW, KH and RT instabilities for a plasma operated at 810 G, 0.13 Pa and 1 kW in the B_{out} configuration are displayed in figure V.11. Azimuthal m modes 1, 3 and 5 are displayed for the sake of clarity, and to remain within the range of observed azimuthal mode numbers. The DW are located at the strong density gradient as expected, *i.e.* at $r < 5$ cm. The RT instability is excited at the azimuthal velocity peak at $r = 7$ cm, and the KH instability is primarily located at the maximal shear locations, namely $r = 6$ and 8 cm. The main LF oscillations being observed at $r > 5$ cm (see figure V.5), it hints at KH or RT instabilities. Then, DW do not seem to contribute significantly to the LF oscillations at the plasma edge.

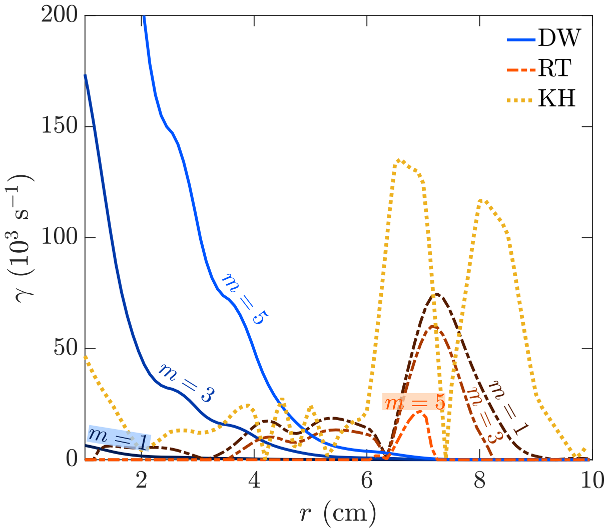

FIGURE V.11 – Growth rates of drift waves (DW), Rayleigh-Taylor (RT) and Kelvin-Helmholtz (KH) instabilities for B_{out}, 810 G, 0.13 Pa and 1 kW. Modes $m = 1$, 3 and 5 are represented.

V.3.2.3 Phase velocity and phase shift based identification

High-speed imaging data is analysed using 2D-FT (see subsection I.3.5). Experiments at 0.13 Pa and 1 kW at magnetic fields ranging from $B = 720$ to 1080 G are analysed at various radii r^*. As a reminder, the radius observed at the camera r^* does not correspond to the probe position r. Because of the widened magnetic field at the probe access port, located at $z = 49$ cm, plus the parallax effect, the light fluctuations observed at a given radius r^* correspond to an increased radius r for probe measurements. A more detailed study can be found in the previous PhD work from Simon Vincent [Vin21]. The conversion factor from r^* to r is roughly 1.6. Then, $r^* = 0.8$, 1, 3.5 and 4.5 cm respectively correspond to $r = 1.3$, 1.6, 5.6 and 7.2 cm. 2D-FT spectra close to the plasma core and at the plasma edge are displayed in figure V.12, respectively at the top row and the bottom row.

Artefacts are observed at $m = 0$, with an unexpected white noise for the last two columns. The first row shows the existence of a counter-clockwise instability at $B = 720$ and 900 G, as shown in figure V.6. The main component is $m = -1$, and the corresponding frequency decreases from 30

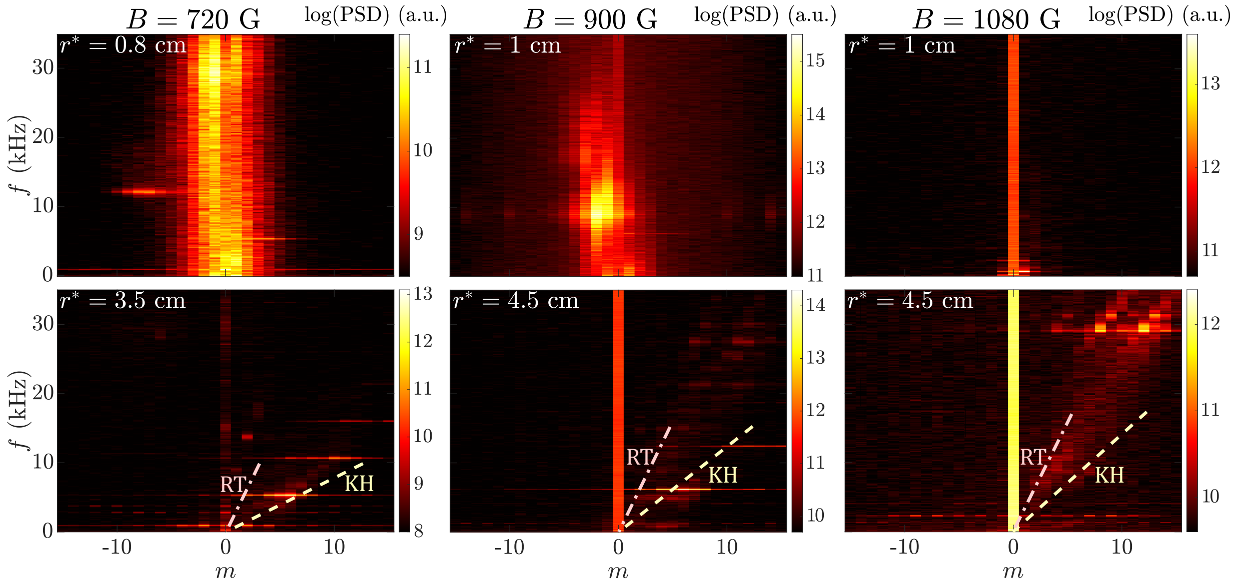

FIGURE V.12 – 2D-FT spectra close to the plasma core *(top row)* and at the plasma edge *(bottom row)*. Experimental conditions are $p_0 = 0.13$ Pa, $P_w = 1$ kW and $B = 720$ G *(left column)*, 900 G *(middle column)* and 1080 G *(right column)*. Estimations of the analytical phase velocities for KH (dashed line) and RT (dotted line) are represented on the bottom row.

to 10 kHz. This component is broadband, as a wide range of frequencies is excited. Additionally, occasional and irregular transitions to $m = -2$ are witnessed. This oscillation is reported only in a short range of B values, and disappears at higher magnetic fields, as can be seen at 1080 G in the top right graph. It was already observed faintly with an emissive probe in figure V.5, but high-speed imaging showed that the insertion of a probe at the plasma core dampens this $m = -1$ mode. This instability is located at the high density gradient region, which hints at a DW induced mode. However, the wave apparently rotates in the ion diamagnetic direction, oppositely to the expected direction of DW. The estimated azimuthal flow at $r < 2$ cm being in the electron diamagnetic direction, the correction of the Doppler shift confirms that this wave propagates in the ion diamagnetic direction. Given the growth rates computation, a RT or KH mode is unlikely at the plasma core. The underlying mechanism behind this wave propagation is still unclear to that day. Besides, one may notice that a secondary component at $m = -7$ and $f = 12$ kHz is reported in that region. Once again, its origin is not understood.

On the other hand, the plasma edge exhibits coherent modes rotating in the clockwise direction. At $B = 720$ and 900 G, a strong $m = 6$ mode at $f = 5$ kHz is seen, along with its first harmonics at $m = 12$ and $f = 10$ kHz. It corresponds most certainly to the major LF oscillation observed in figure V.5. The frequency is mostly unaffected with an increase in B until it disappears at 1080 G. The instability is observed between $r^* = 2$ and 4.5 cm, which corresponds to $r = 3.2$ to 7.2 cm. According to figure V.10, this location correlates with the strong shear layer, and consequently the maximum growth rate region at $r = 6.5$ cm (see figure V.11). Besides, the phase velocity of the KH and RT instabilities are indicated in the 2D-FT spectra. The measured phase velocity of the $m = 6$ mode is in agreement with the phase velocity computed for the KH instability. All these evidence hint at a KH-driven mode. Note that this instability experiences a mild 1 kHz amplitude modulation at 900 G, leading to two faint peaks at $m = 5$, $f = 4$ kHz and $m = 7$, $f = 6$ kHz. The origin of this amplitude modulation seems to be the non-linear interaction with a large-scale 1 kHz mode, presumably visible at $m = 4$ at 900 G and $r^* = 4.5$ cm. This mechanism will be discussed more thoroughly in section V.3.3.

Eventually, a higher frequency instability is hardly visible at 900 G, but well captured at 1080 G. It is accentuated at higher magnetic fields and powers. High azimuthal numbers are measured, with dominant $m = 8$ and 12 components at $f = 29$ kHz. This instability seemingly corresponds to the edge located 22 kHz minor instability noticed at 810 G in figure V.5. The azimuthal number and frequency are mildly affected by B or P_w. This instability is only located further away from the plasma core, beyond $r^* = 4$ cm, *i.e.* $r = 6.4$ cm. This location agrees with the growth rate computation for the RT instability. Besides, the phase velocity for the RT instability agrees fairly well with the modes observed in the 2D-FT spectrum at 1080 G. Furthermore, the 2 kHz ripples mentioned in figure V.5 are reported via the 2D-FT analysis, with the secondary peaks at $f = 32$ kHz for $m = 9$ and $m = 13$. Once again, it might originate from non-linear interactions with a $f = 1 - 2$ kHz mode.

Then, the effect of neutral pressure on the edge instability is highlighted in figure V.13. The experimental parameters are $B = 790$ G and $P_w = 1$ kW, with pressures ranging from $p_0 = 0.07$ Pa to 0.20 Pa. 2D-FT spectra at $r^* = 3.2$ cm are displayed. The $m = 4$ mode at 0.07 Pa is modified to a $m = 5 - 6$ mode at 0.13 Pa, and to $m = 7 - 8$ at 0.20 Pa, with similar frequencies. The phase velocities for each graph is represented as a bold dashed line, whereas the phase velocities at other pressures are shown with a thinner white dotted line. It shows a significant decrease of v_ϕ with respect to p_0. This observation can be extended to the $m = 12$ edge modes. Their azimuthal mode is not affected by p_0, but their frequencies are decreased from 30 kHz down to 25 kHz. The increase in p_0 slows down the plasma rotation, meaning a lower phase velocity and a smaller shear layer. The first effect would cause the frequency to diminish, or the azimuthal mode to increase. Both instabilities exhibit such behaviours. Additionally, the shear layer width would mostly affect the m number of a KH instability, since the azimuthal wave number $k_\theta = m/r^*$ is inversely correlated to the extent of the shear layer.

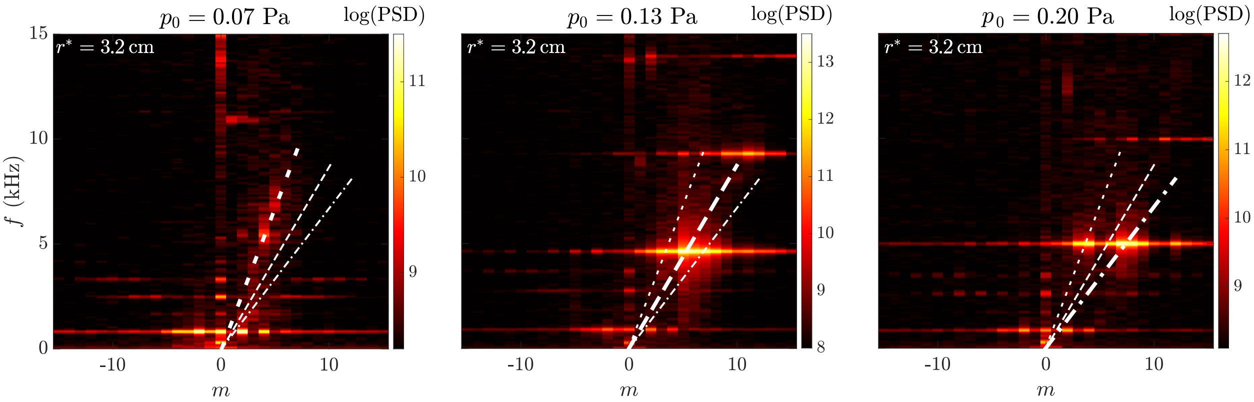

FIGURE V.13 – 2D-FT spectra at 790 G, 1 kW and various pressures. For each graph, the bolder white dotted line highlights the relevant phase velocity, while the thinner lines account for the phase velocities for other pressures.

Note that in spite of dedicated efforts, no coherent modes were observed at 100 kHz, contrary to the oscillations evidenced in figure V.5.

The measurements of the cross-phase shift $\xi\left(\tilde{n}, \tilde{\phi}_p\right)$ is a powerful tool for wave identification. To that end, the 5-tips probe was used for simultaneous I_{is} and ϕ_f measurements up to 810 G before damaging it, but the scarce measurements are still informative. Both signals are decomposed into $\hat{I}_{is}$ and $\hat{\phi}_f$ via Fourier transform. Then, the phase shift $\xi\left(\tilde{n}, \tilde{\phi}_p\right)$ for each frequency f is the complex argument of the product $\hat{I}_{is}(f)\overline{\hat{\phi}_f}(f)$, with $\overline{\hat{\phi}_f}$ the complex conjugate of $\hat{\phi}_f$. The resulting temporally-resolved phase shift is then averaged over time. If no coherent mode exists at f, the phase shift is arbitrary and its value is not significant. If the standard deviation $\sigma(\xi)$ is lower than

$\pi/4$, the variation in ξ is low enough to be considered reliable. The cross-phase shifts for 720 G and 810 G over the range [0 kHz; 10 kHz] are presented in figure V.14a-b), and for 810 G over [0 kHz; 25 kHz] in figure V.14c). The gray points correspond to highly variable cross-phase shifts and are discarded for the analysis.

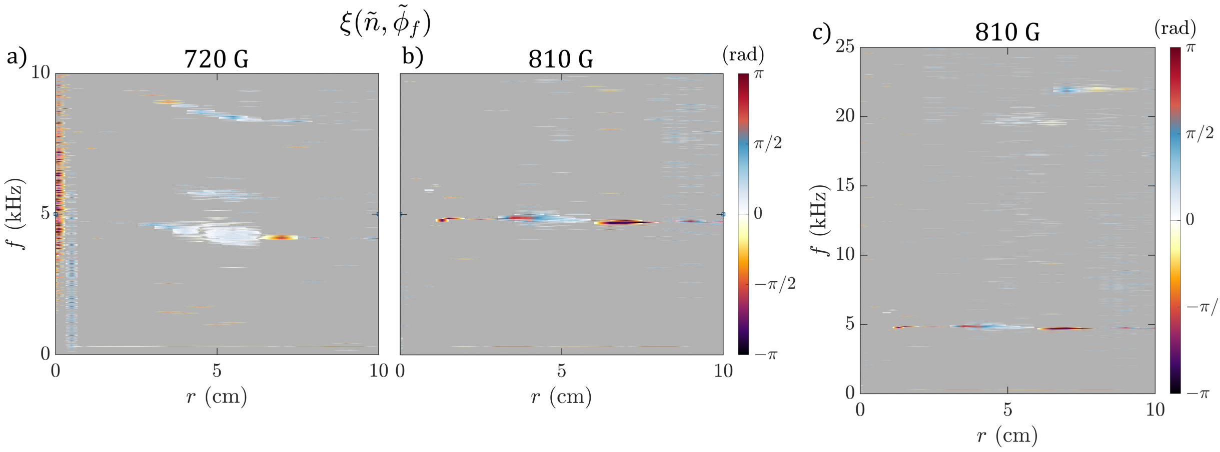

FIGURE V.14 – Cross-shift phase $\xi\left(\tilde{n},\tilde{\phi}_p\right)$ for *a)* 720 G and *b)* 810 G over $0-10$ kHz, and *c)* over $0-25$ kHz. Gray regions correspond to highly variable phase shifts associated to the absence of coherent oscillations.

The 5 kHz oscillations are further documented using these measurements. ξ is below $\pi/4$ at 720 G. This observation is in favour of a resistive DW mode, but this possibility was dismissed previously. Besides, the first harmonics measured at 9 kHz has a phase shift of approximately $\pi/2$, which would agree with a RT or KH instability, as was suggested by the previous observations. The phase shift at 810 G is within $[\pi/2;\pi]$ or $[-\pi;-\pi/2]$, which is a striking evidence of a KH instability. This edge LF oscillation growing continuously from 720 G to 810 G, it is hardly believable that the nature of both these fluctuations is different. In addition, the phase shift measured at 22 kHz at 810 G is faint, but lies in the range $[\pi/4;\pi/2]$. It strengthens the RT instability assumption at the plasma edge.

In conclusion, the W mode in the B_{out} configuration demonstrates the coexistence of two LF oscillations at the plasma edge, which are most probably a 5 kHz KH instability at the shear layer location, and a 25 kHz RT instability at the maximum azimuthal velocity location. Further analysis are required for the identification of the plasma core instability, and the extension to the B_{in} configuration. For instance, the parallel wave number $k_{\parallel}$ was not measured but could be an insightful result for DW investigation.

V.3.3 Core instability

V.3.3.1 Transition to turbulence

The existence of a strong core instability is addressed in the present section. At a given pressure p_0, it can be witnessed by increasing the magnetic field B at a fixed power P_w, or by decreasing P_w at fixed B. This instability is witnessed beyond 900 G while the magnetic field was hard-ware limited at 1080 G. The range in magnetic field being narrow, the core instability investigated here will be studied at a fixed magnetic field value $B = 1080$ G. However, one should notice that since the power required P_w for the H-W transition depends on p_0, it is not possible to study the influence of both these parameters independently. Their values will be systematically mentioned when discussing the results.

The transition to the core instability is now illustrated by analysing 2D-FT spectra at $r^* = 3.5$ cm at $B = 1080$ G, $p_0 = 0.20$ Pa and powers decreasing from 1.15 kW and 0.75 kW in figure V.15.

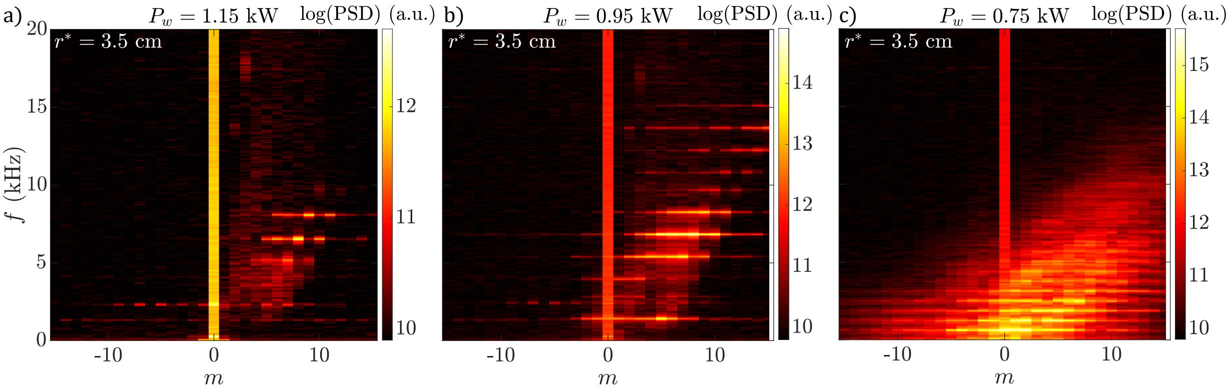

FIGURE V.15 – 2D-FT spectra at $r^* = 3.5$ cm for experiments conducted at 1080 G, 0.20 Pa and *a)* 1.15 kW, *b)* 0.95 kW and *c)* 0.75 kW.

At 1.15 kW (figure V.15a)), the KH edge instability is observed, with a major mode at 6.5 kHz and $m = 8$. Two minor secondary peaks shifted by ± 1.5 kHz and $m = \pm 1$ azimuthal mode number are visible. The decrease in P_w leads to the growth of these secondary peaks and multiple moderately intense ripples, which extend from 4 kHz to 13.7 kHz, while the core is still stable (see figure V.15b)). Additionally, a 1.4 kHz, $m = 5$ mode is visible. At 0.75 kW, the plasma core suddenly becomes unstable, as it is displaced irregularly of about 0.3 cm and rotates clockwise, *i.e.* in the electron diamagnetic direction. The typical frequency of the core instability is 650 Hz. This core instability is accompanied by the suppression of the KH edge mode. Multiscale light fluctuations are reported, which results in the excitation of numerous azimuthal modes over a wide extent of frequencies (see figure V.15c)).

The multiple ripples observed at 1.15 kW and 0.95 kW could arise from a three-wave interaction, often called triadic interaction. They originate from weakly non-linear interactions between two waves of frequencies f_1 and f_2, azimuthal mode numbers m_1 and m_2 and temporal phases ϕ_1 and ϕ_2. The newly generated wave at f_3, m_3 and ϕ_3 is characterised by

$$\begin{cases} f_3 = f_1 + f_2 \\ m_3 = m_1 + m_2 \\ \phi_3 = \phi_1 + \phi_2 \end{cases} \tag{V.6}$$

For a successful triadic interaction identification, 2D bicoherence analysis is necessary but has not been conducted over the course of this thesis. The apparition of multiple ripples via non-linear wave interactions has already been documented as a mechanism of transition to turbulence in CSDX [Bur+05]. There, drift waves were seen to transfer their energy to larger and smaller scales, generating vortices, intermittency and feeding other instabilities like zonal flows [Yan+10]. In the present case however, the origin of the 1.5 kHz spacing will be discussed but is not understood yet. Besides, the displacement of the plasma core breaks the axisymmetry, while the 2D-FT technique strongly relies on this assumption. It explains partially why the 2D-FT conducted in the core instability regime does not exhibit well defined modes. This issue will be addressed in the next subsection.

These data can be completed by the Fourier transform of the plasma potential measured using an emissive probe, displayed in figure V.16. The experimental parameters are 1080 G, 0.13 Pa, while P_w varies from 1.3 kW to 0.9 kW, and the probe is located at $r = 5$ cm. The core instability

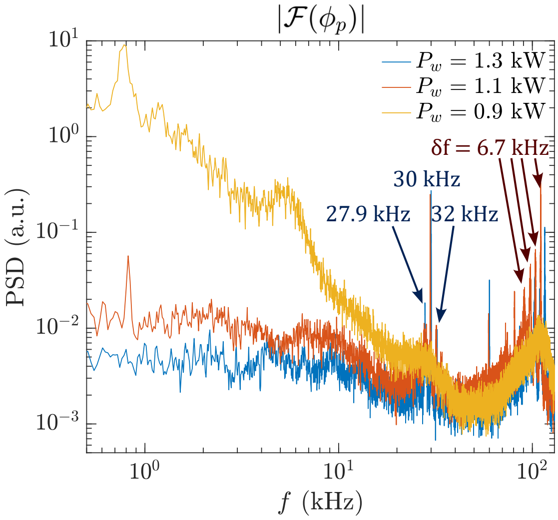

FIGURE V.16 – Fourier transform of the plasma potential at $r = 5$ cm for experiments conducted at 1080 G, 0.13 Pa and variable powers. Core instability is observed below 1 kW.

occurs at $P_w \leq 1$ kW, such that the 0.9 kW data dissociate from the others. The stable operation regimes at $P_w \geq 1.1$ kW present sharp peaks centred around 30 kHz and 110 kHz. Once again, these modes are accompanied by multiple ripples respectively spaced by $\delta f = 2.1$ kHz and 6.7 kHz, similarly to what was shown in figures V.5 and V.15. The lowering of P_w leads to the emergence of a LF peak at 800 Hz. This peak is strongly enhanced at 0.9 kW and accompanied by the striking growth of broadband low-frequency fluctuations up to 30 kHz. Meanwhile, coherent modes at $f > 30$ kHz are damped and smoothed. The emergence of large scale uncoherent fluctuations might cause shear and perturb the growth of these coherent modes.

V.3.3.2 Phenomenology of the core instability

Raw images of the core instability exhibit slow, large scale and mostly uncoherent modes which dominate the plasma dynamics. Several snapshots spaced by 0.125 ms are presented in figure V.17 for the highly unstable 1080 G, 0.07 Pa and 0.9 kW regime. The plasma core is deformed, experiences displacements larger than its own width and rotates clockwise. Additionally, smaller structures at the core periphery are generated, for instance in the upper right corner of the second image ($t_0 + 0.12$ ms). These peripheral structures move faster, and seemingly exhibit inward and outward transport depending on the distance that separate them from the high-density region. Hence, the scale separation observed previously between the helicon blue core and its periphery is no longer observed. Over the typical timescale of 1 ms, the plasma is focused once again at the center of the linear device (see bottom right image, $t_0 + 0.62$ ms), before being perturbed one more time.

The issue of the axisymmetry assumption for the 2D-FT analysis will now be addressed. An improvement was implemented by considering cylindrical coordinates relative to the moving plasma core. In other words, the center of the cylindrical coordinates is adjusted in each frame to track the most luminous plasma region, rather than being fixed at the brightest spot of the temporally averaged image, as previously done. In practice, it is achieved by fitting an ellipse on the brightest region of each frame, thus pointing the center of the plasma core down to a sub-pixel resolution. The location of this ellipse is noted as $r_{core}(t) = \sqrt{x_{core}^2 + y_{core}^2}$, $r_{core} = 0$ being the bottom left pixel. Then, imaging data are centred at r_{core}, so that the axisymmetry issue is mitigated. This analysis was conducted on every high-speed imaging data documenting the core instability. r_{core},

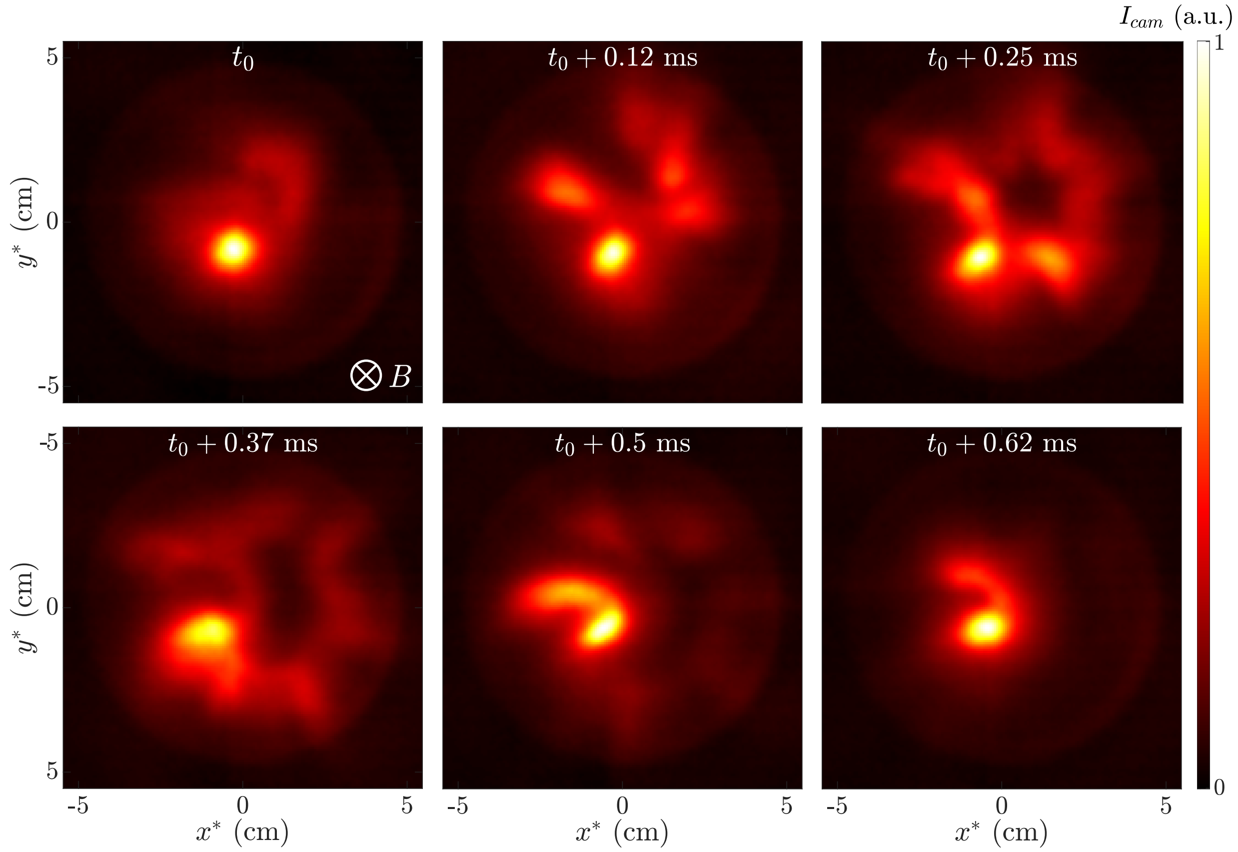

FIGURE V.17 – Snapshots of the core instability at 1080 G, 0.07 Pa and 0.9 kW.

measured in pixels, is shown in figure V.18a), at 1080 G for pressures ranging between 0.07 and 0.20 Pa and adjusted powers. While the plasma core exhibits small and regular displacements at 0.20 Pa, its motion becomes irregular and much more significant at lower pressures.

The corresponding Fourier transforms are shown in figure V.18b). The fluctuations in r_{core} at 0.20 Pa are mostly condensed at 630 Hz and its harmonics, but also exhibit broadband LF frequencies. As the pressure is decreased, the fluctuations are no longer coherent. A plateau is developed below 1 kHz, and fluctuations extend up to 30 kHz. No coherent LF modes were reported at $p_0 \leq 0.13$ Pa in the core instability regime, hinting at the essential role of the neutral pressure in the origin of this core instability. The effect of P_w on r_{core} and its fluctuations is not illustrated here, since its influence appears to be minor. As P_w is decreased, the displacement of the plasma core is moderately enhanced.

In that corrected frame, newly centred high-speed imaging data are analysed with 2D-FT and POD. Here, the analysis is conducted at $r^* = 3$ cm for the three different pressure regimes mentioned above, and their spectra are visible in the upper panel of figure V.19. The 2D-FT spectra were significantly improved by this modification, as can be seen from the comparison between the previous 2D-FT spectra at 0.20 Pa and 0.75 kW (figure V.15c)) and the corrected data (upper right graph in figure V.19). As the pressure is decreased, the transition from 630 Hz coherent modes at $m = 1$ to 3, to much broader and multiscale fluctuations is evidenced. Higher azimuthal modes, *i.e.* finer structures, show higher frequencies but smaller amplitudes. At pressures below 0.13 Pa, the fluctuations are broadband, but mostly contained in the $m = 1$ and $m = 2$ modes. Keep in mind that, in spite of a misleading vertical scale on the 2D-FT spectra, the phase velocity is particularly low, especially compared to the ones observed for the KH and RT instabilities.

POD analysis reveals much more complex structures and complements the 2D-FT analysis.

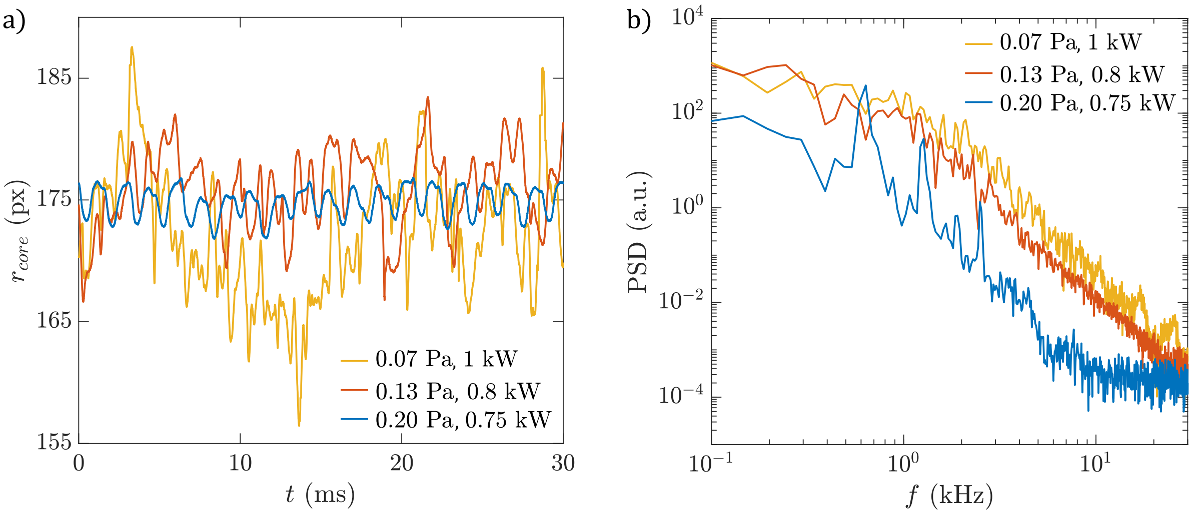

FIGURE V.18 – *a)* Position of the plasma core at 1080 G and various pressures. *b)* Corresponding Fourier transforms.

POD is displayed for the 0.20 and 0.07 Pa cases in figure V.19. One can identify roughly the main azimuthal modes, from $m = 1$ to $m = 3$. In both cases, the most energetic modes are the largest scale modes, as shown by the Ψ_1 and Ψ_2 eigenmodes. The higher is i, meaning the less significant are the eigenmodes, the finer are the spatial structures. In accordance with the 2D-FT data, smaller spatial fluctuations appear at higher frequencies. Besides, fluctuations at low pressure are observed at larger scales, up to $r^* = 4$ cm, while they are mostly constrained below $r^* = 3$ cm at 0.20 Pa. However, an extensive analysis of these complex data is difficult. One can mention that in general, the decrease of p_0, or P_w to a smaller extent, lead to the apparition of large scale fluctuations, broadband LF spectra and irregular fluctuations. The investigation of the radial transport or the bicoherence could be highly valuable additions to this experimental analysis.

V.3.3.3 Discussion of the instability origin

The origin of the core instability phenomenon is unclear, but the goal here is to present a few plausible mechanisms and to discuss their relevancy. The transition to this instability is accompanied by the growth of a $1-2$ kHz predominant mode. Firstly, it weakly interacts with the KH and RT edge modes. Then, it becomes a major large scale $m = 1$ to $m = 3$ mode, suppressing the edge modes. As the core instability develops, the fluctuations become broadband and multiscale. That is why one can safely assume that the KH and RT modes play a minor role in the development of this instability.

Previous studies reported drift-wave induced turbulence in linear devices [Bur+05; Ara+16]. If DW were at the origin of this core instability in the VKP-HS1 set-up, it would be consistent with the growth of LF and broadband fluctuations at high magnetic field B, and waves propagating in the electron diamagnetic drift direction. The effect of the magnetic field increase would be to dissociate efficiently the shear layer at $r^* \simeq 4$ cm from the strong density gradient region at $r^* \simeq 1$ cm. It would enable a separate growth of both instabilities, until DW dominate the global plasma dynamics. Besides, as B increases up to 1080 G, ρ_S is reduced down to 1.2 cm. The energy of the DW turbulence being injected at $k_\theta \rho_S = 1$, it means that a mode $m = 1$ could develop at $r^* \simeq 1$ cm. Then, further away from the plasma center, finer structures may arise, as observed in the snapshots presented in figure V.17. The increase in P_w seems to cause a higher shear at the edge (see figure C.4 in appendix), which might explain why KH and RT instabilities become dominant

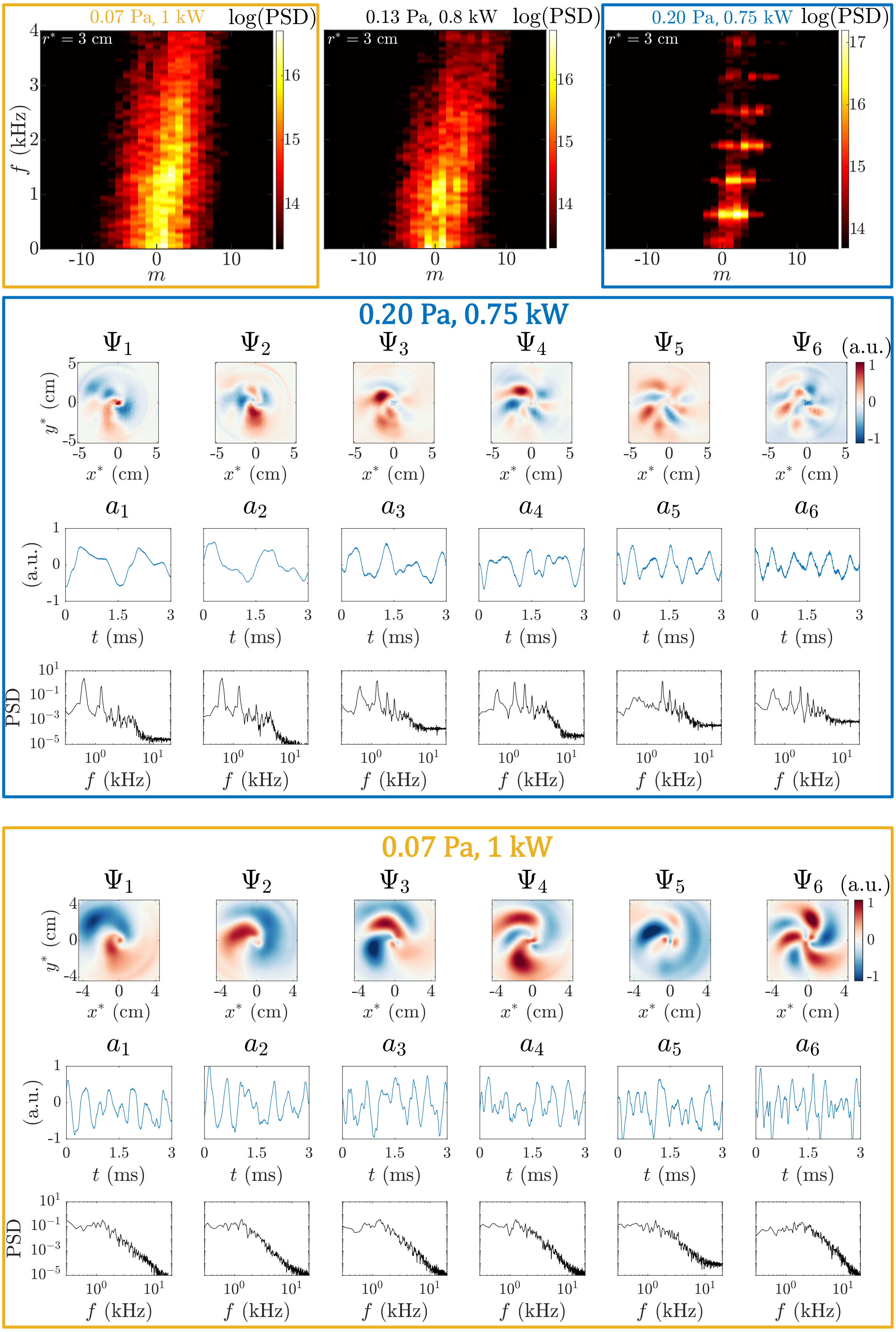

FIGURE V.19 – 2D-FT spectra and associated POD at 1080 G for various pressures.

compared to the core instability. However, multiple evidence do not support the hypothesis of DW modes. The phase velocity observed experimentally is low, while the analytical phase velocity is higher than the ones for the KH and RT instabilities. Indeed, the dominant $m = 1$ mode is expected at $f \simeq 5$ kHz. Additionally, the role of p_0 is not captured by the DW hypothesis. An increase in p_0 results in a lowering of $v_{i,\theta}$ (see plasma potential profiles in figure IV.14) and higher density gradients. These conditions are optimal for the growth of DW and a damping of the KH and RT instabilities. Yet, the regimes at higher pressures reported a mitigated core instability. Maybe the higher collision frequencies damp the growth of large scale structures, but it seems surprisingly efficient. Deeper experimental analysis could be conducted by measuring the cross-phase shift or the parallel wave number $k_{\parallel}$. Besides, the hard-ware limitation in B could be improved in order to reach up to 1800 G, which would provide a wider range in ρ_S for further investigation.

Another explanation might be the existence of neutral depletion. The high plasma density required to sustain the W mode would deplete significantly the neutrals at the narrow plasma core. Then, the power deposited from the helicon wave to the plasma might be deflected to regions where neutrals are denser. This could result in the displacement of the plasma core and a complex antenna-plasma coupling. The core instability is triggered at high B, which corresponds to higher plasma densities. Indeed, 1080 G density profiles revealed a ionisation degree above 50% (see figure IV.12). Moreover, an increase in p_0 and P_w seem to stabilise very efficiently this instability, as it was observed in the case of H-W oscillations (see figure V.2). Both these effects would be easily explained by a neutral depletion mechanism. The typical frequencies are about 1 kHz, which match the order of magnitude briefly discussed in subsection V.3.1. However, the change in pressure from 0.07 Pa to 0.20 Pa did not reveal a significant variation in the observed frequencies. This hypothesis is hardly evaluable experimentally, since temporally and spatially resolved neutral density measurements are particularly challenging. A numerical investigation of the neutral dynamics could be insightful, yet it remains non-trivial.

Other instabilities may be responsible for this core instability. Several papers demonstrated the role of zonal flows in the growth of low-frequency turbulence for instance [Yan+10; Ara+16]. Besides, the Simon-Hoh instability has not been considered, while the radial density gradient and inward electric field at the plasma core are prone to the growth of a Simon-Hoh instability.

V.4 Conclusion

As a conclusion, a wide characterisation of the low-frequency fluctuations has been conducted for the 0.13 Pa case in the B_{out} configuration. Probe measurements and high-speed imaging highlighted the existence of H-W and W-W oscillations, Kelvin-Helmholtz and Rayleigh-Taylor edge instabilities, and a complex core instability. Other instabilities at higher powers were observed, but not extensively studied. Overall, a schematic operation diagram for 0.13 Pa is represented in figure V.20. A preliminary observation of the high-speed imaging data show a low effect of p_0 on this diagram, so that figure V.20 could be extrapolated to 0.07 Pa and 0.20 Pa regimes.

A finer identification of the instabilities could be carried out via enriched probe measurements. Besides, the investigation of the core instability is incomplete, and an improved image analysis could refine the interpretation drawn previously.

Ultimately, a similar approach could be followed for the B_{in} configuration. Yet, the phenomenology revealed to be more simple. A robust and unique 8 kHz, $m = 6$ edge mode dominates at high magnetic fields, and appears to be similar to the Kelvin-Helmholtz instability reported herein.

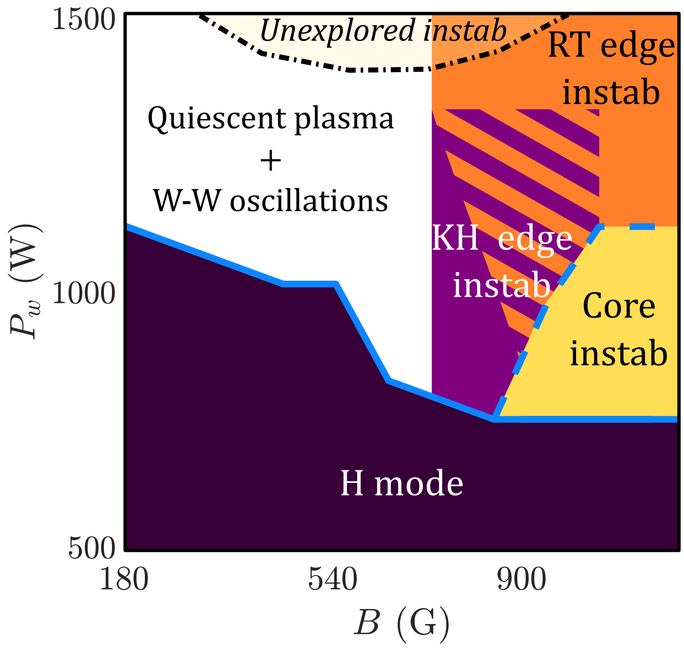

FIGURE V.20 – Sketch of the instability mapping in the B_{out} configuration. Numerical values are for $p_0 = 0.13$ Pa, but the phenomenology is not modified between 0.07 and 0.20 Pa.

CONCLUSION

Les travaux réalisés au cours de ce doctorat ont été dédiés d'une part à la compréhension de l'opération d'une cathode émissive dans une colonne de plasma froid, et d'autre part à l'implémentation d'une source hélicon et à la caractérisation de la colonne de plasma ainsi générée. Cette étude expérimentale nécessite l'exploitation de techniques avancées de diagnostiques. Elle a grandement bénéficié des divers techniques d'analyse et de l'expertise développée au cours des deux précédentes thèses réalisées par Victor Désangles [Dés18] et Simon Vincent [Vin21]. Par conséquent, les sondes électrostatiques telles que la sonde de Langmuir non-compensée, la sonde émissive, la sonde 5-tips et les techniques d'imagerie rapide ont pu être mises à profit efficacement. Cet éventail de solutions a été enrichi par le développement de nouvelles sondes électrostatiques avancées au cours de cette thèse. Une sonde de Langmuir compensée, indispensable à une caractérisation fiable du plasma hélicon, a été développée et validée expérimentalement. Une sonde B-dot tri-dimensionnelle, nécessaire à l'analyse des ondes hélicons radio-fréquences se propageant au sein du plasma, a été assemblée et calibrée en fréquence avec succès. Enfin, un rail mobile a été créé en collaboration avec les services d'ingénierie du laboratoire afin de réaliser des mesures longitudinales des propriétés du plasma. Ces atouts techniques ont d'abord été mis à profit pour étudier les interactions entre une cathode chaude et un plasma ambiant. La compréhension fine de cette cathode a été appliquée à l'étude de la modification du potentiel plasma par injection d'électrons. Les mesures expérimentales ont été confrontées à un modèle analytique, permettant une compréhension qualitative des phénomènes physiques en jeu. Par ailleurs, une antenne hélicon a été implémentée dans le but d'atteindre des taux d'ionisation plus élevés. La riche phénoménologie des plasmas hélicons a été largement documentée, et les propriétés plasma ont été finement caractérisées. Enfin, les techniques d'imagerie rapide et de sondes 5-tips ont été exploitées pour identifier les oscillations basse-fréquences observées au sein du plasma hélicon.

Quatre axes majeurs se dégagent des travaux présentés :

- Les interactions cathode-plasma complexes mènent à l'existence d'un système dynamique riche, présentant plusieurs régimes d'opération qui furent fidèlement reproduits par une résolution numérique du bilan d'enthalpie ;
- Une première comparaison entre un modèle analytique de contrôle de potentiel plasma par injection d'électrons et un vaste jeu de données montre une compréhension qualitative de la modification du potentiel plasma, mais également la nécessité de raffiner le modèle afin d'ouvrir la voie à une approche prédictive du contrôle du potentiel plasma ;
- Une caractérisation complète de la colonne de plasma hélicon indique des taux d'ionisation élevés, et démontre de multiples caractéristiques typiques des plasmas hélicons, tels que la brisure de symétrie induite par le champ magnétique ou les transitions E-H-W ;

- Plusieurs instabilités basse-fréquences coexistent à fort champ magnétique, comme les oscillations de relaxation H-W et W-W, les instabilités de Kelvin-Hemholtz et de Rayleigh-Taylor, ainsi qu'une surprenante instabilité multi-échelle de cœur.

L'utilisation de la cathode émissive en tungstène a démontré un couplage inattendu entre tension de polarisation V_b et courant émis I_b. Une étude de la température de la cathode à l'aide d'un pyromètre optique a révélé l'existence d'un profil fortement hétérogène de température lors de l'émission thermoïonique. Cette caractéristique est accompagnée par une dynamique à l'échelle de la seconde, et l'existence d'un régime stable à faible émission, et d'un régime instable à forte émission. Un modèle thermodynamique, basé sur la résolution du bilan d'enthalpie, a permis une compréhension complète des mécanismes de chauffage et de refroidissement de la cathode. Par exemple, l'émission thermoïonique induite par la haute température de la cathode cause un chauffage par effet Joule supplémentaire, créant une boucle de rétroaction déstabilisante. De plus, l'émission d'électrons primaires augmente la densité du plasma, qui chauffe en retour la cathode uniformément par bombardement ionique. Quant aux boucles de rétroaction stabilisantes, elles trouvent leurs origines dans le refroidissement par évaporation d'électrons primaires, et dans les importantes dissipations radiatives fortement sensibles à la température du métal. La résolution numérique de ce système dynamique complet a révélé un excellent accord avec les mesures expérimentales de température. De plus, les régimes stables et instables ont été caractérisés dans l'espace des phases composé du courant de chauffage I_h et de la tension de polarisation V_b, à conditions expérimentales du plasma égales. Cette compréhension fine de la cathode émissive en tungstène ouvre la voie à une démocratisation de cet outil simple et peu coûteux, et à l'étude de son impact sur les propriétés du plasma.

Dans la continuité des travaux de thèse précédents [Dés18; Vin21], l'impact de cette cathode émissive sur le potentiel plasma a été étudié. Tout d'abord, le modèle analytique développé par Renaud Gueroult et Baptiste Trotabas [Tro+22] est introduit et transposé au cas expérimental de l'expérience VKP-ICP. Il est basé sur la résolution de la loi d'Ohm locale, via l'injection d'électrons au centre d'une colonne de plasma magnétisée et l'existence résultante d'un flux radial de charge. Ainsi, le plasma est assimilé à une résistance radiale $R_\perp$, connectant le cœur du plasma à la paroi mise à la masse, et traversée par un courant I_b imposé par la cathode. Les dépendances de $R_\perp$ vis-à-vis des paramètres expérimentaux sont mis en avant. Ce modèle est comparé à un large éventail de mesures expérimentales réalisées sous trois régimes opérationnels, à savoir ($B = 170$ G, $p_0 = 0.13$ Pa), ($B = 240$ G, $p_0 = 0.26$ Pa) et ($B = 340$ G, $p_0 = 0.13$ Pa), à différents courants I_b et tensions de polarisation V_b. Les profils radiaux des propriétés du plasma ont mis en évidence l'existence d'une chute de potentiel radiale accrue, conformément au modèle analytique. Un accord qualitatif est souligné, alors qu'une différence de moins d'un ordre de grandeur est trouvée entre les valeurs de $R_\perp$ attendues et mesurées. Cependant, ce modèle nécessite l'inclusion d'une gaine anodique prépondérante, de l'ordre de plusieurs T_e, afin de réaliser une prédiction fiable du potentiel électrostatique au sein du plasma. Cette contribution apporterait une compréhension quantitative au contrôle de l'écoulement du plasma sous l'effet de l'injection d'électrons, constatée empiriquement par Victor Désangles au cours de sa thèse [Dés18].

Une source hélicon a été implémentée avec succès au cours de cette thèse. Une antenne hélicon présente un couplage optimal au plasma, et un transfert efficace de la puissance depuis l'onde hélicon radio-fréquence au plasma lui-même. Des valeurs de densité importantes, avec des taux d'ionisation supérieurs à 50% sont atteignables sur une large gamme de paramètres expérimentaux. Une phénoménologie unique des plasmas hélicons est d'abord présentée. La caractérisation expérimentale avancée des propriétés plasma démontrent un excellent accord avec la littérature. Les transitions entre modes E-H-W et les hystérésis associées sont observées, la chiralité induite par le champ magnétique est mise en évidence et la proportionnalité entre densité et champ magnétique est vérifiée. De plus, l'existence privilégiée de modes azimuthaux $m = +1$ est confirmée à l'aide de mesures réalisées à l'aide d'une sonde B-dot, même lorsque la direction du champ magnétique n'y est pas favorable. Enfin, l'effet de l'injection d'électrons sur le plasma hélicon est brièvement exploré, et appuient les mesures réalisées dans l'expérience VKP-ICP.

Une vaste documentation des instabilités basse-fréquences présentes dans le plasma hélicon a été réalisée à l'aide de sondes électrostatiques et d'imagerie rapide. Trois types de fluctuations ont été documentées, à savoir les rares modes de relaxation H-W et W-W, les modes azimuthaux cohérents à fort champ magnétique ($B \geq 720$ G) et les fluctuations multi-échelles et basse-fréquences à très fort champ magnétique ($B = 1080$ G). À l'aide de techniques d'analyse d'image avancées (2D-FT, POD) et de mesures 5-tips, toutes développées par Simon Vincent au cours d'une thèse précédente [Vin21], une riche étude des oscillations basse-fréquences a révélé la coexistence de plusieurs instabilités. Une séparation d'échelle forte entre le cœur du plasma ($r < 2.5$ cm), sa périphérie (2.5 cm $< r <$ 6 cm) et le bord du plasma ($r > 6$ cm) est mise en évidence. Ainsi, jusqu'à trois instabilités majeures ont pu être observées simultanément. Si l'instabilité de cœur est encore énigmatique, les deux autres sont identifiées comme étant respectivement causées par une instabilité de Kelvin-Helmholtz et de Rayleigh-Taylor. Enfin, l'instabilité grande échelle à fort champ magnétique reste inexpliquée et nécessite de plus amples analyses. Sa compréhension est pourtant essentielle afin de générer des plasmas hélicons stables sur une plus large gamme de conditions expérimentales.

Ces travaux ouvrent de nombreuses perspectives. Tout d'abord, l'effet de l'injection d'électrons primaires dans une colonne de plasma hélicon s'avère riche. Au-delà de la modification des propriétés du plasma, l'addition d'énergie localisée a un rôle majeur sur les transitions E-H-W. Des transitions prématurées au mode W sont observées en injectant seulement 30 W supplémentaires à l'aide d'une cathode émissive centrée dans la colonne de plasma. Ce sujet est actuellement à l'étude, et présente des résultats préliminaires encourageants. De plus, une cathode émissive composée de LaB_6 est en cours de fabrication. Elle permettrait d'obtenir une distribution de température plus homogène et une polarisation uniforme de la cathode. Cette nouvelle cathode rendrait possible une injection plus forte d'électrons et un ajustement plus fin du courant émis I_b, se rapprochant alors des modèles théoriques idéaux. Un contrôle fin de la rotation de la colonne de plasma hélicon pourrait être atteint. Enfin, ces connaissances pourront être appliquées à la mise en service et au contrôle opératoire d'une seconde source hélicon. Un écoulement modulable de Von-Kármán pourrait être généré, où deux colonnes de plasma interragiraient, ouvrant ainsi la voie à des études de turbulence et d'interaction d'ondes au sein d'un dispositif expérimental nouveau. Cette amélioration est prévue sous peu. L'étude de ce nouveau système serait complémentée par une collaboration déjà existante avec l'équipe d'Ivo Furno au Swiss Plasma Center, Lausanne (Suisse). L'expérience RAID est dédiée à l'étude des interactions entre deux colonnes de plasma hélicons. Elle bénéficie d'un éventail avancé de diagnostics électrostatiques et optiques, formant donc une plateforme majeure pour l'étude fondamentale des plasmas hélicons. De plus, l'antenne birdcage utilisée sur RAID offre un comparatif instructif de l'impact de la source hélicon sur la génération et l'interaction de deux colonnes de plasma.

APPENDIX

A Supplementary figures - Chapter 1

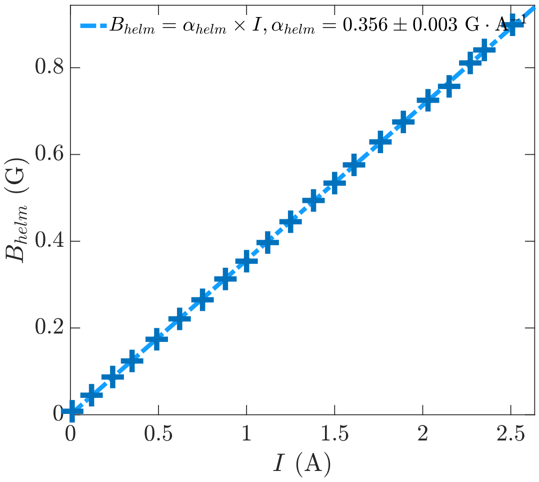

FIGURE A.1 – B_{helm} measurement as a function of I for the single-loop Helmholtz coil engineered. α_{helm} is measured at 0.356 ± 0.003 G $\cdot$ A^{-1}, while the theoretical value predicts 0.360 G $\cdot$ A^{-1}.

B Supplementary figures - Chapter 3

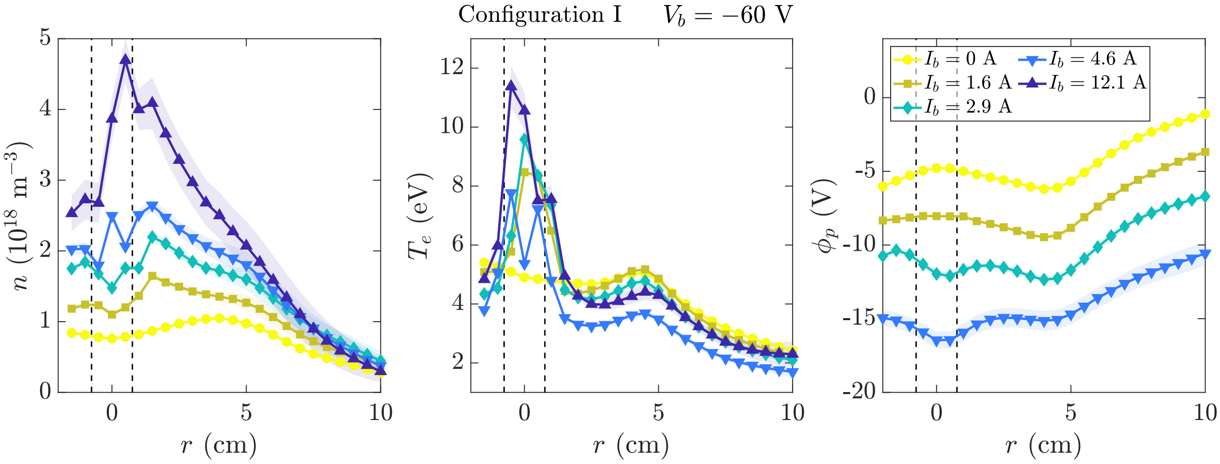

FIGURE B.2 – Radial profiles of plasma density n, electron temperature T_e and plasma potential ϕ_f in configuration I, with $V_b = -60$ V.

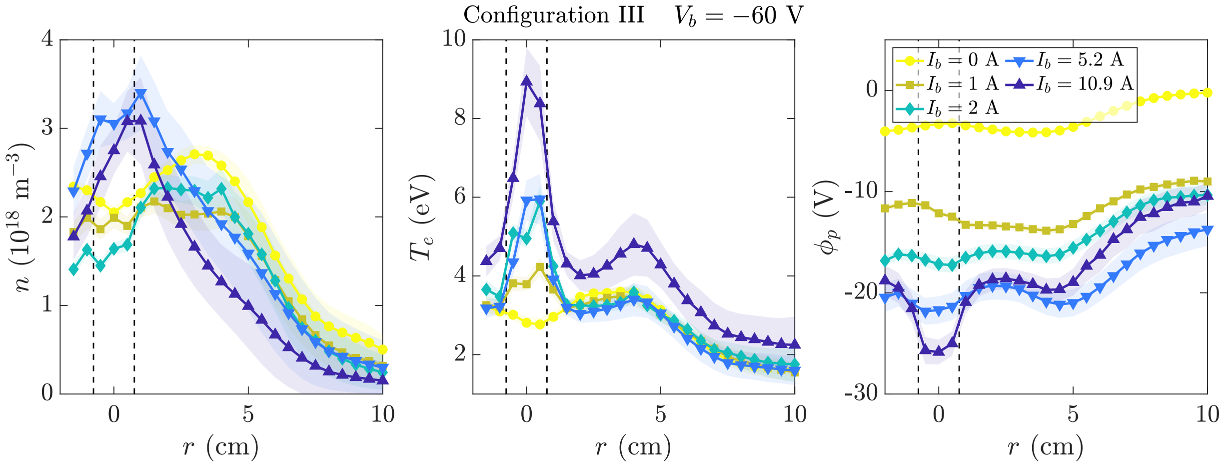

FIGURE B.3 – Radial profiles of plasma density n, electron temperature T_e and plasma potential ϕ_f in configuration III, with $V_b = -60$ V.

C Supplementary figures - Chapter 4

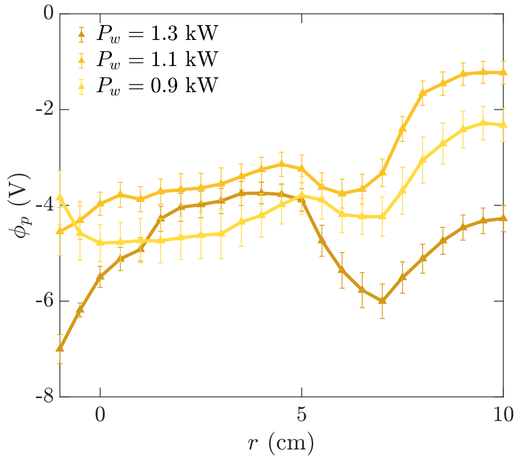

FIGURE C.4 – Plasma potential profiles for the VKP-HS1 set-up in the B_{out} configuration. The experimental parameters are $B = 1080$ G and $p_0 = 0.13$ Pa, while the power is modified.

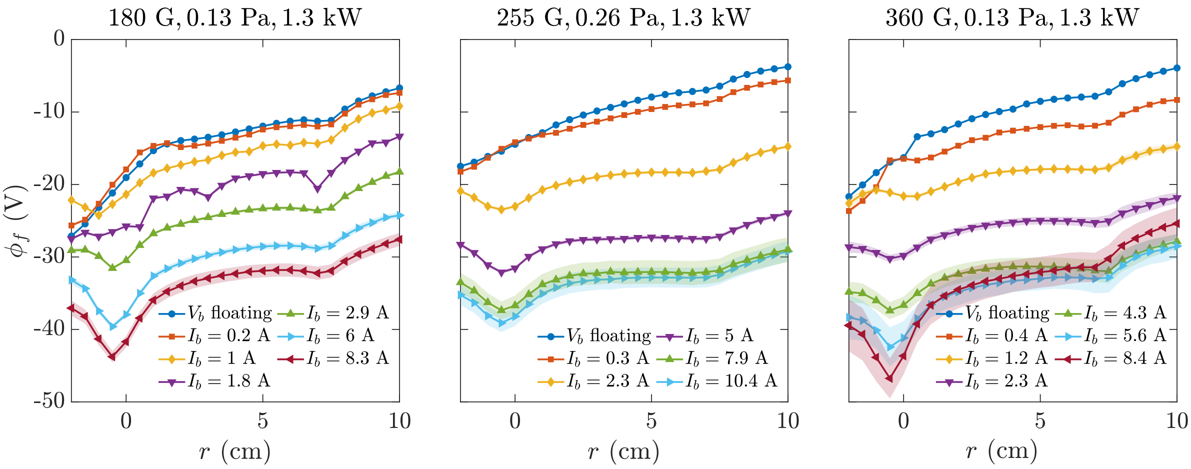

FIGURE C.5 – Floating potential profiles using a cold emissive probe in a helicon plasma with electron injection. V_b was set at -60 V.

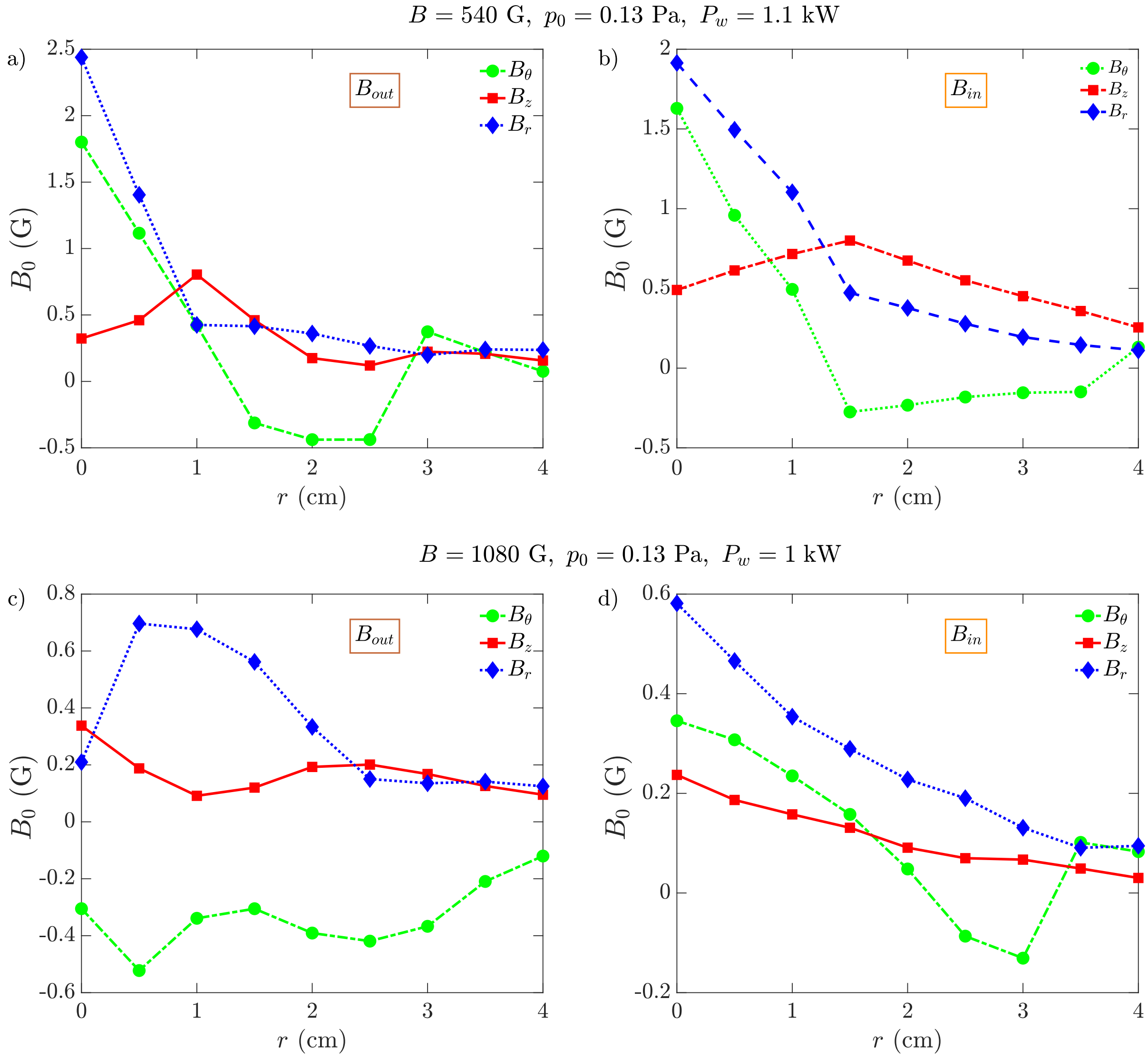

FIGURE C.6 – B-dot wave field structures for $B = 540$ (top row) and 1080 G (bottom row), for the B_{out} (left column) and B_{in} (right column) configurations.

D Supplementary figures - Chapter 5

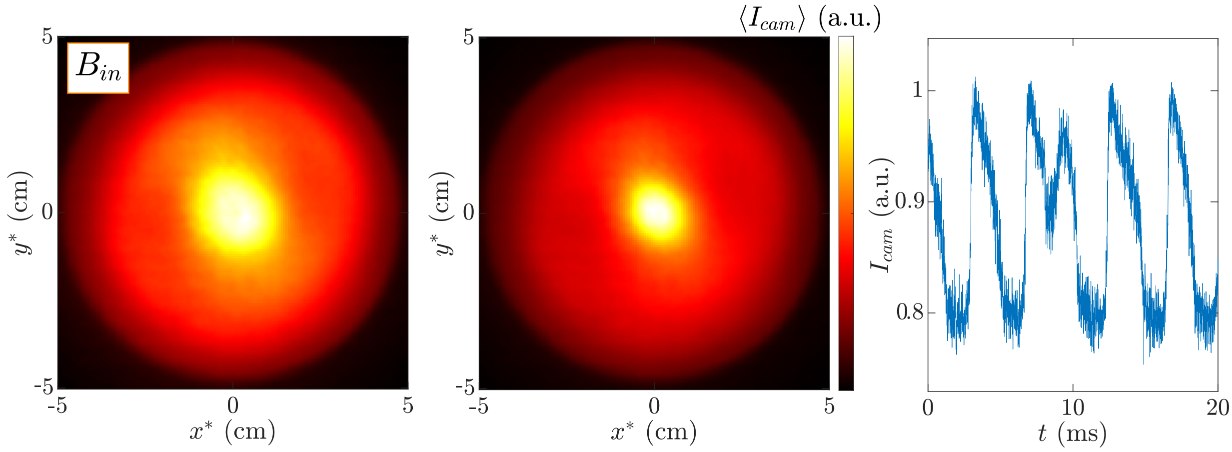

FIGURE D.7 – W-W oscillations in the B_{in} configuration at 720 G, 0.20 Pa and 1.4 kW. The left image corresponds to the wider and less bright mode compared to the right image. The graph represents the light intensity at the center over time.

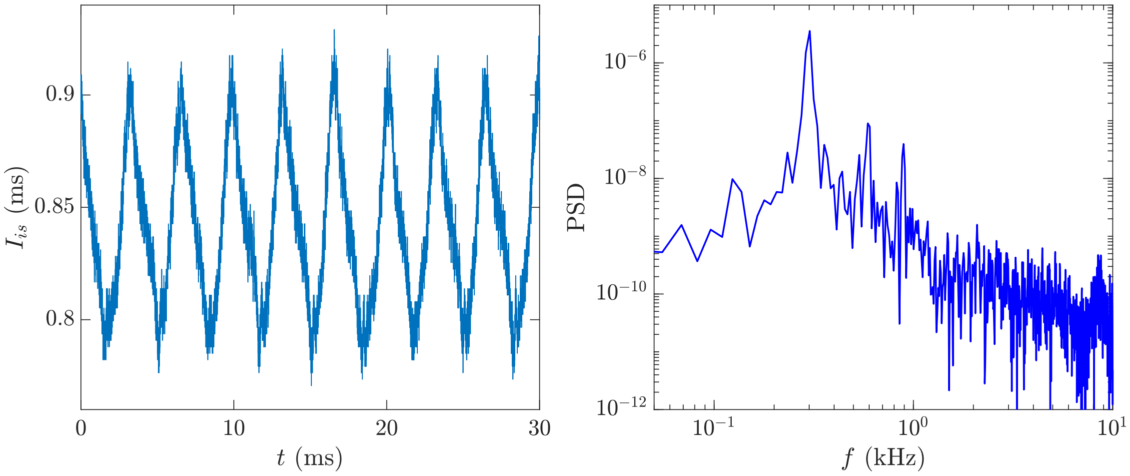

FIGURE D.8 – Ion saturation current at the plasma core for the B_{out} configuration, with $B = 450$ G, $p_0 = 0.13$ Pa and $P_w = 1.05$ kW, and its Fourier transform.

BIBLIOGRAPHIE

[Agg+23] S. Aggarwal, Y. Camenen, A. Escarguel et A. Poyé (2023). Centrifugal instability in a weakly magnetized rotating plasma column. *Journal of Plasma Physics* **89** 3, p. 905890310. DOI : 10.1017/S002237782300051X.

[Alv14] L. L. Alves (2014). The IST-LISBON database on LXCat. *J. Phys. Conf. Ser.* **565** 1, p. 012007. DOI : 10.1088/1742-6596/565/1/012007.

[Ara+16] H. Arakawa, S. Inagaki, M. Sasaki, Y. Kosuga, T. Kobayashi, N. Kasuya, Y. Nagashima, T. Yamada, M. Lesur, A. Fujisawa, K. Itoh et S.-I. Itoh (2016). Eddy, drift wave and zonal flow dynamics in a linear magnetized plasma. *Sci Rep* **6** 1. p. 33371. DOI : 10.1038/srep33371.

[Arn+96] C. Arnas Capeau, G. Prasad, G. Bachet et F. Doveil (1996). Analysis of the self-oscillations instability due to the plasma coupling with an emissive hot cathode sheath. *Physics of Plasmas* **3** 9, p. 3331-3336. DOI : 10.1063/1.871602.

[Ash+22] N. W. Ashcroft et N. D. Mermin. Solid state physics. Cengage Learning, 2022.

[Baa+20] S. D. Baalrud, B. Scheiner, B. T. Yee, M. M. Hopkins et E. Barnat (2020). Interaction of biased electrodes and plasmas : sheaths, double layers, and fireballs. *Plasma Sources Sci. Technol.* **29** 5. p. 053001. DOI : 10.1088/1361-6595/ab8177.

[Bei+98] I. I. Beilis et M. Keidar (1998). Sheath and presheath structure in the plasma–wall transition layer in an oblique magnetic field. *Physics of Plasmas* **5** 5, p. 1545-1553. DOI : 10.1063/1.872813.

[Bei+97] I. I. Beilis, M. Keidar et S. Goldsmith (1997). Plasma-wall transition : The influence of the electron to ion current ratio on the magnetic presheath structure. *Physics of Plasmas* **4** 10, p. 3461-3468. DOI : 10.1063/1.872242.

[Bel06] P. M. Bellan. Fundamentals of Plasma Physics. Cambridge : Cambridge University Press, 2006. DOI : 10.1017/CBO9780511807183.

[Ben08] M. S. Benilov (2008). Understanding and modelling plasma–electrode interaction in high-pressure arc discharges : a review. *J. Phys. D Appl. Phys.* **41** 14, p. 144001. DOI : 10.1088/0022-3727/41/14/144001.

[Ben14] M. S. BENILOV (2014). Multiple solutions in the theory of dc glow discharges and cathodic part of arc discharges. Application of these solutions to the modeling of cathode spots and patterns : a review. *Plasma Sources Sci. Technol.* DOI : `10.1088/0963-0252/23/5/054019`.

[Ben98] M. S. BENILOV (1998). Nonlinear surface heating of a plane sample and modes of current transfer to hot arc cathodes. *Phys. Rev. E* **58** 5. p. 6480-6494. DOI : `10.1103/PhysRevE.58.6480`.

[Ber+93] G. BERKOOZ, P. HOLMES et J. L. LUMLEY (1993). The Proper Orthogonal Decomposition in the Analysis of Turbulent Flows. *Annual Review of Fluid Mechanics* **25** Volume 25, 1993. p. 539-575. DOI : `10.1146/annurev.fl.25.010193.002543`.

[Bla+02] D. D. BLACKWELL, T. G. MADZIWA, D. ARNUSH et F. F. CHEN (2002). Evidence for Trivelpiece-Gould Modes in a Helicon Discharge. *Phys. Rev. Lett.* **88** 14. p. 145002. DOI : `10.1103/PhysRevLett.88.145002`.

[Bos+86] R. A. BOSCH et R. L. MERLINO (1986). Sudden Jumps, Hysteresis, and Negative Resistance in an Argon Plasma Discharge. I. Discharges with No Magnetic Field. *Beiträge aus der Plasmaphysik* **26** 1, p. 1-12. DOI : `https://doi.org/10.1002/ctpp.19860260102`.

[Bos70] R. W. BOSWELL (1970). Plasma production using a standing helicon wave. *Physics Letters A* **33** 7, p. 457-458. DOI : `10.1016/0375-9601(70)90606-7`.

[Bos84] R. W. BOSWELL (1984). Very efficient plasma generation by whistler waves near the lower hybrid frequency. *Plasma Phys. Control. Fusion* **26** 10, p. 1147. DOI : `10.1088/0741-3335/26/10/001`.

[Bou+15] G. BOUSSELIN, N. PLIHON, N. LEMOINE, J. CAVALIER et S. HEURAUX (2015). How plasma parameters fluctuations influence emissive probe measurements. *Phys. Plasmas* **22** 5, p. 053511. DOI : `10.1063/1.4921643`.

[Bou13] G. BOUSSELIN. Caractérisation expérimentale des instabilités et du transport non diffusif dans une colonne de plasma magnétisé. Développement, analyse critique et validation des diagnostics par sondes et imagerie rapide. Thèse de doct. Université de Lorraine, 2013.

[Bow+61] R. BOWERS, C. LEGENDY et F. ROSE (1961). Oscillatory Galvanomagnetic Effect in Metallic Sodium. *Phys. Rev. Lett.* **7** 9. p. 339-341. DOI : `10.1103/PhysRevLett.7.339`.

[Bro+05] F. BROCHARD, E. GRAVIER et G. BONHOMME (2005). Transition from flute modes to drift waves in a magnetized plasma column. *Physics of Plasmas* **12** 6, p. 062104. DOI : `10.1063/1.1921167`.

[Bur+05] M. J. BURIN, G. R. TYNAN, G. Y. ANTAR, N. A. CROCKER et C. HOLLAND (2005). On the transition to drift turbulence in a magnetized plasma column. *Physics of Plasmas* **12** 5, p. 052320. DOI : `10.1063/1.1889443`.

[Bur97] K. H. BURRELL (1997). Effects of E×B velocity shear and magnetic shear on turbulence and transport in magnetic confinement devices. *Physics of Plasmas* **4** 5, p. 1499-1518. DOI : `10.1063/1.872367`.

[But+18] B. BUTTENSCHÖN, N. FAHRENKAMP et O. GRULKE (2018). A high power, high density helicon discharge for the plasma wakefield accelerator experiment AWAKE. *Plasma Phys. Control. Fusion* **60** 7. p. 075005. DOI : `10.1088/1361-6587/aac13a`.

[Cal+11] E. de la Cal, D. Carralero, J. L. de Pablos, A. Alonso, L. Rios, P. García Sánchez et C. Hidalgo (2011). The Visible Intensified Cameras for Plasma Imaging in the TJ-II Stellarator. *Contributions to Plasma Physics* **51** 8. p. 742-753. doi : 10.1002/ctpp.201000039.

[Cam+17] M. D. Campanell et M. V. Umansky (2017). Improved understanding of the hot cathode current modes and mode transitions. *Plasma Sources Science and Technology* **26** 12, p. 124002. doi : 10.1088/1361-6595/aa97a9.

[Cam+15] M. D. Campanell, H. Wang, I. D. Kaganovich et A. V. Khrabrov (2015). Self-amplification of electrons emitted from surfaces in plasmas with E × B fields. *Plasma Sources Sci. Technol.* **24** 3, p. 034010. doi : 10.1088/0963-0252/24/3/034010.

[Cam20] M. D. Campanell (2020). Possible mitigation of tokamak plasma-surface interactions using thermionic divertor plates with inverse sheaths. *Physics of Plasmas* **27** 4, p. 042511. doi : 10.1063/1.5139904.

[Can+15] J. F. Caneses et B. Blackwell (2015). RF compensation of double Langmuir probes : modelling and experiment. *Plasma Sources Sci. Technol.* **24** 3, p. 035024. doi : 10.1088/0963-0252/24/3/035024.

[Cez+96] A. Cezairliyan, S. Krishanan et J. L. McClure (1996). Simultaneous measurements of normal spectral emissivity by spectral radiometry and laser polarimetry at high temperatures in millisecond-resolution pulse-heating experiments : Application to molybdenum and tungsten. *Int J Thermophys* **17** 6, p. 1455-1473. doi : 10.1007/BF01438679.

[Cha+11] P. Chabert et N. Braithwaite. Physics of Radio-Frequency Plasmas. Cambridge : Cambridge University Press, 2011. doi : 10.1017/CBO9780511974342.

[Cha09] C. Charles (2009). Plasmas for spacecraft propulsion. *J. Phys. D Appl. Phys.* **42** 16, p. 163001. doi : 10.1088/0022-3727/42/16/163001.

[Cha+91] P. A. Chatterton, J. A. Rees, W. L. Wu et K. AL-Assadi (1991). A self-compensating Langmuir probe for use in rf (13.56 MHz) plasma systems. *Vacuum* **42** 7, p. 489-493. doi : 10.1016/0042-207X(91)90022-B.

[Che91] F. F. Chen (1991). Plasma ionization by helicon waves. *Plasma Phys. Control. Fusion* **33** 4, p. 339. doi : 10.1088/0741-3335/33/4/006.

[Che01] F. F. Chen (2001). Langmuir probe analysis for high density plasmas. *Physics of Plasmas* **8** 6, p. 3029-3041. doi : 10.1063/1.1368874.

[Che03] F. F. Chen (2003). Lecture Notes on Langmuir Probe Diagnostics. *IEEE-ICOPS meeting.*

[Che15] F. F. Chen (2015). Helicon discharges and sources : a review. *Plasma Sources Sci. Technol.* **24** 1. p. 014001. doi : 10.1088/0963-0252/24/1/014001.

[Che+02] F. F. Chen, J. D. Evans et D. Arnush (2002). A floating potential method for measuring ion density. *Physics of Plasmas* **9** 4, p. 1449-1455. doi : 10.1063/1.1462630.

[Che+95] R. T. S. Chen, R. A. Breun, S. Gross, N. Hershkowitz, M.-K. J. Hsieh et J. Jacobs (1995). Experimental studies of multimode helicon plasma waves. *Plasma Sources Sci. Technol.* **4** 3, p. 337. doi : 10.1088/0963-0252/4/3/003.

[Chi+99] K.-K. Chi, T. E. Sheridan et R. W. Boswell (1999). Resonant cavity modes of a bounded helicon discharge. *Plasma Sources Sci. Technol.* **8** 3, p. 421. doi : 10.1088/0963-0252/8/3/312.

[Cho82] R. CHODURA (1982). Plasma–wall transition in an oblique magnetic field. *The Physics of Fluids* **25** 9, p. 1628-1633. DOI : `10.1063/1.863955`.

[Con+94] J. W. CONNER et H. R. WILSON (1994). Survey of theories of anomalous transport. *Plasma Phys. Control. Fusion* **36** 5, p. 719. DOI : `10.1088/0741-3335/36/5/002`.

[Cot+99] D. R. COTE, S. V. NGUYEN, A. K. STAMPER, D. S. ARMBRUST, D. TOBBEN, R. A. CONTI et G. Y. LEE (1999). Plasma-assisted chemical vapor deposition of dielectric thin films for ULSI semiconductor circuits. *IBM Journal of Research and Development* **43** 1.2. p. 5-38. DOI : `10.1147/rd.431.0005`.

[De 54] J. C. DE VOS (1954). A new determination of the emissivity of tungsten ribbon. *Physica* **20** 7, p. 690-714. DOI : `10.1016/S0031-8914(54)80182-0`.

[Deg+99a] A. W. DEGELING, T. E. SHERIDAN et R. W. BOSWELL (1999). Intense on-axis plasma production and associated relaxation oscillations in a large volume helicon source. *Physics of Plasmas* **6** 9, p. 3664-3673. DOI : `10.1063/1.873624`.

[Deg+99b] A. W. DEGELING, T. E. SHERIDAN et R. W. BOSWELL (1999). Model for relaxation oscillations in a helicon discharge. *Physics of Plasmas* **6** 5, p. 1641-1648. DOI : `10.1063/1.873419`.

[Dém14] B. DÉMOULIN (2014). Éléments sur la théorie des lignes de transmission. *Conversion de l'énergie électrique*.

[Des+84] P. D. DESAI, T. K. CHU, H. M. JAMES et C. Y. HO (1984). Electrical Resistivity of Selected Elements. *Journal of Physical and Chemical Reference Data* **13** 4, p. 1069-1096. DOI : `10.1063/1.555723`.

[Dés18] V. DÉSANGLES. Forçage à grande échelle d'une colonne de plasma faiblement magnétisée : influence d'une cathode émissive de grande taille. These de doctorat. Lyon, 2018.

[Dés+21] V. DÉSANGLES, G. BOUSSELIN, A. POYÉ et N. PLIHON (2021). Rotation and shear control of a weakly magnetized plasma column using current injection by emissive electrodes. *Journal of Plasma Physics* **87** 3. DOI : `10.1017/S0022377821000544`.

[Des+16] T. R. DESJARDINS et M. GILMORE (2016). Dynamics of flows, fluctuations, and global instability under electrode biasing in a linear plasma device. *Physics of Plasmas* **23** 5, p. 055710. DOI : `10.1063/1.4948282`.

[Dia+05] P. H. DIAMOND, S.-I. ITOH, K. ITOH et T. S. HAHM (2005). Zonal flows in plasma—a review. *Plasma Phys. Control. Fusion* **47** 5, p. R35. DOI : `10.1088/0741-3335/47/5/R01`.

[Doy+07] E. J. DOYLE, W. A. HOULBERG, Y. KAMADA, V. MUKHOVATOV, T. H. OSBORNE, A. POLEVOI, G. BATEMAN, J. W. CONNOR, J. G. CORDEY, T. FUJITA, X. GARBET, T. S. HAHM, L. D. HORTON, A. E. HUBBARD, F. IMBEAUX, F. JENKO, J. E. KINSEY, Y. KISHIMOTO, J. LI, T. C. LUCE, Y. MARTIN, M. OSSIPENKO, V. PARAIL, A. PEETERS, T. L. RHODES, J. E. RICE, C. M. ROACH, V. ROZHANSKY, F. RYTER, G. SAIBENE, R. SARTORI, A. C. C. SIPS, J. A. SNIPES, M. SUGIHARA, E. J. SYNAKOWSKI, H. TAKENAGA, T. TAKIZUKA, K. THOMSEN, M. R. WADE, H. R. WILSON, I. T. P. T. GROUP, I. C. DATABASE, M. T. GROUP, I. PEDESTAL et E. T. GROUP (2007). Chapter 2 : Plasma confinement and transport. *Nucl. Fusion* **47** 6, p. S18. DOI : `10.1088/0029-5515/47/6/S02`.

[DuB+12] A. M. DUBOIS, A. C. EADON et E. THOMAS Jr. (2012). Suppression of drift waves in a linear magnetized plasma column. *Physics of Plasmas* **19** 7, p. 072102. DOI : `10.1063/1.4731711`.

[DuB+14] A. M. DuBois, J. Thomas Edward, W. E. Amatucci et G. Ganguli (2014). Density gradient effects on transverse shear driven lower hybrid waves. *Physics of Plasmas* **21** 6, p. 062117. DOI : `10.1063/1.4886145`.

[Dur+01] T. Durakiewicz, A. Arko, J. Joyce, D. Moore et S. Halas (2001). Thermal work function shifts for polycrystalline metal surfaces. *Surface Science* **478** 1-2, p. 72-82. DOI : `10.1016/S0039-6028(01)00898-6`.

[Dys+00] A. Dyson, P. Bryant et J. E. Allen (2000). Multiple harmonic compensation of Langmuir probes in rf discharges. *Meas. Sci. Technol.* **11** 5, p. 554-559. DOI : `10.1088/0957-0233/11/5/316`.

[Fan06] U. Fantz (2006). Basics of plasma spectroscopy. *Plasma Sources Sci. Technol.* **15** 4, p. S137. DOI : `10.1088/0963-0252/15/4/S01`.

[Fil+23] F. Filleul, A. Caldarelli, K. Takahashi, R. W. Boswell, C. Charles, J. E. Cater et N. Rattenbury (2023). Helicon waves in a converging-diverging magnetoplasma. *Plasma Sources Sci. Technol.* **32** 11. p. 115015. DOI : `10.1088/1361-6595/ad0b96`.

[Fle04] J. A. Fleming. Improvements in Instruments for Detecting and Measuring Alternating Electric Currents. Patent GB190424850A. 1904.

[Fra+02] C. M. Franck, O. Grulke et T. Klinger (2002). Magnetic fluctuation probe design and capacitive pickup rejection. *Rev. Sci. Instrum.* **73** 11. DOI : `10.1063/1.1512341`.

[Fra+03] C. M. Franck, O. Grulke et T. Klinger (2003). Mode transitions in helicon discharges. *Physics of Plasmas* **10** 1, p. 323-325. DOI : `10.1063/1.1528903`.

[Fru17] A. Fruchtman (2017). Neutral gas depletion in low temperature plasma. *J. Phys. D Appl. Phys.* **50** 47. p. 473002. DOI : `10.1088/1361-6463/aa87a9`.

[Fun+07] W. Fundamenski et O. E. Garcia (2007). Comparison of Coulomb Collision Rates in the Plasma Physics and Magnetically Confined Fusion Literature. *EFDA-JET Report* **7** 1, p. 1-13.

[Gao+20] J.-Y. Gao, Y.-F. Yang, X.-K. Zhang, S.-L. Li, P. Hu et J.-S. Wang (2020). A review on recent progress of thermionic cathode. *Tungsten* **2** 3, p. 289-300. DOI : `10.1007/s42864-020-00059-1`.

[Gar+03] X. Garbet, L. Garzotti, P. Mantica, H. Nordman, M. Valovic, H. Weisen et C. Angioni (2003). Turbulent Particle Transport in Magnetized Plasmas. *Phys. Rev. Lett.* **91** 3. p. 035001. DOI : `10.1103/PhysRevLett.91.035001`.

[Gar99] F. L. S. Garcia (1999). Modélisation des composants électromagnétiques haute fréquence par la méthode des éléments finis, p. 149.

[Gek+16] W. Gekelman, P. Pribyl, Z. Lucky, M. Drandell, D. Leneman, J. Maggs, S. Vincena, B. Van Compernolle, S. K. P. Tripathi, G. Morales, T. A. Carter, Y. Wang et T. DeHaas (2016). The upgraded Large Plasma Device, a machine for studying frontier basic plasma physics. *Rev. Sci. Instrum.* **87** 2, p. 025105. DOI : `10.1063/1.4941079`.

[Gha+12] M. R. Ghanbari, M. Ghoranneviss, A. S. Elahi, S. Mohamadi et R. Arvin (2012). Controlling the energy of runaway electrons by emissive limiter biasing in tokamaks. *Physica Scripta* **85** 5, p. 055502. DOI : `10.1088/0031-8949/85/05/055502`.

[Gil+15] M. Gilmore, A. G. Lynn, T. R. Desjardins, Y. Zhang, C. Watts, S. C. Hsu, S. Betts, R. Kelly et E. Schamiloglu (2015). The HelCat basic plasma science device. *Journal of Plasma Physics* **81** 1, p. 345810104. DOI : `10.1017/S0022377814000919`.

[God+11] V. A. Godyak et V. I. Demidov (2011). Probe measurements of electron-energy distributions in plasmas : what can we measure and how can we achieve reliable results ? *Appl. Phys.*, p. 31.

[Goe+07] D. M. Goebel, R. M. Watkins et K. K. Jameson (2007). LaB6 Hollow Cathodes for Ion and Hall Thrusters. *Journal of Propulsion and Power* **23** 3, p. 552-558. DOI : `10.2514/1.25475`.

[Gon+20] V. Gonzalez-Fernandez, P. David, R. Baude, A. Escarguel et Y. Camenen (2020). Spatially resolved determination of the electronic density and temperature by a visible spectro-tomography diagnostic in a linear magnetized plasma. *Sci Rep* **10** 1. p. 5389. DOI : `10.1038/s41598-020-62426-9`.

[Gra+23] M. Granetzny, O. Schmitz et M. Zepp (2023). Preference of right-handed whistler modes and helicon discharge directionality due to plasma density gradients. *Physics of Plasmas* **30** 12, p. 120701. DOI : `10.1063/5.0173918`.

[Gra+04] E. Gravier, F. Brochard, G. Bonhomme, T. Pierre et J. L. Briançon (2004). Low-frequency instabilities in a laboratory magnetized plasma column. *Physics of Plasmas* **11** 2, p. 529-537. DOI : `10.1063/1.1636479`.

[Gre+93] F. Greiner, T. Klinger, H. Klostermann et A. Piel (1993). Experiments and particle-in-cell simulation on self-oscillations and period doubling in thermionic discharges at low pressure. *Phys. Rev. Lett.* **70**, p. 3071-3074. DOI : `10.1103/PhysRevLett.70.3071`.

[Gru+07] O. Grulke, S. Ullrich, T. Windisch et T. Klinger (2007). Laboratory studies of drift waves : nonlinear mode interaction and structure formation in turbulence. *Plasma Phys. Control. Fusion* **49** 12B, p. B247. DOI : `10.1088/0741-3335/49/12B/S23`.

[Gsc+22] E. Gschwendtner et al. (2022). The AWAKE Run 2 Programme and Beyond. *Symmetry* **14** 8. p. 1680. DOI : `10.3390/sym14081680`.

[Gue+18] R. Gueroult, J. M. Rax et N. J. Fisch (2018). Opportunities for plasma separation techniques in rare earth elements recycling. *Journal of Cleaner Production* **182**, p. 1060-1069. DOI : `10.1016/j.jclepro.2018.02.066`.

[Gue+24] R. Gueroult, S. K. P. Tripathi, F. Gaboriau, T. R. Look et N. J. Fisch. Plasma potential shaping using end-electrodes in the Large Plasma Device. en. Rapp. tech. arXiv :2401.06480. arXiv, 2024.

[Gue+19] R. Gueroult, J.-M. Rax et N. J. Fisch (2019). A necessary condition for perpendicular electric field control in magnetized plasmas. *Physics of Plasmas* **26** 12, p. 122106. DOI : `10.1063/1.5126083`.

[Gui+21] P. Guittienne, R. Jacquier, B. P. Duteil, A. A. Howling, R. Agnello et I. Furno (2021). Helicon wave plasma generated by a resonant birdcage antenna : magnetic field measurements and analysis in the RAID linear device. *Plasma Sources Sci. Technol.* **30** 7. p. 075023. DOI : `10.1088/1361-6595/ac0da3`.

[H P+02] K. H. Pae et S. J. Hahn (2002). Self-Oscillation and Chaos in Positive-Bias Plasma Diodes. *Journal of the Physical Society of Japan* **71** 9, p. 2169-2173. DOI : `10.1143/JPSJ.71.2169`.

[Han+17] K. M. Hanquist, K. Hara et I. D. Boyd (2017). Detailed modeling of electron emission for transpiration cooling of hypersonic vehicles. *Journal of Applied Physics* **121** 5, p. 053302. doi : 10.1063/1.4974961.

[Har+22] K. Hara, A. R. Mansour et S. Tsikata (2022). Theory of gradient drift instabilities in low-temperature, partially magnetised plasmas. *Journal of Plasma Physics* **88** 4, p. 905880408. doi : 10.1017/S002237782200068X.

[Her+49] C. Herring et M. H. Nichols (1949). Thermionic Emission. *Rev. Mod. Phys.* **21** 2, p. 185-270. doi : 10.1103/RevModPhys.21.185.

[Hop95] M. B. Hopkins (1995). Langmuir Probe Measurements in the Gaseous Electronics Conference RF Reference Cell. *J Res Natl Inst Stand Technol* **100** 4, p. 415-425. doi : 10.6028/jres.100.031.

[Hop94] J. Hopwood (1994). Planar RF induction plasma coupling efficiency. *Plasma Sources Sci. Technol.* **3**, p. 460-464. doi : 10.1088/0963-0252/3/4/002.

[Hor99] W. Horton (1999). Drift waves and transport. *Rev. Mod. Phys.* **71** 3. p. 735-778. doi : 10.1103/RevModPhys.71.735.

[Hor+87] W. Horton, T. Tajima et T. Kamimura (1987). Kelvin–Helmholtz instability and vortices in magnetized plasma. *The Physics of Fluids* **30** 11, p. 3485-3495. doi : 10.1063/1.866429.

[Hou+12] S. Houshmandyar et E. E. Scime (2012). Enhanced neutral depletion in a static helium helicon discharge. *Plasma Sources Sci. Technol.* **21** 3. p. 035008. doi : 10.1088/0963-0252/21/3/035008.

[Isa+19] S. Isayama, S. Shinohara, T. Hada et S. H. Chen (2019). Spatio-temporal behavior of density jumps and the effect of neutral depletion in high-density helicon plasma. *Physics of Plasmas* **26** 5, p. 053504. doi : 10.1063/1.5093920.

[Jac+23] R. Jacquier, R. Agnello, M. Baquero-Ruiz, H. Bergerioux, P. Guittienne, A. A. Howling, L. Kadi, R. Karimov, C. Stollberg, S. Vincent et I. Furno (2023). A double-ended helicon source to symmetrize RAID plasma. *Fusion Engineering and Design* **192**, p. 113614. doi : 10.1016/j.fusengdes.2023.113614.

[Jac+19] R. Jacquier, R. Agnello, B. Pouradier Duteil, P. Guittienne, A. Howling, G. Plyushchev, C. Marini, A. Simonin, I. Morgal, S. Bechu et I. Furno (2019). First B-dot measurements in the RAID device, an alternative negative ion source for DEMO neutral beams. *Fusion Engineering and Design* **146**, p. 1140-1144. doi : 10.1016/j.fusengdes.2019.02.025.

[Jas72] D. L. Jassby (1972). Transverse Velocity Shear Instabilities within a Magnetically Confined Plasma. *The Physics of Fluids* **15** 9, p. 1590-1604. doi : 10.1063/1.1694135.

[Jim+23] P. Jiménez, J. Zhou, J. Navarro-Cavallé, P. Fajardo, M. Merino et E. Ahedo (2023). Analysis of a cusped helicon plasma thruster discharge. *Plasma Sources Sci. Technol.* **32** 10. p. 105013. doi : 10.1088/1361-6595/ad01da.

[Jin+19] S. Jin, M. J. Poulos, B. Van Compernolle et G. J. Morales (2019). Plasma flows generated by an annular thermionic cathode in a large magnetized plasma. *Physics of Plasmas* **26** 2, p. 022105. doi : 10.1063/1.5063597.

[Kag+20] I. D. Kaganovich, A. Smolyakov, Y. Raitses, E. Ahedo, I. G. Mikellides, B. Jorns, F. Taccogna, R. Gueroult, S. Tsikata, A. Bourdon, J.-P. Boeuf, M. Keidar, A. T. Powis, M. Merino, M. Cappelli, K. Hara, J. A. Carlsson, N. J. Fisch, P. Chabert, I. Schweigert, T. Lafleur, K. Matyash, A. V. Khrabrov, R. W. Boswell et A. Fruchtman (2020). Physics of E × B discharges relevant to plasma propulsion and similar technologies. *Physics of Plasmas* **27** 12, p. 120601. DOI : 10.1063/5.0010135.

[Kam+96] I. V. Kamenski et G. G. Borg (1996). An evaluation of different antenna designs for helicon wave excitation in a cylindrical plasma source. *Physics of Plasmas* **3** 12, p. 4396-4409. DOI : 10.1063/1.872057.

[Kar+22] S. Karbashewski, R. D. Sydora, B. V. Compernolle, T. Simala-Grant et M. J. Poulos (2022). Magnetized plasma pressure filaments : Analysis of chaotic and intermittent transport events driven by drift-Alfvén modes. *Physics of Plasmas* **29** 11, p. 112309. DOI : 10.1063/5.0104283.

[Kaw08] H. Kawano (2008). Effective work functions for ionic and electronic emissions from mono- and polycrystalline surfaces. *Progress in Surface Science* **83** 1-2, p. 1-165. DOI : 10.1016/j.progsurf.2007.11.001.

[Kaw22] H. Kawano (2022). Effective Work Functions of the Elements. *Progress in Surface Science* **97** 1, p. 100583. DOI : 10.1016/j.progsurf.2020.100583.

[Ken+69] G. I. Kent, N. C. Jen et F. F. Chen (1969). Transverse Kelvin-Helmholtz Instability in a Rotating Plasma. *The Physics of Fluids* **12** 10, p. 2140-2151. DOI : 10.1063/1.1692323.

[Ker+01] H. Kersten, H. Deutsch, H. Steffen, G. Kroesen et R. Hippler (2001). The energy balance at substrate surfaces during plasma processing. *Vacuum* **63** 3, p. 385-431. DOI : 10.1016/S0042-207X(01)00350-5.

[Ker+94] H. Kersten, R. J. M. M. Snijkers, J. Schulze, G. M. W. Kroesen, H. Deutsch et F. J. de Hoog (1994). Energy transfer from radio frequency sheath accelerated $\mathrm{CF}^{+}{}_{3}$ and Ar^{+} ions to a Si wafer. *Appl. Phys. Lett.* **64** 12, p. 1496-1498. DOI : 10.1063/1.111870.

[Klo+65] J. P. Klozenberg, B. McNamara et P. C. Thonemann (1965). The dispersion and attenuation of helicon waves in a uniform cylindrical plasma. *Journal of Fluid Mechanics* **21** 3, p. 545-563. DOI : 10.1017/S0022112065000320.

[Kom+17] M. Komm, S. Ratynskaia, P. Tolias, J. Cavalier, R. Dejarnac, J. P. Gunn et A. Podolnik (2017). On thermionic emission from plasma-facing components in tokamak-relevant conditions. *Plasma Physics and Controlled Fusion* **59** 9, p. 094002. DOI : 10.1088/1361-6587/aa78c4.

[Kon92] M. Konuma. Film Deposition by Plasma Techniques. Berlin, Heidelberg : Springer Berlin Heidelberg, 1992. DOI : 10.1007/978-3-642-84511-6.

[Krä99] M. Krämer (1999). Propagation and damping of m=+1 and m=-1 helicon modes in an inhomogeneous plasma column. *Physics of Plasmas* **6** 4, p. 1052-1058. DOI : 10.1063/1.873352.

[Kra+23] A. Kramida, Y. Ralchenko et J. Reader (2023). NIST Atomic Spectra Database (version 5.11). *[Online]*.

[Lee+23] H. Y. Lee, J. H. Kim, H. H. Wi, J. G. Kwak et S. J. Wang (2023). RF conditioning to suppress multipactor discharge for helicon wave current drive in KSTAR. *Fusion Engineering and Design* **193**, p. 113782. DOI : 10.1016/j.fusengdes.2023.113782.

[Leh+65] J. A. Lehane et P. C. Thonemann (1965). An experimental study of helicon wave propagation in a gaseous plasma. *Proc. Phys. Soc.* **85** 2, p. 301. DOI : 10.1088/0370-1328/85/2/312.

[Leh73] B. Lehnert (1973). The Partially Ionized Plasma Centrifuge. *Phys. Scr.* **7** 3, p. 102. DOI : 10.1088/0031-8949/7/3/002.

[Lie+05] M. A. Lieberman et A. J. Lichtenberg. Principles of Plasma Discharges and Materials Processing. John Wiley & Sons, Ltd, 2005. DOI : 10.1002/0471724254.

[Lig+02] M. Light, F. F. Chen et P. L. Colestock (2002). Quiescent and unstable regimes of a helicon plasma. *Plasma Sources Sci. Technol.* **11** 3, p. 273. DOI : 10.1088/0963-0252/11/3/308.

[Lig+01] M. Light, F. F. Chen et P. L. Colestock (2001). Low frequency electrostatic instability in a helicon plasma. *Physics of Plasmas* **8** 10, p. 4675-4689. DOI : 10.1063/1.1403415.

[Lig+95] M. Light, I. D. Sudit, F. F. Chen et D. Arnush (1995). Axial propagation of helicon waves. *Physics of Plasmas* **2** 11, p. 4094-4103. DOI : 10.1063/1.871032.

[Liu+23] H. Liu, Y. Yu, C. Xiao, Z. Yuan, H. Wang, L. Nie, R. Ke, T. Long, S. Gong et M. Xu (2023). Radially inward particle transport driven by low-frequency instability in cylindrical magnetized plasma. *Plasma Phys. Control. Fusion* **65** 5. p. 055017. DOI : 10.1088/1361-6587/acc209.

[Liz+21a] G. Liziakin, N. Antonov, R. Usmanov, A. Melnikov, R. Timirkhanov, N. Vorona, V. S. Smirnov, A. Oiler, S. Kislenko, A. Gavrikov et V. P. Smirnov (2021). Experimental demonstration of plasma mass separation in a configuration with a potential well and crossed electric and magnetic fields. *Plasma Phys. Control. Fusion*. DOI : 10.1088/1361-6587/abd25e.

[Liz+20] G. Liziakin, A. Gavrikov et V. Smirnov (2020). Negative electric potential in a cylindrical plasma column with magnetized electrons. *Plasma Sources Sci. Technol.* **29** 1, p. 015008. DOI : 10.1088/1361-6595/ab5ad5.

[Liz+21b] G. Liziakin, A. Oiler, A. Gavrikov, N. Antonov et V. Smirnov (2021). Radial distribution of the plasma potential in a cylindrical plasma column with a longitudinal magnetic field. *Journal of Plasma Physics* **87** 4, p. 905870414. DOI : 10.1017/S0022377821000829.

[Liz+21c] G. Liziakin, A. Oiler, A. Gavrikov, N. Antonov et V. Smirnov (2021). Radial distribution of the plasma potential in a cylindrical plasma column with a longitudinal magnetic field. *Journal of Plasma Physics* **87** 4, p. 905870414. DOI : 10.1017/S0022377821000829.

[Luc+20] R. Lucken, A. Tavant, A. Bourdon, M. A. Lieberman et P. Chabert (2020). Saturation of the magnetic confinement in weakly ionized plasma. *Plasma Sources Sci. Technol.* **29** 6. p. 065014. DOI : 10.1088/1361-6595/ab38b2.

[Lum67] J. L. Lumley (1967). The structure of inhomogeneous turbulent flows. *Atmospheric Turbulence and Radio Wave Propagation*, p. 166-178.

[Lum+20] A. Lumsdaine, S. C. Thakur, J. Tipton, M. Simmonds, J. F. Caneses Marin, R. Goulding, D. McGinnis, G. Tynan, J. Rapp et J. Burnett (2020). Testing and analysis of steady-state helicon plasma source for the Material Plasma Exposure eXperiment (MPEX). *Fusion Engineering and Design* **160**, p. 112001. DOI : 10.1016/j.fusengdes.2020.112001.

[Mat+99] T. MATSUMOTO, A. CEZAIRLIYAN et D. BASAK (1999). Hemispherical Total Emissivity of Niobium, Molybdenum, and Tungsten at High Temperatures Using a Combined Transient and Brief Steady-State Technique. *International Journal of Thermophysics* **20** 3, p. 943-952. DOI : `10.1023/A:1022699622719`.

[Mes+06] S. MESSER, D. D. BLACKWELL, W. E. AMATUCCI et D. N. WALKER (2006). Broadband calibration of radio-frequency magnetic induction probes. *Rev. Sci. Instrum.* **77**, p. 115104.

[Mil+98a] D. G. MILJAK et F. F. CHEN (1998). Density limit in helicon discharges. *Plasma Sources Sci. Technol.* **7** 4, p. 537. DOI : `10.1088/0963-0252/7/4/011`.

[Mil+98b] D. G. MILJAK et F. F. CHEN (1998). Helicon wave excitation with rotating antenna fields. *Plasma Sources Sci. Technol.* **7** 1, p. 61. DOI : `10.1088/0963-0252/7/1/009`.

[Mon+09] R. MONCHAUX, M. BERHANU, S. AUMAÎTRE, A. CHIFFAUDEL, F. DAVIAUD, B. DUBRULLE, F. RAVELET, S. FAUVE, N. MORDANT, F. PÉTRÉLIS, M. BOURGOIN, P. ODIER, J.-F. PINTON, N. PLIHON et R. VOLK (2009). The von Kármán Sodium experiment : Turbulent dynamical dynamos. *Physics of Fluids* **21** 3, p. 035108. DOI : `10.1063/1.3085724`.

[Mor+16] J. MORITZ, E. FAUDOT, S. DEVAUX et S. HEURAUX (2016). Plasma sheath properties in a magnetic field parallel to the wall. *Physics of Plasmas* **23** 6, p. 062509. DOI : `10.1063/1.4953897`.

[Mor+18] J. MORITZ, E. FAUDOT, S. DEVAUX et S. HEURAUX (2018). The plasma-wall transition layers in the presence of collisions with a magnetic field parallel to the wall. *Physics of Plasmas* **25** 1, p. 013534. DOI : `10.1063/1.5010852`.

[Mor+23] J. MORITZ, S. HEURAUX, N. LEMOINE, M. LESUR, E. GRAVIER, F. BROCHARD, L. MAROT et P. HIRET (2023). Thermionic emission of a tungsten surface in high heat flux plasma : PIC simulations. *Physics of Plasmas* **30**, p. 083514. DOI : `10.1063/5.0160767`.

[Mor+19] J. MORITZ, M. LESUR, E. FAUDOT, S. DEVAUX, S. HEURAUX et J. LEDIG (2019). The plasma-wall transition with collisions and an oblique magnetic field : Reversal of potential drops at grazing incidences. *Physics of Plasmas* **26** 1, p. 013507. DOI : `10.1063/1.5061832`.

[Nie+08] K. NIEMI et M. KRÄMER (2008). Helicon mode formation and radio frequency power deposition in a helicon-produced plasma. *Physics of Plasmas* **15** 7, p. 073503. DOI : `10.1063/1.2947561`.

[Old+10] S. OLDENBÜRGER, C. BRANDT, F. BROCHARD, N. LEMOINE et G. BONHOMME (2010). Spectroscopic interpretation and velocimetry analysis of fluctuations in a cylindrical plasma recorded by a fast camera. *Review of Scientific Instruments* **81** 6, p. 063505. DOI : `10.1063/1.3442029`.

[Oos+03] G. V. OOST, J. ADÁMEK, V. ANTONI, P. BALAN, J. A. BOEDO, P. DEVYNCK, I. ĎURAN, L. ELISEEV, J. P. GUNN, M. HRON, C. IONITA, S. JACHMICH, G. S. KIRNEV, E. MARTINES, A. MELNIKOV, R. SCHRITTWIESER, C. SILVA, J. STÖCKEL, M. TENDLER, C. VARANDAS, M. V. SCHOOR, V. VERSHKOV et R. R. WEYNANTS (2003). Turbulent transport reduction by E×B velocity shear during edge plasma biasing : recent experimental results. *Plasma Phys. Control. Fusion* **45** 5, p. 621. DOI : `10.1088/0741-3335/45/5/308`.

[Pag+23] F. PAGAUD, V. DOLIQUE, N. CLAIRE et N. PLIHON (2023). Emissive cathode immersed in a plasma : plasma–cathode interactions, operation and stability. *Plasma Sources Sci. Technol.* **32** 11. p. 115019. DOI : `10.1088/1361-6595/ad0b2f`.

[Ped+15] D. PEDRINI, R. ALBERTONI, F. PAGANUCCI et M. ANDRENUCCI (2015). Theoretical Model of a Lanthanum Hexaboride Hollow Cathode. *IEEE Transactions on Plasma Science* **43** 1, p. 209-217. DOI : `10.1109/TPS.2014.2367815`.

[Phe94] A. V. PHELPS (1994). The application of scattering cross sections to ion flux models in discharge sheaths. *Journal of Applied Physics* **76** 2, p. 747-753. DOI : `10.1063/1.357820`.

[Pie+92] R. B. PIEJAK, V. A. GODYAK et B. M. ALEXANDROVICH (1992). A simple analysis of an inductive RF discharge. *Plasma Sources Sci. Technol.* **1**, p. 179-186. DOI : `10.1088/0963-0252/1/3/006`.

[Pin+18] R. I. PINSKER, R. PRATER, C. P. MOELLER, J. S. DEGRASSIE, C. C. PETTY, M. PORKOLAB, J. P. ANDERSON, A. M. GAROFALO, C. LAU, A. NAGY, D. C. PACE, H. TORREBLANCA, J. G. WATKINS et L. ZENG (2018). Experiments on helicons in DIII-D—investigation of the physics of a reactor-relevant non-inductive current drive technology*. *Nucl. Fusion* **58** 10. p. 106007. DOI : `10.1088/1741-4326/aad1f8`.

[Pli+15] N. PLIHON, G. BOUSSELIN, F. PALERMO, J. MORALES, W. J. T. BOS, F. GODEFERD, M. BOURGOIN, J. F. PINTON, M. MOULIN et A. AANESLAND (2015). Flow dynamics and magnetic induction in the von-Kármán plasma experiment. *J. Plasma Phys.* **81** 1, p. 345810102. DOI : `10.1017/S002237781400083X`.

[Pol+17] K. A. POLZIN, C. S. HILL, P. J. TURCHI, R. L. BURTON, S. MESSER, R. H. LOVBERG et A. K. HALLOCK (2017). Recommended Practice for Use of Inductive Magnetic Field Probes in Electric Propulsion Testing. *Journal of Propulsion and Power* **33** 3, p. 659-667. DOI : `10.2514/1.B35406`.

[Pou19] M. J. POULOS (2019). Model for the operation of an emissive cathode in a large magnetized-plasma. *Physics of Plasmas* **26** 2, p. 022104. DOI : `10.1063/1.5063596`.

[Pre85] W. H. PREECE (1885). II. On a peculiar behaviour of glow-lamps when raised to high incandescence. *Proceedings of the Royal Society of London* **38** 235-238, p. 219-230. DOI : `10.1098/rspl.1884.0093`.

[Rax+19] J. M. RAX, E. J. KOLMES, I. E. OCHS, N. J. FISCH et R. GUEROULT (2019). Nonlinear ohmic dissipation in axisymmetric DC and RF driven rotating plasmas. *Physics of Plasmas* **26** 1, p. 012303. DOI : `10.1063/1.5064520`.

[Rax05] J.-M. RAX. Physique des plasmas. Sciences Sup. Dunod, 2005.

[Rei+09] M. P. REILLY, W. LEWIS et G. H. MILEY (2009). Magnetic field probes for use in radio frequency plasma. *Review of Scientific Instruments* **80** 5, p. 053508. DOI : `10.1063/1.3136907`.

[Rie91] K.-U. RIEMANN (1991). The Bohm criterion and sheath formation. *J. Phys. D Appl. Phys.* **24** 4, p. 493. DOI : `10.1088/0022-3727/24/4/001`.

[Ros+62] F. E. ROSE, M. T. TAYLOR et R. BOWERS (1962). Low-Frequency Magneto-Plasma Resonances in Sodium. *Phys. Rev.* **127** 4. p. 1122-1124. DOI : `10.1103/PhysRev.127.1122`.

[Sak+93] O. SAKAI, Y. YASAKA et R. ITATANI (1993). High radial confinement mode induced by dc limiter biasing in the HIEI tandem mirror. *Physical Review Letters* **70** 26. DOI : `10.1103/PhysRevLett.70.4071`.

[Sch+05] C. SCHRÖDER, O. GRULKE, T. KLINGER et V. NAULIN (2005). Drift waves in a high-density cylindrical helicon discharge. *Physics of Plasmas* **12** 4, p. 042103. DOI : `10.1063/1.1864076`.

[Sci+07] E. SCIME, R. HARDIN, C. BILOIU, A. M. KEESEE et X. SUN (2007). Flow, flow shear, and related profiles in helicon plasmas. *Physics of Plasmas* **14** 4, p. 043505. DOI : `10.1063/1.2716687`.

[Sha+01] K. P. SHAMRAI et S. SHINOHARA (2001). Spectral and spatial characterization of a radio frequency power absorption in high pressure helicon plasmas. *Physics of Plasmas* **8** 10, p. 4659-4674. DOI : `10.1063/1.1394779`.

[She+11] J. P. SHEEHAN et N. HERSHKOWITZ (2011). Emissive probes. *Plasma Sources Sci. Technol.* **20** 6, p. 063001. DOI : `10.1088/0963-0252/20/6/063001`.

[Shi18] S. SHINOHARA (2018). Helicon high-density plasma sources : physics and applications. *Advances in Physics X* **3** 1. p. 1420424. DOI : `10.1080/23746149.2017.1420424`.

[Shi22] S. SHINOHARA. High-Density Helicon Plasma Science From Basics to Applications. Springer Series in Plasma Science and Technology. Springer Nature, 2022. DOI : `10.1007/978-981-19-2900-7`.

[Shi+02] S. SHINOHARA et S. MATSUYAMA (2002). Observation of bistable density transitions in magnetized plasma by voltage-biased electrode. *Physics of Plasmas* **9** 11, p. 4540-4550. DOI : `10.1063/1.1516217`.

[Shi+96] S. SHINOHARA, Y. MIYAUCHI et Y. KAWAI (1996). Dynamic Formation of Excited Helicon Wave Structure and Estimation of Wave Energy Flux Distribution. *Jpn. J. Appl. Phys.* **35** 6A. p. L731. DOI : `10.1143/JJAP.35.L731`.

[Sil+10] J. A. SILLERO, D. ORTEGA, E. MUÑOZ-SERRANO et E. CASADO (2010). An experimental study of thoriated tungsten cathodes operating at different current intensities in an atmospheric-pressure plasma torch. *J. Phys. D Appl. Phys.* **43** 18, p. 185204. DOI : `10.1088/0022-3727/43/18/185204`.

[Sil+04] C. SILVA, I. NEDZELSKIY, H. FIGUEIREDO, R. GALVÃO, J. CABRAL et C. VARANDAS (2004). Improved confinement events triggered by emissive electrode biasing on the tokamak ISTTOK. *Nuclear Fusion* **44** 7, p. 799. DOI : `10.1088/0029-5515/44/7/012`.

[Smi+05] T. R. SMITH, J. MOEHLIS et P. HOLMES (2005). Low-Dimensional Modelling of Turbulence Using the Proper Orthogonal Decomposition : A Tutorial. *Nonlinear Dyn* **41** 1, p. 275-307. DOI : `10.1007/s11071-005-2823-y`.

[Smo+16] A. I. SMOLYAKOV, O. CHAPURIN, W. FRIAS, O. KOSHKAROV, I. ROMADANOV, T. TANG, M. UMANSKY, Y. RAITSES, I. D. KAGANOVICH et V. P. LAKHIN (2016). Fluid theory and simulations of instabilities, turbulent transport and coherent structures in partially-magnetized plasmas of E x B discharges. *Plasma Phys. Control. Fusion* **59** 1. p. 014041. DOI : `10.1088/0741-3335/59/1/014041`.

[Son+01] P. SONG, T. I. GOMBOSI et A. J. RIDLEY (2001). Three-fluid Ohm's law. *Journal of Geophysical Research Space Physics* **106** A5. p. 8149-8156. DOI : `10.1029/2000JA000423`.

[Ste+14] R. L. STENZEL et J. M. URRUTIA (2014). Magnetic antenna excitation of whistler modes. II. Antenna arrays. *Physics of Plasmas* **21** 12, p. 122108. DOI : `10.1063/1.4904360`.

[Ste+15] R. L. STENZEL et J. M. URRUTIA (2015). Helicons in Unbounded Plasmas. *Phys. Rev. Lett.* **114** 20. p. 205005. DOI : `10.1103/PhysRevLett.114.205005`.

[Sud+94] I. D. SUDIT et F. F. CHEN (1994). RF compensated probes for high-density discharges. *Plasma Sources Sci. Technol.* **3** 2. p. 162-168. DOI : `10.1088/0963-0252/3/2/006`.

[Sun+05] X. Sun, C. Biloiu et E. Scime (2005). Observation of resistive drift Alfvén waves in a helicon plasma. *Physics of Plasmas* **12** 10, p. 102105. doi : `10.1063/1.2054547`.

[Syd+19] R. D. Sydora, S. Karbashewski, B. Van Compernolle, M. J. Poulos et J. Loughran (2019). Drift-Alfvén fluctuations and transport in multiple interacting magnetized electron temperature filaments. *Journal of Plasma Physics* **85** 6, p. 905850612. doi : `10.1017/S0022377819000886`.

[Tak+14a] K. Takahashi, A. Chiba et A. Ando (2014). Modifications of wave and plasma structures by a mechanical aperture in a helicon plasma thruster. *Plasma Sources Sci. Technol.* **23** 6. p. 064005. doi : `10.1088/0963-0252/23/6/064005`.

[Tak+14b] K. Takahashi, T. Motomura, A. Ando, Y. Kasashima, K. Kikunaga, F. Uesugi et S. Hara (2014). Transport of a helicon plasma by a convergent magnetic field for high speed and compact plasma etching. *J. Phys. D Appl. Phys.* **47** 42. p. 425201. doi : `10.1088/0022-3727/47/42/425201`.

[Tar+09] A. Taran, D. Voronovich, S. Plankovskyy, V. Paderno et V. Filipov (2009). Review of LaB_6, Re-W Dispenser, and$BaHfO_3$-W Cathode Development. *IEEE Transactions on Electron Devices* **56** 5, p. 812-817. doi : `10.1109/TED.2009.2015615`.

[Tay+89] R. J. Taylor, M. L. Brown, B. D. Fried, H. Grote, J. R. Liberati, G. J. Morales, P. Pribyl, D. Darrow et M. Ono (1989). H-mode behavior induced by cross-field currents in a tokamak. *Phys. Rev. Lett.* **63**, p. 2365-2368. doi : `10.1103/PhysRevLett.63.2365`.

[Tha+14] S. C. Thakur, C. Brandt, L. Cui, J. J. Gosselin, A. D. Light et G. R. Tynan (2014). Multi-instability plasma dynamics during the route to fully developed turbulence in a helicon plasma. *Plasma Sources Sci. Technol.* **23** 4. p. 044006. doi : `10.1088/0963-0252/23/4/044006`.

[Tha+15] S. C. Thakur, C. Brandt, L. Cui, J. J. Gosselin et G. R. Tynan (2015). Formation of the Blue Core in Argon Helicon Plasma. *IEEE Transactions on Plasma Science* **43** 8. p. 2754-2759. doi : `10.1109/TPS.2015.2446537`.

[The+11] C. Theiler, I. Furno, A. Kuenlin, P. Marmillod et A. Fasoli (2011). Practical solutions for reliable triple probe measurements in magnetized plasmas. *Review of Scientific Instruments* **82** 1, p. 013504. doi : `10.1063/1.3516045`.

[The+89] K. Theilhaber et C. K. Birdsall (1989). Kelvin-Helmholtz Vortex Formation and Particle Transport in a Cross-Field Plasma Sheath. *Phys. Rev. Lett.* **62** 7. p. 772-775. doi : `10.1103/PhysRevLett.62.772`.

[Tho+05] E. Thomas Jr., A. Eadon et E. A. Wallace (2005). Suppression of low frequency plasma instabilities in a magnetized plasma column. *Physics of Plasmas* **12** 4, p. 042109. doi : `10.1063/1.1878833`.

[Tho+03] E. Thomas Jr., J. D. Jackson, E. A. Wallace et G. Ganguli (2003). Observations of low frequency oscillations due to transverse sheared flows. *Physics of Plasmas* **10** 5, p. 1191-1194. doi : `10.1063/1.1567287`.

[Tol14] P. Tolias (2014). On secondary electron emission and its semi-empirical description. *Plasma Phys. Control. Fusion* **56** 12, p. 123002. doi : `10.1088/0741-3335/56/12/123002`.

[Tol+20] P. Tolias, M. Komm, S. Ratynskaia et A. Podolnik (2020). Origin and nature of the emissive sheath surrounding hot tungsten tokamak surfaces. *Nuclear Materials and Energy* **25**, p. 100818. doi : `https://doi.org/10.1016/j.nme.2020.100818`.

[Tro+22] B. Trotabas et R. Gueroult (2022). Trade-off in perpendicular electric field control using negatively biased emissive end-electrodes. *Plasma Sources Sci. Technol.*, p. 13. DOI : 10.1088/1361-6595/ac4847.

[Tro22] B. Trotabas. Electric potential distribution control in a magnetized plasma column from emissive and biased electrodes. These de doctorat. Toulouse 3, 2022.

[Tsa+22] T. V. Tsankov, P. Chabert et U. Czarnetzki (2022). Foundations of magnetized radio-frequency discharges. *Plasma Sources Sci. Technol.* **31** 8. p. 084007. DOI : 10.1088/1361-6595/ac869a.

[Tsu+91] A. Tsushima et N. Sato (1991). Control of Radial Potential Profile by Biased Segmented Endplates in an ECR Plasma. *Journal of the Physical Society of Japan* **60** 8, p. 2665-2672. DOI : 10.1143/JPSJ.60.2665.

[Tyn+09] G. R. Tynan, A. Fujisawa et G. McKee (2009). A review of experimental drift turbulence studies. *Plasma Phys. Control. Fusion* **51** 11, p. 113001. DOI : 10.1088/0741-3335/51/11/113001.

[Tyn+06] G. R. Tynan, C. Holland, J. H. Yu, A. James, D. Nishijima, M. Shimada et N. Taheri (2006). Observation of turbulent-driven shear flow in a cylindrical laboratory plasma device. *Plasma Phys. Control. Fusion* **48** 4, p. S51. DOI : 10.1088/0741-3335/48/4/S05.

[Uri+15] L. Uribarri et E. H. Allen. Electron Transpiration Cooling for Hot Aerospace Surfaces. 20th AIAA International Space Planes and Hypersonic Systems and Technologies Conferen 2015. DOI : 10.2514/6.2015-3674.

[Urr+14] J. M. Urrutia et R. L. Stenzel (2014). Magnetic antenna excitation of whistler modes. I. Basic properties. *Physics of Plasmas* **21** 12, p. 122107. DOI : 10.1063/1.4904354.

[Van+19] B. Van Compernolle, M. J. Poulos et G. J. Morales (2019). Modifications produced on a large magnetized plasma column by a floating end-plate that is partially emissive : Experiment and theory. *Physics of Plasmas* **26** 12, p. 122102. DOI : 10.1063/1.5126415.

[Vin+22] S. Vincent, V. Dolique et N. Plihon (2022). High-speed imaging of magnetized plasmas : When electron temperature matters. *Physics of Plasmas* **29** 3, p. 032104. DOI : 10.1063/5.0083130.

[Vin+23] S. Vincent, V. Dolique et N. Plihon (2023). Nonlinear interactions of ion acoustic waves explored using fast imaging decompositions. *Physics of Plasmas* **30** 1, p. 012109. DOI : 10.1063/5.0131745.

[Vin21] S. P. H. Vincent. Azimuthal waves modification by current injection in a magnetized plasma column. Thèse de doct. Université Lyon 1, 2021.

[Vir+03] V. F. Virko, G. S. Kirichenko et K. P. Shamrai (2003). Parametric ion-acoustic turbulence in a helicon discharge. *Plasma Sources Sci. Technol.* **12** 2, p. 217. DOI : 10.1088/0963-0252/12/2/313.

[Wen+21] U. Wenzel, G. Schlisio, T. S. Pedersen, M. Marquardt, D. Pilopp, N. Rüter et A. Graband (2021). On the stability of thoriated tungsten cathodes in strong magnetic fields. *Review of Scientific Instruments* **92** 8, p. 083510. DOI : 10.1063/5.0049430.

[Whi+97] G. K. White et M. L. Minges (1997). Thermophysical properties of some key solids : An update. *Int J Thermophys* **18** 5, p. 1269-1327. DOI : 10.1007/BF02575261.

[Wur+22] S. E. WURZEL et S. C. HSU (2022). Progress toward fusion energy breakeven and gain as measured against the Lawson criterion. *Physics of Plasmas* **29** 6, p. 062103. DOI : `10.1063/5.0083990`.

[Yan+14] Z. YAN, G. R. MCKEE, R. FONCK, P. GOHIL, R. J. GROEBNER et T. H. OSBORNE (2014). Observation of the L-H Confinement Bifurcation Triggered by a Turbulence-Driven Shear Flow in a Tokamak Plasma. *Phys. Rev. Lett.* **112** 12. p. 125002. DOI : `10.1103/PhysRevLett.112.125002`.

[Yan+10] Z. YAN, G. R. TYNAN, C. HOLLAND, M. XU, S. H. MÜLLER et J. H. YU (2010). Shear flow and drift wave turbulence dynamics in a cylindrical plasma device. *Physics of Plasmas* **17** 3, p. 032302. DOI : `10.1063/1.3322823`.

[Yas+94] Y. Y. Y. YASAKA et Y. H. Y. HARA (1994). Role of Helicon Waves on High-Density Plasma Production. *Jpn. J. Appl. Phys.* **33** 10R. p. 5950. DOI : `10.1143/JJAP.33.5950`.

[Ye+00] M. Y. YE et S. TAKAMURA (2000). Effect of space-charge limited emission on measurements of plasma potential using emissive probes. *Physics of Plasmas* **7** 8, p. 3457-3463. DOI : `10.1063/1.874210`.

[Yos+99] M. YOSHINUMA, M. INUTAKE, R. HATAKEYAMA, T. KANEKO, K. HATTORI, A. ANDO et N. SATO (1999). Control of radial potential profile and related low-frequency fluctuations in an ECR-produced plasma. *Physics Letters A* **255** 4, p. 301-306. DOI : `10.1016/S0375-9601(99)00171-1`.

[Zha+24] T. ZHANG, Y. CUI, Z. XIA, B. ZHENG, F. HE et J. OUYANG (2024). Effects of cavity resonance and antenna resonance on mode transitions in helicon plasma. *Plasma Sources Sci. Technol.* **33** 4. p. 045016. DOI : `10.1088/1361-6595/ad3bea`.

[Zhu+23] W. ZHU, R. CUI, R. HAN, F. HE et J. OUYANG (2023). Observation of low-frequency oscillation in argon helicon discharge. *Plasma Sci. Technol.* **25** 2. p. 025401. DOI : `10.1088/2058-6272/ac8850`.

[Zie+21] D. ZIELKE, D. RAUNER, S. BRIEFI, S. LISHEV et U. FANTZ (2021). Self-consistent fluid model for simulating power coupling in hydrogen ICPs at 1 MHz including the non-linear RF Lorentz force. *Plasma Sources Sci. Technol.* **30** 6, p. 065011. DOI : `10.1088/1361-6595/ac0396`.

[Zoh96] H. ZOHM (1996). Edge localized modes (ELMs). *Plasma Phys. Control. Fusion* **38** 2, p. 105. DOI : `10.1088/0741-3335/38/2/001`.

[Zwe+07] S. J. ZWEBEN, J. A. BOEDO, O. GRULKE, C. HIDALGO, B. LABOMBARD, R. J. MAQUEDA, P. SCARIN et J. L. TERRY (2007). Edge turbulence measurements in toroidal fusion devices. *Plasma Phys. Control. Fusion* **49** 7, p. S1. DOI : `10.1088/0741-3335/49/7/S01`.

[Zwe+18] S. J. ZWEBEN, R. GUEROULT et N. J. FISCH (2018). Plasma mass separation. *Physics of Plasmas* **25** 9, p. 090901. DOI : `10.1063/1.5042845`.

ABSTRACT

Radial transport, azimuthal waves and instabilities are common features in magnetised plasmas, causing major challenges for plasma propulsion, plasma wakefield particle acceleration or fusion devices. Plasma properties control is desirable yet complex. This PhD thesis follows two goals, one being the use of an emissive cathode as a new parameter control and the other being the fundamental understanding of the helicon plasma operational stability.

Firstly, the role of the injection of electrons inside a magnetised plasma column has been studied experimentally and numerically. The experimental set-up is a 80 cm long and 20 cm diameter vacuum vessel connected to a 11 cm wide glass tube. The argon gas at a base pressure of 0.13 Pa is ionised by a 3-turns inductive radio-frequency antenna supplied at 1 kW. Magnetic field ranging from 170 G to 340 G, ensures a weak magnetisation of the plasma. A large tungsten hot cathode was placed at the end of the plasma column to inject an important thermionic current. Electrical and optical measurements of the cathode temperature revealed a highly inhomogeneous cathode temperature profile due to plasma–cathode interactions. A detailed thermal modelling solved numerically accurately reproduces the heterogeneous rise in temperature witnessed experimentally. The operating regime was predicted in excellent agreement with experimental results.

The fine understanding of the emissive cathode behaviour in presence of a surrounding magnetised plasma permitted to explore its influence on the plasma properties, and especially the plasma potential. An analytical approach based on a two-fluids plasma model and anisotropic electrical conductivities, predicting plasma potential control and plasma rotation regulation as a function of thermionic emission, has been applied and compared to a wide experimental dataset of plasma properties. The works presented confront the role of cross-field ion transport to experimental radial plasma potential scans with a semi-quantitative agreement, highlighting a new major application of emissive cathodes.

Finally, a state-of-the-art helicon plasma source has been implemented to produce higher ionisation rates. This new system required a complete characterisation of plasma properties through electrostatic probes and high-speed camera imaging. It reproduced well-known helicon plasma features such as E-H-W mode transitions, bistability and hysteresis, chirality emerging from the external magnetic field direction and the propagation of $m = +1$ whistler waves. Besides, it displayed complex behaviours such as H-W and W-W oscillations, or coexisting low-frequency Kelvin-Helmholtz and Rayleigh-Taylor instabilities. A strong multiscale core instability at 1080 G was also briefly investigated. Wave-mode identification based on theoretical growth rates, 2D-FT modal decomposition and POD has been conducted, unravelling the physical mechanisms at stake.